SORBONNE UNIVERSITÉ
CRÉATEURS DE FUTURS
DEPUIS 1257

Université Libanaise
École Doctorale
Sciences et Technologies
Doyen

Sorbonne Université
Université Libanaise

École Doctorale (397) Physique et Chimie des Matériaux
École Doctorale des Sciences et Technologie (EDST)
laboratoire de Chimie de la Matière Condensée de Paris / Centre de Recherche Scientifique en Ingénierie

Conception de Nouvelles Nanostructures de ZnO pour une Dégradation Photocatalytique Améliorée des Polluants Organiques

Par Elias Daher

Thèse de doctorat de Science des Matériaux

Dirigée par Wael Hamd et Christel Robert-Laberty

Présentée et soutenue publiquement le 18-09-2023

Devant un jury composé de :

M. Hubert Perrot, Directeur de Recherche, Sorbonne Université	Président
Mme Nathalie Herlin-Boime, Directrice de Recherche, CEA, Université Paris-Saclay	Rapporteur
M. Stéphane Parola, Professeur, Université Claude Bernard Lyon 1	Rapporteur
M. Houssam Rassy, Professeur, Université Américaine de Beyrouth	Examinateur
M. Wael Hamd, Professeur, Université Libanaise/Université de Balamand	Directeur
Mme Christel Robert-Laberty, Professeur, Sorbonne Université	Directrice
M. Cédric Boissière, Directeur de Recherche au CNRS, Sorbonne Université	Membre invité
M. Jean Chamoun, Professeur Assistant, Université Libanaise	Membre invité

Acknowledgment

This thesis is dedicated to every single person who helped me along my journey, both in their direct and indirect ways. First and foremost, I would love to thank my Directors, Professors Wael Hamd and Christel Laberty-Robert, for whom I express my sincere appreciation.

As this work began in the Lebanese University in Lebanon during a period of tremendous crisis, and sorrow, reaching this point would not have been possible without the enormous contribution of Wael. His unwavering support, guidance, and dedication to my scientific and personal development have left an indelible mark during this long and challenging journey. His belief in my abilities and his tireless investment of time and energy have played a crucial role in reaching this milestone. Wael's mentorship played a crucial part in offering me priceless scientific guidance throughout my academic path. It is his passion for scientific research that served as my driving force throughout all the obstacles I faced. I will never forget what he did, and especially his impact on my future! I am forever grateful for his mentorship and for the friendship!

In addition, as the second part of this work was completed at Sorbonne University in Paris, I would also love to thank Christel for all her sincere devotion and significant contributions to this thesis. With her mentorship and commitment, Christel played an essential role in providing invaluable scientific guidance to my academic journey. Her dedication have made a lasting impression on my path. I will always be grateful to her pivotal support in my career development, and her infectious positivity that has consistently brightened my path.

I would like thank my co-director, Jean Chamoun for his guidance and support throughout this endeavor, and Dr. Cedric Boissière for the stimulating scientific discussions and knowledge exchange that enriched my Ph.D. experience and made it more engaging and fulfilling. In this regard, I would like also to thank, Dr. Natasha Krins, Dr. François Ribot, Dr. Guylène Costentin, the RMES team, and all the members of the LCMCP, CRSI, and FCMT for the fruitful scientific discussions during my Ph.D., the CSTs, and the experimental work as well.

I would like also to thank the directors, and the deans of the doctoral schools at Sorbonne and Lebanese University, Professors Nadine Witkowski and Hassan Moubayed, as well as Fawaz Ali El Omar, in addition to all the staff members for all the support during in the administrative procedures.

I would love also to thank the dean of the engineering faculty of the Lebanese University, Professor Rafic Younes, and Prof. Clovis Francis for the chance of receiving this scholarship that financed my work, through the Horizon 2020 CLAIM project.

I am grateful to my jury members, Dr. Nathalie Herlin-Boime, Prof. Stéphane Parola, Prof. Houssam Rassi and Prof. Hubert Perrot, for their time, effort, and valuable feedback on my manuscript, which greatly contributed to the final evaluation of this work.

I would like to express my heartfelt appreciation to my family in Lebanon, the Mulsant family in France, and Marie Sylvie Buisson for their crucial support during my Ph.D.

Lastly, I deeply thank Liliana, who has been an incredible source of encouragement, and a part of my professional growth. Her presence has brought immense joy and motivation during this challenging journey.

Table of Contents

General Introduction **1**
Chapter I **9**
1. Introduction 10
2. Experimental Section 12
    2.1 Chemicals 12
    2.2 Synthesis of ZnO NRs on Glass Substrates 12
    2.3 Characterization Techniques 13
    2.4 Set-Up of the Photocatalytic System 14
3. Results and Discussion 15
    3.1 ZnO NRs Microstructure 15
    3.2 Kinetic Degradation of Phenol, Methylene Blue (MB), and Humic Acid (HA) 22
4. Conclusion 31

Chapter II **40**
1. Introduction 41
2. Experimental Section 44
    2.1 Chemicals 44
    2.2 Hydrothermal Growth of ZnO NRs on Glass Fiber Substrates 44
    2.3 Characterization Techniques 45
    2.4 Photocatalytic Set-Up 46
3. Results and Discussion 47
    3.1 Characterization of ZnO NRs 47
    3.2 Photocatalytic Degradation of Low-Density PP MPS 51
4. Conclusion 56

Chapter III **63**
1. Introduction 64
2. Experimental Section 66
    2.1 Chemicals 66
    2.2 ZnO Sol Preparation 66
    2.3 Synthesis of Wrinkled and Porous ZnO Multilayers 67
    2.4 Characterization 69
    2.5 Set-Up of the Photocatalytic System 70
3. Results and Discussion 71
    3.1 Microstructure of ZnO Thin Films 71

3.2 Pores and Wrinkle Evolution Mechanism 75
3.3 The Effect of Wrinkled Structure on ZnO Optical Properties 80
3.4 Photocatalytic efficiency of ZnO films 83
3.4.1 Optimization of ZnO Photocatalytic Activity 84
Conclusion 91
Chapter IV 99
1. Introduction 100
2. Experimental Section 102
2.1 Reagents and Materials 102
2.2 Characterization 102
2.3 Synthesis of Wrinkled and Porous ZnO Photocatalyst 103
2.4 Photo Fenton and Photocatalysis Processes 103
3. Results and Discussion 105
3.1 Characterization of the ZnO Photocatalyst 105
3.2 Optimization of H_2O_2 and Fe^{3+} Concentrations 107
3.3 Coupling of the Photocatalytic and Photo-Fenton-Like Process 111
Conclusion 114
Chapter V 121
1. Introduction 122
2. Results and Discussion 124
3. Conclusion and Outlook 137
4. Experimental Section 138
4.1 Reagents and Materials 138
4.2 Fabrication of Porous ZnO Thin Films 138
4.2.1 Sol-Gel Formulation 138
4.2.2 Dip Coating of the ZnO Thin Films 140
4.3 Characterization 140
4.3.1 Scanning Electron Microscopy (SEM) Coupled with Energy Dispersive X-ray Spectroscopy 140
4.3.2 X-ray Diffraction (XRD) 140
4.3.3 Spectroscopic Ellipsometry 141
4.3.4 In Situ Thermal Ellipsometry 141
4.3.5 Dynamic Light Scattering (DLS) 141
4.3.6 Fourier-Transformed Infradred 142
4.3.7 UV-vis Absrobance 142
4.3.8 Electrochemical Measuremnets 141

4.4 Set-Up of the Photocatalytic Self-Cleaning Systems 143

Conclusions and Perspectives 150

Annex: Novel 3D ZnO/TiO$_2$/FTO Coating 155

Glossary

FEG-SEM	Field Emission Gun – Scanning Electron Microscope
HRTEM	High-Resolution Transmission Electron Microscopy
XRD	X-ray diffraction
ATR-FTIR	Attenuated Total Reflection Fourier Transform Infrared Spectroscopy
UV-vis	Ultraviolet-Visible spectroscopy
EDX	Energy Dispersive X-ray
SAED	Selected Area Electron Diffraction
Eg	Bandgap Energy
NHE	Normal Hydrogen Electrode
ZnO	Zinc Oxide
TiO_2	Titanium Dioxide
CB	Conduction Band
VB	Valence Band
NRs	Nanorods
BCP	Block Copolymer
DiBCP	DiBlock Copolymer
TriBCP	TriBlock Copolymer
P(B)-*b*-P(EO)	Poly(Butadiene)-*b*-Poly(Ethylene Oxide)
PS	Polystyrene
P(EO)-P(PO)-P(EO)	Poly(Ethylene Oxide)–Poly(Propylene Oxide)–Poly(Ethylene Oxide)
FTO	Fluorine-doped Tin Oxide
EDLC	Electrochemical Double-Layer Capacitance
Cs	Specific Capacitance
ECSA	Electrochemical Surface Area
Kapp	Apparent Rate Constant
ROS	Reactive Oxygen Species

ZAD	Zinc Acetate Dihydrate
MEA	MonoEthanolAmine
MB	Methylene Blue
LA	Lauric Acid
MPs	Microplastics
LD-PP	Low-density Polypropylene
wt %	Weight Percentage

General Introduction

Environmental pollution has become a significant concern due to its detrimental effect on the environment, human health, and the economy[1]. Nowadays, the increasing levels of pollution can be directly attributed to the global trends of urbanization and industrialization, which are often driven by economic development[2,3]. Particularly, with a demographic burden of 8 billion people, and a continuously growing global industrialization reaching 6.1 % in 2021, today's world is facing an unprecedented existential threat to the sustainability of surface and groundwater[4–6]. For instance, loaded effluents with recalcitrant organic toxic molecules/particles from refineries, petrochemicals, pharmaceuticals, plasticizers, and many other industries, are continuously accumulating in aquatic mediums[3]. According to the World Health Organization (WHO), 80 % of human diseases are waterborne[7]. Recent studies also disclosed that 50 % of child deaths are correlated with water pollutants[8]. For example, phenol is used for the synthesis of a wide range of goods including herbicides, paints, cosmetics, lubricants, phenolic resins, plastics, and nylons, in addition to alkylphenols and ethoxylated products[9]. However, when reaching potable water, the molecules are broadly known for their harmful and recalcitrant nature[10,11], causing acute toxicity for humans above 0.001 mg/L[12]. Another comprehensive example is the contamination by microplastic (MP) particles. These are water-insoluble synthetic polymers of diverse shapes, with sizes ranging from 1 μm to 5 mm[13]. Because of their infinitesimal size, they can easily find their way into our food chain to threaten human health[14]. In this view, it was reported that a single human can ingest between 39,000 – 52,000 MPs per year via food and beverages, along with 4000 MPs to 90,000 MPs if tap and bottled water are respectively consumed[15]. Thus, there is an urgent need to tackle the menace of these pollutants.

In this regard, several technologies have been implemented including, but not limited to, flocculation, coagulation, activated carbon, chemical precipitation, biodegradation, filtration, evaporation, solvent extraction, ionic exchange, membrane separation/bioreactors, thermal degradation, incineration, and landfills[16–18]. However, these technologies show low efficiency, large utilization of energy and are bounded by economic constraints[16–18]. Consequently, advanced oxidation processes (AOPs) have emerged as efficient, promising, and inexpensive techniques, to tackle different types of organic pollutants in aquatic mediums[19,20]. Among these AOPs, heterogeneous photocatalysis is considered an efficient and cost-effective method due to the photocatalyst reusability and lack of secondary disposal requirements[3,21,22]. It is based on generating highly reactive oxygen species (ROS) such as hydroxyl radical ($OH^{\bullet}$) and superoxide radical ($O_2^{\bullet -}$) upon the exposure of a photocatalytic material to light[23]. These ROS are well-known for their strong oxidation capacity toward organic matter, leading to their mineralization into less harmful molecules such as H_2O and CO_2[24]. For instance, hydroxyl radical ranks as the second-highest oxidizing species with a potential $E^o(OH/H_2O) = +2.8$ vs. normal hydrogen electrode (NHE)[20].

Amongst different types of photocatalytic materials, Zinc oxide (ZnO) has been attracting large attention due to its strong oxidation ability, low production price, and low degree of toxicity to marine/human life[18,25–27]. Furthermore, ZnO is an intrinsic n-type semiconductor due to the presence of native defects such as O vacancies and Zn interstitials in its crystalline structure, which can potentially increase the range of its visible light absorption[28,29]. Moreover, its wurtzite structure consists of alternatively arranged Zn^{2+} and O^{2-} ions along the c-axis, leading to different polarity behavior at the polar c-planes and the nonpolar m-planes. This, polarity effect has been shown to strongly affect the surface reactivity and stability in addition to the optical and electrical properties[30]. Because the crystalline structure and the physical properties of ZnO are dependent on the synthesis methods, thus, its photocatalytic activity is quite different according to the selected preparation procedure[28,31–34].

Although different works have reported the synthesis of nanostructured ZnO for photocatalytic applications[25], few studies discussed the effect of different microstructures on the degradation kinetics. Moreover, to the best of our knowledge, no previous research focused on how the difference in molecular structures and bond energy affects the rate of decomposition. Thus, this thesis addresses the removal of organic pollutants over different ZnO nanostructures, synthesized by sol-gel and hydrothermal growth processes. Particularly, it focuses on: i) the degradation mechanisms of organic molecules with different chemical structures, ii) the photo-oxidation of low – density polypropylene microplastics under natural sunlight, and iii) the enhancement of a ZnO/Fenton coupled process. The objective and novelty of this work are developed in the following section.

- **Objectives of the Ph.D. work and Manuscript outline**

First, the degradation mechanisms and kinetics were investigated on different pollutant molecules (phenol, methylene blue, and humic acid) and polypropylene microplastics over ZnO thin films and nanorods. Porous and wrinkled films were synthesized by finely tuning the heat treatment during the sol-gel dip coating technique, while ZnO nanorods were deposited on mesh and glass substrates via seeding and hydrothermal growth. Although the new materials exhibited high surface area and showed improved degradation kinetics, nonetheless the rapid recombination rate of the e^-/h^+ pairs continued hampering its photocatalytic activity. To overcome this limitation, ZnO films were coupled to other oxide materials (TiO_2) or an oxidation process (photo-Fenton-like). The creation of this semiconductor-semiconductor heterojunction enables an enhancement of electron transfer in the new structure. Moreover, with the ZnO/Fenton processes running concurrently some of the photo-generated electrons by the photocatalyst are trapped by the iron catalyst, thus inhibiting electron-hole recombination from one side, and accelerating the regeneration of the Fenton reagent (Fe^{3+}/Fe^{2+}) from the other side.

Furthermore, novel ZnO thin films were designed for self-cleaning applications. The system couples the sol-gel chemistry with the self-assembly of polymers under optimized heat treatment. Our approach reported for the first time the successful fabrication of macroporous ZnO coatings by controlling the heat treatment of hybrid organic/inorganic films. Different templating agents were used spanning from homo to di- and tri-block copolymers. The results of this study provide valuable insights into the development of highly efficient photocatalytic systems for environmental remediation. These themes are further developed in the following chapter.

In Chapter I, we address the impact of the pollutant's molecular structure on the degradation kinetics. Although closely related parameters to the degradation kinetics such as the wavelength and intensity of the irradiation light, the type of semiconductor, and the photocatalyst-pollutant ratio, have been extensively studied in the literature. However, the effect of the structure of organic is barely investigated. For this reason, ZnO nanorods (NRs) were coated on glass substrates to evaluate the influence of the oxidative pathway of three different aromatic structures: i) a single aromatic ring (phenol), ii) a poly-aromatic ring (methylene blue), and iii) a complex macromolecule (humic acid). The kinetics of all the chosen molecules were studied to disclose the correlation between the apparent degradation rate constants with the dissociation bond energy and the number of oxidation steps in each organic molecule.

In Chapter II, the photocatalytic degradation was further investigated at the macroscopic level, on polymeric particles such as Microplastics (MPs). In this view, the photodegradation of low-density polypropylene (LD-PP) microplastics (300 μm) was studied over 16 consecutive days of real sunlight irradiation. ZnO nanorods (NRs) were hydrothermally coated on a glass-fibers mesh to trap the LD-PP particles close to the photocatalyst. The evolution of the microplastics' oxidation was quantified by tracking their carbonyl index (CI) over the experimental time through the ATR-FTIR technique and by evaluating the cracks formation and the changes in their microstructure by SEM-FEG.

In Chapter III, novel template-free, porous, and wrinkled ZnO thin films were designed by sol-gel dip-coating technique. The material was characterized by SEM, HRTEM, XRD, UV-vis, and ellipsometry. A wrinkled structure with a porosity of ~ 22–25 % and an average pore diameter of ~ 24 nm were revealed, promoting the adsorption of pollutants onto the films' surface. The photocatalytic activity of ZnO films denoted the efficiency of this facile and low-cost approach of synthesis compared to some laborious methods using organic templates and/or doping metals.

In Chapter IV, a homogenous photo-Fenton-like process was coupled with the previously designed ZnO thin films at near-neutral pH. The photo-generated electrons by the photocatalyst are trapped by the iron catalyst, thus inhibiting electron-hole recombination, and accelerating the Fe^{3+}/Fe^{2+} regeneration respectively.

In Chapter V, a novel macroporous ZnO structure was designed by coupling the sol-gel chemistry with the self-assembly of polymers. The advanced synthesis approach resulted in macroporous ZnO films of controlled pore diameter. The photodegradation of organic species at ZnO interfaces demonstrated that this new porous structure exhibited higher degradation kinetics due to its unique porosity that provides a higher surface area with respect to the amount of the coated material. These results highlight the potential of these ZnO coatings for self-cleaning coatings with photocatalytic properties.

References

(1) Manisalidis, I.; Stavropoulou, E.; Stavropoulos, A.; Bezirtzoglou, E. Environmental and Health Impacts of Air Pollution: A Review. *Front. Public Health* **2020**, *8*, 14. https://doi.org/10.3389/fpubh.2020.00014.

(2) Hamd, W.; Daher, E. A.; Tofa, T. S.; Dutta, J. Recent Advances in Photocatalytic Removal of Microplastics: Mechanisms, Kinetic Degradation, and Reactor Design. *Front. Mar. Sci.* **2022**, *9*, 885614. https://doi.org/10.3389/fmars.2022.885614.

(3) Daher, E. A.; Riachi, B.; Chamoun, J.; Laberty-Robert, C.; Hamd, W. New Approach for Designing Wrinkled and Porous ZnO Thin Films for Photocatalytic Applications. *Colloids and Surfaces A: Physicochemical and Engineering Aspects* **2023**, *658*, 130628. https://doi.org/10.1016/j.colsurfa.2022.130628.

(4) *World Bank National Accounts Data, and OECD National Accounts Data Files.*; World Bank Group. https://data.worldbank.org/indicator/NV.IND.TOTL.KD.ZG (accessed 2023-02-23).

(5) Kumar, P. S.; Prasannamedha, G. Biological and Chemical Impacts on Marine Biology. In *Modern Treatment Strategies for Marine Pollution*; Elsevier, 2021; pp 11–27. https://doi.org/10.1016/B978-0-12-822279-9.00006-3.

(6) Zhao, B.; Huang, F.; Zhang, C.; Huang, G.; Xue, Q.; Liu, F. Pollution Characteristics of Aromatic Hydrocarbons in the Groundwater of China. *Journal of Contaminant Hydrology* **2020**, *233*, 103676. https://doi.org/10.1016/j.jconhyd.2020.103676.

(7) Qadri, R.; Faiq, M. A. Freshwater Pollution: Effects on Aquatic Life and Human Health. In *Fresh Water Pollution Dynamics and Remediation*; Qadri, H., Bhat, R. A., Mehmood, M. A., Dar, G. H., Eds.; Springer Singapore: Singapore, 2020; pp 15–26. https://doi.org/10.1007/978-981-13-8277-2_2.

(8) Lin, L.; Yang, H.; Xu, X. Effects of Water Pollution on Human Health and Disease Heterogeneity: A Review. *Front. Environ. Sci.* **2022**, *10*, 880246. https://doi.org/10.3389/fenvs.2022.880246.

(9) Mohammadi, S.; Kargari, A.; Sanaeepur, H.; Abbassian, K.; Najafi, A.; Mofarrah, E. Phenol Removal from Industrial Wastewaters: A Short Review. *Desalination and Water Treatment* **2015**, *53* (8), 2215–2234. https://doi.org/10.1080/19443994.2014.883327.

(10) Anku, W. W.; Mamo, M. A.; Govender, P. P. Phenolic Compounds in Water: Sources, Reactivity, Toxicity and Treatment Methods. In *Phenolic Compounds - Natural Sources, Importance and Applications*; Soto-Hernández, M., Palma-Tenango, M., Garcia-Mateos, M. del R., Eds.; InTech, 2017. https://doi.org/10.5772/66927.

(11) Rodríguez, I.; Llompart, M. P.; Cela, R. Solid-Phase Extraction of Phenols. *Journal of Chromatography A* **2000**, *885* (1–2), 291–304. https://doi.org/10.1016/S0021-9673(00)00116-3.

(12) Subramaniam, K.; Ahmad, S. A.; Shaharuddin, N. A. Mini Review on Phenol Biodegradation in Antarctica Using Native Microorganisms. *APJMBB* **2020**, 77–89. https://doi.org/10.35118/apjmbb.2020.028.1.08.

(13) Frias, J. P. G. L.; Nash, R. Microplastics: Finding a Consensus on the Definition. *Marine Pollution Bulletin* **2019**, *138*, 145–147. https://doi.org/10.1016/j.marpolbul.2018.11.022.

(14) Hodson, M. E.; Duffus-Hodson, C. A.; Clark, A.; Prendergast-Miller, M. T.; Thorpe, K. L. Plastic Bag Derived-Microplastics as a Vector for Metal Exposure in Terrestrial Invertebrates. *Environ. Sci. Technol.* **2017**, *51* (8), 4714–4721. https://doi.org/10.1021/acs.est.7b00635.

(15) Cox, K. D.; Covernton, G. A.; Davies, H. L.; Dower, J. F.; Juanes, F.; Dudas, S. E. Human Consumption of Microplastics. *Environ. Sci. Technol.* **2019**, *53* (12), 7068–7074. https://doi.org/10.1021/acs.est.9b01517.

(16) Amin, M. T.; Alazba, A. A.; Manzoor, U. A Review of Removal of Pollutants from Water/Wastewater Using Different Types of Nanomaterials. *Advances in Materials Science and Engineering* **2014**, *2014*, 1–24. https://doi.org/10.1155/2014/825910.

(17) Crini, G.; Lichtfouse, E. Advantages and Disadvantages of Techniques Used for Wastewater Treatment. *Environ Chem Lett* **2019**, *17* (1), 145–155. https://doi.org/10.1007/s10311-018-0785-9.

(18) Uheida, A.; Mejía, H. G.; Abdel-Rehim, M.; Hamd, W.; Dutta, J. Visible Light Photocatalytic Degradation of Polypropylene Microplastics in a Continuous Water Flow System. *Journal of Hazardous Materials* **2021**, *406*, 124299. https://doi.org/10.1016/j.jhazmat.2020.124299.

(19) Zhang, M.; Dong, H.; Zhao, L.; Wang, D.; Meng, D. A Review on Fenton Process for Organic Wastewater Treatment Based on Optimization Perspective. *Science of The Total Environment* **2019**, *670*, 110–121. https://doi.org/10.1016/j.scitotenv.2019.03.180.

(20) Hamd, W. S.; Dutta, J. Heterogeneous Photo-Fenton Reaction and Its Enhancement upon Addition of Chelating Agents. In *Nanomaterials for the Detection and Removal of Wastewater Pollutants*; Elsevier, 2020; pp 303–330. https://doi.org/10.1016/B978-0-12-818489-9.00011-6.

(21) Ghosh, S.; Kouamé, N. A.; Ramos, L.; Remita, S.; Dazzi, A.; Deniset-Besseau, A.; Beaunier, P.; Goubard, F.; Aubert, P.-H.; Remita, H. Conducting Polymer Nanostructures for Photocatalysis under Visible Light. *Nature Mater* **2015**, *14* (5), 505–511. https://doi.org/10.1038/nmat4220.

(22) Zeng, L.; Guo, X.; He, C.; Duan, C. Metal–Organic Frameworks: Versatile Materials for Heterogeneous Photocatalysis. *ACS Catal.* **2016**, *6* (11), 7935–7947. https://doi.org/10.1021/acscatal.6b02228.

(23) Miklos, D. B.; Remy, C.; Jekel, M.; Linden, K. G.; Drewes, J. E.; Hübner, U. Evaluation of Advanced Oxidation Processes for Water and Wastewater Treatment – A Critical Review. *Water Research* **2018**, *139*, 118–131. https://doi.org/10.1016/j.watres.2018.03.042.

(24) Habib, I. Y.; Burhan, J.; Jaladi, F.; Lim, C. M.; Usman, A.; Kumara, N. T. R. N.; Tsang, S. C. E.; Mahadi, A. H. Effect of Cr Doping in CeO2 Nanostructures on Photocatalysis and H2O2 Assisted Methylene Blue Dye Degradation. *Catalysis Today* **2021**, *375*, 506–513. https://doi.org/10.1016/j.cattod.2020.04.008.

(25) Lee, K. M.; Lai, C. W.; Ngai, K. S.; Juan, J. C. Recent Developments of Zinc Oxide Based Photocatalyst in Water Treatment Technology: A Review. *Water Research* **2016**, *88*, 428–448. https://doi.org/10.1016/j.watres.2015.09.045.

(26) Dobretsov, S.; Sathe, P.; Bora, T.; Barry, M.; Myint, M. T. Z.; Abri, M. A. Toxicity of Different Zinc Oxide Nanomaterials at 3 Trophic Levels: Implications for Development of Low-Toxicity Antifouling Agents. *Environ Toxicol Chem* **2020**, *39* (7), 1343–1354. https://doi.org/10.1002/etc.4720.

(27) Li, Y.; Wei, G.; Shao, L.; Li, Z.; Yu, F.; Liu, J.; Yang, X.; Lu, Q.; Li, A.; Huang, Y.; Zhang, L. Green Synthesis of Red Mud Based ZnO Fe2O3 Composite Used for Photo-Fenton Reaction under Visible Light. *Journal of Cleaner Production* **2019**, *207*, 717–727. https://doi.org/10.1016/j.jclepro.2018.10.051.

(28) Rezapour, M.; Talebian, N. Comparison of Structural, Optical Properties and Photocatalytic Activity of ZnO with Different Morphologies: Effect of Synthesis Methods and Reaction Media. *Materials Chemistry and Physics* **2011**, *129* (1–2), 249–255. https://doi.org/10.1016/j.matchemphys.2011.04.012.

(29) Al-Sabahi, J.; Bora, T.; Al-Abri, M.; Dutta, J. Efficient Visible Light Photocatalysis of Benzene, Toluene, Ethylbenzene and Xylene (BTEX) in Aqueous Solutions Using Supported Zinc Oxide Nanorods. *PLoS ONE* **2017**, *12* (12), e0189276. https://doi.org/10.1371/journal.pone.0189276.

(30) Guillemin, S.; Rapenne, L.; Roussel, H.; Sarigiannidou, E.; Brémond, G.; Consonni, V. Formation Mechanisms of ZnO Nanowires: The Crucial Role of Crystal Orientation and Polarity. *J. Phys. Chem. C* **2013**, *117* (40), 20738–20745. https://doi.org/10.1021/jp407120j.

(31) Han, X.-G.; He, H.-Z.; Kuang, Q.; Zhou, X.; Zhang, X.-H.; Xu, T.; Xie, Z.-X.; Zheng, L.-S. Controlling Morphologies and Tuning the Related Properties of Nano/Microstructured ZnO Crystallites. *J. Phys. Chem. C* **2009**, *113* (2), 584–589. https://doi.org/10.1021/jp808233e.

(32) Huang, M.; Yan, Y.; Feng, W.; Weng, S.; Zheng, Z.; Fu, X.; Liu, P. Controllable Tuning Various Ratios of ZnO Polar Facets by Crystal Seed-Assisted Growth and Their Photocatalytic Activity. *Crystal Growth & Design* **2014**, *14* (5), 2179–2186. https://doi.org/10.1021/cg401676r.

(33) Mekasuwandumrong, O.; Pawinrat, P.; Praserthdam, P.; Panpranot, J. Effects of Synthesis Conditions and Annealing Post-Treatment on the Photocatalytic Activities of ZnO Nanoparticles in the Degradation of Methylene Blue Dye. *Chemical Engineering Journal* **2010**, *164* (1), 77–84. https://doi.org/10.1016/j.cej.2010.08.027.

(34) Giraldi, T. R.; Santos, G. V. F.; De Mendonca, V. R.; Ribeiro, C.; Weber, I. T. Effect of Synthesis Parameters on the Structural Characteristics and Photocatalytic Activity of ZnO. *Materials Chemistry and Physics* **2012**, *136* (2–3), 505–511. https://doi.org/10.1016/j.matchemphys.2012.07.018.

Chapitre I

Ce chapitre a été soumis au journal: Catalysis Communication (Under Review)

Impact de la Structure Chimique des Polluants sur le Taux de Dégradation Photocatalytique

Les cinétiques de dégradation photocatalytiques dépendent généralement de plusieurs paramètres, tels que la longueur d'onde, l'intensité de la source d'irradiation, les propriétés physicochimiques du semi-conducteur, le pH, ainsi que le rapport molaire photocatalyseur:polluant[1–4]. Bien que ces paramètres aient été largement étudiés dans la literature[5–7], très peu de travaux discutent l'effet de la structure chimiques sur la cinétique de dégradation. Plus spécialement, cette discussion a été principalement abordé d'un point de vue mécanistique.

Dans ce chapitre, nous étudions l'effet de la structure chimique de polluants sur leurs cinétiques de dégradation photocatalytique. Plus précisément, le photocatalyseur est composé des nano bâtonnets d'oxyde de zinc (ZnO) déposés sur des substrats de verre par une méthode de croissance hydrothermale. Le choix de ce photocatalyseur se justifie par son caractère peu polaire entrainant une sélectivité d'adsorption comparable aux molécules polaires choisies: i) le phénol (un seul cycle aromatique), ii) le bleu de méthylène (MB : plusieurs cycles aromatiques), iii) l'acide humique (HA : macromolécule complexe)[8]. L'extraction des constants de vitesses apparents ($kaap$) à partir des données cinétiques, montrent l'ordre de dégradation suivant : MB ($kaap$ 0.0486 min^{-1}) > HA ($kaap$ 0.0314 min^{-1}) > phénol ($kaap$ 0.0228 min^{-1}). Bien que les structures moléculaires du bleu de méthylène (MB) et d'acide humique (HA) soient plus complexes que celle du phénol, ils présentent des taux de dégradation relativement plus élevés. Cette observation est à relier à la structure des molécules et donc à leur énergie de dissociation. Plus précisément, étant donné que le MB présente une énergie de dissociation de liaison relativement faible (~ 76 kcal.mol^{-1}) notamment au niveau du ($C–S^{+}=C$), ce dernier a tendance à s'oxyder plus facilement que le phénol sous l'attaque des espèces réactives de l'oxygène (ROS)[9–12]. De manière similaire, l'acide humique possède une énergie de dissociation de liaisons (C–N–C et C–O–

C) beaucoup plus faible (~ 79 kcal.mol^{-1})[13], comparée au phénol (minimum ~ 97 kcal.mol^{-1})[10], ce qui accélère visiblement sa dégradation. Ces résultats montrent le lien entre l'énergie de liaison des différentes molécules (ou énergie de dissociation) et les cinétiques de dégradation. Plus elle est faible, plus les cinétiques sont rapides.

Références

(1) Chaudhari, S. M.; Gawal, P. M.; Sane, P. K.; Sontakke, S. M.; Nemade, P. R. Solar Light-Assisted Photocatalytic Degradation of Methylene Blue with Mo/TiO2: A Comparison with Cr- and Ni-Doped TiO2. *Res Chem Intermed* **2018**, *44* (5), 3115–3134. https://doi.org/10.1007/s11164-018-3296-1.

(2) Enesca, A.; Isac, L. The Influence of Light Irradiation on the Photocatalytic Degradation of Organic Pollutants. *Materials (Basel)* **2020**, *13* (11), 2494. https://doi.org/10.3390/ma13112494.

(3) Afkari, M.; Masoudpanah, S. M.; Hasheminiasari, M.; Alamolhoda, S. Effects of Iron Oxide Contents on Photocatalytic Performance of Nanocomposites Based on G-C3N4. *Sci Rep* **2023**, *13* (1), 6203. https://doi.org/10.1038/s41598-023-33338-1.

(4) Kumar, A. A Review on the Factors Affecting the Photocatalytic Degradation of Hazardous Materials. *MSEIJ* **2017**, *1* (3). https://doi.org/10.15406/mseij.2017.01.00018.

(5) Reza, K. M.; Kurny, A.; Gulshan, F. Parameters Affecting the Photocatalytic Degradation of Dyes Using TiO2: A Review. *Appl Water Sci* **2017**, *7* (4), 1569–1578. https://doi.org/10.1007/s13201-015-0367-y.

(6) Ni, C.; Huang, M.; Ren, M.; Li, X.; Yan, X.; Sun, S. Effect of Microstructure and Reaction Medium on Photocatalytic Performance and Stability of BiO Catalyst for CO2 Reduction. *Catalysis Communications* **2023**, *173*, 106565. https://doi.org/10.1016/j.catcom.2022.106565.

(7) Bel Hadjltaief, H.; Ben Ameur, S.; Da Costa, P.; Ben Zina, M.; Elena Galvez, M. Photocatalytic Decolorization of Cationic and Anionic Dyes over ZnO Nanoparticle Immobilized on Natural Tunisian Clay. *Applied Clay Science* **2018**, *152*, 148–157. https://doi.org/10.1016/j.clay.2017.11.008.

(8) Rogé, V.; Guignard, C.; Lamblin, G.; Laporte, F.; Fechete, I.; Garin, F.; Dinia, A.; Lenoble, D. Photocatalytic Degradation Behavior of Multiple Xenobiotics Using MOCVD Synthesized ZnO Nanowires. *Catalysis Today* **2018**, *306*, 215–222. https://doi.org/10.1016/j.cattod.2017.05.088.

(9) Luo, Y.-R. *Handbook of Bond Dissociation Energies in Organic Compounds*, 0 ed.; CRC Press, 2002. https://doi.org/10.1201/9781420039863.

(10) Leopoldini, M.; Marino, T.; Russo, N.; Toscano, M. Antioxidant Properties of Phenolic Compounds: H-Atom versus Electron Transfer Mechanism. *J. Phys. Chem. A* **2004**, *108* (22), 4916–4922. https://doi.org/10.1021/jp037247d.

(11) Huang, F.; Chen, L.; Wang, H.; Yan, Z. Analysis of the Degradation Mechanism of Methylene Blue by Atmospheric Pressure Dielectric Barrier Discharge Plasma. *Chemical Engineering Journal* **2010**, *162* (1), 250–256. https://doi.org/10.1016/j.cej.2010.05.041.

(12) Su, S.; Liu, Y.; Liu, X.; Jin, W.; Zhao, Y. Transformation Pathway and Degradation Mechanism of Methylene Blue through β-FeOOH@GO Catalyzed Photo-Fenton-like System. *Chemosphere* **2019**, *218*, 83–92. https://doi.org/10.1016/j.chemosphere.2018.11.098.

(13) Moldoveanu, S. C. General Information About Pyrolysis. In *Pyrolysis of Organic Molecules*; Elsevier, 2019; pp 1–33. https://doi.org/10.1016/B978-0-444-64000-0.00001-9.

(14) Andrady, A. L. Microplastics in the Marine Environment. *Marine Pollution Bulletin* **2011**, *62* (8), 1596–1605. https://doi.org/10.1016/j.marpolbul.2011.05.030.

(15) Uheida, A.; Mejía, H. G.; Abdel-Rehim, M.; Hamd, W.; Dutta, J. Visible Light Photocatalytic Degradation of Polypropylene Microplastics in a Continuous Water Flow System. *Journal of Hazardous Materials* **2021**, *406*, 124299. https://doi.org/10.1016/j.jhazmat.2020.124299.

(16) Frias, J. P. G. L.; Nash, R. Microplastics: Finding a Consensus on the Definition. *Marine Pollution Bulletin* **2019**, *138*, 145–147. https://doi.org/10.1016/j.marpolbul.2018.11.022.

(17) Cox, K. D.; Covernton, G. A.; Davies, H. L.; Dower, J. F.; Juanes, F.; Dudas, S. E. Human Consumption of Microplastics. *Environ. Sci. Technol.* **2019**, *53* (12), 7068–7074. https://doi.org/10.1021/acs.est.9b01517.

(18) Hamd, W.; Daher, E. A.; Tofa, T. S.; Dutta, J. Recent Advances in Photocatalytic Removal of Microplastics: Mechanisms, Kinetic Degradation, and Reactor Design. *Front. Mar. Sci.* **2022**, *9*, 885614. https://doi.org/10.3389/fmars.2022.885614.

(19) Liu, Q.; Liu, S.; Xia, L.; Hu, P.; Lv, Y.; Liu, J.; Chen, Z.; Huang, Y.; Li, G. Effect of Annealing-Induced Microstructure on the Photo-Oxidative Degradation Behavior of Isotactic Polypropylene. *Polymer Degradation and Stability* **2019**, *162*, 180–195. https://doi.org/10.1016/j.polymdegradstab.2019.02.023.

Investigating the Impact of Chemical Structures on the Photocatalytic Degradation Rates over ZnO Nanorods: An Oxidative Pathways Perspective

Elie A. Daher[‡†], *Cédric Boissière*[†], *Christel Laberty Robert*[†⁑], *Wael Hamd* [₱]*

[‡] Petrochemical Engineering Department, Faculty of Engineering III, CRSI, Lebanese University, Rafic Hariri Campus, Hadat, Lebanon.

[†] Laboratoire Chimie de la Matière Condensée de Paris LCMCP, Sorbonne Université, UPMC Paris 06, 4 Place Jussieu, 75005 Paris, France

[⁑] RS2E, Réseau Français sur le Stockage Electrochimique de l’Energie, CNRS 3459, 80039 Cedex 1 Amiens, France

[₱] Chemical Engineering Department, Faculty of Engineering, University of Balamand, P.O. Box 33, El-Koura, Lebanon.

KEYWORDS: ZnO Nanorods, Photocatalysis, Organic pollutants, Molecular structures, Degradation rate, Pseudo-first order.

ABSTRACT: The kinetics of photocatalytic degradation depend closely on several parameters, such as the source and intensity of the irradiation light, as well as the semiconductor nature, the photocatalyst-pollutant ratio, and the structure of organic molecules. However, the effect of the latter on degradation rates is rarely investigated in the literature and is mostly discussed from a mechanistic point of view. In this work, ZnO nanorods were coated on glass substrates and used as photocatalysts

to evaluate the kinetic behavior of three different aromatic structures: i) a single aromatic ring (phenol), ii) a poly-aromatic ring (methylene blue), and iii) a complex macromolecule (humic acid). The kinetics of all the tested molecules obey a pseudo-first-order model regardless of the initial concentrations (5, 10, and 20 ppm), and the apparent rate constants are largely controlled by the bond dissociation energy and the number of oxidation steps in each organic molecule. For instance, methylene blue presents the weakest dissociation bond energy and the highest degradation rate constant ($k = 0.0714\ min^{-1}$) compared to humic acid ($k = 0.0314\ min^{-1}$) and phenol ($k = 0.0228\ min^{-1}$) for 5 ppm initial concentrations. Thus, its degradation is 3 and 1.4 times faster than that of humic acid and phenol respectively.

1. INTRODUCTION

A prospering chemical industry plays a pivotal role in today's economy by contributing to 4% of global GDP and directly employing over 15 million people[1–3]. Furthermore, the progressive industrial development is continuously providing the main economic sectors with a wide range of chemicals that are used in the production of many end products spanning from pharmaceuticals[4] and fertilizers[5], to smartphones[6] and machinery components[7]. However, when some of these chemicals reach out into the ecosystem, they become a major environmental concern[8–10]. Amongst these, phenol for example is used either as a raw material or an intermediate (35% of its total usage) to synthesize a variety of products, including herbicides, paints, cosmetics, lubricants, phenolic resins, plastics, and nylons, in addition to alkylphenols and ethoxylated components[11]. However, the phenolic molecule is broadly known for its acute toxicity and recalcitrant nature[12,13], causing great harm once discharged into the environment[14,15].

Humic acid (HA) conversely, is a macromolecule of polymeric phenolic structure, classified as a natural organic matter (NOM) and widely found in soil and surface water[16–18]. The substance has been mainly known for its important role in soil fertility in addition to its usage in chemical industries such as the production of concrete, ceramics, plastics, and papers[19]. However, the existence of these molecules in water supplies is very undesirable because they display a high sorbing capacity for other pollutants in aquatic mediums and increase the level of total organic pollution[20–22]. For instance, their reaction with halogen-based oxidants leads to the formation of trihalomethanes (THM) with potential carcinogenic effects[23,24]. HA is also known for inducing cytotoxicity in many mammalian cells, growth retardation, and apoptosis in fibroblasts[25–27].

Methylene blue (MB) is a hetero-polyaromatic dye of wide industrial application, however, as the molecule is non-biodegradable, its accumulation in aquatic mediums could increase its toxicity to harmful levels[28,29]. In addition, the molecule was recently found to be toxic and carcinogenic[30].

On the other side, due to the recalcitrant nature of these molecules, conventional treatment techniques (flocculation, coagulation, activated carbon, chemical precipitation, biodegradation, and filtration) and established recovery processes (evaporation, solvent extraction, ionic exchange, membrane separation/bioreactors, and electrochemical) have proven to be quite inefficient[31,32]. In this context, advanced oxidation processes (AOPs) such as photochemical oxidation, catalytic wet oxidation, sonochemical oxidation, O_3 oxidation, electrochemical oxidation, Fenton oxidation, and photocatalysis are viewed as advantageous and cost-effective technologies for treating a wide spectrum of recalcitrant organic molecules in aquatic environments[33]. Particularly heterogeneous photocatalysis, a technique that is based on harvesting light energy, has been rapidly gaining attention[34–38]. Generally, the system consists of generating electron-hole pairs when a semiconducting material is exposed to a light source[39]. These electron-hole pairs are known for their capability of producing highly reactive oxygen species (ROS) such as hydroxyl radical ($OH^\bullet$) and superoxide radical ($O_2^{\bullet -}$) with strong oxidation ability toward organic matter, leading to their total mineralization into less harmful compounds such as H_2O and CO_2[40]. Therefore, secondary disposal treatments are not required.

The photocatalytic degradation of these molecules is mainly governed by several parameters, such as the pH, molecules' initial concentrations, light source/intensity, and the presence of electron and hole scavengers[41,42]. Although the effect of such parameters on the degradation kinetics has been extensively studied in numerous works[41,43–46], to the best of our knowledge, one has reported yet how the difference in molecular structures and bond energy impact the rate of decomposition. In this sense, as each molecule follows a specific degradation pathway, the resulting oxidation steps will determine the apparent rate constant. In this work, we present a comparative degradation study of different molecular structures over zinc oxide (ZnO) nanorods (NRs) deposited on glass substrates by a hydrothermal growth method. The choice of ZnO nanorods is supported by the non-polar characteristic of the majority of its surface, which exhibits low selectivity toward polar molecules[47]. For this reason, the kinetic data was extracted from the photocatalytic degradation of i) single aromatic ring (phenol, M.W. = 94.11 g/mol), ii) poly-aromatic rings (MB, M.W. = 319.85 g/mol), and iii) complex macromolecules (HA, M.W. > 1000 g/mol).

2. Experimental Section

2.1 Chemicals

Analytical grade Zinc acetate dihydrate ($Zn(CH_3COO)_2 \cdot 2H_2O$) (97%), Zinc nitrate hexahydrate ($Zn(NO_3)_2 \cdot 6H_2O$), and Hexamethylenetetramine ($(CH_2)_6N_4$) were purchased from ACROS organics Spain. Phenol detached crystals (99+ %) were obtained from Fischer Scientific U.K. Humic Acid (technical grade) was obtained from Sigma–Aldrich Canada. Methylene Blue (laboratory reagent) was obtained from Paskem, India.

2.2 Synthesis of ZnO NRs on Glass Substrate

ZnO NRs were coated on microscope glass slides (4.5 cm × 2.5 cm) by a hydrothermal growth process[48]. First, the glass substrates were successively cleaned with soap water, ethanol, acetone, and deionized water (DI). Then, a ZnO layer was seeded on the preheated substrates at 350 ºC, by spraying 10 mM zinc acetate in DI water at a flow rate of 1 mL/min as seen in Scheme 1. Subsequently, the seeded substrates were soaked in a chemical bath at 90 ºC, containing equimolar concentrations (10 mM) of zinc nitrate hexahydrate as a precursor and hexamethylenetetramine as a nanostructuring agent. The bath was replenished with both solutions every 5 hours, and the cycle was repeated 3 times. The as-grown NRs were thoroughly washed with DI water and post-heated in the air at T = 350 ºC for 1 h to ensure the removal of any remaining organic compounds within the metal oxide structure.

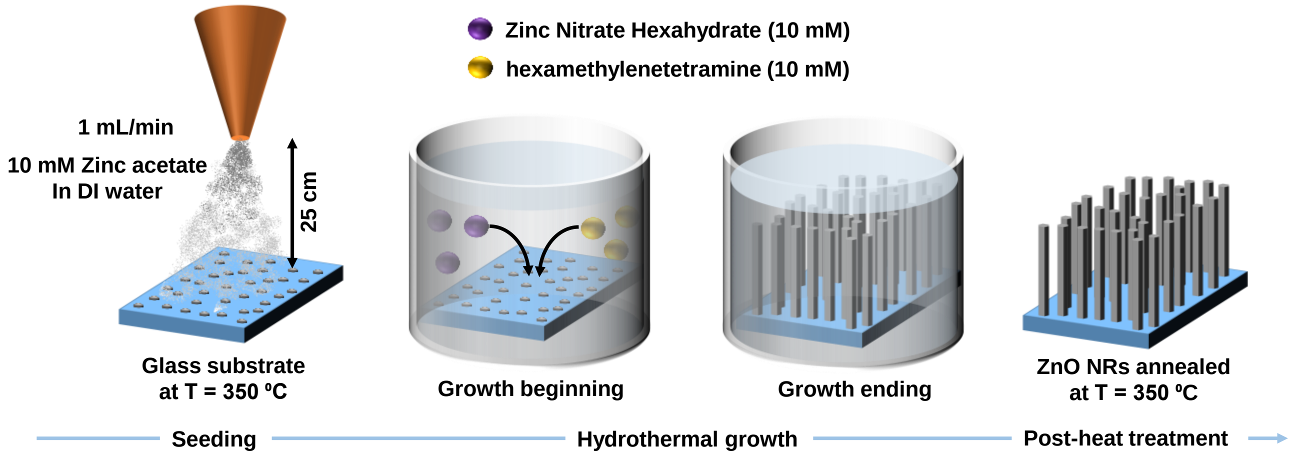

Scheme 1. Synthesis procedure of the ZnO nanorods.

2.3 Characterization Techniques

The crystalline structure of the ZnO films was analyzed with a D8 Discover X-ray diffractometer, equipped with a Cu emitter anode (Kα_1 and Kα_2 of wavelength 1.54056 and 1.5444 Å respectively) and a 1D LYNEXEYE XE-T detector (Bruker).

The surface morphology and the film's thickness were evaluated by a field emission gun scanning electron microscope (FEG-SEM) model MIRA 3 TESCAN, set to a voltage of 15 kV.

The nanostructure and the lattice fringes' spacing were examined by a transmission electron microscope (TEM) model TWIN 120 (TECNAI SPIRIT) equipped with a JEOL 100CF apparatus and coupled with selected area electron diffraction (SAED).

The functional groups at the film's surface were analyzed by Fourier-transformed infrared (FTIR) in attenuated total reflection (ATR) mode with an incidence angle of 45^o and a 4 cm^{-1} resolution using a Spectrum 400 model from PerkinElmer, equipped with an FR-DTGS detector (fast recovery Deuterated Triglycine Sulfate detector).

The absorbance of the deposited ZnO nanorod films and the tracking of the degradation of organic molecules were performed at room temperature by using a Specord 50 plus UV-visible spectrophotometer from Analytic-Jena, Germany.

2.4 Set-Up of the Photocatalytic System

The as-prepared ZnO (NRs) films were immersed inside Pyrex photocatalytic reactors of 50 ml, filled with 45 ml MB, phenol, and HA aqueous solutions, respectively. Three different concentrations of 5, 10, and 20 ppm were used for each molecule. In all cases, the dipped area of the films corresponds to 10 cm^2. The photocatalytic reactors were initially kept in the dark for 12 h to demonstrate the insignificant adsorption of the polar molecules at the non-polar surface of the ZnO NRs. The photocatalytic tests were carried out at RT for 6 hours using a UVA lamp of $\lambda = 365$ nm. The light source was placed 5 cm from the photocatalyst surface. The received illuminance by the photocatalysts was measured by a Testo 450 luxmeter of ±3 % precision (from Testo, France) and found to be equal to ~ 500 lux. The photocatalytic degradation of the organic molecules was tracked by UV-visible spectroscopy with a sampling interval of 1 hour.

3. Results and Discussion

3.1 ZnO NRs Microstructure

- **Morphology**

A field emission gun scanning electron microscope was used to evaluate the films' microstructure. Figure 1a reveals well-aligned nanorods with respect to each other. All the rods are characterized by hexagonal shapes, straight sides, and regular ends (Figures 1a & b). The lengths, and diameters of ZnO NRs were estimated by analyzing the SEM micrographs with ImageJ software. For that purpose, the rods' boundaries were carefully highlighted by a threshold segmentation step to identify them. As a result, the nanorods are characterized by an average diameter (w) of ~ 50 nm (population standard deviation $\sigma = 4.7$ nm), a length (l) of ~ 1.55 µm (population standard deviation $\sigma = 0.14$ µm), and a remarkably high ratio of l:w ~ 31.

The morphology was further investigated by transmission electron microscopy. Figure 1c shows a typical low-magnification TEM image of an intact section that was finely extracted from the ZnO film. As could be seen, each nanorod has a uniform diameter along its entire length, indicating their anisotropic growth along the +c-axis direction (inset of Figure 1c). Moreover, the individual rods appear to be well-faceted along the ±c-axis (Figure 1d) with highly defined crystal boundaries and very low surface defects (inset of Figure 1d).

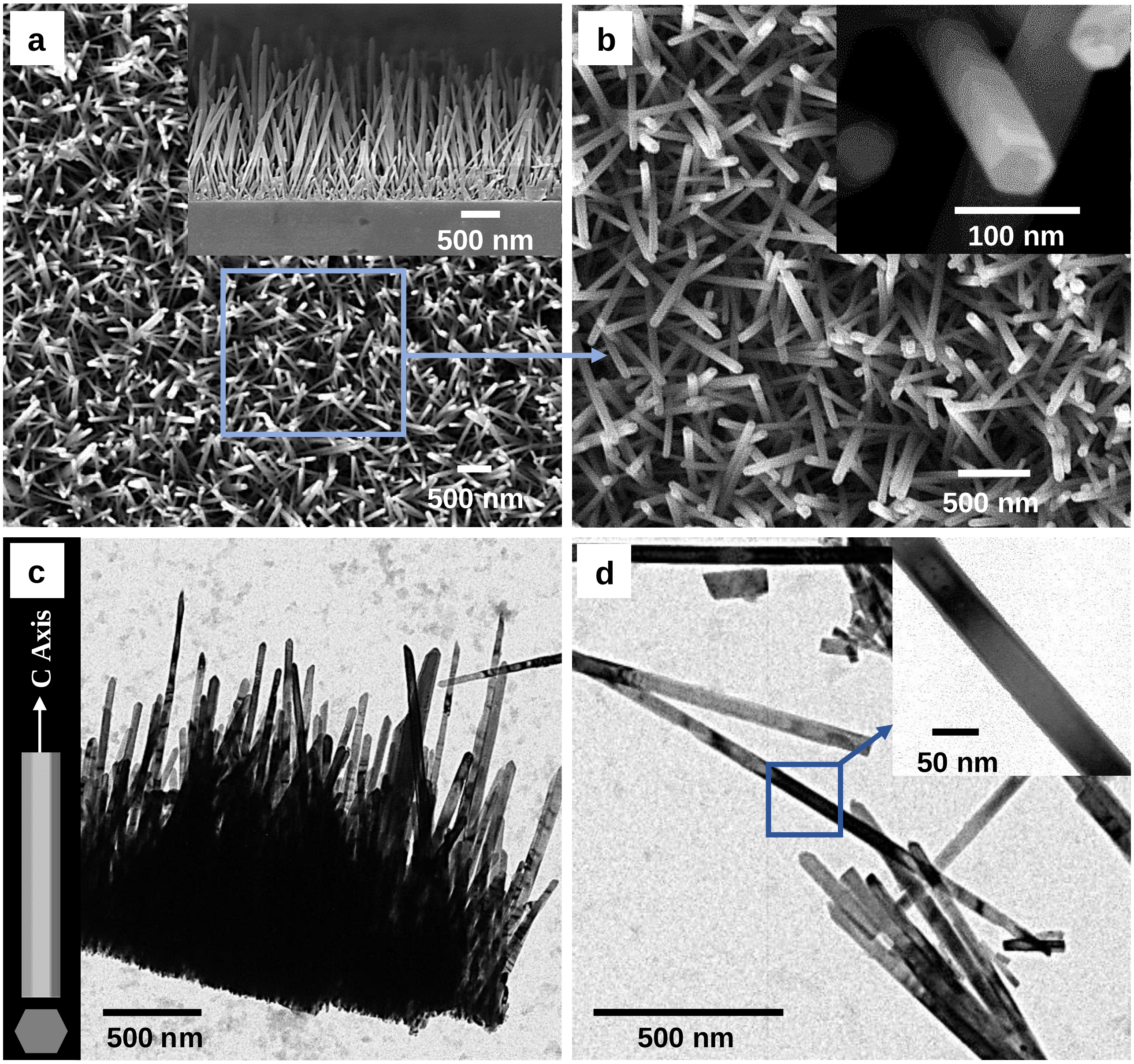

Figure 1. **(a)** SEM top view image for ZnO NRs after post-heat treatment in the air at 350 ºC for 1h. Inset: Cross-sectional view of "a", **(b)** High magnification view of "a". Inset: Nanorods with a common hexagonal shape, **(c)** TEM images of an extracted bush-like fragment from the ZnO film of "a". Inset: Schematic illustration of a grown rod in the +c direction, **(d)** Free-standing ZnO nanorod separated with sonication. Inset: Zoomed-in view of "d".

- **Surface Area**

Because the BET technique requires both destructive removal of the thin film and large sample size (over 100 coated glass substrates), the exposed surface area (SA) of the ZnO nanorod films was estimated from Eq. 1 assuming that all the rods are characterized by a regular hexagonal shape[49]:

$$\mathrm{SA} = \left[\frac{1}{4}\left(3\sqrt{3}w^{2}\right) + 3wl\right] d \qquad \text{(Eq. 1)}$$

where *w*, *l,* and *d* refer to the average diameter, the average length, and the average density of the nanorods (counting per μm^2), respectively. The latter was obtained from the analysis of the SEM micrographs as previously depicted (~5.5 NRs/μm^2). Therefore, a SA of ~ 350 cm^2 was measured, corresponding to a 10 cm^2 coated substrate. After measuring this surface area, the film was carefully extracted with a fine blade and weighted with an analytical balance. As a result, a specific surface area of ~ 25 m^2/g was obtained, quite comparable to its observed counterpart on synthesized material with similar procedures[49] and threefold higher than that of commercial ZnO nanorods[50]. Moreover, the obtained SA is higher than most of the reported values for different microstructures of ZnO such as tetrapods[50], flower-like microparticles[51], nanowires[52], macroporous foam[53], and porous thin films[54]. Although hollow sphere ZnO films exhibit a relatively higher SA, their fabrication procedure is quite complex and expensive, in addition to the requirement of carbon-based templates[55]. The synthesis approaches, type of nanostructure, and surface areas of ZnO coatings in this work and other recent studies are listed in Table 1.

Table 1. Synthesis approaches and surface areas of ZnO coatings with different morphologies.

Reference	**Synthesis Approach**	**ZnO micro/nanostructure**	**Surface-Pore diameter**
Sulciute et al. [50]	combustion method	Tetrapods	~22 m^2/g
Pugliese et al. [51]	hydrothermal process	Flower-like nanoparticles	~20 m^2/g
Gu et al. [52]	Hydrothermal method	Nanowires	~10.4 m^2/g
Kovačič et al.[53]	High Internal Phase Emulsion Technique	Macroporous foam	~5.5 m^2/g
Smith et al. [54]	Magnetron sputtering	Porous thin films	~~11.8 m^2/g
Zhang et al. [55]	Template-based method with carbon microspheres	Hollow spheres	~ 37 m^2/g
This study	**Hydrothermal method**	**Nanorods**	**~ 25 m^2/g**

- **Crystalline Structure**

The XRD data of the as-synthesized ZnO nanorods show a characteristic pattern of hexagonal wurtzite crystal structure confirmed by JCPDS No. 01-086-3978 with a = b = 3.248 Å and c = 5.202 Å (Figure 2a)[56–58]. The strongest diffraction at 34.46° demonstrates a preferential orientation along the (002) crystal plane, confirming the anisotropic growth in the +c-axis direction. The formation of this nanostructure during the hydrothermal-growth mechanism is primarily directed by the hexamethylenetetramine structuration agent (non-polar). It was suggested that this molecule preferentially chelates and covers the non-polar sides of the hexagonal rods, leaving, therefore, its top polar facet exposed for growth[59]. Consequently, this leads to the formation of ZnO nanorods with high crystallinity.

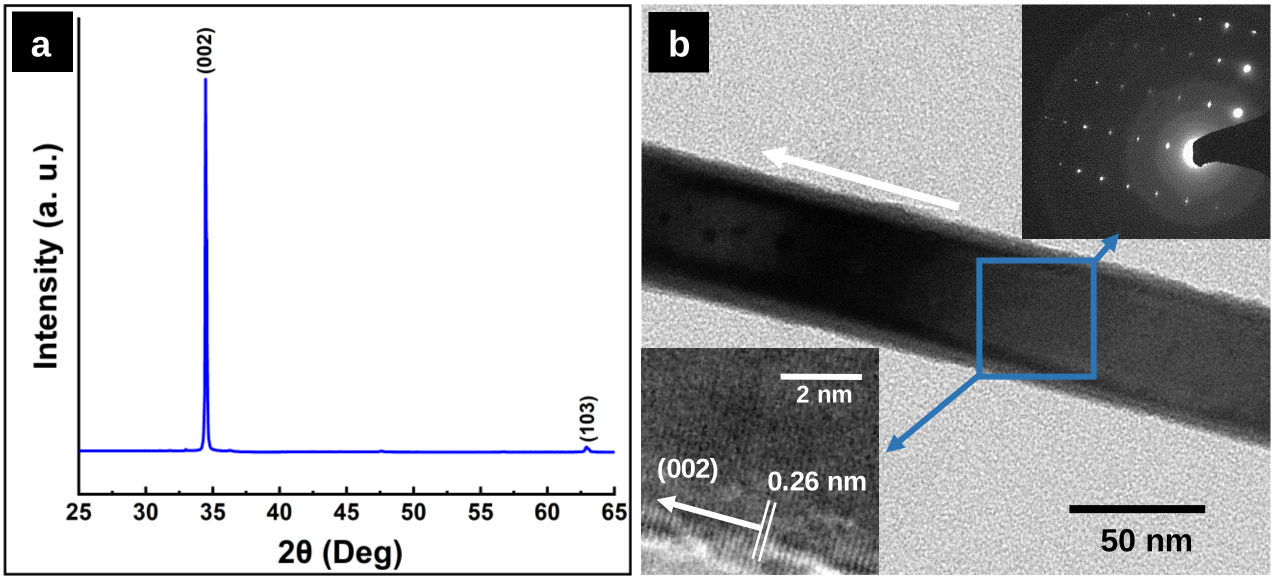

Figure 2. **(a)** XRD pattern of ZnO NRs after post-heating in the air at 350 °C for 1h, **(b)** TEM image of a free-standing ZnO nanorod. The insets show a high magnification area of "b" and its SAED respectively.

Additionally, the TEM images in Figure 2b (lower inset) clearly reveal that the crystal boundaries are well-defined and characterized by regular lattice fringes of 0.262 nm. This value corresponds to the interplanar spacing of d_{002} and further supports the nanorods' preferential orientation in the (002) direction. The SAED pattern on the other side came to combine altogether regularly organized dots that correspond to the (002) growth direction with a weakly pronounced circular ring representing the (103) plan (Figure 2b (upper inset)). This agrees well with the XRD measurement.

Besides the well-known impact of the crystallinity on the photoactivity of ZnO, another important factor that significantly affects it, is the material texturization[60,61]. Therefore, mono-crystal ZnO with a low-defected surface was reported to exhibit superior photocatalytic activity, making it a good candidate for the removal of organic contaminants[58,62].

- **Surface Functions**

The vibrational behavior of Zn-O bonds was characterized by FTIR spectroscopy and plotted in Figure 3. The spectrum of zinc oxide nanorods shows 4 functional groups located at 540, 750, 895, and 1063 cm^{-1}.

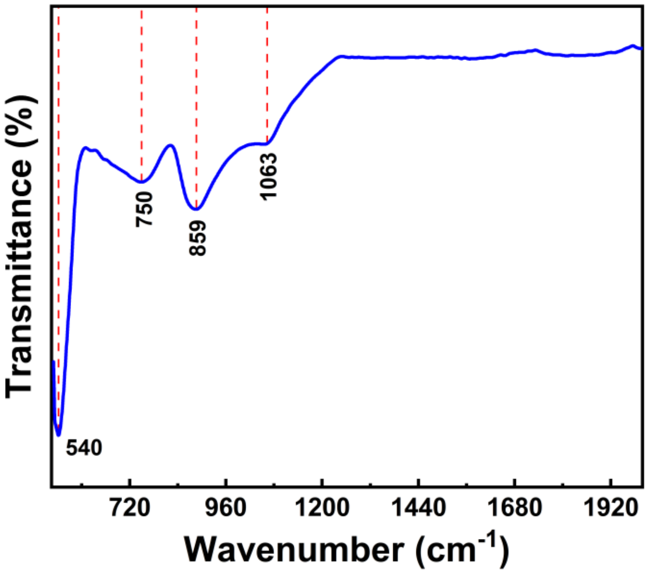

Figure 3. ATR-FTIR spectrum of the ZnO NRs after a post-heating in the air at 350 ºC for 1h.

The strong absorption peaks at ~ 540 and 750 cm^{-1} represent the stretching vibrations of Zn–O bonds[63–66] and thus confirm the formation of zinc oxide coatings. In addition, it was suggested by da Silva-Neto et al. that the observed peak in the region of 895 cm^{-1} is mainly associated with the tetrahedral coordination of Zn within the wurtzite ZnO lattice[67]. The weakest peak at ~ 1063 cm^{-1} mainly arises from the C–O stretching vibration band of chemisorbed organic molecules at the film's surface[63]. This confirms the need for annealing the as-synthesized films at T > 350 ºC.

- **Optical Properties**

The optical properties of the films were determined at various steps of the synthesis of ZnO i) after deposition of seeded particles: ii) after drying the as-grown ZnO nanorods at RT, and iii) after annealing the nanorods at 350 ºC. As seen in Figure 4a, the seeded ZnO layer (black curve) shows a significant absorption in the UV region < 400 nm corresponding to its intrinsic bandgap energy[68].

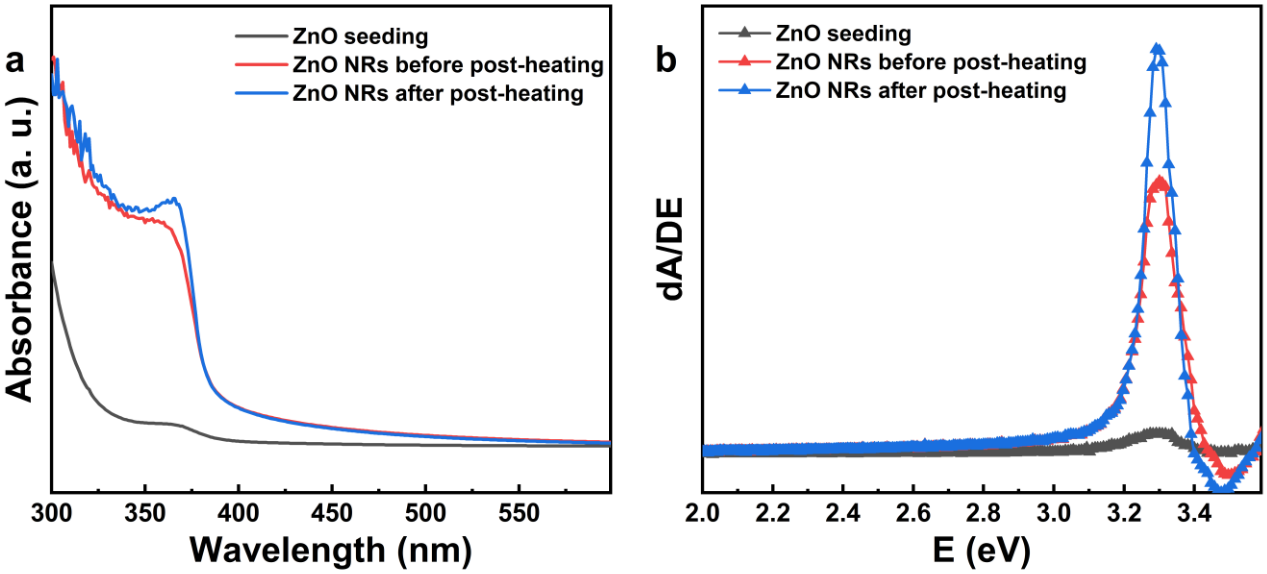

Figure 4. **(a)** Room-temperature UV-vis absorbance spectrum of seeded ZnO, ZnO NRs after the hydrothermal growth and ZnO NRs after the post-heat treatment in the air for 1h, **(b)** Optical bandgap (Eg) obtained from the derivative of the absorbance spectrum of (c).

As the ZnO nanorods are grown and the film thickens, the absorbance intensity strongly increases by ~ 10 times at λ = 367 nm. This surge is accompanied by the appearance of a weak absorption area in the visible region from 400 to 800 nm (red curve). Such a progressive increase in the absorption profile from the visible to UV range is probably due to the film's diffusivity. Moreover, the effect of heat treatment on the nanorods resulted in a slight increase in the light absorbance below 400 nm. This behavior is probably due to the complete removal of chemisorbed organic precursors and the fine enhancement in crystallinity (blue curve)[69,70]. The optical band gap (Eg) of ZnO was also calculated at each of the synthesis stages. For this reason, the first derivative of the absorbance with respect to photon energy (dA/dE), was plotted as a function of photon energy (E) (Figure 4b)[71]. Hence, Eg could be found at the first maximum on the lower energy side. It is observed that upon the heat treatment, the optical bandgap slightly decreases from 3.30 to 3.29 eV, probably due to the formation of new donor and/or acceptor levels within the ZnO energy gap, such as oxygen and zinc defects[58].

3.2 Kinetic Degradation of Phenol, Methylene Blue (MB) and Humic Acid (HA)

The photodegradation kinetics are intimately related to the type and intensity of irradiation sources, the bandgap energy of the photocatalyst, and the initial concentration of organic molecules, in addition to their molecular structures[41,72,73]. The latter could strongly affect the degradation rate due to the difference in the molecular geometry and bond energy of each component. Thus, the photocatalytic degradation was performed as a function of the type and the initial concentration of organic molecules under UVA irradiation of $\lambda = 365$ nm. The choice of a 365 nm irradiation wavelength is encouraged by the very low absorbance of organic molecules in the UVA range, limiting their degradation by photolysis.

- **Effect of the initial concentrations**

Generally, the generation/migration of the photo-generated electron-hole pairs and subsequently their direct reaction (or that of the produced ROS) with the organic molecules occur successively[74]. In this respect, each of these steps may become rate-determining for the photocatalytic mechanisms. Hence, it was shown that at high initial concentrations (C_0) of organic compounds ($K.C_0 \gg 1$), the reaction rate is mainly governed by the generation and migration of $e^- - h^+$ pairs, and thus it slowly increases with C_0 or remains constant (zero-order reaction)[75]. However, at relatively low initial concentrations ($1 \gg K.C_0$), the chemical reactions between the ROS and the molecules determine the reaction rate, which may be commonly noticed by a significant increase of K while increasing C_0[75–77]. Thus, to predict the effect of the molecule structures on the degradation rate and oxidative mechanisms, a relatively low initial concentration range between 5 and 20 ppm was chosen. The photocatalytic degradations of phenol and humic acid (5, 10, and 20 ppm) were conducted at RT, under an irradiation source of 365 nm, and over an experimental time of 360 minutes, as shown in Figures 5a & b.

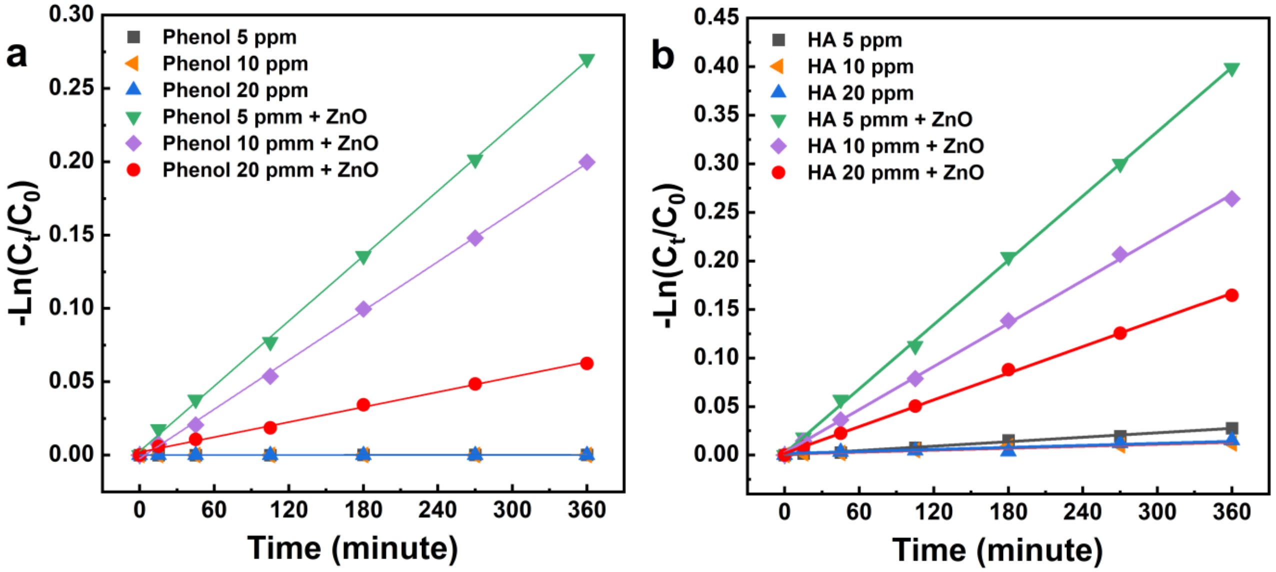

Figure 5. Comparative photodegradation kinetics under UVA light of λ = 365 nm between $C_0 = 5$, 10, and 20 ppm of **(a)** Phenol and **(b)** Humic acid.

The degradation kinetics were calculated from the Langmuir–Hinshelwood kinetic model (Eq.2)[78]:

$$r = -\frac{dC}{dt} = \frac{Kr.K.C}{1+K.C} \tag{Eq.2}$$

where r, C, K, K_r, and t represent the reaction rate, molecule concentration at time t, adsorption equilibrium constant, limiting rate constant of reaction at maximum coverage, and contact time, respectively.

At small (mM) initial concentrations, $(K.C_0 \ll 1)$, Eq. 2 may be simplified to the apparent rate order (Eq.3)[78]:

$$r = -\frac{dC}{dt} = K_{app}.C \tag{Eq.3}$$

where K_{app}, is the apparent degradation rate. Simple integration of this equation for $C = C_0$ at $t = 0$ gives Eq. 4:

$$\ln\left(\frac{C_0}{C}\right) = K_{app}.t \qquad \text{(Eq.4)}$$

Therefore, K_{app} may be obtained from the slope of the linear curve in the plot of $Ln\ (C_0/C)$ vs. t, where (C_0/C) is equal to (A_0/A)according to the Beer-Lambert law Eq.5.

$$A_0 = \varepsilon \times L \times C_0 \qquad \text{(Eq.5)}$$

wherein A_0, A, C_0, C, ε & L refer respectively to the molecule light absorbance at t_0, molecule light absorbance at t, molecule concentration at t_0, molecule concentration at t, molar absorptivity, and length of the light path.

The photocatalytic degradation curves reveal that the kinetics of all the tested molecules obey the pseudo-first order. In the absence of the ZnO NRs, the blank solutions manifest insignificant K_{apps}. For instance, slightly detectable rates of ~ 6×10^{-7} min^{-1}, and 8×10^{-5} min^{-1}, are observed independently of the initial concentrations of phenol, and HA, respectively, indicating the negligible effect of photolysis (Figure 5). However, this behavior is more pronounced in the case of MB where a K_{apps} of 1×10^{-4} min^{-1} is detected due to its higher absorbance in the UVA range (data not shown). After using the photocatalysts, the kinetic rates drastically increase, for different initial concentrations of the three pollutants. For example, the degradation rate of HA registers higher values of 0.0314 min^{-1} and 0.013 min^{-1} for 5 and 20 ppm, respectively, compared to the blank sample (8×10^{-5} min^{-1}). The decrease in the observed first-order rate constant at high concentration is certainly due to the occupation of all catalytic sites on the ZnO NRs surface. The photocatalytic performance of the synthesized nanorods came quite comparable to the reported kinetic data for various ZnO photocatalysts[79,80]. In addition, the non-polar characteristic of the majority of ZnO NRs surface, which exhibits low selectivity toward polar molecules[47] makes them a suitable material for this study.

- **Influence of oxidative pathways on degradation rates**

The effect of the oxidative pathways on the degradation rate was investigated by choosing the lowest initial concentration of 5 ppm (shorter experimental time) for each of the organic molecules. The evolution of the UV-vis spectra of the MB, phenol, and HA is reported in Figures 6a, b, and c for over 6 hours of irradiation.

MB is generally characterized by 3 absorption bands (Figure 6a). The first two are of high energy $\pi - \pi^*$ transition, corresponding to the B-Band and E-Band of the benzene ring, and located at $\lambda \sim 247$ and 293 nm, respectively[81,82]. The third peak, which is responsible for the blue color of the dissolved dye, corresponds to the low energy $n - \pi^*$ transition around 665 nm (where n is the free doublet on the nitrogen and sulfur atom of the chromophore groups, –C=N and –S=C, respectively)[83]. The observed shoulder at 605 nm refers to a vibronic transition 0-1 (level 0 of the ground state to level 1 of the excited state)[81,84]. To monitor the decomposition of the MB at the different molecular bonds, its photodegradation was tracked at the wavelengths 247, 293, and 665 nm. The same analytical method was applied to the phenol molecule. Its photodegradation was then tracked at $\lambda \sim 192$, 212, and 270 nm, referring to the $\pi - \pi^*$ transitions of the E_1-Band, E_2-Band, and B-Band, respectively, as seen in Figure 6b[82]. The inset provides better visualization of the absorbance variation of the molecule at $\lambda \sim 270$ nm. As for the humic acid, the photodegradation of the molecule was studied at the single peak of $\lambda \sim 250$ nm. This peak corresponds to the $\pi - \pi^*$ electronic transitions of the polycyclic aromatic structure, including the phenolic group, aniline derivatives of benzoic acids, and polyenes (Figure 6c)[85].

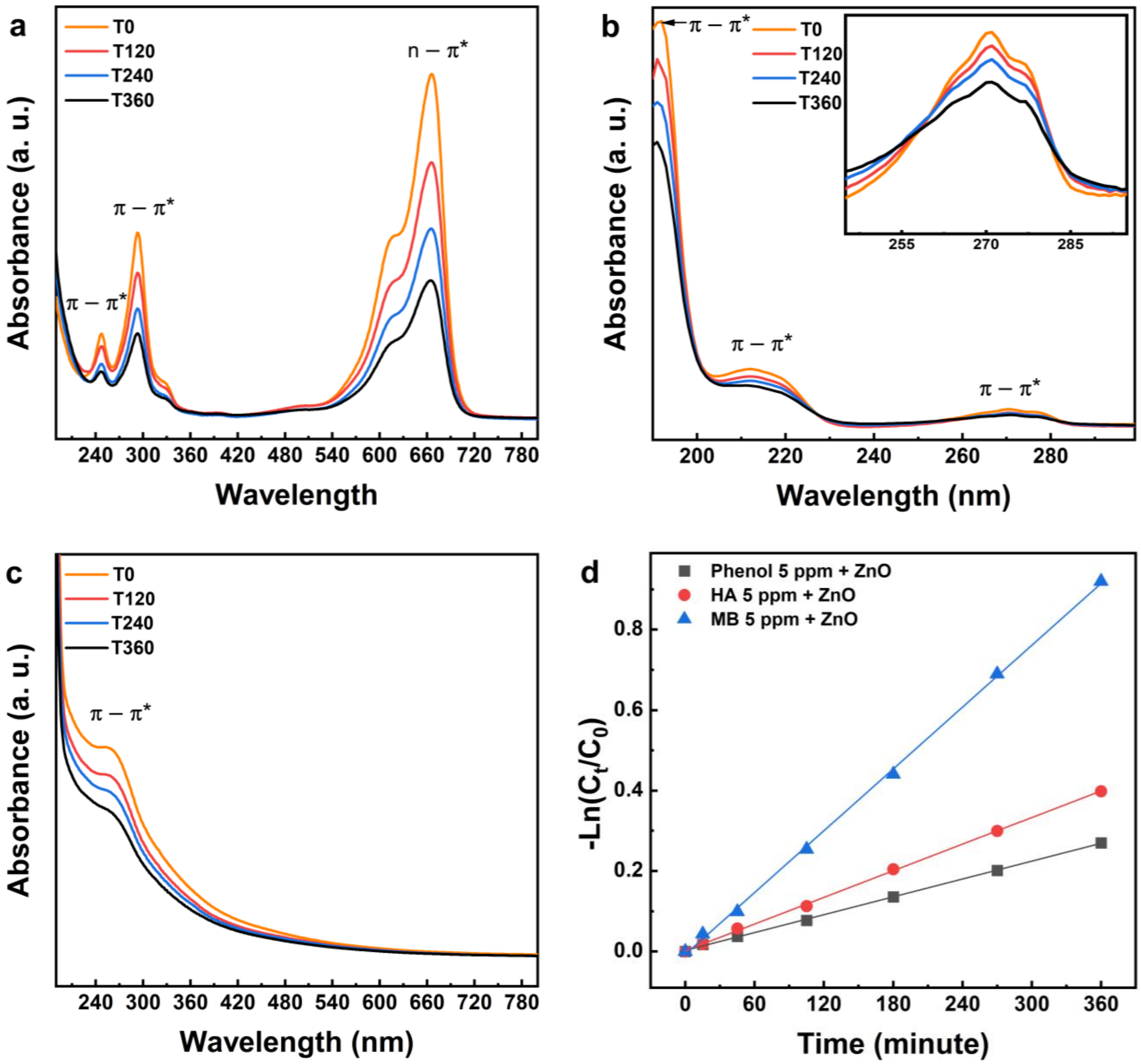

Figure 6. UV-vis spectra of the UVA-photodegradation (λ = 365 nm), carried out over the as-prepared ZnO NRs film and plotted in function of experimental time for **(a)** 5 ppm MB **(b)** 5 ppm phenol, and **(c)** 5 ppm HA, **(d)** Comparative photodegradation kinetics of 5 ppm phenol (tracked at λ = 270 nm), 5 ppm HA (tracked at λ = 250 nm), and 5 ppm MB (tracked at λ = 665 nm).

The photocatalytic degradation behavior, in Figure 6d, reveals that the apparent degradation rates are the following: MB $K_{app_{min}}$ (0.0486 min^{-1}) > HA K_{app} (0.0314 min^{-1}) > Phenol K_{app} (0.0228 min^{-1}). $K_{app_{min}}$ of methylene blue represents the slowest measured rate at λ = 247 nm. The apparent degradation rates for MB, HA, and phenol molecules that were recorded at the different absorbance peaks, are summarized in Table 2.

Table 2. Apparent degradation rates for MB, HA, and phenol molecules, recorded at the different absorbance peaks of each and normalized to the immersed specific area of ZnO NRs (~ 0.035 m^2).

λ (nm)	**MB** ***Kapp*** **(min^{-1})**	**Phenol** ***Kapp*** **(min^{-1})**	**HA** ***Kapp*** **(min^{-1})**	**Transition Type**
192	-	0.0228	-	$\pi - \pi^*$
212	-	0.0222	-	$\pi - \pi^*$
247	0.0486	-	-	$\pi - \pi^*$
250	-	-	0.0314	$\pi - \pi^*$
270	-	0.0228	-	$\pi - \pi^*$
293	0.06	-	-	$\pi - \pi^*$
665	0.0714	-	-	$n - \pi^*$

The degradation rates of HA, MB, and phenol are mainly governed by the amount of hydroxyl radicals and the chemical structures of the organic molecules[86–88]. The presence of these radicals was verified by measuring the photocatalytic efficiency of ZnO NRs before and after the addition of isopropanol quenching agent, in the case of MB (data not shown). Furthermore, as all the prepared ZnO NRs photocatalysts are highly homogeneous, the expected amount of hydroxyl radicals is similar for all experiments. Thus, the kinetic degradation rates are controlled by the complexity of pollutant structures. In this regard, the oxidative pathways of each molecule are estimated based on the obtained kinetic data from the UV-vis measurements. For instance, the changes in the UV-vis spectra of phenol show quite a similar degradation kinetic of ~ 0.0222 min^{-1} at the three absorbance peaks of 192, 212, and 270 nm (Table 2). This relatively low rate constant is due to the high dissociation molecular bond energy of ~ 97.12 kcal/mol[89]. As these peaks reflect the E_1-, E_2-, and B-band transitions, their reduction at the same rate indicates a complete transformation of the molecule. This is confirmed by the absence of any absorbance peaks that arise from the formation of intermediates (Figure 6b). As reported elsewhere, the phenolic ring reacts with the $^{\bullet}$OH to produce dihydroxy benzene, where its further oxidation either leads to a ring cleavage or the formation of quinone-like intermediates[90,91]. The faster degradation of the latter compared to phenol leads directly to its ring cleavage via a single oxidation step, giving oxalic and maleic acids[91,92]. Thus, the rupture of the phenolic ring is the rate-determining step[92]. The proposed mechanism of phenol degradation is illustrated in Figure 7a.

On the other side, methylene blue demonstrates distinct rates of decline for its absorbance peaks at λ = 247, 293, and 665 nm, namely at ~ 0.0486, 0.06, and 0.0714 min^{-1}, respectively (Table 2). This implies that the decomposition of the conjugated system of phenothiazine chromophores (–C=N and –C=S) and the rest of the benzene structure follow different kinetics. When the MB molecules are attacked by the ROS, their degradation can undergo three different paths simultaneously. In consequence, the demethylation and N-demethylation of the MB were commonly observed at the beginning of the degradation due to the high vulnerability of the N–CH_3 bond that breaks down to form dimethylamino-intermediates[93]. Such molecules were frequently reported elsewhere, where intermediates such as formaldehyde (HCHO) or formic acid (HCOOH) were detected as soon as the degradation started[93–97]. In addition, the oxidation of the weak chromophore C–S^+=C at very early stages of the degradation paves the way for the hemolytic cleavage of the thionine ring via a desulfurization pathway, resulting in various sulfoxide or sulphone intermediates[94]. Accordingly, Houas et al. (2001) reported the formation of sulfoxide intermediates and SO_4^{2-} ions during the beginning of MB photocatalytic degradation by TiO_2, confirming the opening of the thionine ring[98]. In addition to the desulphonation and demethylation reactions, the imino-group at the central heterocyclic rings is also prone to early oxidation, producing aniline and nitrate anions[93,94]. Moreover, the behavior of the MB in a highly rich medium with hydroxyl radicals was investigated by Huang et al. (2010) who also found that the molecule's degradation follows the same pathway[95]. Such an oxidation mechanism agrees with the bond dissociation energy theory, wherein bonds of lower energy tend to decompose first: CH_3–$N(CH_3)C_6H_5$ (70.8 kcal/mol) < C–S^+=C (76 kcal/mol) < C–N=C (87.4 kcal/mol) < $N(CH_3)_2$–C_6H_5 (93.2 kcal/mol) < H_2N–C_6H_5 (10.2.6 kcal/mol)[89,94,95,99].

Once the central ring is broken (Step 1, Figure 7b), the resulting hydroxylated species, such as the relatively less stable hydroquinone or hydroquinone-like intermediates, are well known to undergo fast oxidation into acetic acids, maleic acids, oxalic acid, CO_2, and H_2O_2 (Step 2, Figure 7b)[56]. Because these benzene rings are already hydroxylated with two or more –OH, their ring opening at this stage requires only one oxidation step, contrarily to phenol (which needs two or more oxidation steps). Consequently, due to this unique mechanism of MB degradation that bypasses the formation of highly stable species like phenol, methylene blue shows faster degradation kinetics[100–103]. The proposed mechanism of MB degradation is visualized in Figure 7b.

Similarly, the degradation of the macromolecular HA into smaller polyaromatic intermediates begins at its weakest bonds: C–N–C, and C–O–C[104,105]. Herein, the slower photodegradation rate of HA (0.0314 min^{-1}) compared to that of MB (0.0714 min^{-1}) indicates that the weakest molecular bond of MB (BDE of C_6H_5–SC_6H_5 = 76 ± 2 kcal/mol) is oxidized faster than that of HA (BDE of C_6H_5–O (C_6H_5) = 79.4 ± 2 kcal/mol)[104]. Hence, the HA molecule decomposes into various structures of polyaromatics, with absorption bands ranging between ~ 180 and 320 nm, corresponding to high-energy $\pi - \pi^*$ (K-, B-, and E-bands) transitions. Because the UV-vis spectrums of the HA and its intermediates are expected to overlap with each other, the real degradation kinetics may be hindered. For instance, the degradation of the HA byproducts was shown to proceed with ring cleavage steps to give new intermediates such as dibutyl phthalate, and glyoxylic acid[23]. Further oxidation of the latter can result in aliphatic species like octadecanoic or hexadecanoic acids[23]. Relatively small molecules i.

e. the glyoxylic acid are also observed at advanced degradation time[23]. Although the photodegradation kinetics of humic acids appear to be slightly higher than those of phenol, the complete mineralization of the HA molecule and its byproducts generally follows a longer pathway. The formation of intermediates in the course of HA degradation is shown in Figure 7c.

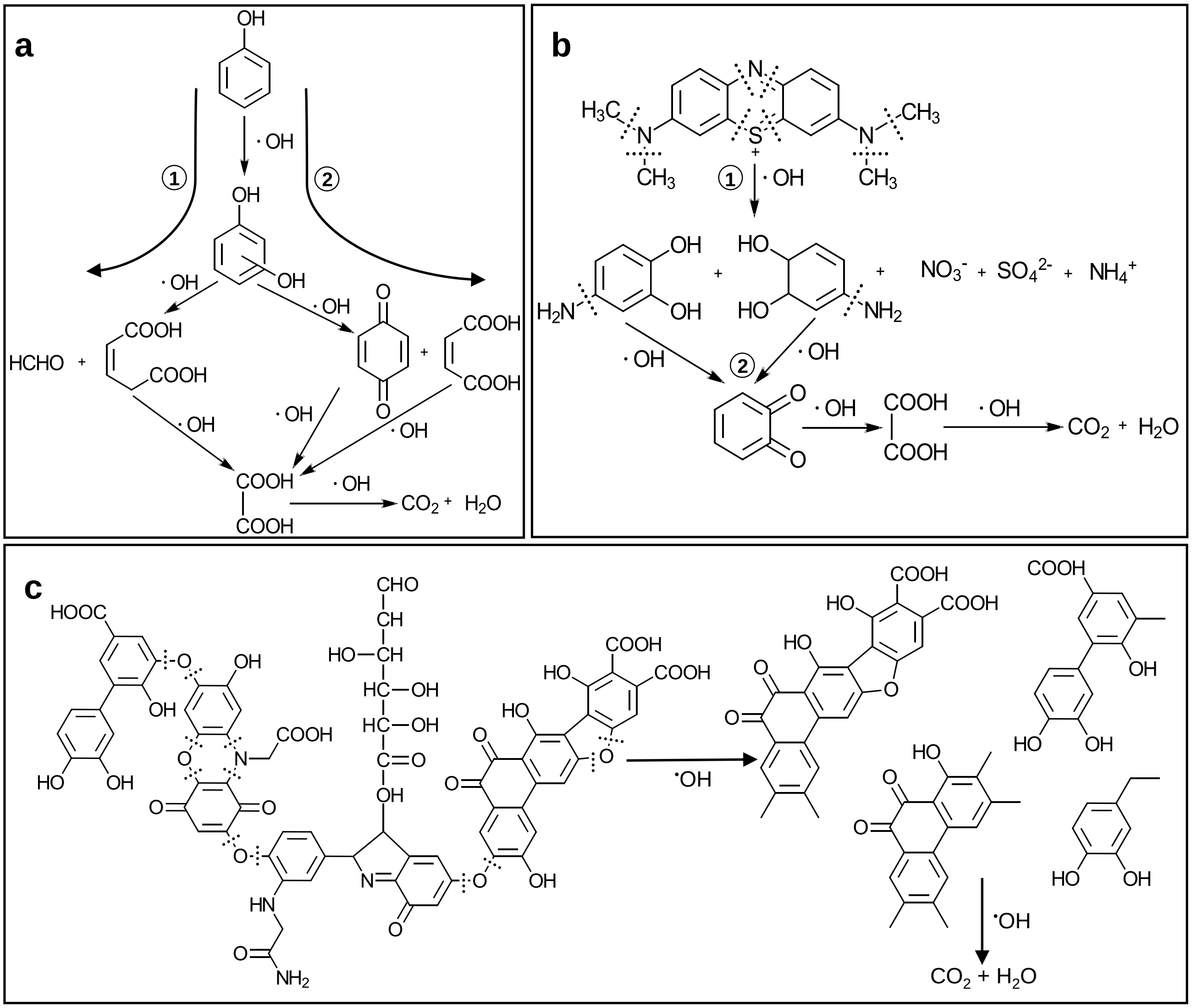

Figure 7. Photocatalytic degradation pathway of dissolved **(a)** Phenol, **(b)** Methylene Blue, and **(c)** Humic acid.

4. Conclusion

In this study, ZnO nanorods were synthesized by hydrothermal growth. The influence of the oxidative pathway on the degradation rate was investigated through different chemical structures, including phenol, methylene blue (MB), and humic acid (HA). Although the molecular sizes of MB and HA are larger than those of phenol, they show relatively higher degradation rates. For instance, the removal of 90% of MB and HA is 3 and 1.4 times faster than the removal of phenol at the same concentration. This is due to the structure and bond energy differences between the concerned molecules. More specifically, as MB presents relatively weak dissociation bond energy (~ 76 kcal/mol) at the thionine ring, the latter tends to easily oxidize under the attack of ROS and dissociate into hydroxylated aromatics with more than two –OH groups. As such highly hydroxylated intermediates require relatively fewer oxidation steps than phenol to achieve the ring cleavage, MB blue registers higher apparent constant rates. In a similar way, the HA molecule possesses much weaker dissociation molecular bond energy (~ 79.4 kcal/mol), compared to phenol (minimum ~ 97.12 kcal/mol) and therefore shows more rapid degradation. Therefore, despite the complexity of the molecule, its degradation kinetics are mainly governed by the cleavage of the weakest molecular bonds.

AUTHOR INFORMATION

Corresponding Author

Dr. Wael Hamd

E-mail: wael.hamd@balamand.edu.lb

Acknowledgment

This work has been supported by two projects: CLAIM, H2020-BG-2016–2017 [grant number 774586], “Cleaning Litter by Developing and Applying Innovative Methods in European Seas” and SWaTH, “Sustainable Wastewater Treatment for Hospitals” co-funded by the Erasmus Plus Programme of the European Union. Mr. David Montero, Mr. Patrick Le Griel, and Mr. Mohamed Selmane are gratefully acknowledged for conducting SEM-FEG, TEM, and XRD measurements at Sorbonne University.

References

(1) Keijer, T.; Bakker, V.; Slootweg, J. C. Circular Chemistry to Enable a Circular Economy. *Nat. Chem.* **2019**, *11* (3), 190–195. https://doi.org/10.1038/s41557-019-0226-9.

(2) Naoko Ishii; Martin Stuchtey. *Pathways for the Chemical Industry to Enable a Sustainable Global Economy*; systemiq, 2022. https://www.systemiq.earth/wp-content/uploads/2022/10/Main-report-v1.22.pdf (accessed 2023-01-03).

(3) El Hajj Chehade, A. M.; Daher, E. A.; Assaf, J. C.; Riachi, B.; Hamd, W. Simulation and Optimization of Hydrogen Production by Steam Reforming of Natural Gas for Refining and Petrochemical Demands in Lebanon. *Int. J. Hydrog. Energy* **2020**, *45* (58), 33235–33247. https://doi.org/10.1016/j.ijhydene.2020.09.077.

(4) Cushman-Roisin, B.; Cremonini, B. T. Industries. In *Data, Statistics, and Useful Numbers for Environmental Sustainability*; Elsevier, 2021; pp 179–237. https://doi.org/10.1016/B978-0-12-822958-3.00006-6.

(5) Dixon, M. W. Chemical Fertilizer in Transformations in World Agriculture and the State System, 1870 to Interwar Period. *J. Agrar. Change* **2018**, *18* (4), 768–786. https://doi.org/10.1111/joac.12259.

(6) Chen, Y.; Chen, M.; Li, Y.; Wang, B.; Chen, S.; Xu, Z. Impact of Technological Innovation and Regulation Development on E-Waste Toxicity: A Case Study of Waste Mobile Phones. *Sci. Rep.* **2018**, *8* (1), 7100. https://doi.org/10.1038/s41598-018-25400-0.

(7) Bobba, S.; Tecchio, P.; Ardente, F.; Mathieux, F.; dos Santos, F. M.; Pekar, F. Analysing the Contribution of Automotive Remanufacturing to the Circularity of Materials. *Procedia CIRP* **2020**, *90*, 67–72. https://doi.org/10.1016/j.procir.2020.02.052.

(8) Kumar, P. S.; Prasannamedha, G. Biological and Chemical Impacts on Marine Biology. In *Modern Treatment Strategies for Marine Pollution*; Elsevier, 2021; pp 11–27. https://doi.org/10.1016/B978-0-12-822279-9.00006-3.

(9) Zhao, B.; Huang, F.; Zhang, C.; Huang, G.; Xue, Q.; Liu, F. Pollution Characteristics of Aromatic Hydrocarbons in the Groundwater of China. *J. Contam. Hydrol.* **2020**, *233*, 103676. https://doi.org/10.1016/j.jconhyd.2020.103676.

(10) Hamd, W. S.; Dutta, J. Heterogeneous Photo-Fenton Reaction and Its Enhancement upon Addition of Chelating Agents. In *Nanomaterials for the Detection and Removal of Wastewater Pollutants*; Elsevier, 2020; pp 303–330. https://doi.org/10.1016/B978-0-12-818489-9.00011-6.

(11) Mohammadi, S.; Kargari, A.; Sanaeepur, H.; Abbassian, K.; Najafi, A.; Mofarrah, E. Phenol Removal from Industrial Wastewaters: A Short Review. *Desalination Water Treat.* **2015**, *53* (8), 2215–2234. https://doi.org/10.1080/19443994.2014.883327.

(12) Anku, W. W.; Mamo, M. A.; Govender, P. P. Phenolic Compounds in Water: Sources, Reactivity, Toxicity and Treatment Methods. In *Phenolic Compounds - Natural Sources,*

Importance and Applications; Soto-Hernández, M., Palma-Tenango, M., Garcia-Mateos, M. del R., Eds.; InTech, 2017. https://doi.org/10.5772/66927.

(13) Rodríguez, I.; Llompart, M. P.; Cela, R. Solid-Phase Extraction of Phenols. *J. Chromatogr. A* **2000**, *885* (1–2), 291–304. https://doi.org/10.1016/S0021-9673(00)00116-3.

(14) Liu, D.; Zheng, Z.; Wang, C.; Yin, Y.; Liu, S.; Yang, B.; Jiang, Z. CdTe Quantum Dots Encapsulated ZnO Nanorods for Highly Efficient Photoelectrochemical Degradation of Phenols. *J. Phys. Chem. C* **2013**, *117* (50), 26529–26537. https://doi.org/10.1021/jp410692y.

(15) Martínez, D.; Pocurull, E.; Marcé, R. M.; Borrull, F.; Calull, M. Separation of Eleven Priority Phenols by Capillary Zone Electrophoresis with Ultraviolet Detection. *J. Chromatogr. A* **1996**, *734* (2), 367–373. https://doi.org/10.1016/0021-9673(95)01299-0.

(16) Wu, Z.; Zhang, X.; Pang, J.; Zhang, X.; Li, J.; Li, J.; Zhang, P. Humic Acid Removal from Water with PAC-Al $_{30}$: Effect of Calcium and Kaolin and the Action Mechanisms. *ACS Omega* **2020**, *5* (27), 16413–16420. https://doi.org/10.1021/acsomega.0c00532.

(17) Chowdhury, R. R.; Charpentier, P. A.; Ray, M. B. Photodegradation of 17β-Estradiol in Aquatic Solution under Solar Irradiation: Kinetics and Influencing Water Parameters. *J. Photochem. Photobiol. Chem.* **2011**, *219* (1), 67–75. https://doi.org/10.1016/j.jphotochem.2011.01.019.

(18) Martínez-Zapata, M.; Aristizábal, C.; Peñuela, G. Photodegradation of the Endocrine-Disrupting Chemicals 4n-Nonylphenol and Triclosan by Simulated Solar UV Irradiation in Aqueous Solutions with Fe(III) and in the Absence/Presence of Humic Acids. *J. Photochem. Photobiol. Chem.* **2013**, *251*, 41–49. https://doi.org/10.1016/j.jphotochem.2012.10.009.

(19) Peña-Méndez, E. M.; Havel, J.; Patočka, J. Humic Substances - Compounds of Still Unknown Structure: Applications in Agriculture, Industry, Environment, and Biomedicine. *J. Appl. Biomed.* **2005**, *3* (1), 13–24. https://doi.org/10.32725/jab.2005.002.

(20) Richnow, H. H.; Seifert, R.; Hefter, J.; Link, M.; Francke, W.; Schaefer, G.; Michaelis, W. Organic Pollutants Associated with Macromolecular Soil Organic Matter: Mode of Binding. *Org. Geochem.* **1997**, *26* (11–12), 745–758. https://doi.org/10.1016/S0146-6380(97)00054-5.

(21) Kabsch-Korbutowicz, M.; Winnicki, T. Application of Modified Polysulfone Membranes to the Treatment of Water Solutions Containing Humic Substances and Metal Ions. *Desalination* **1996**, *105* (1–2), 41–49. https://doi.org/10.1016/0011-9164(96)00056-2.

(22) Dobranskyte, A.; Jugdaohsingh, R.; McCrohan, C. R.; Stuchlik, E.; Powell, J. J.; White, K. N. Effect of Humic Acid on Water Chemistry, Bioavailability and Toxicity of Aluminium in the Freshwater Snail, Lymnaea Stagnalis, at Neutral PH. *Environ. Pollut.* **2006**, *140* (2), 340–347. https://doi.org/10.1016/j.envpol.2005.06.030.

(23) Li, A.; Zhao, X.; Liu, H.; Qu, J. Characteristic Transformation of Humic Acid during Photoelectrocatalysis Process and Its Subsequent Disinfection Byproduct Formation Potential. *Water Res.* **2011**, *45* (18), 6131–6140. https://doi.org/10.1016/j.watres.2011.09.012.

(24) Zhang, H.; Yang, M. Characterization of Brominated Disinfection Byproducts Formed during Chloramination of Fulvic Acid in the Presence of Bromide. *Sci. Total Environ.* **2018**, *627*, 118–124. https://doi.org/10.1016/j.scitotenv.2018.01.215.

(25) Steinberg, C. E. W.; Meinelt, T.; Schreckenbach, K.; Knopf, K.; Wienke, A.; St�ber, A. Humic Substances Affect Physiological Condition and Sex Ratio of Swordtail (Xiphophorus Helleri Heckel). *Aquat. Sci. - Res. Boundaries* **2004**, *66* (2), 239–245. https://doi.org/10.1007/s00027-004-0706-9.

(26) Yang, C.-M.; Wang, M.-C.; Lu, Y.-F.; Chang, I.-F.; Chou, C.-H. Humic Substances Affect the Activity of Chlorophyllase. *J. Chem. Ecol.* **2004**, *30* (5), 1057–1065. https://doi.org/10.1023/B:JOEC.0000028467.82191.f9.

(27) Cheng, M.-L.; Ho, H.-Y.; Huang, Y.-W.; Lu, F.-J.; Chiu, D. T.-Y. Humic Acid Induces Oxidative DNA Damage, Growth Retardation, and Apoptosis in Human Primary Fibroblasts. *Exp. Biol. Med.* **2003**, *228* (4), 413–423. https://doi.org/10.1177/153537020322800412.

(28) Hassanpour, M.; Safardoust-Hojaghan, H.; Salavati-Niasari, M. Degradation of Methylene Blue and Rhodamine B as Water Pollutants via Green Synthesized Co3O4/ZnO Nanocomposite. *J. Mol. Liq.* **2017**, *229*, 293–299. https://doi.org/10.1016/j.molliq.2016.12.090.

(29) Hasnat, M. A.; Safwan, J. A.; Islam, M. S.; Rahman, Z.; Karim, M. R.; Pirzada, T. J.; Samed, A. J.; Rahman, M. M. Electrochemical Decolorization of Methylene Blue at Pt Electrode in KCl Solution for Environmental Remediation. *J. Ind. Eng. Chem.* **2015**, *21*, 787–791. https://doi.org/10.1016/j.jiec.2014.04.013.

(30) Khan, I.; Saeed, K.; Zekker, I.; Zhang, B.; Hendi, A. H.; Ahmad, A.; Ahmad, S.; Zada, N.; Ahmad, H.; Shah, L. A.; Shah, T.; Khan, I. Review on Methylene Blue: Its Properties, Uses, Toxicity and Photodegradation. *Water* **2022**, *14* (2), 242. https://doi.org/10.3390/w14020242.

(31) Amin, M. T.; Alazba, A. A.; Manzoor, U. A Review of Removal of Pollutants from Water/Wastewater Using Different Types of Nanomaterials. *Adv. Mater. Sci. Eng.* **2014**, *2014*, 1–24. https://doi.org/10.1155/2014/825910.

(32) Crini, G.; Lichtfouse, E. Advantages and Disadvantages of Techniques Used for Wastewater Treatment. *Environ. Chem. Lett.* **2019**, *17* (1), 145–155. https://doi.org/10.1007/s10311-018-0785-9.

(33) Zhang, M.; Dong, H.; Zhao, L.; Wang, D.; Meng, D. A Review on Fenton Process for Organic Wastewater Treatment Based on Optimization Perspective. *Sci. Total Environ.* **2019**, *670*, 110–121. https://doi.org/10.1016/j.scitotenv.2019.03.180.

(34) Loeb, S. K.; Alvarez, P. J. J.; Brame, J. A.; Cates, E. L.; Choi, W.; Crittenden, J.; Dionysiou, D. D.; Li, Q.; Li-Puma, G.; Quan, X.; Sedlak, D. L.; David Waite, T.; Westerhoff, P.; Kim, J.-H. The Technology Horizon for Photocatalytic Water Treatment: Sunrise or Sunset? *Environ. Sci. Technol.* **2019**, *53* (6), 2937–2947. https://doi.org/10.1021/acs.est.8b05041.

(35) Cui, X.; Li, W.; Ryabchuk, P.; Junge, K.; Beller, M. Bridging Homogeneous and Heterogeneous Catalysis by Heterogeneous Single-Metal-Site Catalysts. *Nat. Catal.* **2018**, *1* (6), 385–397. https://doi.org/10.1038/s41929-018-0090-9.

(36) Zhang, L.; Ma, P.; Dai, L.; Li, S.; Yu, W.; Guan, J. *In Situ* Crystallization and Growth of TiO_2 Nanospheres between MXene Layers for Improved Adsorption and Visible Light Photocatalysis. *Catal. Sci. Technol.* **2021**, *11* (11), 3834–3844. https://doi.org/10.1039/D1CY00239B.

(37) Zhang, L.; Dai, L.; Li, X.; Yu, W.; Li, S.; Guan, J. 3D Structured TiO_2 -Based Aerogel Photocatalyst for the High-Efficiency Degradation of Toluene Gas. *New J. Chem.* **2022**, *46* (5), 2272–2281. https://doi.org/10.1039/D1NJ05395G.

(38) Zhang, L.; Ma, P.; Dai, L.; Bu, Z.; Li, X.; Yu, W.; Cao, Y.; Guan, J. Removal of Pollutants via Synergy of Adsorption and Photocatalysis over MXene-Based Nanocomposites. *Chem. Eng. J. Adv.* **2022**, *10*, 100285. https://doi.org/10.1016/j.ceja.2022.100285.

(39) Miklos, D. B.; Remy, C.; Jekel, M.; Linden, K. G.; Drewes, J. E.; Hübner, U. Evaluation of Advanced Oxidation Processes for Water and Wastewater Treatment – A Critical Review. *Water Res.* **2018**, *139*, 118–131. https://doi.org/10.1016/j.watres.2018.03.042.

(40) Habib, I. Y.; Burhan, J.; Jaladi, F.; Lim, C. M.; Usman, A.; Kumara, N. T. R. N.; Tsang, S. C. E.; Mahadi, A. H. Effect of Cr Doping in CeO2 Nanostructures on Photocatalysis and H2O2 Assisted Methylene Blue Dye Degradation. *Catal. Today* **2021**, *375*, 506–513. https://doi.org/10.1016/j.cattod.2020.04.008.

(41) Reza, K. M.; Kurny, A.; Gulshan, F. Parameters Affecting the Photocatalytic Degradation of Dyes Using TiO2: A Review. *Appl. Water Sci.* **2017**, *7* (4), 1569–1578. https://doi.org/10.1007/s13201-015-0367-y.

(42) Ni, C.; Huang, M.; Ren, M.; Li, X.; Yan, X.; Sun, S. Effect of Microstructure and Reaction Medium on Photocatalytic Performance and Stability of BiO Catalyst for CO2 Reduction. *Catal. Commun.* **2023**, *173*, 106565. https://doi.org/10.1016/j.catcom.2022.106565.

(43) Hamad, H. A.; Sadik, W. A.; Abd El-latif, M. M.; Kashyout, A. B.; Feteha, M. Y. Photocatalytic Parameters and Kinetic Study for Degradation of Dichlorophenol-Indophenol (DCPIP) Dye Using Highly Active Mesoporous TiO 2 Nanoparticles. *J. Environ. Sci.* **2016**, *43*, 26–39. https://doi.org/10.1016/j.jes.2015.05.033.

(44) Yanagi, R.; Zhao, T.; Solanki, D.; Pan, Z.; Hu, S. Charge Separation in Photocatalysts: Mechanisms, Physical Parameters, and Design Principles. *ACS Energy Lett.* **2022**, *7* (1), 432–452. https://doi.org/10.1021/acsenergylett.1c02516.

(45) Wu, Z.; Zhang, C.; Liu, J.; Wen, F.; Cao, H.; Pei, Y. The Investigation of Microstructure, Photocatalysis and Corrosion Resistance of C-Doped Ti–O Films Fabricated by Reactive Magnetron Sputtering Deposition with CO2 Gas. *Coatings* **2021**, *11* (8), 881. https://doi.org/10.3390/coatings11080881.

(46) Balakrishnan, G.; Velavan, R.; Mujasam Batoo, K.; Raslan, E. H. Microstructure, Optical and Photocatalytic Properties of MgO Nanoparticles. *Results Phys.* **2020**, *16*, 103013. https://doi.org/10.1016/j.rinp.2020.103013.

(47) Rogé, V.; Guignard, C.; Lamblin, G.; Laporte, F.; Fechete, I.; Garin, F.; Dinia, A.; Lenoble, D. Photocatalytic Degradation Behavior of Multiple Xenobiotics Using MOCVD Synthesized ZnO Nanowires. *Catal. Today* **2018**, *306*, 215–222. https://doi.org/10.1016/j.cattod.2017.05.088.

(48) Mahmood, M. A.; Jan, S.; Shah, I. A.; Khan, I. Growth Parameters for Films of Hydrothermally Synthesized One-Dimensional Nanocrystals of Zinc Oxide. *Int. J. Photoenergy* **2016**, *2016*, 1–12. https://doi.org/10.1155/2016/3153170.

(49) Baruah, S.; Mahmood, M. A.; Myint, M. T. Z.; Bora, T.; Dutta, J. Enhanced Visible Light Photocatalysis through Fast Crystallization of Zinc Oxide Nanorods. *Beilstein J. Nanotechnol.* **2010**, *1*, 14–20. https://doi.org/10.3762/bjnano.1.3.

(50) Sulciute, A.; Nishimura, K.; Gilshtein, E.; Cesano, F.; Viscardi, G.; Nasibulin, A. G.; Ohno, Y.; Rackauskas, S. ZnO Nanostructures Application in Electrochemistry: Influence of Morphology. *J. Phys. Chem. C* **2021**, *125* (2), 1472–1482. https://doi.org/10.1021/acs.jpcc.0c08459.

(51) Pugliese, D.; Bella, F.; Cauda, V.; Lamberti, A.; Sacco, A.; Tresso, E.; Bianco, S. A Chemometric Approach for the Sensitization Procedure of ZnO Flowerlike Microstructures for Dye-Sensitized Solar Cells. *ACS Appl. Mater. Interfaces* **2013**, *5* (21), 11288–11295. https://doi.org/10.1021/am403527m.

(52) Gu, C.; Shanshan, L.; Huang, J.; Shi, C.; Liu, J. Preferential Growth of Long ZnO Nanowires and Its Application in Gas Sensor. *Sens. Actuators B Chem.* **2013**, *177*, 453–459. https://doi.org/10.1016/j.snb.2012.11.044.

(53) Kovačič, S.; Anžlovar, A.; Erjavec, B.; Kapun, G.; Matsko, N. B.; Žigon, M.; Žagar, E.; Pintar, A.; Slugovc, C. Macroporous ZnO Foams by High Internal Phase Emulsion Technique: Synthesis and Catalytic Activity. *ACS Appl. Mater. Interfaces* **2014**, *6* (21), 19075–19081. https://doi.org/10.1021/am5050482.

(54) Smith, M. F.; Limwichean, S.; Horprathum, M.; Chaiprapa, J.; Aye, W. W.; Chananonnawathorn, C.; Patthanasettakul, V.; Eiamchai, P.; Nuntawong, N.; Klamchuen, A.; Songsiriritthigul, P. Determination of Density and Specific Surface Area of Nanostructured Zinc

Oxide Films by X-Ray Fluorescence and Scanning Electron Microscopy. *Thin Solid Films* **2022**, *751*, 139207. https://doi.org/10.1016/j.tsf.2022.139207.

(55) Zhang, J.; Wang, S.; Wang, Y.; Xu, M.; Xia, H.; Zhang, S.; Huang, W.; Guo, X.; Wu, S. ZnO Hollow Spheres: Preparation, Characterization, and Gas Sensing Properties. *Sens. Actuators B Chem.* **2009**, *139* (2), 411–417. https://doi.org/10.1016/j.snb.2009.03.014.

(56) Liu, Y.; Gao, W. Growth Process, Crystal Size and Alignment of ZnO Nanorods Synthesized under Neutral and Acid Conditions. *J. Alloys Compd.* **2015**, *629*, 84–91. https://doi.org/10.1016/j.jallcom.2014.12.139.

(57) Demianets, L. N.; Kostomarov, D. V. Mechanism of Zinc Oxide Single Crystal Growth under Hydrothermal Conditions. *Ann. Chim. Sci. Matér.* **2001**, *26* (1), 193–198.

(58) Bora, T.; Sathe, P.; Laxman, K.; Dobretsov, S.; Dutta, J. Defect Engineered Visible Light Active ZnO Nanorods for Photocatalytic Treatment of Water. *Catal. Today* **2017**, *284*, 11–18. https://doi.org/10.1016/j.cattod.2016.09.014.

(59) Sugunan, A.; Warad, H. C.; Boman, M.; Dutta, J. Zinc Oxide Nanowires in Chemical Bath on Seeded Substrates: Role of Hexamine. *J. Sol-Gel Sci. Technol.* **2006**, *39* (1), 49–56. https://doi.org/10.1007/s10971-006-6969-y.

(60) Daher, E. A.; Riachi, B.; Chamoun, J.; Laberty-Robert, C.; Hamd, W. New Approach for Designing Wrinkled and Porous ZnO Thin Films for Photocatalytic Applications. *Colloids Surf. Physicochem. Eng. Asp.* **2023**, *658*, 130628. https://doi.org/10.1016/j.colsurfa.2022.130628.

(61) Ohyama, M.; Kouzuka, H.; Yoko, T. Sol-Gel Preparation of ZnO Films with Extremely Preferred Orientation along (002) Plane from Zinc Acetate Solution. *Thin Solid Films* **1997**, *306* (1), 78–85. https://doi.org/10.1016/S0040-6090(97)00231-9.

(62) Jin, Z.; Zhang, Y.-X.; Meng, F.-L.; Jia, Y.; Luo, T.; Yu, X.-Y.; Wang, J.; Liu, J.-H.; Huang, X.-J. Facile Synthesis of Porous Single Crystalline ZnO Nanoplates and Their Application in Photocatalytic Reduction of Cr(VI) in the Presence of Phenol. *J. Hazard. Mater.* **2014**, *276*, 400–407. https://doi.org/10.1016/j.jhazmat.2014.05.059.

(63) S, M.; N, H.; P.P, V. In Vitro Biocompatibility and Antimicrobial Activities of Zinc Oxide Nanoparticles (ZnO NPs) Prepared by Chemical and Green Synthetic Route— A Comparative Study. *BioNanoScience* **2020**, *10* (1), 112–121. https://doi.org/10.1007/s12668-019-00698-w.

(64) Valerio, T. L.; Maia, G. A. R.; Gonçalves, L. F.; Viomar, A.; Banczek, E. do P.; Rodrigues, P. R. P. Study of the Nb2O5 Insertion in ZnO to Dye-Sensitized Solar Cells. *Mater. Res.* **2019**, *22* (suppl 1), e20180864. https://doi.org/10.1590/1980-5373-mr-2018-0864.

(65) Singh, J.; Kaur, S.; Kaur, G.; Basu, S.; Rawat, M. Biogenic ZnO Nanoparticles: A Study of Blueshift of Optical Band Gap and Photocatalytic Degradation of Reactive Yellow 186 Dye under Direct Sunlight. *Green Process. Synth.* **2019**, *8* (1), 272–280. https://doi.org/10.1515/gps-2018-0084.

(66) Bai, S.; Hu, J.; Li, D.; Luo, R.; Chen, A.; Liu, C. C. Quantum-Sized ZnO Nanoparticles: Synthesis, Characterization and Sensing Properties for NO2. *J. Mater. Chem.* **2011**, *21* (33), 12288. https://doi.org/10.1039/c1jm11302j.

(67) da Silva-Neto, M. L.; de Oliveira, M. C. A.; Dominguez, C. T.; Lins, R. E. M.; Rakov, N.; de Araújo, C. B.; Menezes, L. de S.; de Oliveira, H. P.; Gomes, A. S. L. UV Random Laser Emission from Flexible ZnO-Ag-Enriched Electrospun Cellulose Acetate Fiber Matrix. *Sci. Rep.* **2019**, *9* (1), 11765. https://doi.org/10.1038/s41598-019-48056-w.

(68) Malek, M. F.; Mamat, M. H.; Khusaimi, Z.; Sahdan, M. Z.; Musa, M. Z.; Zainun, A. R.; Suriani, A. B.; Md Sin, N. D.; Abd Hamid, S. B.; Rusop, M. Sonicated Sol–Gel Preparation of Nanoparticulate ZnO Thin Films with Various Deposition Speeds: The Highly Preferred c-Axis

(002) Orientation Enhances the Final Properties. *J. Alloys Compd.* **2014**, *582*, 12–21. https://doi.org/10.1016/j.jallcom.2013.07.202.

(69) Hidayat, N.; Sunaryono; Taufiq, A.; Saputro, R. E.; Kusnunnahari; Chuenchom, L. Temperature Effect on Crystal Structures, Morphological Shapes, and Functional Groups of Zinc Oxide; Tangerang Selatan, Indonesia, 2020; p 030017. https://doi.org/10.1063/5.0000910.

(70) Jiménez-González, A.; Suárez-Parra, R. Effect of Heat Treatment on the Properties of ZnO Thin Films Prepared by Successive Ion Layer Adsorption and Reaction (SILAR). *J. Cryst. Growth* **1996**, *167* (3–4), 649–655. https://doi.org/10.1016/0022-0248(96)00308-9.

(71) Poulopoulos, P.; Baskoutas, S.; Pappas, S. D.; Garoufalis, C. S.; Droulias, S. A.; Zamani, A.; Kapaklis, V. Intense Quantum Confinement Effects in Cu_2O Thin Films. *J. Phys. Chem. C* **2011**, *115* (30), 14839–14843. https://doi.org/10.1021/jp203145n.

(72) Wang, S.; Teng, F.; Zhao, Y. Effect of the Molecular Structure and Surface Charge of a Bismuth Catalyst on the Adsorption and Photocatalytic Degradation of Dye Mixtures. *RSC Adv.* **2015**, *5* (93), 76588–76598. https://doi.org/10.1039/C5RA14931B.

(73) Jenks, W. S. Photocatalytic Reaction Pathways – Effects of Molecular Structure, Catalyst, and Wavelength. In *Photocatalysis and Water Purification*; Pichat, P., Ed.; Wiley, 2013; pp 25–51. https://doi.org/10.1002/9783527645404.ch2.

(74) Hamd, W.; Daher, E. A.; Tofa, T. S.; Dutta, J. Recent Advances in Photocatalytic Removal of Microplastics: Mechanisms, Kinetic Degradation, and Reactor Design. *Front. Mar. Sci.* **2022**, *9*, 885614. https://doi.org/10.3389/fmars.2022.885614.

(75) Chen, D. Photocatalytic Kinetics of Phenol and Its Derivatives over UV Irradiated TiO2. *Appl. Catal. B Environ.* **1999**, *23* (2–3), 143–157. https://doi.org/10.1016/S0926-3373(99)00068-5.

(76) Gerischer, H.; Heller, A. The Role of Oxygen in Photooxidation of Organic Molecules on Semiconductor Particles. *J. Phys. Chem.* **1991**, *95* (13), 5261–5267. https://doi.org/10.1021/j100166a063.

(77) Wang, C. M.; Heller, A.; Gerischer, H. Palladium Catalysis of O2 Reduction by Electrons Accumulated on TiO2 Particles during Photoassisted Oxidation of Organic Compounds. *J. Am. Chem. Soc.* **1992**, *114* (13), 5230–5234. https://doi.org/10.1021/ja00039a039.

(78) Kumar, K. V.; Porkodi, K.; Rocha, F. Langmuir–Hinshelwood Kinetics – A Theoretical Study. *Catal. Commun.* **2008**, *9* (1), 82–84. https://doi.org/10.1016/j.catcom.2007.05.019.

(79) Navidpour, A. H.; Kalantari, Y.; Salehi, M.; Salimijazi, H. R.; Amirnasr, M.; Rismanchian, M.; Azarpour Siahkali, M. Plasma-Sprayed Photocatalytic Zinc Oxide Coatings. *J. Therm. Spray Technol.* **2017**, *26* (4), 717–727. https://doi.org/10.1007/s11666-017-0541-x.

(80) Vallejo, W.; Cantillo, A.; Díaz-Uribe, C. Methylene Blue Photodegradation under Visible Irradiation on Ag-Doped ZnO Thin Films. *Int. J. Photoenergy* **2020**, *2020*, 1–11. https://doi.org/10.1155/2020/1627498.

(81) Heger, D.; Jirkovský, J.; Klán, P. Aggregation of Methylene Blue in Frozen Aqueous Solutions Studied by Absorption Spectroscopy. *J. Phys. Chem. A* **2005**, *109* (30), 6702–6709. https://doi.org/10.1021/jp050439j.

(82) Yadav, L. D. S. *Organic Spectroscopy*; Springer Netherlands: Dordrecht, 2005. https://doi.org/10.1007/978-1-4020-2575-4.

(83) Dinh, V.-P.; Huynh, T.-D.-T.; Le, H. M.; Nguyen, V.-D.; Dao, V.-A.; Hung, N. Q.; Tuyen, L. A.; Lee, S.; Yi, J.; Nguyen, T. D.; Tan, L. V. Insight into the Adsorption Mechanisms of Methylene Blue and Chromium(III) from Aqueous Solution onto Pomelo Fruit Peel. *RSC Adv.* **2019**, *9* (44), 25847–25860. https://doi.org/10.1039/C9RA04296B.

(84) Lewis, G. N.; Goldschmid, O.; Magel, T. T.; Bigeleisen, J. Dimeric and Other Forms of Methylene Blue: Absorption and Fluorescence of the Pure Monomer [1]. *J. Am. Chem. Soc.* **1943**, *65* (6), 1150–1154. https://doi.org/10.1021/ja01246a037.

(85) Rodríguez, F. J.; Schlenger, P.; García-Valverde, M. Monitoring Changes in the Structure and Properties of Humic Substances Following Ozonation Using UV–Vis, FTIR and 1 H NMR Techniques. *Sci. Total Environ.* **2016**, *541*, 623–637. https://doi.org/10.1016/j.scitotenv.2015.09.127.

(86) Singh, J.; Juneja, S.; Palsaniya, S.; Manna, Ashis. K.; Soni, R. K.; Bhattacharya, J. Evidence of Oxygen Defects Mediated Enhanced Photocatalytic and Antibacterial Performance of ZnO Nanorods. *Colloids Surf. B Biointerfaces* **2019**, *184*, 110541. https://doi.org/10.1016/j.colsurfb.2019.110541.

(87) Al-Sabahi, J.; Bora, T.; Al-Abri, M.; Dutta, J. Efficient Visible Light Photocatalysis of Benzene, Toluene, Ethylbenzene and Xylene (BTEX) in Aqueous Solutions Using Supported Zinc Oxide Nanorods. *PLOS ONE* **2017**, *12* (12), e0189276. https://doi.org/10.1371/journal.pone.0189276.

(88) Wang, Y.; Yuan, P.-H.; Fan, C.-M.; Wang, Y.; Ding, G.-Y.; Wang, Y.-F. Preparation of Zinc Titanate Nanoparticles and Their Photocatalytic Behaviors in the Photodegradation of Humic Acid in Water. *Ceram. Int.* **2012**, *38* (5), 4173–4180. https://doi.org/10.1016/j.ceramint.2012.01.078.

(89) Leopoldini, M.; Marino, T.; Russo, N.; Toscano, M. Antioxidant Properties of Phenolic Compounds: H-Atom versus Electron Transfer Mechanism. *J. Phys. Chem. A* **2004**, *108* (22), 4916–4922. https://doi.org/10.1021/jp037247d.

(90) Devi, L. G.; Rajashekhar, K. E. A Kinetic Model Based on Non-Linear Regression Analysis Is Proposed for the Degradation of Phenol under UV/Solar Light Using Nitrogen Doped TiO2. *J. Mol. Catal. Chem.* **2011**, *334* (1–2), 65–76. https://doi.org/10.1016/j.molcata.2010.10.025.

(91) Vinu, R.; Madras, G. Photocatalytic Degradation of Water Pollutants Using Nano-TiO2. In *Energy Efficiency and Renewable Energy Through Nanotechnology*; Zang, L., Ed.; Green Energy and Technology; Springer London: London, 2011; pp 625–677. https://doi.org/10.1007/978-0-85729-638-2_19.

(92) Wang, N.; Zhu, L.; Huang, Y.; She, Y.; Yu, Y.; Tang, H. Drastically Enhanced Visible-Light Photocatalytic Degradation of Colorless Aromatic Pollutants over TiO2 via a Charge-Transfer-Complex Path: A Correlation between Chemical Structure and Degradation Rate of the Pollutants. *J. Catal.* **2009**, *266* (2), 199–206. https://doi.org/10.1016/j.jcat.2009.06.006.

(93) Wang, Q.; Tian, S.; Ning, P. Degradation Mechanism of Methylene Blue in a Heterogeneous Fenton-like Reaction Catalyzed by Ferrocene. *Ind. Eng. Chem. Res.* **2014**, *53* (2), 643–649. https://doi.org/10.1021/ie403402q.

(94) Su, S.; Liu, Y.; Liu, X.; Jin, W.; Zhao, Y. Transformation Pathway and Degradation Mechanism of Methylene Blue through β-FeOOH@GO Catalyzed Photo-Fenton-like System. *Chemosphere* **2019**, *218*, 83–92. https://doi.org/10.1016/j.chemosphere.2018.11.098.

(95) Huang, F.; Chen, L.; Wang, H.; Yan, Z. Analysis of the Degradation Mechanism of Methylene Blue by Atmospheric Pressure Dielectric Barrier Discharge Plasma. *Chem. Eng. J.* **2010**, *162* (1), 250–256. https://doi.org/10.1016/j.cej.2010.05.041.

(96) Song, P.; Yang, Z.; Zeng, G.; Yang, X.; Xu, H.; Wang, L.; Xu, R.; Xiong, W.; Ahmad, K. Electrocoagulation Treatment of Arsenic in Wastewaters: A Comprehensive Review. *Chem. Eng. J.* **2017**, *317*, 707–725. https://doi.org/10.1016/j.cej.2017.02.086.

(97) Kuan, W.-H.; Chen, C.-Y.; Hu, C.-Y.; Tzou, Y.-M. Kinetic Modeling for Microwave-Enhanced Degradation of Methylene Blue Using Manganese Oxide. *Int. J. Photoenergy* **2013**, *2013*, 1–9. https://doi.org/10.1155/2013/916849.

(98) Houas, A. Photocatalytic Degradation Pathway of Methylene Blue in Water. *Appl. Catal. B Environ.* **2001**, *31* (2), 145–157. https://doi.org/10.1016/S0926-3373(00)00276-9.

(99) Luo, Y.-R. *Handbook of Bond Dissociation Energies in Organic Compounds*, 0 ed.; CRC Press, 2002. https://doi.org/10.1201/9781420039863.

(100) Zhao, S.; Jia, H.; Nulaji, G.; Gao, H.; Wang, F.; Wang, C. Photolysis of Polycyclic Aromatic Hydrocarbons (PAHs) on Fe3+-Montmorillonite Surface under Visible Light: Degradation Kinetics, Mechanism, and Toxicity Assessments. *Chemosphere* **2017**, *184*, 1346–1354. https://doi.org/10.1016/j.chemosphere.2017.06.106.

(101) Nguyen, V.-H.; Phan Thi, L.-A.; Van Le, Q.; Singh, P.; Raizada, P.; Kajitvichyanukul, P. Tailored Photocatalysts and Revealed Reaction Pathways for Photodegradation of Polycyclic Aromatic Hydrocarbons (PAHs) in Water, Soil and Other Sources. *Chemosphere* **2020**, *260*, 127529. https://doi.org/10.1016/j.chemosphere.2020.127529.

(102) Radwan, M.; Gar Alalm, M.; El-Etriby, H. K. Application of Electro-Fenton Process for Treatment of Water Contaminated with Benzene, Toluene, and p-Xylene (BTX) Using Affordable Electrodes. *J. Water Process Eng.* **2019**, *31*, 100837. https://doi.org/10.1016/j.jwpe.2019.100837.

(103) Andreozzi, M.; Álvarez, M. G.; Contreras, S.; Medina, F.; Clarizia, L.; Vitiello, G.; Llorca, J.; Marotta, R. Treatment of Saline Produced Water through Photocatalysis Using RGO-TiO2 Nanocomposites. *Catal. Today* **2018**, *315*, 194–204. https://doi.org/10.1016/j.cattod.2018.04.048.

(104) Moldoveanu, S. C. General Information About Pyrolysis. In *Pyrolysis of Organic Molecules*; Elsevier, 2019; pp 1–33. https://doi.org/10.1016/B978-0-444-64000-0.00001-9.

(105) Abedi, K.; Shahmoradi, B.; Wantala, K.; Suwannaruang, T.; Amini, N.; Maleki, A.; Lee, S. M.; Shivaraju, H. P. Immobilized Mo:TiO2 Nanoparticles for Humic Acid Removal in an Aqueous Medium Using Solar Spectrum. *J. Mater. Sci. Mater. Electron.* **2022**, *33* (21), 16777–16788. https://doi.org/10.1007/s10854-022-08542-w.

Chapter II

Ce chapitre a été soumis à: Journal of Marine Pollution Bulletin

De l'Échelle Moléculaire à l'Échelle Microscopique : Compréhension de la Photodégradation des Particules de Microplastiques de Polypropylene

Après l'étude de la photodégradation au niveau moléculaire, il était important d’étudier l’efficacité des nano bâtonnets de ZnO sur des particules polymériques aux masses moléculaires beaucoup plus importantes comme les microplastiques (dizaines de milliers de g/mol)[1]. Ces particules non traitées présentent un danger majeur sur l’écosystème et la vie humaine[2]. Leur taille comprise entre 1 µm et 5 mm les rendent accessibles aux animaux marins, envahissant ainsi la chaîne alimentaire et menaçant la santé humaine[3]. En effet, il a récemment été rapporté qu'une personne pourrait ingérer entre 39 000 et 52 000 particules microplastiques (MPs) par an via les aliments et les boissons, à cela s’ajoute entre 4 000 et 90 000 MPs par an si l'eau du robinet et l'eau en bouteille sont respectivement consommées[4]. De plus, ces MPs sont connus pour leur nature récalcitrante, leur grande résistance à la dégradation naturelle et leurs capacités d’adsorber à leurs surfaces d’autres molécules nocives[5]. Dans ce contexte, des particules de polypropylène ayant une faible densité de 905 Kg/m^3 (LD-PP) et un diamètre de 300 µm, ont été sélectionnées comme polluants aquatiques modèles.

Dans ce chapitre, les nano bâtonnets de ZnO, ont été déposés sur une grille en fibres de verre (synthèse hydrothermale). Ce type de substrats de grande surface spécifique a été choisi afin de piéger les LD-PPs ayant tendance à flotter à la surface de l’eau et d'augmenter par conséquent le temps/surface de contact avec le photocatalyseur. La dégradation photocatalytique de ces billes a été évaluée pendant 16 jours consécutifs d'irradiation au soleil, en suivant l'évolution de l'indice de carbonyle (obtenu via ATR-FTIR) et de leur microstructure (via microscopie MEB). L’indice de carbonyle (CI) représente le degré d'oxydation des particules de polypropylènes et est définie comme étant le rapport d'absorbance entre la bande attribuée aux fonctions carbonyles (entre ~ 1550 – 1850 cm^{-1}) et celle d'une fonction alkyle de référence (CH et CH_3 entre ~ 2700 – 2750 cm^{-1})[2,6]. Dans le système dépourvu du photocatalyseur de ZnO, un indice de carbonyle de 11.6 a été enregistré, présentant un faible taux d'oxydation après 196 heures d'irradiation. Cependant, l'utilisation du ZnO permet une augmentation importante du CI allant jusqu'à 57,2 dans les mêmes conditions qu'auparavant. Dans ce cas, nous avons distingué deux régimes aux cinétiques différentes. Entre 0 et 117 heures, la faible valeur de CI est attribuée à une oxydation graduelle de la surface des particules. Entre 117 et 196 heures, l'évolution de la microstructure des LD-PPs par microscopie MEB a révélé un processus de dégradation de la surface et la formation de cavités et des fissures. Ces modifications augmentent significativement la cinétique d'oxydation des billes de polypropylène, à cause d'une plus grande surface disponible pour l'attaque des espèces réactives de l'oxygène (ROS). Cette étude met en évidence le potentiel de cette approche « photocatalytique » pour lutter contre les microplastiques présents dans les eaux usées.

Références

(1) Andrady, A. L. Microplastics in the Marine Environment. *Marine Pollution Bulletin* **2011**, *62* (8), 1596–1605. https://doi.org/10.1016/j.marpolbul.2011.05.030.

(2) Uheida, A.; Mejía, H. G.; Abdel-Rehim, M.; Hamd, W.; Dutta, J. Visible Light Photocatalytic Degradation of Polypropylene Microplastics in a Continuous Water Flow System. *Journal of Hazardous Materials* **2021**, *406*, 124299. https://doi.org/10.1016/j.jhazmat.2020.124299.

(3) Frias, J. P. G. L.; Nash, R. Microplastics: Finding a Consensus on the Definition. *Marine Pollution Bulletin* **2019**, *138*, 145–147. https://doi.org/10.1016/j.marpolbul.2018.11.022.

(4) Cox, K. D.; Covernton, G. A.; Davies, H. L.; Dower, J. F.; Juanes, F.; Dudas, S. E. Human Consumption of Microplastics. *Environ. Sci. Technol.* **2019**, *53* (12), 7068–7074. https://doi.org/10.1021/acs.est.9b01517.

(5) Hamd, W.; Daher, E. A.; Tofa, T. S.; Dutta, J. Recent Advances in Photocatalytic Removal of Microplastics: Mechanisms, Kinetic Degradation, and Reactor Design. *Front. Mar. Sci.* **2022**, *9*, 885614. https://doi.org/10.3389/fmars.2022.885614.

(6) Liu, Q.; Liu, S.; Xia, L.; Hu, P.; Lv, Y.; Liu, J.; Chen, Z.; Huang, Y.; Li, G. Effect of Annealing-Induced Microstructure on the Photo-Oxidative Degradation Behavior of Isotactic Polypropylene. *Polymer Degradation and Stability* **2019**, *162*, 180–195. https://doi.org/10.1016/j.polymdegradstab.2019.02.023.

Natural Sunlight Accelerated Photocatalytic Degradation of Polypropylene Microplastics over ZnO Nanorods

Elie A. Daher[‡†], *Yara Hammoud* [‡], *Christel Laberty Robert*[†⁑], *Wael Hamd* [₽*]

[‡] Petrochemical Engineering Department, Faculty of Engineering III, CRSI, Lebanese University, Rafic Hariri Campus, Hadat, Lebanon.

[†] Laboratoire Chimie de la Matière Condensée de Paris LCMCP, Sorbonne Université, UPMC Paris 06, 4 Place Jussieu, 75005 Paris, France

[⁑] RS2E, Réseau Français sur le Stockage Electrochimique de l'Energie, CNRS 3459, 80039 Cedex 1 Amiens, France

[₽] Chemical Engineering Department, Faculty of Engineering, University of Balamand, P.O. Box 33, El-Koura, Lebanon.

KEYWORDS: Polypropylene microplastics, photocatalysis, sunlight irradiation, ZnO nanorods, glass fibers, carbonyl index.

ABSTRACT: Microplastic pollution has become one of the major concerns of our time. With over 5 trillion plastic particles floating in oceans and seas, these pollutants pose a severe threat to the environment and human health. Recently, advanced oxidation processes have emerged as a promising technology to tackle this issue. In this context, many studies have focused on heterogeneous photocatalysis as an effective process. Therefore, we fabricated ZnO-based photocatalysts, hydrothermally coated onto a glass fiber mesh. Photocatalytic degradation of low-density polypropylene MPs (300 μm) was carried out under natural solar irradiation in a batch reactor. The evolution of microplastics' oxidation was quantified by monitoring the carbonyl index (CI) over 16 consecutive days. A significant CI of 57 was obtained, around 5 times higher than the natural degradation process (without photocatalyst).

1. Introduction

Since the synthesis of the 1st plastic in 1907 by Leo Hendrik Baekeland, the material's global production has at least amplified by around 6 times, an amount that sums up to approximately surpassing 300 million tons per year[1,2]. As a result of this booming, today's world is producing twice as much plastic waste as two decades ago, with ~ 91 % being either discharged in landfills, incinerated, or leaked into the environment whereas just ~ 9 % successfully recycled[3]. With such a relentlessly growing industry, ineffective waste management procedures resulted in plastic litter infiltrating the ecosystem, and endangering aquatic and groundwater sustainability[4]. In this scope, it was reported that more than 5 trillion plastic debris weighing over 260,000 tons have been released into the world's oceans and seas[5]. Among these floating plastics, more than 92 % are classified as microplastics (MPs)[5]. These latter are water-insoluble synthetic polymers of diverse shapes, with sizes ranging from 1 μm to 5 mm[6] formed either as engineered micro-sized plastic beads to be used in cosmetics and beauty products (primary sources), or through the gradual disintegration of larger plastic objects (secondary sources)[7].

The level of toxicity of MPs primarily depends on their chemical structures in addition to additives' integration, which ensures better cross-linking during the polymerization process[8].

Microplastics are relatively stable, and persistent particles with a chemical structure falling into two categories: i) homo-chain plastics (C-C bond in the main chain like polystyrene (PS), polypropylene (PP), polyethylene (PE), etc.) and ii) hetero-chain plastics (different bonds in the main chain like polyethylene terephthalate (PET), polyamide (PA), etc.)[9]. Owing to their hydrophobic and physicochemical properties, MPs can attract a wide spectrum of pollutants to their surface such as heavy metals, polycyclic aromatic hydrocarbons, antibiotics, aromatic, and aliphatic compounds, etc. which can potentially increase their toxicity to a variety of living organisms[10–12].

The main exposure pathways to microplastics are ingestion, inhalation, and dermal contact[13]. Furthermore, their infinitesimal size makes them accessible to marine animals, invading the food chain and threatening human health[14]. In this view, it was recently reported that a person might ingest between 39,000–52,000 MPs per year via food and beverages, where 4000 MPs to 90,000 MPs could be added annually if tap water and bottled water are consumed, respectively. [15]. When ingested by living organisms and depending on their chemical structures[16], MPs showed a variety of harmful effects, including i) clogging and histological injury in the intestine, digestive tracts, and liver (e.g., polyethylene, polypropylene, polystyrene, polyamide, and polyvinyl chloride caused cracking of villi and splitting of enterocytes in zebrafish Danio Rerio)[17,18], ii) endocrine disorders, oxidative stress, immune responses, and altered gene expression[19,19], and iii) the impact on the behavioral pattern, fecundity, and survival[20,21].

Thus, the removal of microplastics from aquatic systems has become an emerging public health matter, increasing in a significant way the amount of research in the last decade. In addition, due to the low detectability of MPs and their ability to bypass the various stages of conventional wastewater treatment plants (WWTPs)[22,23], various technologies, such as physical, chemical, and biological treatments, have been researched[24–26]. However, these techniques present major limitations, including the additional treatment of the produced sludge, the formation of secondary MPs, and non-reusability, making them unappealing for MPs' treatment[2]. In this view, advanced oxidation processes (AOPs) are promising technologies due to their ability to remove non-biodegradable and chemically stable contaminants[27–29]. Among these processes, solar photocatalysis is considered to be one of the most practical and environmentally-friendly technologies, due to its low cost, the use of sunlight as a clean energy source, and the absence of subsequent disposal procedures[30,31]. It involves the formation of highly reactive radical species such as hydroxyl ($HO^{\bullet}$), superoxide ($O_2^{\bullet-}$), and hydroperoxyl ($HO_2^{\bullet}$) radicals, capable of converting recalcitrant organic molecules or particles to less harmful products like CO_2 and water[32]. Although numerous studies have been reported on the photocatalytic removal of microplastics, they exhibit major limitations such as[31,33–41]: i) the necessity of a filtration step to recover the photocatalyst; ii) the need for mechanical mixing of the photocatalyst and the MP particles; iii) low surface contact between the photocatalyst and the MPs, and iv) the usage of artificial irradiations.

To address these limitations, ZnO nanorods deposited onto glass fiber mesh were used to degrade 300 µm PP microplastics under natural sunlight irradiations. The usage of glass fiber substrates is ideal to trap the low-density particles close to the coated photocatalysts. In addition, natural sunlight correctly mimics the real situation and provides zero-cost sources of irradiation. Low-density polypropylene (LD-PP) microplastics were selected as a pollutant model due to their ubiquitous existence in aquatic mediums[50]. ZnO was chosen as the photocatalyst for its high conversion efficiency of photonic energy, low synthesis cost, and low degree of toxicity to marine/human life[52]. The photocatalytic degradation of LD-PP microplastics was assessed by following the evolution of the carbonyl index over time through the ATR-FTIR technique and by analyzing the evolution of their microstructure by SEM-FEG microscopy.

2. Experimental Section

2.1 Chemicals

Zinc nitrate hexahydrate ($Zn(NO_3)_2.6H_2O$), zinc acetate dihydrates ($Zn(CH_3COO)_2.2H_2O$), and hexamethylenetetramine ($(CH_2)_6N_4$), were purchased from ACROS organics Spain. PP microplastics of diameter = 300 μm and density = 905 Kg/m^3 were provided by PPPolymer AB, Sweden. The glass fiber mesh of ~ 16 μm thickness, was purchased from Sigma Aldrich. Deionized water (DI) with a resistivity of 18 MΩ·cm was used in all the experiments.

2.2 Hydrothermal Growth of ZnO NRs on the Glass Fibers Substrate

First, ~ 1 g of glass fiber substrates was carefully cleaned with ethanol, acetone, and deionized water (DI). Next, a seeding layer of ZnO was coated on the pre-heated substrate at 350 ^oC by spraying 25 mL of 10 mM solution of zinc acetate dehydrate in DI water with a flow rate of ~ 1 mL/min. The fibers were then immersed in a chemical bath filled up with 500 ml of an aqueous solution containing equimolar concentrations (10 mM) of zinc nitrate hexahydrate (precursor) and hexamethylenetetramine (structuring agent). The hydrothermal growth was conducted at 90 ^oC for 65 hours. Due to the non-polarity of the structuring agent, this latter chelates and covers the non-polar sides of the hexagonal ZnO lattice, leaving the top polar sides exposed for growth. Finally, the coated fibers were properly washed with DI water and then post-heated in the air at 350 ^oC for 1 hour, to ensure that any leftover organics within the oxide structure are removed. The preparation steps of ZnO NRs on glass fiber substrates are visualized in scheme 1.

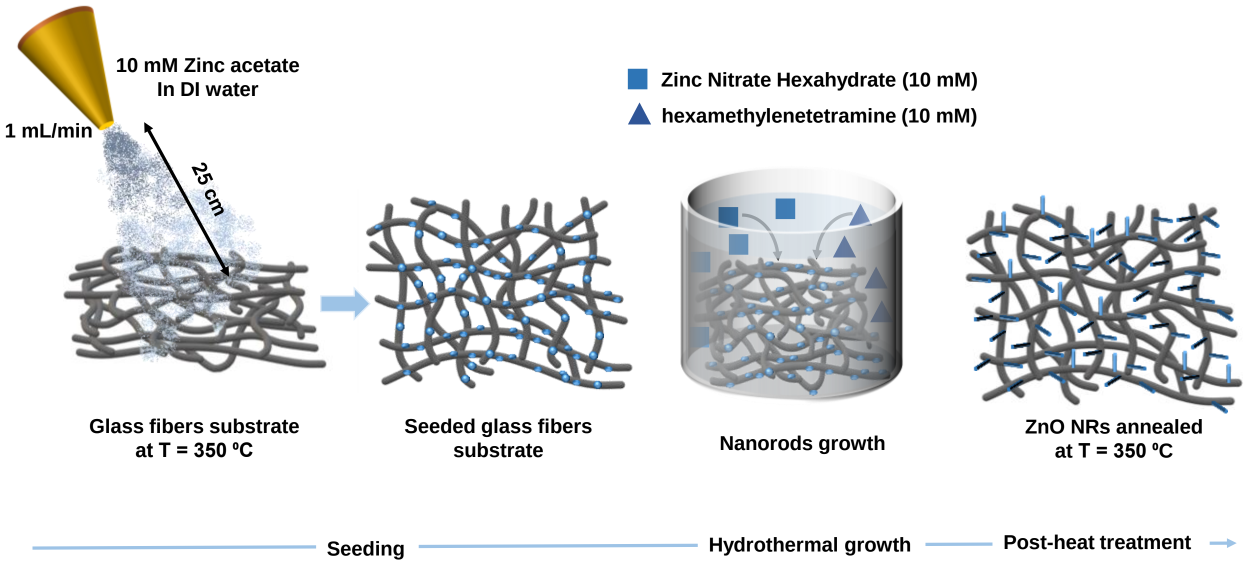

Scheme 1. Preparation procedures of the coated ZnO NRs over the glass fibers mesh.

2.3 Characterization

The crystalline structure of the ZnO NRs was examined with a D8 Discover X-ray diffractometer, fitted with a Cu emitter anode (Kα_1 and Kα_2 of wavelength 1.54056 and 1.5444 Å respectively) and a 1D LYNEXEYE XE-T detector (Bruker).

The crystal nature was also investigated by a transmission electron microscope FEG S/TEM model JEOL 2100 plus, coupled with selected area electron diffraction (SAED). The high-resolution mode was carried out at 200 kV. The HRTEM is equipped with a spherical aberration probe corrector (Cs from CEOS), a high-resolution objective lens pole piece, and an UltraScan 1000 CCD array detector (GATAN). Samples were deposited on a holey carbon-coated TEM grid.

A field emission gun scanning electron microscope, model Hitachi SU-70 FESEM was used to analyze the morphologies of the ZnO NRs and PP microplastics (before and after degradation) at operating voltages of 15 kV and 1 kV respectively. The PP particles were mounted to a conductive carbon tape after being sputtered with a thin coating of platinum (7 nm) to avoid electrical charging during the electron microscope.

The ZnO NRs absorbance was measured by a dual-beam Carry 5000 UV-Vis spectrophotometer from Agilent technology, equipped with an R928 PMT detector, and mounted in powder mode. The ZnO NRs were placed in a powder cell holder over Barium Sulfate ($BaSO_4$) background.

The functional groups in ZnO NRs and the PP microplastics were monitored with a Fourier-transformed infrared (FTIR) in attenuated total reflection (ATR) mode with an incidence angle of 45°, and a 4 cm^{-1} resolution, using a Spectrum 400 model from PerkinElmer, equipped with an FR-DTGS detector (fast recovery Deuterated Triglycine Sulfate detector).

2.4 Photocatalytic Set-Up

The Photocatalytic degradation of LD-PP was carried out in a batch photoreactor (100 ml) made from borosilicate glass, for 16 consecutive days, including daytime and nighttime, in July (Beirut, Lebanon). The reactor was filled with 90 ml of DI water containing the nanocoated glass fiber mesh wherein 27 particles of the PP microplastics ~ 26 mg were suspended, equivalent to a high concentration of 300 particles/L. The reactor was tightly sealed to prevent any loss in water volume by evaporation. The sampling was done at fixed time intervals during the photo-irradiation to quantify the evolution of the MPs' carbonyl index (CI). The sun luminosity was tracked during every daytime by using a Testo 450 luxmeter of ±3 % precision from Testo, France. The sun's luminosity increased gradually every day from a minimum of ~ 45,000 lux at 7 a.m., reaching ~ 100,000 lux at around 12:30 p.m., and then decreases progressively to 50,000 lux by 7 p.m. (Figure S1). Considering these light hours from 7 am to 7 pm, the total irradiation time sums up to 196 hours.

3. Results and Discussion

3.1 Characterization of ZnO NRs

• SEM and TEM Analysis

The morphology of the deposited material was examined using a field emission gun scanning electron microscope. The micrographs in Figure 1a and its inset show that almost all the seeding grew into vertically-oriented nanorods. The majority of the NRs are characterized by an average length (l) of ~ 3.2 µm (population standard deviation $\sigma = 3.5$ nm), a diameter (d) of ~94 nm (population standard deviation $\sigma = 1.11$ µm), resulting in a high ratio of l:d ~ 32. These parameters were assessed using ImageJ software to treat the SEM micrographs, where a threshold segmentation step was used to precisely highlight the rods' boundaries. Generally, the synthesis of long and thin nanorods is beneficial for any photocatalytic application, due to their important surface area. However, increasing the length of the ZnO nanorods beyond 2.4 µm while maintaining a high l:d ratio of ~ 35 is still challenging, as the rods tend to increase their diameter size with respect to their length[43–45], and therefore decrease the coating surface area. The obtained nanorods herein registered notably higher dimensions (l and d) than those reported by other hydrothermal procedures, thermal decomposition, or electrochemical deposition while maintaining a high l:d ratio[43,44,46–48]. On the other hand, only chemical vapor deposition yielded much bigger rods in length and diameter with a range of 40 – 50 µm and 100 – 500 nm respectively. This is at the cost of employing an ultra-high temperature of ~ 1055 °C that requires both specific equipment and substrates[49]. The lengths, diameters, and l:d ratios of ZnO NRs synthesized by different techniques are listed in Table 1.

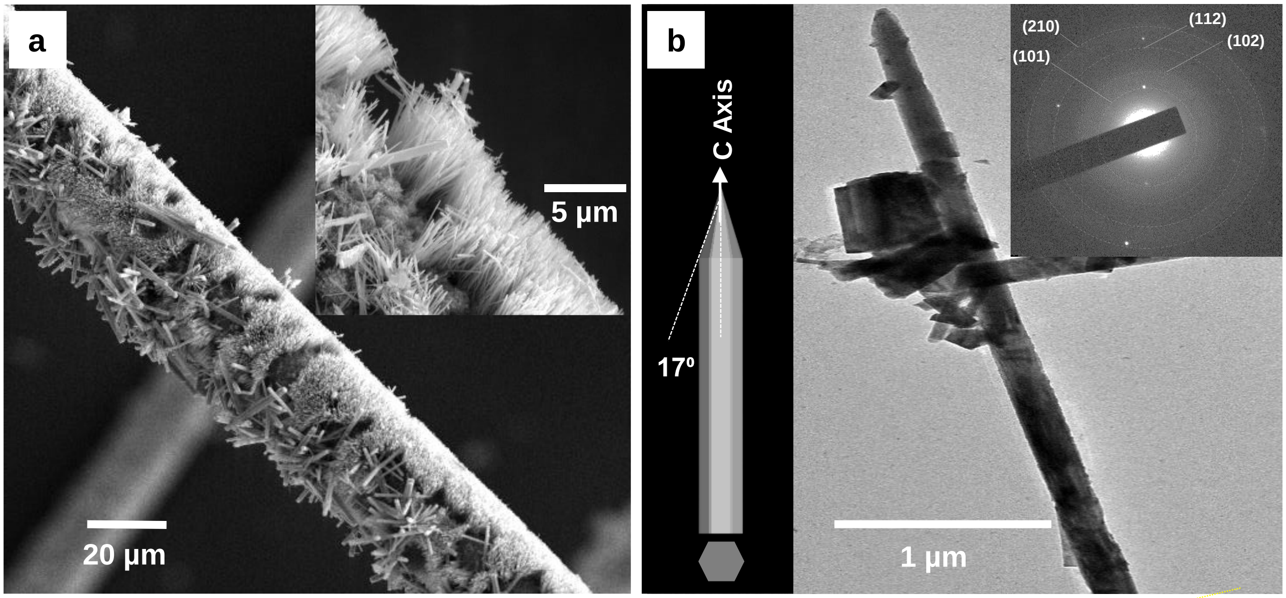

Figure 1. **(a)** SEM-FEG image of glass fibers coated ZnO NRs after the post-heat treatment at 350 °C, the inset: Zoomed-in view of "a". **(b)** TEM image of a free-standing ZnO nanorod separated with sonication. Left inset: Schematic illustration of a grown rod in +c direction ended with a conical-like shape. Right inset: Inset: Relative selected area electronic diffraction pattern (SAED).

Furthermore, the nanorods' structure was investigated by transmission electron microscopy. Figure 1b shows a low-magnification image of an individual nanorod. The diameter is uniform along the entire length, confirming anisotropic growth along the +c axis throughout the hydrothermal synthesis (65 h). Most of the NRs are terminated with a conical shape (Left inset of Figure 1b) corresponding to the a-planes family of the wurtzite ZnO[50]. The SAED measurement confirms this crystalline phase as it shows a ring-like pattern with 4 distinctive rings, corresponding to the lattice spacing of the (101), (102), (112), and (210) planes of the wurtzite crystal (Right inset of Figure 1b).

Table 1. Dimensions of ZnO NRs obtained with different synthesis Techniques.

Reference	**Synthesis Technique**	**Length (*l*) µm**	**Diameter (*d*) nm**	***l*:*d***
Chandraiahgari et al.[48]	Thermal decomposition of zinc acetate dihydrate followed by probe sonication in acetone	~ 0.47	~ 330	~ 1.42
Liu et al.[47]	Hydrothermal growth of mobilized ZnO NRs powder	~ 1.54	~ 45.6	~ 34
Xu et al.[43]	Electrochemical deposition	~ 2	~ 300 – 400	~ 5 – 6.7
Wu et al.[44]	Hydrothermal growth on Si (100) substrate	~ 2.4	~ 120	~ 20
Lausecker et al.[45]	Hydrothermal growth on polycrystalline Au seed layer	~ 2.4	~ 180	~13.3
Chrissanthopoulos et al.[49]	Chemical vapor deposition	~ 40 – 50	~ 100 – 500	~ 100 – 400
This study	**Tuned Hydrothermal Growth**	**~ 3.4**	**~ 91**	**~ 37**

- ## Microstructural and Optical Properties

The microstructural and optical properties of the heat-treated NRs at 350 ºC (Figure 2a) were then investigated. The XRD pattern of the nanorods is shown in Figure 2b. All the diffraction peaks are indexed to the wurtzite ZnO structure with lattice constants of a = b = 3.248 Å and c = 5.202 Å (JCPDS No. 01-086-3978)[51–53]. This result is in good agreement with the SAED pattern, indicating the main diffraction planes of the wurtzite structure.

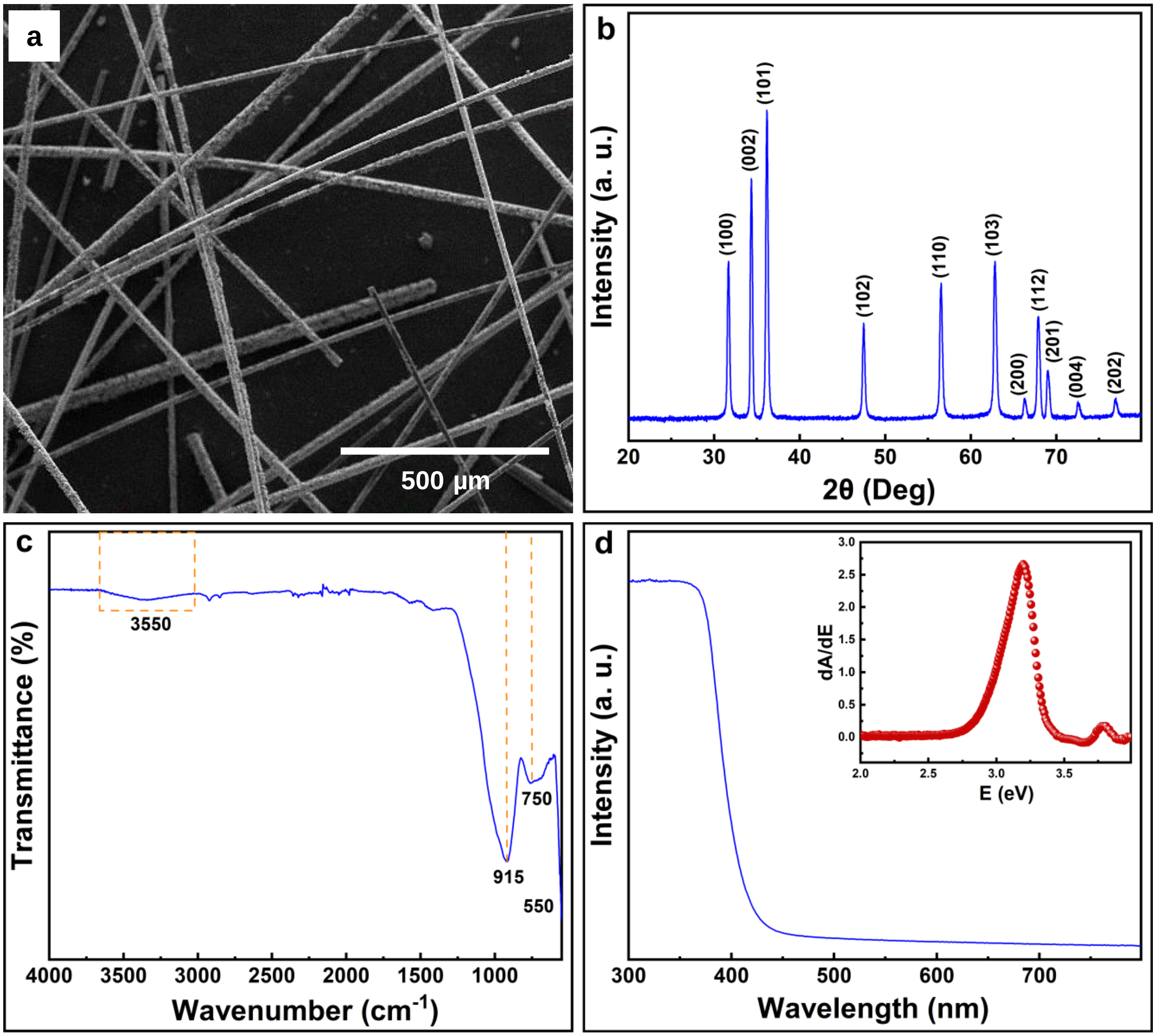

Figure 2. (a) SEM image of the coated glass fibers with ZnO NRs and post-heated at 350 °C **(b)** XRD pattern of "a", **(c)** ATR-FTIR spectrum of "a", **(d)** Room-temperature UV-vis absorbance spectrum of "a". Inset: Optical bandgap (Eg) obtained from the first derivative of the absorbance spectrum with respect to photon energy.

The functional groups of ZnO NRs were characterized by ATR-FTIR spectroscopy and plotted in Figure 2c. The infra-red spectrum reveals 5 prominent peaks. The located peaks at ~ 550 cm^{-1}, and ~ 750 cm^{-1} correspond to the stretching vibrations of Zn–O bonds, while the strongest absorption at ~ 915 cm^{-1} is associated with the tetrahedral coordination of Zn within the wurtzite ZnO lattice[54–58]. The broad peak at ~ 3350 cm^{-1} mainly arises from the stretching of intermolecular –OH hydroxyl group[57]. The insignificant peaks in the region of ~ 1550 cm^{-1} are typical characteristics of chemisorbed organic molecules at the films' surface (C–O and C=O stretching vibrations)[58]. These peaks are still present (trace level) even after a post-heat treatment at high temperatures. This is linked to the adsorption of organic contaminants from the surrounding medium.

The photocatalytic activity of oxide materials is fundamentally dependent on their optical properties, such as the absorption capacity and the presence of defect states within the intrinsic bandgap. For this reason, the absorption spectrum of the ZnO NRs was recorded at room temperature and plotted in Figure 2d. As noticed, the nanorods show a significant absorption in the UV region below 400 nm, typically corresponding to its intrinsic bandgap energy[59]. The weak absorption in the visible area is probably due to the light diffusion phenomena of the ZnO as powder. Moreover, the optical bandgap (Eg) was also estimated. This latter can be generally found by plotting the first derivative of the absorbance with respect to photon energy (dA/dE), as a function of photon energy (E), and then finding the first maxima at the lower energy side (inset of Figure 2d)[30]. We found an optical bandgap of ~ 3.19 eV which is lower than the theoretical one (3.37 eV at RT). This may indicate the formation of defects states including oxygen vacancies (V_o) and interstitial zinc ions (Zn_i)[53].

3.2 Photocatalytic Degradation of Low-Density PP MPs

ATR-FTIR spectroscopy was used to systematically track the oxidation of the polypropylene beads over the irradiation time. This characterization technique has been widely used to evaluate the variation of the carbonyl index during the photocatalytic processes[2]. Figure 3 shows the changes in the PP infrared spectrum (without photocatalyst) during 196 hours of sunlight irradiation (Figure 3a). The un-irradiated PP presents 2 main prominent peaks identified as the $–CH_3$ strong symmetric stretching, –

CH_2 strong symmetric stretching at ~ 2950 cm^{-1}, and ~ 2838 cm^{-1}, respectively, in addition to smaller absorbance peaks detailed in Table S1[60–62]. After being exposed to the sunlight, oxygenated (–OH & –OOH) groups arise in the broadband between ~ 3300 – 3700 cm^{-1}, indicating moderate oxidation of the PP polymer[41,63,64]. As the oxidation proceeds, a small carbonyl peak is detected between ~ 1550 – 1850 cm^{-1}. This observation suggests that the photo-oxidation of polypropylene (PP) is first driven by the generation of hydroxyl groups via a photolysis process. The UV irradiation of the sun has enough energy to break down the bonds C–C (375 kJ/mol) and C–H (420 kJ/mol)[33]. Consequently, the resulting alkyl radicals react with the O_2 molecules to generate peroxy radicals ($ROO^{\bullet}$), and therefore hydroperoxide groups (ROOH)[33,65–67]. Due to the weak stability of the latter, hydroperoxide compounds can react rapidly with the dissolved oxygen to form organic compounds of low molecular weight with carbonyl groups[33].

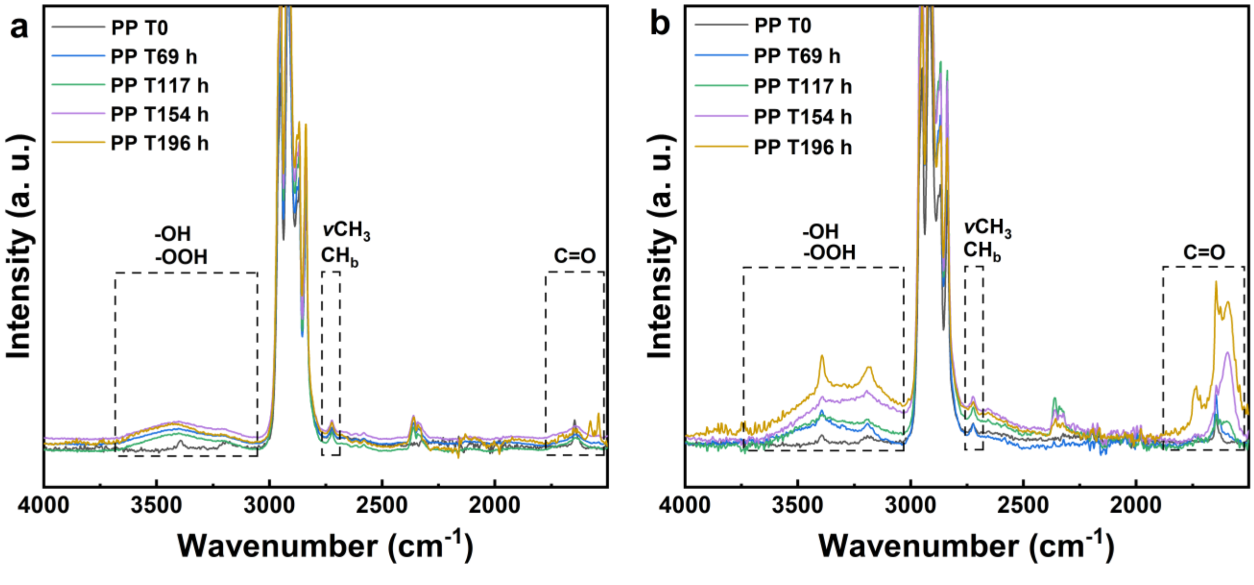

Figure 3. Evolution of the FTIR spectra of PP beads **(a)** without the photocatalyst, **(b)** over the course of their photodegradation with the ZnO NRs.

However, the oxidation of the PP-MPs is faster when the ZnO photocatalyst is used, due to the active participation of highly reactive oxygen species (ROS). These species are formed by the electron (e^-) – hole (h^+) pairs, once ZnO absorbs the sunlight energy of the solar spectrum. At the beginning of the photocatalytic degradation, the strong absorption band detected at ~ 1641 cm^{-1}, is associated with the formation of carboxylic acids (Figure 3b)[63]. In parallel, a significant increase is observed in the associated band with the stretching mode of the hydrogen-bonded hydroxyl group between 3300 – 3700 cm^{-1}. As the photocatalytic degradation progresses, the carbonyl peak becomes more pronounced exhibiting an asymmetric broad and medium intensity band between 1550 – 1850 cm^{-1}. This behavior is correlated with the important increase of carboxylic acid groups at the PP surface[63]. With the advancement of the oxidation (at 196 hours), this peak continues increasing concomitantly with the appearance of ketone, aldehyde, and anhydride groups at 1710 cm^{-1}, 1740 cm^{-1}, and 1772 cm^{-1}, respectively[63] (Figure S2b). The appearance of these groups mainly indicates a scission of the large chains of polypropylene[33,41,68]. Normally, once formed, the further degradation of ketones, aldehydes, and anhydrides into CO_2 and H_2O proceeds with the Norrish mechanism as described elsewhere[41,69].

The carbonyl index (CI) was well established to quantify the oxidation degree of MPs and defined herein as the absorbance ratio of the carbonyl band over a reference band (Eq. 1)[37,41,70,71], as seen in Figure S2.

$$CI = \frac{Abs_{1550\ -\ 1850\,\mathrm{cm}-1}}{Abs_{2700\ -\ 2750\,\mathrm{cm}-1}} \qquad \text{(Eq. 1)}$$

As the evolution in the absorption band at ~ 1550 – 1850 cm^{-1} reflects the formation of the main carbonyls (carboxyl acids, ketones, aldehydes, and anhydrides) without any interference with other functional groups, it was used to track the carbonyl index of PP during their oxidation process. The reference was set at the absorption band at ~ 2700 – 2750 cm^{-1}, wherein the main 2722 cm^{-1} absorbance peak refers to the angular molecular vibrations in CH and axial molecular vibrations in CH_3[72]. Figure 4 depicts the evolution of the carbonyl index during natural (without ZnO) and photocatalytic oxidations of PP MPs. The CI of the blank samples shows a modest increment of approximately 3.8 times (slope value of ~ 0.046), reaching a value of 11.6 after 196 hours of irradiation. Yet, with the introduction of the photocatalyst, the kinetics of the photocatalytic degradation are largely enhanced and follow two different regimes. Between 0 and 117 hours, a slow degradation rate is observed (slope value of ~ 0.158) demonstrating the gradual oxidation of the PP outer surface with a CI reaching 19.1 (corresponding to an increment of 6.5 times). However, a rapid degradation kinetic (slope value of ~ 0.54) is noticed between 117 and 196 hours indicating an important increase in the carbonyl groups concentrations after the appearance of new PP surfaces. Thus, a CI of 57.2 is registered after 196 hours.

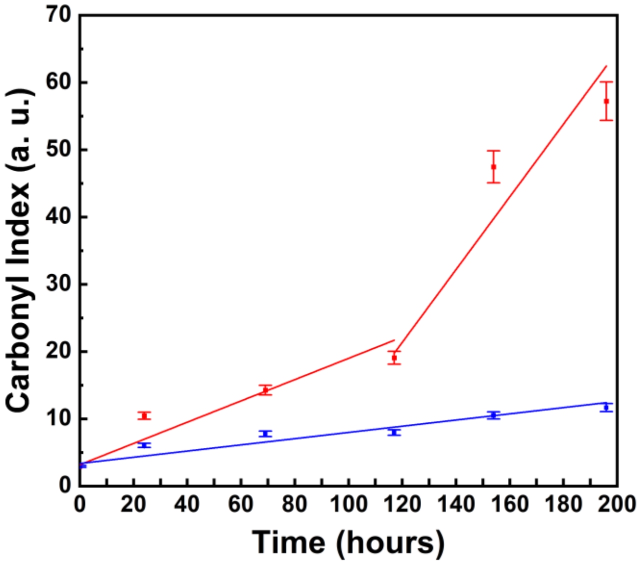

Figure 4. Evolution of the carbonyl index (CI) of the PP MPs under sunlight irradiation with the usage of the ZnO NRs (red square) and without (blue circle).

To understand better this behavior, the morphological evolution within the MPs' microstructure was evaluated by SEM-FEG at 0, 117, and 196 hours (Figure 5). For instance, the unirradiated particles exhibit a smooth surface and a low number of cavities. However, after 117 hours of irradiation in the presence of a photocatalyst, the roughness of the particles' surface becomes more pronounced with the appearance of some cracks. This is due to the surface oxidation of the PP by the generated ROS species. Finally, at 196 hours, a significant number of cavities is detected in agreement with the recorded high CI. This is explained by the increase of particle surface area after crack propagation.

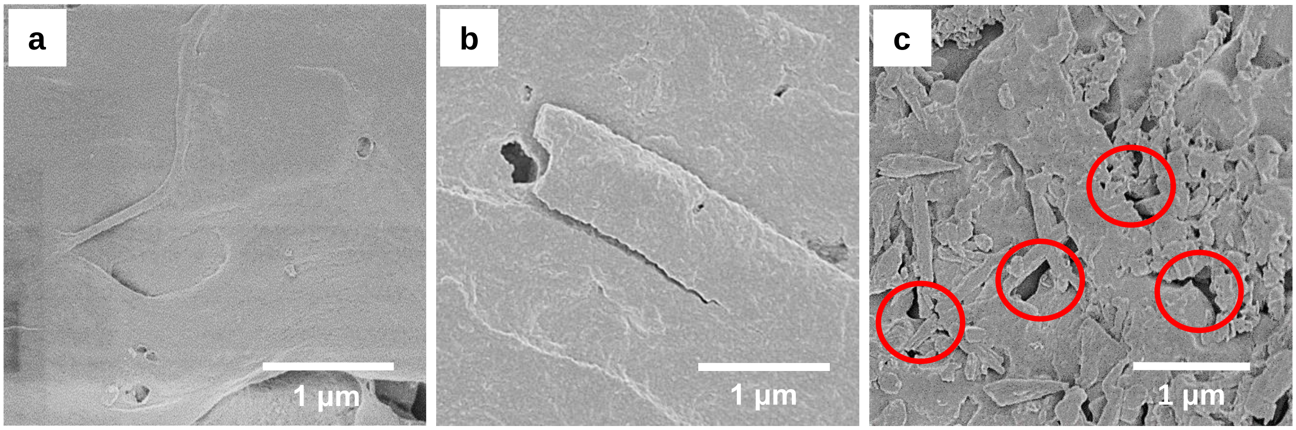

Figure 5. SEM-FEG images of **(a)** as-received PP MPs, **(b)** after 117 h of photocatalytic degradation with ZnO NRs, **(c)** after 196 h of photocatalytic degradation with ZnO NRs.

The important value of CI (57.2) highlights the higher efficiency of natural sunlight/ZnO NRs/glass fibers mesh system for the degradation of microplastics, compared to other works. For instance, Verma et al. used TiO_2 films and reported a carbonyl index 10 times lower than this study[35]. One reason for this lower efficiency is probably due to the low contact between TiO_2 and the low-density PP floating on the water surface, reducing, therefore, its exposure to ROS. Accordingly, several reports on MPs oxidation over ZnO or TiO_2 films also resulted in low degradation efficiencies[37,38,64]. In addition, although Uheida et al.[41] previously obtained a carbonyl index of 40 after 456 hours of irradiation of PP-MPs under a halogen lamp, other studies (Table 2) show lower efficiencies than that obtained here. Several factors may explain this result: i) the type and size of the particles; ii) the source and intensity of the irradiation; iii) the type and morphology of the photocatalyst; iv) and the photocatalyst support[35,36,38,41,71].

Table 2. Comparative photodegradation efficiency of microplastics over different photocatalysts with the as-synthesized ZnO nanorods. The carbonyl indexes of this study were compared to each literature according to the reported absorbance reference.

Reference	**Photocatalyst**	**Irradiation Source**	**Microplastics Type**	**CI**	**Extracted CI from this study**
Verma et al.[35]	TiO_2 film	Solar irradiation	LD PP	~ 1.5 at 216 h	~ 57 at 196 h
Llorente-García et al.[36]	N doped TiO_2 film	Visible irradiation	LD PE	~ 1.23 at 50 h	~ 10 at 24 h
Tofa et al.[37]	Pt doped ZnO film	Visible irradiation	LD PE	~ 1.49 at 175 h	~ 47 at 154 h
Tofa et al.[38]	ZnO film	Visible irradiation	LD PE	~ 1.41 at 175 h	~ 47 at 154 h
Uheida et al.[41]	ZnO nanorods	Visible irradiation	PP	~ 40 at 456 h	~ 57 at 196 h

3 Conclusion

In this work, a glass fiber mesh was coated with a hydrothermal synthesis of ZnO NRs to study the photodegradation of low-density PP MPs in a batch reactor. The carbonyl index was tracked over 16 consecutive days of natural sunlight irradiation to quantify the microplastics’ oxidation. A slow evolution of the carbonyl and hydroxyl absorption bands was detected between 0 and 117 h, due to the small external surfaces of polypropylene beads that are exposed to oxidation. However, as the irradiation evolves, the photooxidation kinetics significantly increased because of the appearance of cracks providing an additional pathway for oxygen to penetrate deeper into the particles. This analysis was supported by the formation of relatively deep cavities after 196 h of irradiation, demonstrating the scission of the polypropylene chains. Consequently, the use of natural sunlight coupled with the ZnO NRs/glass fiber mesh system enables a significant improvement in the degradation of polypropylene beads with a carbonyl index of ~ 57.

AUTHOR INFORMATION

Corresponding Author

Dr. Wael Hamd

E-mail: wael.hamd@balamand.edu.lb

Acknowledgment

This work has been supported by the project: CLAIM, H2020-BG-2016–2017 [grant number 774586], “Cleaning Litter by developing and Applying Innovative Methods in European seas”. Mr. David Montero**,** Mr. Mohemed Selmane, Dr. Ferdaous Ben Romdhane, and Professor Olivier Durupthy are gratefully acknowledged for conducting SEM-FEG, HRTEM, XRD, and UV-vis measurements at Sorbonne University.

References

(1) Geyer, R.; Jambeck, J. R.; Law, K. L. Production, Use, and Fate of All Plastics Ever Made. *Sci. Adv.* **2017**, *3* (7), e1700782. https://doi.org/10.1126/sciadv.1700782.
(2) Hamd, W.; Daher, E. A.; Tofa, T. S.; Dutta, J. Recent Advances in Photocatalytic Removal of Microplastics: Mechanisms, Kinetic Degradation, and Reactor Design. *Front. Mar. Sci.* **2022**, *9*, 885614. https://doi.org/10.3389/fmars.2022.885614.
(3) *Global Plastics OutlookEconomic Drivers, Environmental Impacts and Policy Options*; OECD. https://read.oecd-ilibrary.org/view/?ref=1128_1128022-j5crhacc6w&title=Global-plastics-outlook-highlights (accessed 2022-01-30).
(4) Browne, M. A.; Galloway, T.; Thompson, R. Microplastic-an Emerging Contaminant of Potential Concern?: Learned Discourses. *Integr Environ Assess Manag* **2007**, *3* (4), 559–561. https://doi.org/10.1002/ieam.5630030412.
(5) Eriksen, M.; Lebreton, L. C. M.; Carson, H. S.; Thiel, M.; Moore, C. J.; Borerro, J. C.; Galgani, F.; Ryan, P. G.; Reisser, J. Plastic Pollution in the World’s Oceans: More than 5 Trillion Plastic Pieces Weighing over 250,000 Tons Afloat at Sea. *PLoS ONE* **2014**, *9* (12), e111913. https://doi.org/10.1371/journal.pone.0111913.
(6) Frias, J. P. G. L.; Nash, R. Microplastics: Finding a Consensus on the Definition. *Marine Pollution Bulletin* **2019**, *138*, 145–147. https://doi.org/10.1016/j.marpolbul.2018.11.022.
(7) Boucher, J.; Friot, D. *Primary Microplastics in the Oceans: A Global Evaluation of Sources*; IUCN International Union for Conservation of Nature, 2017. https://doi.org/10.2305/IUCN.CH.2017.01.en.

(8) Meeker, J. D.; Sathyanarayana, S.; Swan, S. H. Phthalates and Other Additives in Plastics: Human Exposure and Associated Health Outcomes. *Phil. Trans. R. Soc. B* **2009**, *364* (1526), 2097–2113. https://doi.org/10.1098/rstb.2008.0268.

(9) Gewert, B.; Plassmann, M. M.; MacLeod, M. Pathways for Degradation of Plastic Polymers Floating in the Marine Environment. *Environ. Sci.: Processes Impacts* **2015**, *17* (9), 1513–1521. https://doi.org/10.1039/C5EM00207A.

(10) Zhang, H.; Pap, S.; Taggart, M. A.; Boyd, K. G.; James, N. A.; Gibb, S. W. A Review of the Potential Utilisation of Plastic Waste as Adsorbent for Removal of Hazardous Priority Contaminants from Aqueous Environments. *Environmental Pollution* **2020**, *258*, 113698. https://doi.org/10.1016/j.envpol.2019.113698.

(11) Andrady, A. L. Microplastics in the Marine Environment. *Marine Pollution Bulletin* **2011**, *62* (8), 1596–1605. https://doi.org/10.1016/j.marpolbul.2011.05.030.

(12) Yuan, W.; Zhou, Y.; Chen, Y.; Liu, X.; Wang, J. Toxicological Effects of Microplastics and Heavy Metals on the Daphnia Magna. *Science of The Total Environment* **2020**, *746*, 141254. https://doi.org/10.1016/j.scitotenv.2020.141254.

(13) Domenech, J.; Marcos, R. Pathways of Human Exposure to Microplastics, and Estimation of the Total Burden. *Current Opinion in Food Science* **2021**, *39*, 144–151. https://doi.org/10.1016/j.cofs.2021.01.004.

(14) Hodson, M. E.; Duffus-Hodson, C. A.; Clark, A.; Prendergast-Miller, M. T.; Thorpe, K. L. Plastic Bag Derived-Microplastics as a Vector for Metal Exposure in Terrestrial Invertebrates. *Environ. Sci. Technol.* **2017**, *51* (8), 4714–4721. https://doi.org/10.1021/acs.est.7b00635.

(15) Cox, K. D.; Covernton, G. A.; Davies, H. L.; Dower, J. F.; Juanes, F.; Dudas, S. E. Human Consumption of Microplastics. *Environ. Sci. Technol.* **2019**, *53* (12), 7068–7074. https://doi.org/10.1021/acs.est.9b01517.

(16) Meeker, J. D.; Sathyanarayana, S.; Swan, S. H. Phthalates and Other Additives in Plastics: Human Exposure and Associated Health Outcomes. *Phil. Trans. R. Soc. B* **2009**, *364* (1526), 2097–2113. https://doi.org/10.1098/rstb.2008.0268.

(17) Capó, X.; Company, J. J.; Alomar, C.; Compa, M.; Sureda, A.; Grau, A.; Hansjosten, B.; López-Vázquez, J.; Quintana, J. B.; Rodil, R.; Deudero, S. Long-Term Exposure to Virgin and Seawater Exposed Microplastic Enriched-Diet Causes Liver Oxidative Stress and Inflammation in Gilthead Seabream Sparus Aurata, Linnaeus 1758. *Science of The Total Environment* **2021**, *767*, 144976. https://doi.org/10.1016/j.scitotenv.2021.144976.

(18) Lei, L.; Wu, S.; Lu, S.; Liu, M.; Song, Y.; Fu, Z.; Shi, H.; Raley-Susman, K. M.; He, D. Microplastic Particles Cause Intestinal Damage and Other Adverse Effects in Zebrafish Danio Rerio and Nematode Caenorhabditis Elegans. *Science of The Total Environment* **2018**, *619–620*, 1–8. https://doi.org/10.1016/j.scitotenv.2017.11.103.

(19) Qiao, R.; Sheng, C.; Lu, Y.; Zhang, Y.; Ren, H.; Lemos, B. Microplastics Induce Intestinal Inflammation, Oxidative Stress, and Disorders of Metabolome and Microbiome in Zebrafish. *Science of The Total Environment* **2019**, *662*, 246–253. https://doi.org/10.1016/j.scitotenv.2019.01.245.

(20) Ma, H.; Pu, S.; Liu, S.; Bai, Y.; Mandal, S.; Xing, B. Microplastics in Aquatic Environments: Toxicity to Trigger Ecological Consequences. *Environmental Pollution* **2020**, *261*, 114089. https://doi.org/10.1016/j.envpol.2020.114089.

(21) Khalid, N.; Aqeel, M.; Noman, A.; Hashem, M.; Mostafa, Y. S.; Alhaithloul, H. A. S.; Alghanem, S. M. Linking Effects of Microplastics to Ecological Impacts in Marine Environments. *Chemosphere* **2021**, *264*, 128541. https://doi.org/10.1016/j.chemosphere.2020.128541.

(22) Lasee, S.; Mauricio, J.; Thompson, W. A.; Karnjanapiboonwong, A.; Kasumba, J.; Subbiah, S.; Morse, A. N.; Anderson, T. A. Microplastics in a Freshwater Environment Receiving Treated Wastewater Effluent: Microplastics in Urban Surface Water. *Integr Environ Assess Manag* **2017**, *13* (3), 528–532. https://doi.org/10.1002/ieam.1915.

(23) Murphy, F.; Ewins, C.; Carbonnier, F.; Quinn, B. Wastewater Treatment Works (WwTW) as a Source of Microplastics in the Aquatic Environment. *Environ. Sci. Technol.* **2016**, *50* (11), 5800–5808. https://doi.org/10.1021/acs.est.5b05416.

(24) Mumford, A. C.; Barringer, J. L.; Benzel, W. M.; Reilly, P. A.; Young, L. Y. Microbial Transformations of Arsenic: Mobilization from Glauconitic Sediments to Water. *Water Research* **2012**, *46* (9), 2859–2868. https://doi.org/10.1016/j.watres.2012.02.044.

(25) Talvitie, J.; Mikola, A.; Koistinen, A.; Setälä, O. Solutions to Microplastic Pollution – Removal of Microplastics from Wastewater Effluent with Advanced Wastewater Treatment Technologies. *Water Research* **2017**, *123*, 401–407. https://doi.org/10.1016/j.watres.2017.07.005.

(26) Ziajahromi, S.; Neale, P. A.; Rintoul, L.; Leusch, F. D. L. Wastewater Treatment Plants as a Pathway for Microplastics: Development of a New Approach to Sample Wastewater-Based Microplastics. *Water Research* **2017**, *112*, 93–99. https://doi.org/10.1016/j.watres.2017.01.042.

(27) Antonopoulou, M.; Kosma, C.; Albanis, T.; Konstantinou, I. An Overview of Homogeneous and Heterogeneous Photocatalysis Applications for the Removal of Pharmaceutical Compounds from Real or Synthetic Hospital Wastewaters under Lab or Pilot Scale. *Science of The Total Environment* **2021**, *765*, 144163. https://doi.org/10.1016/j.scitotenv.2020.144163.

(28) Zhang, M.; Dong, H.; Zhao, L.; Wang, D.; Meng, D. A Review on Fenton Process for Organic Wastewater Treatment Based on Optimization Perspective. *Science of The Total Environment* **2019**, *670*, 110–121. https://doi.org/10.1016/j.scitotenv.2019.03.180.

(29) Konstas; Kosma; Konstantinou; Albanis. Photocatalytic Treatment of Pharmaceuticals in Real Hospital Wastewaters for Effluent Quality Amelioration. *Water* **2019**, *11* (10), 2165. https://doi.org/10.3390/w11102165.

(30) Daher, E. A.; Riachi, B.; Chamoun, J.; Laberty-Robert, C.; Hamd, W. New Approach for Designing Wrinkled and Porous ZnO Thin Films for Photocatalytic Applications. *Colloids and Surfaces A: Physicochemical and Engineering Aspects* **2023**, *658*, 130628. https://doi.org/10.1016/j.colsurfa.2022.130628.

(31) Ariza-Tarazona, M. C.; Villarreal-Chiu, J. F.; Barbieri, V.; Siligardi, C.; Cedillo-González, E. I. New Strategy for Microplastic Degradation: Green Photocatalysis Using a Protein-Based Porous N-TiO2 Semiconductor. *Ceramics International* **2019**, *45* (7), 9618–9624. https://doi.org/10.1016/j.ceramint.2018.10.208.

(32) Potakis, N.; Frontistis, Z.; Antonopoulou, M.; Konstantinou, I.; Mantzavinos, D. Oxidation of Bisphenol A in Water by Heat-Activated Persulfate. *Journal of Environmental Management* **2017**, *195*, 125–132. https://doi.org/10.1016/j.jenvman.2016.05.045.

(33) García-Montelongo, X. L.; Martínez-de la Cruz, A.; Vázquez-Rodríguez, S.; Torres-Martínez, L. M. Photo-Oxidative Degradation of TiO2/Polypropylene Films. *Materials Research Bulletin* **2014**, *51*, 56–62. https://doi.org/10.1016/j.materresbull.2013.11.040.

(34) Nabi, I.; Bacha, A.-U.-R.; Li, K.; Cheng, H.; Wang, T.; Liu, Y.; Ajmal, S.; Yang, Y.; Feng, Y.; Zhang, L. Complete Photocatalytic Mineralization of Microplastic on TiO2 Nanoparticle Film. *iScience* **2020**, *23* (7), 101326. https://doi.org/10.1016/j.isci.2020.101326.

(35) Verma, R.; Singh, S.; Dalai, M. K.; Saravanan, M.; Agrawal, V. V.; Srivastava, A. K. Photocatalytic Degradation of Polypropylene Film Using TiO2-Based Nanomaterials under Solar Irradiation. *Materials & Design* **2017**, *133*, 10–18. https://doi.org/10.1016/j.matdes.2017.07.042.

(36) Llorente-García, B. E.; Hernández-López, J. M.; Zaldívar-Cadena, A. A.; Siligardi, C.; Cedillo-González, E. I. First Insights into Photocatalytic Degradation of HDPE and LDPE Microplastics by a Mesoporous N–TiO2 Coating: Effect of Size and Shape of Microplastics. *Coatings* **2020**, *10* (7), 658. https://doi.org/10.3390/coatings10070658.

(37) Tofa, T. S.; Ye, F.; Kunjali, K. L.; Dutta, J. Enhanced Visible Light Photodegradation of Microplastic Fragments with Plasmonic Platinum/Zinc Oxide Nanorod Photocatalysts. *Catalysts* **2019**, *9* (10), 819. https://doi.org/10.3390/catal9100819.

(38) Tofa, T. S.; Kunjali, K. L.; Paul, S.; Dutta, J. Visible Light Photocatalytic Degradation of Microplastic Residues with Zinc Oxide Nanorods. *Environ Chem Lett* **2019**, *17* (3), 1341–1346. https://doi.org/10.1007/s10311-019-00859-z.

(39) Ariza-Tarazona, M. C.; Villarreal-Chiu, J. F.; Hernández-López, J. M.; Rivera De la Rosa, J.; Barbieri, V.; Siligardi, C.; Cedillo-González, E. I. Microplastic Pollution Reduction by a Carbon and Nitrogen-Doped TiO2: Effect of PH and Temperature in the Photocatalytic Degradation Process. *Journal of Hazardous Materials* **2020**, *395*, 122632. https://doi.org/10.1016/j.jhazmat.2020.122632.

(40) Zhong, Y.; Chen, H.; Chen, X.; Zhang, B.; Chen, W.; Lu, W. Abiotic Degradation Behavior of Polyacrylonitrile-Based Material Filled with a Composite of TiO2 and g-C3N4 under Solar Illumination. *Chemosphere* **2022**, *299*, 134375. https://doi.org/10.1016/j.chemosphere.2022.134375.

(41) Uheida, A.; Mejía, H. G.; Abdel-Rehim, M.; Hamd, W.; Dutta, J. Visible Light Photocatalytic Degradation of Polypropylene Microplastics in a Continuous Water Flow System. *Journal of Hazardous Materials* **2021**, *406*, 124299. https://doi.org/10.1016/j.jhazmat.2020.124299.

(42) Dobretsov, S.; Sathe, P.; Bora, T.; Barry, M.; Myint, M. T. Z.; Abri, M. A. Toxicity of Different Zinc Oxide Nanomaterials at 3 Trophic Levels: Implications for Development of Low-Toxicity Antifouling Agents. *Environ Toxicol Chem* **2020**, *39* (7), 1343–1354. https://doi.org/10.1002/etc.4720.

(43) Xu, L.; Guo, Y.; Liao, Q.; Zhang, J.; Xu, D. Morphological Control of ZnO Nanostructures by Electrodeposition. *J. Phys. Chem. B* **2005**, *109* (28), 13519–13522. https://doi.org/10.1021/jp051007b.

(44) Wu, T.; Wang, A.; Zheng, L.; Wang, G.; Tu, Q.; Lv, B.; Liu, Z.; Wu, Z.; Wang, Y. Evolution of Native Defects in ZnO Nanorods Irradiated with Hydrogen Ion. *Sci Rep* **2019**, *9* (1), 17393. https://doi.org/10.1038/s41598-019-53951-3.

(45) Lausecker, C.; Salem, B.; Baillin, X.; Roussel, H.; Sarigiannidou, E.; Bassani, F.; Appert, E.; Labau, S.; Consonni, V. Formation Mechanisms of ZnO Nanowires on Polycrystalline Au Seed Layers for Piezoelectric Applications. *Nanotechnology* **2019**, *30* (34), 345601. https://doi.org/10.1088/1361-6528/ab1d6e.

(46) Sulciute, A.; Nishimura, K.; Gilshtein, E.; Cesano, F.; Viscardi, G.; Nasibulin, A. G.; Ohno, Y.; Rackauskas, S. ZnO Nanostructures Application in Electrochemistry: Influence of Morphology. *J. Phys. Chem. C* **2021**, *125* (2), 1472–1482. https://doi.org/10.1021/acs.jpcc.0c08459.

(47) Liu, B.; Zeng, H. C. Hydrothermal Synthesis of ZnO Nanorods in the Diameter Regime of 50 Nm. *J. Am. Chem. Soc.* **2003**, *125* (15), 4430–4431. https://doi.org/10.1021/ja0299452.

(48) Chandraiahgari, C. R.; De Bellis, G.; Ballirano, P.; Balijepalli, S. K.; Kaciulis, S.; Caneve, L.; Sarto, F.; Sarto, M. S. Synthesis and Characterization of ZnO Nanorods with a Narrow Size Distribution. *RSC Adv.* **2015**, *5* (62), 49861–49870. https://doi.org/10.1039/C5RA02631H.

(49) Chrissanthopoulos, A.; Baskoutas, S.; Bouropoulos, N.; Dracopoulos, V.; Poulopoulos, P.; Yannopoulos, S. N. Synthesis and Characterization of ZnO/NiO p–n Heterojunctions: ZnO

Nanorods Grown on NiO Thin Film by Thermal Evaporation. *Photonics and Nanostructures - Fundamentals and Applications* **2011**, *9* (2), 132–139. https://doi.org/10.1016/j.photonics.2010.11.002.

(50) Zhou, T.; Hu, M.; He, J.; Xie, R.; An, C.; Li, C.; Luo, J. Enhanced Catalytic Performance of Zinc Oxide Nanorods with Crystal Plane Control. *CrystEngComm* **2019**, *21* (36), 5526–5532. https://doi.org/10.1039/C9CE01073D.

(51) Liu, Y.; Gao, W. Growth Process, Crystal Size and Alignment of ZnO Nanorods Synthesized under Neutral and Acid Conditions. *Journal of Alloys and Compounds* **2015**, *629*, 84–91. https://doi.org/10.1016/j.jallcom.2014.12.139.

(52) Demianets, L. N.; Kostomarov, D. V. Mechanism of Zinc Oxide Single Crystal Growth under Hydrothermal Conditions. *Annales de Chimie Science des Matériaux* **2001**, *26* (1), 193–198.

(53) Bora, T.; Sathe, P.; Laxman, K.; Dobretsov, S.; Dutta, J. Defect Engineered Visible Light Active ZnO Nanorods for Photocatalytic Treatment of Water. *Catalysis Today* **2017**, *284*, 11–18. https://doi.org/10.1016/j.cattod.2016.09.014.

(54) Bai, S.; Hu, J.; Li, D.; Luo, R.; Chen, A.; Liu, C. C. Quantum-Sized ZnO Nanoparticles: Synthesis, Characterization and Sensing Properties for NO2. *J. Mater. Chem.* **2011**, *21* (33), 12288. https://doi.org/10.1039/c1jm11302j.

(55) Valerio, T. L.; Maia, G. A. R.; Gonçalves, L. F.; Viomar, A.; Banczek, E. do P.; Rodrigues, P. R. P. Study of the Nb2O5 Insertion in ZnO to Dye-Sensitized Solar Cells. *Mat. Res.* **2019**, *22* (suppl 1), e20180864. https://doi.org/10.1590/1980-5373-mr-2018-0864.

(56) Singh, J.; Kaur, S.; Kaur, G.; Basu, S.; Rawat, M. Biogenic ZnO Nanoparticles: A Study of Blueshift of Optical Band Gap and Photocatalytic Degradation of Reactive Yellow 186 Dye under Direct Sunlight. *Green Processing and Synthesis* **2019**, *8* (1), 272–280. https://doi.org/10.1515/gps-2018-0084.

(57) da Silva-Neto, M. L.; de Oliveira, M. C. A.; Dominguez, C. T.; Lins, R. E. M.; Rakov, N.; de Araújo, C. B.; Menezes, L. de S.; de Oliveira, H. P.; Gomes, A. S. L. UV Random Laser Emission from Flexible ZnO-Ag-Enriched Electrospun Cellulose Acetate Fiber Matrix. *Sci Rep* **2019**, *9* (1), 11765. https://doi.org/10.1038/s41598-019-48056-w.

(58) S, M.; N, H.; P.P, V. In Vitro Biocompatibility and Antimicrobial Activities of Zinc Oxide Nanoparticles (ZnO NPs) Prepared by Chemical and Green Synthetic Route— A Comparative Study. *BioNanoSci.* **2020**, *10* (1), 112–121. https://doi.org/10.1007/s12668-019-00698-w.

(59) Malek, M. F.; Mamat, M. H.; Khusaimi, Z.; Sahdan, M. Z.; Musa, M. Z.; Zainun, A. R.; Suriani, A. B.; Md Sin, N. D.; Abd Hamid, S. B.; Rusop, M. Sonicated Sol–Gel Preparation of Nanoparticulate ZnO Thin Films with Various Deposition Speeds: The Highly Preferred c-Axis (002) Orientation Enhances the Final Properties. *Journal of Alloys and Compounds* **2014**, *582*, 12–21. https://doi.org/10.1016/j.jallcom.2013.07.202.

(60) Tobin, M. C. THE INFRARED SPECTRA OF POLYMERS. III. THE INFRARED AND RAMAN SPECTRA OF ISOTACTIC POLYPROPYLENE [1]. *J. Phys. Chem.* **1960**, *64* (2), 216–219. https://doi.org/10.1021/j100831a007.

(61) Andreassen, E. Infrared and Raman Spectroscopy of Polypropylene. In *Polypropylene*; Karger-Kocsis, J., Ed.; Polymer Science and Technology Series; Springer Netherlands: Dordrecht, 1999; Vol. 2, pp 320–328. https://doi.org/10.1007/978-94-011-4421-6_46.

(62) Rabello, M. S.; White, J. R. Photodegradation of Polypropylene Containing a Nucleating Agent. *J. Appl. Polym. Sci.* **1997**, *64* (13), 2505–2517. https://doi.org/10.1002/(SICI)1097-4628(19970627)64:13<2505::AID-APP4>3.0.CO;2-H.

(63) Abdouss, M.; Sharifi-Sanjani, N.; Bataille, P. Oxidation of Polypropylene in a Solution of Monochlorobenzene. *J. Appl. Polym. Sci.* **1999**, *74* (14), 3417–3424. https://doi.org/10.1002/(SICI)1097-4628(19991227)74:14<3417::AID-APP16>3.0.CO;2-G.

(64) Ali, S. S.; Qazi, I. A.; Arshad, M.; Khan, Z.; Voice, T. C.; Mehmood, Ch. T. Photocatalytic Degradation of Low Density Polyethylene (LDPE) Films Using Titania Nanotubes. *Environmental Nanotechnology, Monitoring & Management* **2016**, *5*, 44–53. https://doi.org/10.1016/j.enmm.2016.01.001.

(65) Bolland, J. L.; Gee, G. Kinetic Studies in the Chemistry of Rubber and Related Materials. II. The Kinetics of Oxidation of Unconjugated Olefins. *Trans. Faraday Soc.* **1946**, *42*, 236. https://doi.org/10.1039/tf9464200236.

(66) Gijsman, P.; Dozeman, A. Comparison of the UV-Degradation Chemistry of Unstabilized and HALS-Stabilized Polyethylene and Polypropylene. *Polymer Degradation and Stability* **1996**, *53* (1), 45–50. https://doi.org/10.1016/0141-3910(96)00027-4.

(67) Mani, R.; Singh, R. P.; Sivaram, S. The Oxidative Degradation of Heterophasic Ethylene-Propylene Copolymers: A Comparison of Photoproduct Formation under Natural and Accelerated Conditions. *Polym. Int.* **1997**, *44* (2), 137–142. https://doi.org/10.1002/(SICI)1097-0126(199710)44:2<137::AID-PI808>3.0.CO;2-W.

(68) Pino-Ramos, V. H.; Bucio, E.; Díaz, D. Fast Photocatalytic Polypropylene Degradation by Nanostructured Bismuth Catalysts. *Polymer Degradation and Stability* **2021**, *190*, 109648. https://doi.org/10.1016/j.polymdegradstab.2021.109648.

(69) Rånby, B. Photodegradation and Photo-Oxidation of Synthetic Polymers. *Journal of Analytical and Applied Pyrolysis* **1989**, *15*, 237–247. https://doi.org/10.1016/0165-2370(89)85037-5.

(70) Mylläri, V.; Ruoko, T.-P.; Syrjälä, S. A Comparison of Rheology and FTIR in the Study of Polypropylene and Polystyrene Photodegradation. *J. Appl. Polym. Sci.* **2015**, *132* (28), n/a-n/a. https://doi.org/10.1002/app.42246.

(71) Tofa, T. S.; Ye, F.; Kunjali, K. L.; Dutta, J. Enhanced Visible Light Photodegradation of Microplastic Fragments with Plasmonic Platinum/Zinc Oxide Nanorod Photocatalysts. *Catalysts* **2019**, *9* (10), 819. https://doi.org/10.3390/catal9100819.

(72) Liu, Q.; Liu, S.; Xia, L.; Hu, P.; Lv, Y.; Liu, J.; Chen, Z.; Huang, Y.; Li, G. Effect of Annealing-Induced Microstructure on the Photo-Oxidative Degradation Behavior of Isotactic Polypropylene. *Polymer Degradation and Stability* **2019**, *162*, 180–195. https://doi.org/10.1016/j.polymdegradstab.2019.02.023.

Supporting Information

Natural Sunlight Accelerated Photocatalytic Degradation of Polypropylene Microplastics over ZnO Nanorods

Elie A. Daher[‡†], Yara Hamoud[‡], Christel Laberty Robert[†⁑], Wael Hamd[₱]*

[‡] Petrochemical Engineering Department, Faculty of Engineering III, CRSI, Lebanese University, Rafic Hariri Campus, Hadat, Lebanon.

[†] Laboratoire Chimie de la Matière Condensée de Paris LCMCP, Sorbonne Université, UPMC Paris 06, 4 Place Jussieu, 75005 Paris, France

[⁑] RS2E, Réseau Français sur le Stockage Electrochimique de l'Energie, CNRS 3459, 80039 Cedex 1 Amiens, France

[₱] Chemical Engineering Department, Faculty of Engineering, University of Balamand, P.O. Box 33, El-Koura, Lebanon.

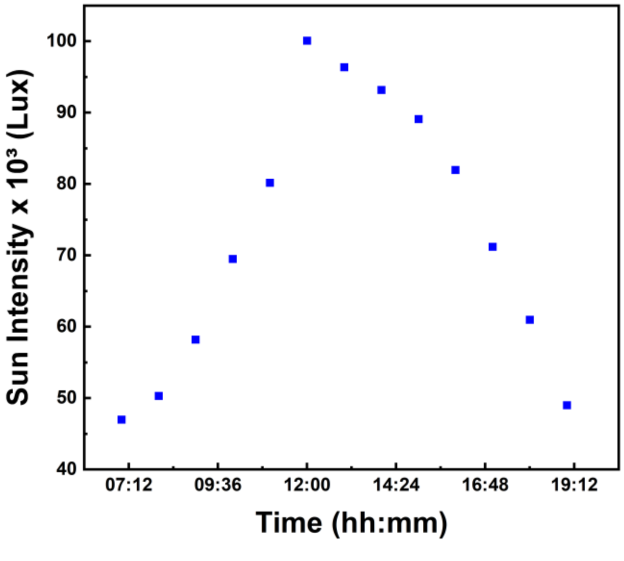

Figure S1. Evolution of the solar luminosity, measured between 7:00 and 19:00 during the last week of July 2022 in Beirut, Lebanon.

Table S1. Vibrational functions of polypropylene. b = backbone, m = medium, s = strong, sh = shoulder, v = very, W = weak, δ = bending, *v* = stretching, ρ = rocking, ᴛ = twisting, ϖ = wagging.

2956vvs	vCH$_3$ asym.
2953vvs	vCH$_3$ asym.
2921vvs	vCH$_2$ asym
2907sh	vCH
2877vs	vCH$_3$ sym
2869vs	vCH$_2$ sym
2840vs	vCH$_2$ sym
2722vw	CH$_b$, vCH$_3$
1460s	δCH$_3$ asym., δCH$_2$
1434m	δCH$_3$ asym.
1370s	δCH$_3$ sym., ϖCH$_2$, δCH, vCC$_b$
1357m	δCH$_3$ sym., δCH
1326vw	δCH, ᴛCH$_2$
1305w	ϖCH$_2$, ᴛCH$_2$
1296vw	ϖCH$_2$, ᴛCH$_2$, δCH
1255w	δCH, ᴛCH$_2$, ρCH$_3$
1220vw	TCH$_2$, δCH, vCCb
1164m	vCC$_b$, ρCH$_3$, δCH
1154w	vCC$_b$, vC-CH$_3$, δCH, ρCH$_3$
1101vw	vCC$_b$, ρCH$_3$, ϖCH$_2$, ᴛCH, δCH
1045vw	vC-CH$_3$, vCC$_b$, δCH
998m	ρCH$_3$, δCH, ϖCH$_2$
973m	ρCH$_3$, vCC$_b$
940vw	ρCH$_3$, vCC$_b$
900w	ρCH$_3$, vCH$_2$, δCH
841m	vCH$_2$, vCC$_b$, vC-CH$_3$, ρCH
809w	pCH$_2$, vCC$_b$, vC-CH$_3$
528w	ϖCH$_2$, vC-CH$_3$, ρCH$_2$
456vw	ϖCH$_2$
396vvw	ϖCH$_2$, δCH
320vvw	ϖCH$_2$
248vvw	ϖCH$_2$, δCH

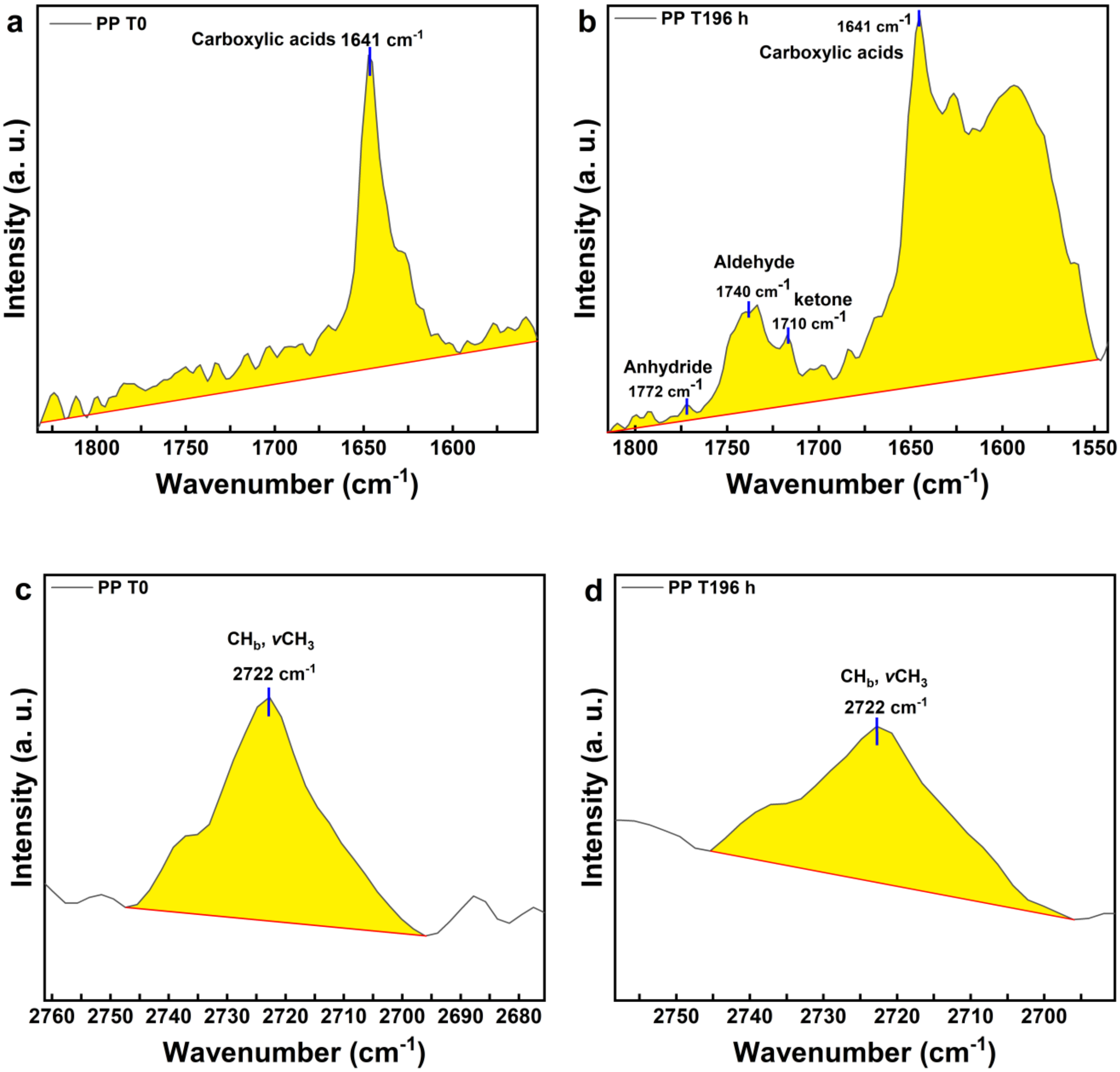

Figure S2. **(a)** Carbonyl band with possible peaks and shoulders at T0 (polypropylene with ZnO NRs), **(b)** Carbonyl band with possible peaks and shoulders at T196 h (polypropylene with ZnO NRs), **(c)** Reference band at T0, **(d)** Reference band at T196 h.

Chapitre III

Ce chapitre a été publié dans Colloids and Surfaces A: Physicochemical and Engineering Aspects

https://doi.org/10.1016/j.colsurfa.2022.130628

Impact de la Microstructure du ZnO sur les Performances de Photodégradation : Conception Novatrice de Films minces de ZnO Plissés et Poreux pour des Applications Photocatalytiques

Le lien entre la microstructure des oxydes métalliques et leurs performances photocatalytiques a été largement étudié dans la littérature[1–3]. Plus spécialement, la structuration du film d'oxyde de zinc (ZnO) joue un rôle primordial dans la cinétique de dégradation de polluants organiques[4–7]. Par exemple, il a été rapporté que les nano-bâtonnets de ZnO obtenus par une synthèse hydrothermale possèdent des facettes non polaires, rendant difficile l'adsorption des molécules d'eau et d'oxygène à leur surface[8,9]. Cela modifie la quantité d'espèces réactives de l'oxygène (ROS) produite et diminue par la suite l'efficacité du système photocatalytique. Dans ce contexte, nous proposons un nouveau procédé de synthèse de couches minces de ZnO poreuses, plissées et obtenues sans additifs organiques (templates). Ces films ont été obtenus par le procédé sol-gel couplé à la méthode de trempage retrait (dip-coating). La formation spontanée de cette nanostructure est le résultat d'un processus de réorganisation induit par l'instabilité interne du film, lié à « une compression thermique ». Les films minces de ZnO ainsi élaborés présentent une structure « plissée », poreuse d'environ 22-25 % avec un diamètre de pore ~ 24 nm. Cette structure poreuse offre davantage de sites catalytiques pour la production d'espèces réactives de l'oxygène (ROS). Les mesures de diffraction des rayons X, confirment la structure wurtzite et que le ZnO est polycristallin. Les performances photocatalytiques ont été testées via la dégradation du bleu de méthylène (10 μM) choisi comme molécule modèle sous deux irradiations différentes. Une efficacité de dégradation élevée de 92% a été obtenue avec des constantes de vitesse de 0.0049 min^{-1} sous UVA et 0.0121 min^{-1} sous lumière visible, après 180 minutes. Par rapport à certains photocatalyseurs à base de ZnO obtenus par des méthodes complexes nécessitant des molécules organiques à façon pour leur structuration et/ou nécessitant un dopage de la du ZnO, les valeurs obtenues dans ce travail montrent qu'une amélioration de l'activité photocatalytique est possible en mettant en œuvre un procédé simple.

Références

(1) Balakrishnan, G.; Velavan, R.; Mujasam Batoo, K.; Raslan, E. H. Microstructure, Optical and Photocatalytic Properties of MgO Nanoparticles. *Results in Physics* **2020**, *16*, 103013. https://doi.org/10.1016/j.rinp.2020.103013.

(2) Thilagavathi, T.; Venugopal, D.; Marnadu, R.; Chandrasekaran, J.; Alshahrani, T.; Shkir, Mohd. An Investigation on Microstructural, Morphological, Optical, Photoluminescence and Photocatalytic Activity of WO3 for Photocatalysis Applications: An Effect of Annealing. *J Inorg Organomet Polym* **2021**, *31* (3), 1217–1230. https://doi.org/10.1007/s10904-020-01731-2.

(3) Saha, T.; Podder, J.; Rakibul Islam, M.; Das, H. N. Effect of Tungsten Doping on the Microstructure, Optical and Photocatalytic Activity of Titanium Dioxide Thin Films Deposited by Spray Pyrolysis. *Optical Materials* **2022**, *133*, 113065. https://doi.org/10.1016/j.optmat.2022.113065.

(4) Xie, J.; Li, Y.; Zhao, W.; Bian, L.; Wei, Y. Simple Fabrication and Photocatalytic Activity of ZnO Particles with Different Morphologies. *Powder Technology* **2011**, *207* (1–3), 140–144. https://doi.org/10.1016/j.powtec.2010.10.019.

(5) Wang, H.; Dong, S.; Chang, Y.; Zhou, X.; Hu, X. Microstructures and Photocatalytic Properties of Porous ZnO Films Synthesized by Chemical Bath Deposition Method. *Applied Surface Science* **2012**, *258* (10), 4288–4293. https://doi.org/10.1016/j.apsusc.2011.12.080.

(6) Chen, G.; Wang, Y.; Shen, Q.; Song, Y.; Chen, G.; Yang, H. Synthesis and Enhanced Photocatalytic Activity of 3D Flowerlike ZnO Microstructures on Activated Carbon Fiber. *Materials Letters* **2014**, *123*, 145–148. https://doi.org/10.1016/j.matlet.2014.03.029.

(7) Alkaim, A. F.; Alrobayi, E. M.; Algubili, A. M.; Aljeboree, A. M. Synthesis, Characterization, and Photocatalytic Activity of Sonochemical/Hydration–Dehydration Prepared ZnO Rod-like Architecture Nano/Microstructures Assisted by a Biotemplate. *Environmental Technology* **2017**, *38* (17), 2119–2129. https://doi.org/10.1080/09593330.2016.1246615.

(8) Guillemin, S.; Rapenne, L.; Roussel, H.; Sarigiannidou, E.; Brémond, G.; Consonni, V. Formation Mechanisms of ZnO Nanowires: The Crucial Role of Crystal Orientation and Polarity. *J. Phys. Chem. C* **2013**, *117* (40), 20738–20745. https://doi.org/10.1021/jp407120j.

(9) Rogé, V.; Guignard, C.; Lamblin, G.; Laporte, F.; Fechete, I.; Garin, F.; Dinia, A.; Lenoble, D. Photocatalytic Degradation Behavior of Multiple Xenobiotics Using MOCVD Synthesized ZnO Nanowires. *Catalysis Today* **2018**, *306*, 215–222. https://doi.org/10.1016/j.cattod.2017.05.088.

New Approach for Designing Wrinkled and Porous ZnO Thin Films for Photocatalytic Applications

Elie A. Daher[‡†], *Bassam Riachi*[‡], *Jean Chamoun*[‡], *Christel Laberty Robert*[†⁑], *Wael Hamd* [₱*]

[‡] Petrochemical Engineering Department, Faculty of Engineering III, CRSI, Lebanese University, Rafic Hariri Campus, Hadat, Lebanon.

[†] Laboratoire Chimie de la Matière Condensée de Paris LCMCP, Sorbonne Université, UPMC Paris 06, 4 Place Jussieu, 75005 Paris, France

[⁑] RS2E, Réseau Français sur le Stockage Electrochimique de l'Energie, CNRS 3459, 80039 Cedex 1 Amiens, France

[₱] Chemical Engineering Department, Faculty of Engineering, University of Balamand, P.O. Box 33, El-Koura, Lebanon.

KEYWORDS: Porous Zinc Oxide; Thin Films; Sol-Gel Dip-Coating; Wrinkled Structure; Photocatalysis; Degradation Rate.

ABSTRACT: A new template-free, porous, and wrinkled ZnO thin films were designed by sol-gel dip-coating technique for enhancing the photocatalytic degradation of organic pollutants in water. The spontaneous formation of such nanostructure represents a certain type of instability-driven organization under intrinsic stress, such as thermal compression. The surface evolution was tracked by in situ thermo-ellipsometry technique through the changes in the film's thickness and refractive index. The engineered nanostructure was obtained by a pre-heat treatment at 150 ºC in the infrared chamber of the dip-coater followed by a post-annealing in the air at 450 º C for 1 hour. A wrinkled structure with a porosity of ~ 22 to 25 % and an average pore Ferret diameter of ~24 nm were revealed, promoting the adsorption of pollutants onto the films' surface. The photocatalytic activity of ZnO films was tested via the degradation of methylene blue probe molecule under two different irradiation sources. A high removal efficiency above 92% and degradation rate constants of 0.0049 min^{-1} and 0.0121 min^{-1} were registered under UVA and visible light respectively.

1. INTRODUCTION

Annual growth in global industrialization of 1.916 % in 2019 (before the Covid 19 pandemic)[1] and a projected world population of 9.9 billion by 2050[2], are placing today's ecosystem in jeopardy[3]. Notably, urban and industrial effluents, loaded with recalcitrant organic molecules from petrochemical[4], pharmaceutical[5], pesticide[6], plasticizer[7], and other industries, are endangering surface and groundwater water sustainability due to their persistence and low degradability, even when they are found in trace levels[8]. Conventional treatment techniques such as flocculation, coagulation, activated carbon, chemical precipitation, biodegradation, and filtration in addition to the established recovery processes including evaporation, solvent extraction, ionic exchange, membrane separation/bioreactors, and electrochemical treatment are bounded by economic constraints and show poor efficiency in addressing adequately, the removal of a wide spectrum of toxic chemicals[9,10]. In this scope, advanced oxidation processes (AOPs) such as photochemical oxidation, catalytic wet oxidation, sonochemical oxidation, O_3 oxidation, electrochemical oxidation, Fenton oxidation, and photocatalysis have emerged as efficient, promising, and inexpensive techniques, capable of tackling different types of organic molecules in aquatic mediums[11,12]. Among these techniques, photocatalysis is considered one of the most practical methods that has proven its efficiency due to its low cost, reusability, and no requirement for secondary disposal methods[13–15]. Photocatalysis is a phenomenon, in which electron-hole pairs are being generated upon the exposure of a semiconducting material to light[16,17]. These electron-hole pairs can migrate to form oxidizing species such as the hydroxyl radical ($OH^\bullet$) and superoxide radical ($O_2^{\bullet-}$) that exhibit strong oxidation of organic matters leading to the total mineralization of recalcitrant organic molecules into less harmful products such as H_2O and CO_2[18]. Although homogeneous photocatalysis is broadly employed due to its high reaction rate, short process time, and high accessibility, it presents some drawbacks such as the high cost of post-separation processes and reactor corrosion[19,20]. To overcome these difficulties, various types and structures of heterogeneous oxide photocatalysts were developed in the literature. More specifically, films of zinc oxide (ZnO) photocatalyst presenting strong oxidation ability and low production price have been prepared in different nanostructures[21] throughout several physical and chemical approaches, including, thermal evaporation[22], chemical vapor deposition[23], pulsed laser deposition[24], metal-organic chemical vapor deposition[25], molecular beam epitaxy[26], solvothermal[27], sonochemical[28], electrodeposition[29] and sol-gel techniques[30]. Particularly, the sol-gel technology can be easily adapted to large surfaces and different substrates to prepare thin layers with tailored thickness and microstructure owing to its distinctive advantages, e. g., process simplicity, moderate temperatures, excellent reproducibility, precise control of synthesis conditions, film uniformity/homogeneity, and waste-free process[31–33]. Nevertheless, making nanocoated films with high surface area remains a big challenge in this technique[34]. Although, mesoporous ZnO thin films have been elaborated by the evaporation-induced self-assembly method (EISA)[35,36], yet, the organic templates are of high cost, and their removal during heat treatment could render thick films prone to defaults such as cracks[37,38]. Moreover, delicate experimental conditions, including initial alcohol/water/surfactant molar ratio, atmosphere humidity, substrate temperature, and inorganic precursor concentrations, should be subtly controlled to obtain the desired nanostructured films[39,40].

To avoid such complexity, this study has successfully reported a new practical approach to design template-free, nano-porous, and highly ordered wrinkled ZnO multilayers by sol-gel dip coating. Although this kind of synthesis was already mentioned in few works before[41–46], the detailed steps involved in the preparation of homogeneous porous and wrinkled structures and its usage in photocatalytic applications were never discussed. Herein, the subtle control of dip-coating parameters was optimized and allows the formation of a new homogeneous ZnO microstructure. The nanostructured photocatalysts offer a relatively large surface-to-volume ratio allowing higher adsorption of the target molecules. Consequently, with a large number of active sites, ZnO exhibits very high surface reactivity, rendering the material an efficient photocatalyst. The photocatalytic performance of the films was tested on a methylene blue (MB) heteropolyaromatic probe-molecule as a function of i) heat treatment, ii) source light irradiation (UVA and LED lights), iii) number of deposited layers, and vi) two different concentrations of the dye molecule.

2. Experimental Section

2.1 Chemicals

Zinc acetate dihydrate ($Zn (CH_3COO)_2 \cdot 2H_2O$) (97 %) ZAD (analytical grade) obtained from ACROS organics Spain, propan-2-ol (analytical reagent grade) obtained from Fisher Scientific, U.K., monoethanolamine (MEA) (98 % analytical grade) obtained from Fisher Scientific, U.K., methylene blue MB (laboratory reagent) obtained from Paskem, India, deionized water (DIW).

2.2 ZnO Sol Preparation

ZnO sol of 0.1 M was prepared by dissolving ZAD into a mixture of 2-PrOH and MEA with a molar ratio of Zn^{2+}:MEA = 1. This concentration was chosen to be the optimum after an extensive characterization and testing of the photocatalytic activity of the synthesized films from various sols with concentrations ranging from 0.03 to 0.6 M (result not shown in this manuscript). In such a low-water concertation medium, the hydrolysis rate is relatively slow. In addition, nucleophilic species such as the MEA, and the acetate counter ion (CH_3COO^-) compete for complexing Zn^{2+} Lewis acid center, therefore, delaying its condensation (see scheme 1)[41,47]. For this reason, the solution was stirred in a closed vessel for 1 hour at T= 70 ºC; below the boiling-point temperature of the 2-PrOH (82.4 ºC), and MEA (170 ºC); followed by 24 hours of aging at room temperature (RT). These two successive steps aim to accelerate the slow hydrolysis/condensation rate of Zn^{2+} ions and minor quantities of small zinc-oxo-acetate oligomers at early stages[48]. As a result, the obtained sol mainly contains inside Zn–CH_3COO and Zn–MEA soluble complexes, apt to form a ZnO skeleton during the dip-coating process.

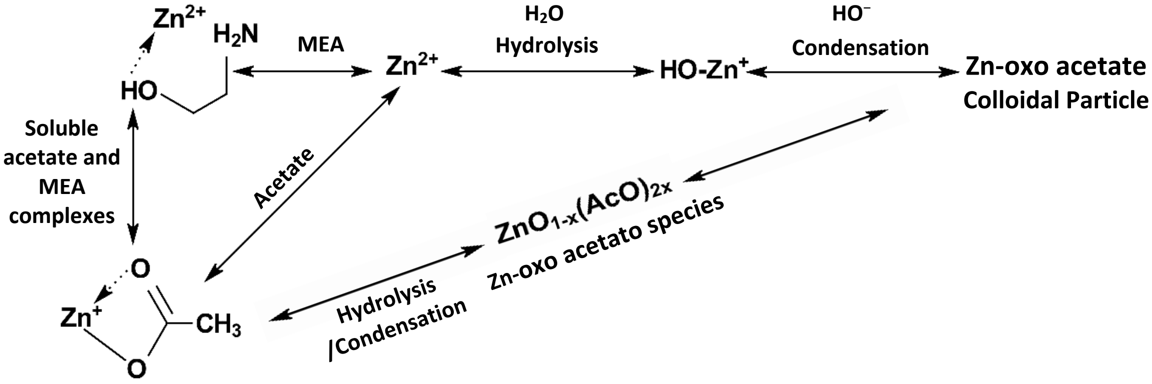

Scheme 1. The reactions equilibrium in a zinc acetate, monoethanolamine, and isopropanol in the sol-gel system.

2.3 Synthesis of Wrinkled and Porous ZnO Multilayers

A Holmarc dip-coating unit equipped with an infrared (IR) heating chamber (Model: HO-TH-02B) was used to enable the adjustment of the film's thickness and the preheating temperature between RT and 200 ºC. All films were deposited on glass slides (4.5 cm × 2.5 cm) made of low thermal-expansion Borosilicate after being cleaned in acetone, ethanol, and deionized water (DIW). The glass substrates were then dipped in the sol for 10 seconds to minimize the generated vibrations by the contact between the substrate and the liquid surface before being removed at 9 mm.s^{-1} (see Scheme 2). The preheating temperature control is crucial in preventing the film's dewetting, and the induced formation of undesired cracks by solvent evaporation in addition to initiating the nano-structuration of the ZnO network. For that reason, the coated layer was then dried in the infra-red pre-heating chamber at an optimum temperature of 150 ^{o}C. Finally, the monolayers were post-heated in the air at 250, 350, 450, and 550 ^{o}C respectively for 60 minutes, to turn the ZnO inorganic network into a crystalline structure and allow for the decomposition of the rest of the volatile organic by-products.

Multi-layers (up to 7 layers) were prepared by repeating the same procedure to increase the thickness of ZnO films and therefore, their light absorption. After the preparation of the first layer, the film was air-cooled for 30 seconds before being dipped again. This process was repeated until reaching the desired number of layers (7 layers). The obtained multilayers were finally annealed in air at 250, 350, 450, and 550 ^{o}C for 60 minutes respectively.

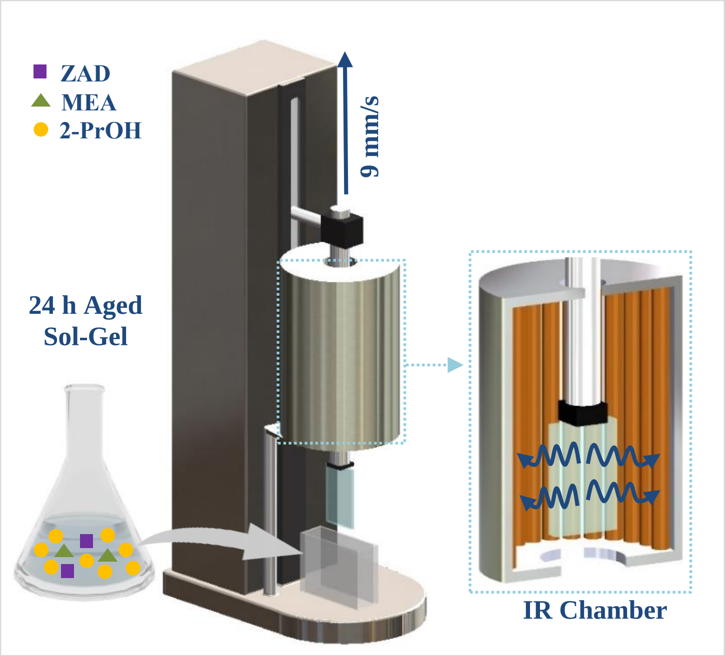

Scheme 2. ZnO dip-coating at a withdraw speed of 9 mm/s followed by a pre-heating at 150 ºC in the air for 5 minutes in the IR chamber.

2.4 Characterization

The films' thickness and porosity were measured by using an M-2000 spectroscopic ellipsometer from J. A. Woolllam, operating between 450 and 850 nm. Ellipsometric ψ and Δ angle plots were recorded at 70º and fitted by using the Cauchy model.

Thermal ellipsometry analysis was conducted with an M2000DI ellipsometer (from Woollam), equipped with a thermal environmental chamber, in order to define the most adequate heat treatment for the films' structuration and crystallization. Measurements were performed at 70º in the wavelength range of 350 to 850 nm. After immediate dip-coating, the deposited films on silicon wafer were first heated to 50 °C before gradually increasing the temperature to 500 ºC with a programmed ramp of 10 ºC/minute. The recorded data were fitted using the Cauchy model.

The crystalline structure of the ZnO films was analyzed by using a D8 Discover X-ray diffractometer, equipped with a Cu emitter anode (Kα_1 and Kα_2 of wavelength 1.54056 and 1.5444 Å respectively) and a 1D LYNEXEYE XE-T detector (Bruker). Grazing scanning mode was set up with an incidence angle fixed at 2º.

The surface nanostructure of the films was evaluated by a field emission gun scanning electron microscope (FEG-SEM) model MIRA 3 TESCAN, employed at a voltage of 15 kV. As for the cross-sectional view, a Hitachi SU-70 FESEM apparatus operating at 5 kV was used.

The optical absorbance of the deposited films on glass slides was measured at room temperature by using a Specord 50 plus UV-visible spectrophotometer from Analytic-Jena, Germany.

2.5 Set-Up of the Photocatalytic System

The as-prepared ZnO thin films were immersed inside Pyrex photocatalytic reactors of 50 ml, filled with 45 ml MB aqueous solution of 10 and 30 μM, respectively. The dipped area of the films in all cases corresponded to 11 cm^2 (the photocatalytic activity was measured per 1 cm^2 irradiated surface). The photocatalytic reactors were initially kept in the dark to avoid any reflected sunlight from the surrounding. After equilibration in the dark for 12 h according to the ISO 10678:2010[49], the photocatalytic tests were carried out at RT for a maximum time of 8 hours, where two irradiation sources were individually employed, covering two ranges of the solar spectrum:

- The first one corresponds to a UVA lamp of λ = 365 nm placed at 5 cm from the photocatalyst surface with a measured emitted illuminance equal to ~ 500 lux;
- The second one corresponds to a visible LED lamp (200W flood day-light) with no UV or IR emission, fixed at 15 cm from the surface of the photocatalyst, to deliver a similar luminous flux of direct sunlight equal (98 Klux), measured at noon.

3. Results and Discussion

3.1 Microstructure of ZnO Thin Films

A field emission gun scanning electron microscope was employed for the nanostructure analysis of the films' surface. Highly homogenous, porous, and crack-free films with a spinodal-like pattern of ridges and valleys, also known as surface wrinkling, were identified in Figures 1a & b. The protrusive parts (ridges) were characterized by a width between ~ 100 to 220 nm and separated by a regular distance stretching from ~ 90 to 200 nm, forming the hollow parts (valleys). The cross-section in the inset of Figure 1b revealed that the 7 layers' film is homogenous and continuous with a thickness of ~ 250 and 190 nm at each of the ridges and valleys, respectively. This observation came to be comparable with the measured thickness by ellipsometry that resulted in a ~ 250 nm film.

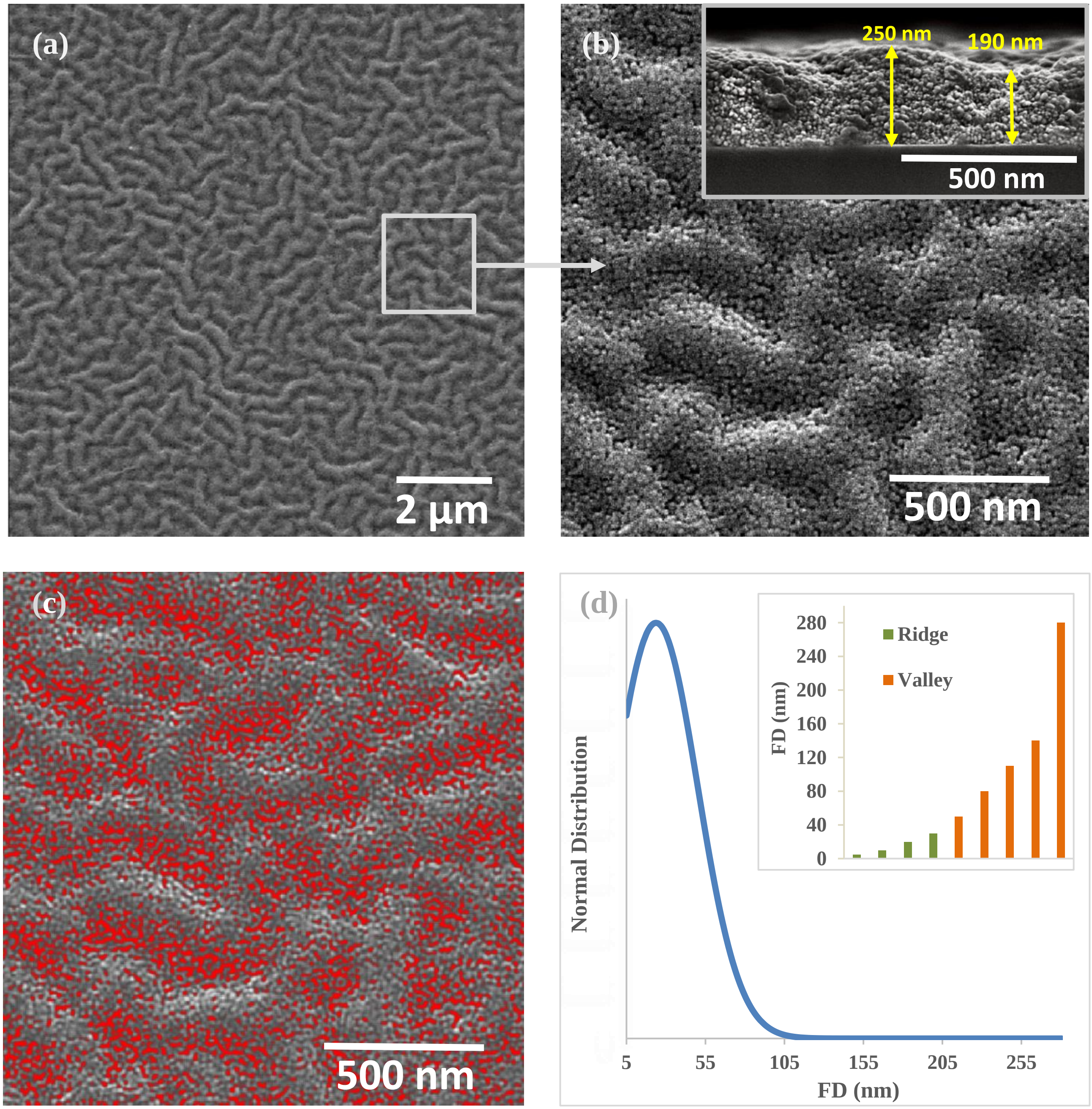

Figure 1. (a) SEM top view image for 7 layers' ZnO thin films after post-heat treatment at 450 ºC, **(b)** Zoomed-in view of "a", the inset represents a cross-sectional view of figure 2b, **(c)** Pores distribution on ridges and valleys by treating Figure 2b using Image J software, **(d)** Pores' Feret diameter (FD) distribution from figure 1 , the inset represents the FD of distributed pores between ridges and valleys.

To assess the surface porosity, the SEM micrographs were treated through successive segmentation steps. First, a binary image was obtained by a threshold segmentation following the Otsu method[50]. Residual pixels formed by segmentation errors were excluded using the 'Remove outliers' noise filter. Next, the pore boundaries were defined by watershed segmentation (Figure 1c), and their microstructural properties, including, the count of pores by area, pores' Feret-diameter, and porosity, were extracted and plotted in Figure 1d. Herein, the maximum Feret diameter for each pore was recorded.

Non-spherical and hierarchical pores were distributed along the film's surface and mainly concentrated in hollow areas (valleys). The distribution of pores' Feret-diameter (Figure 1d) revealed that almost 93 % of pores were characterized by 5 nm [51]< FD < 60 nm and a minority of 7 % was characterized by 60 nm < FD < 280 nm. As a result, a concentration of ~ 912 pores.mm^{-2} with an average FD of ~ 24 nm were obtained, relatively bigger than their reported counterparts by conventional synthesis methods. As summarized in Table 1, approaches such as hydrothermal growth, electrodeposition with and without a structure-directing agent (such as Eosin Y & B), and sol-gel dip-coating, resulted in 2 nm < Pore Diameters < 8 nm. Although ZnO films with pore diameters between 10-20 nm were obtained via electrodeposition, cracks were unable to be avoided[52]. On the other side, porous ZnO with a diameter exceeding 200 nm, was only observed with the employment of templates and more specifically when utilizing big particles of latex polystyrene[53].

Table 1. Synthesis approaches and pore diameter of porous zinc oxide thin films compared with the as-prepared porous wrinkled ZnO.

Reference	Synthesis Approach	Surface-Pore diameter
	Template-Free	
Yu et al.[54]	Classic sol-gel dip-coating	~2-5 nm
Pauporté et al.[55]	Electrochemical deposition using Eosin Y as a structure-directing agent	~2-8 nm
Zhang et al.[56]	Hydrothermal method	~6.92 nm
Nguyen et al.[57]	Electrodeposition in the presence of Eosin Y/B as a structure-directing agent (SDA)	~8 nm
Venditti et al.[52]	Electrodeposition	~10–20 nm (presence of cracks)
	Template Based Techniques	
Xu et al.[58]	Self-assembly of modified colloidal ZnO nanocrystallites and P-123 copolymers.	~2.7 nm
Zhang et al.[59]	Bio-template (Maize) based method	~10.8 nm
Kim et al.	Atomic layer deposition (ALD) based on self-assembled block copolymer	~30 nm
Kousik et al.[60]	chemical bath deposition-polystyrene (PS) based	~50 nm
Liu et al.[53]	latex PS spheres as templates	~230-280 nm
This study	**Sol-gel dip-coating**	**~ 24 nm (Crack-free)**

In addition, a comparable porosity of ~ 25 % was revealed from the top view SEM and the ellipsometry measurements, demonstrating that these pores were mainly concentrated in the first few nanometers of the film. This porosity was relatively higher than the obtained one by some conventional synthesis techniques and comparable to the reported one by advanced methods where expensive templates and more complex systems were used. For instance, surface porosities of ~ 12-13 %, were reported when atmospheric plasma spraying or classic sol-gel dip-coating were employed[61,62]. However, higher surface porosities > 34 %, were reported only in cases of usage of templates such as polymeric nanofoams[63]. Thus, this homogeneous distribution of pores would contribute to enhancing the photocatalytic activity by increasing the contact area between the ZnO thin films and the probe molecule. The formation mechanism of such nanostructure is predicted through the thermo-ellipsometry technique as explained in the following section.

3.2 Pores & Wrinkle Evolution Mechanism

The evolution of the ZnO microstructure as a function of heat treatment was monitored via thermo-ellipsometry analysis (Figure 2). The as-prepared films underwent first a ~ 60 nm shrinkage as the temperature increased from 50 to 120 ºC indicating the evaporation of the isopropanol solvent and some of the MEA molecules (step I). Accordingly, a remarkable increase in the refractive index (η) reaching ~ 1.54 was observed owing to the partial densification of the film. Increasing the temperature from 120 to 140 ºC induced a sharp decrease in the thickness to almost 53 nm, and the refractive index plummeted to 1.498, mostly due to the evaporation of the remaining MEA and the formation of Zn-oxoacetate (step II)[48]. This intense drop in the refractive index value could fairly represent the formation of pores filled with air of η ~1 in the 3D network film. When the temperature continued to ascend to 285 ºC, the refractive index increased rapidly reaching 1.57, indicating the beginning of the crystallization (step III)[47]. This observation came in accordance with the XRD measurements that reveal a film's crystallization starting from ~ 250 ºC (Figure S2). However, the last shrinkage occurred beyond 285 ºC, in conformity with the sudden observed reduction in the refractive index to 1.52, within the range where the acetate starts to thermally decompose, creating an additional porosity (step IV)[47]. Finally, as the crystallization continued as a function of the temperature elevation till 500 ºC, and thus the film densified, η took back a gradual ascension behavior (step V).

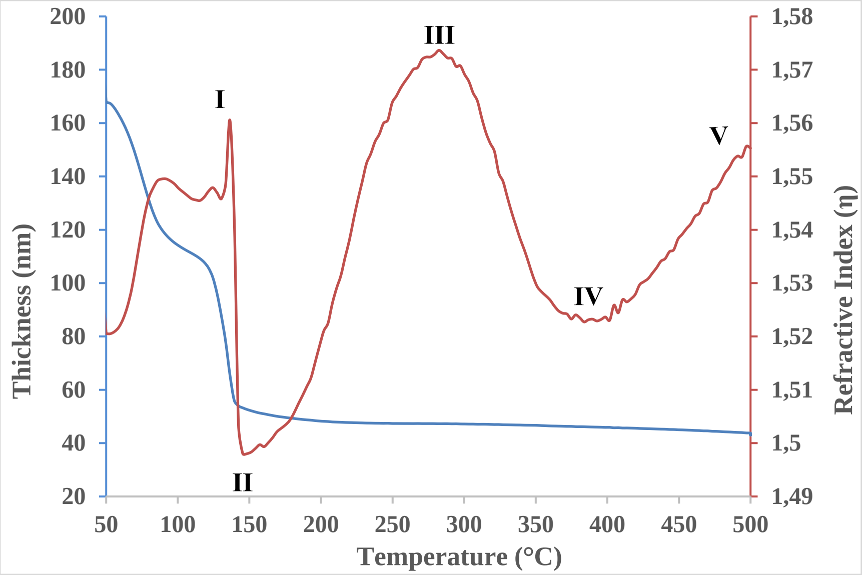

Figure. 2 Thermo-ellipsometry analysis (10 ºC.min^{-1}) of the deposited films visualizing the variation of its thickness (dark blue) and its refractive index at λ = 632 nm (dark red) as a function of the temperature increase.

Based on the above thermo-ellipsometry data, a mechanism of pore and wrinkle formation was proposed. Wrinkling is a well-known phenomenon in nature, usually observed in different length scales, from macro to nano, and most often studied in systems with rigid skin established on visco-elastic foundations[64,65]. The spontaneous formation of such surface wrinkles represents a certain type of instability-driven self-organization[66] under extrinsic stress, such as mechanical compression[67], or intrinsic, such as thermal expansion or compression[68]. In this scope, when such types of compressive stress exceed the critical force of the film and under lateral contractions, induced by the Poisson effect[64], the film tends to bend its flat surface and create an ordered pattern of ridges and valleys called wrinkle structure (perpendicularly oriented to the axis of principal compressive stress)[69,70]. The physics behind the wrinkling (or buckling) in a bilayer system of thin films founded on a compliant substrate is well known[71]. However, the type of wrinkling that usually occurs in a sol-gel thin film during the initial stages of pre-nucleation, is more complicated as it is affected by a complex of chemical and physical processes such as gelation, wetting, chemical/phase transformations, & crystallization[48,72]. The observed film wrinkling & porosity in this study was a consequence of the chemical/physical evolution of the ZnO network, driven by the application of a specific pre-heat treatment. For instance, finding the adequate synthesis conditions for the as-prepared sol-gel system, and applying them in the right order was of great importance because, at the pre-nucleation state, the dip-coated film is still an elastic gel, retaining inside a certain amount of organic molecules (prop-2-ol, MEA, acetic acid, soluble acetate, and complex MEA-acetate group)[47].

To induce the film wrinkling, a fast pre-heat treatment, provided by the IR chamber, was applied to the dip-coated gel. This thermal curing drove the drying process to begin from the top of the film and to turn its upper surface into a rigid skin with a much higher elastic module than its viscous interior (Scheme 3a), wherein the solvent vapor was building up and the skin became prone to bending[71]. As the prop-2-ol exhibits the lowest boiling point compared to the other organics, it was assumed that the viscosity gradient created by the drying process was mainly governed by the evaporation rate of the solvent.

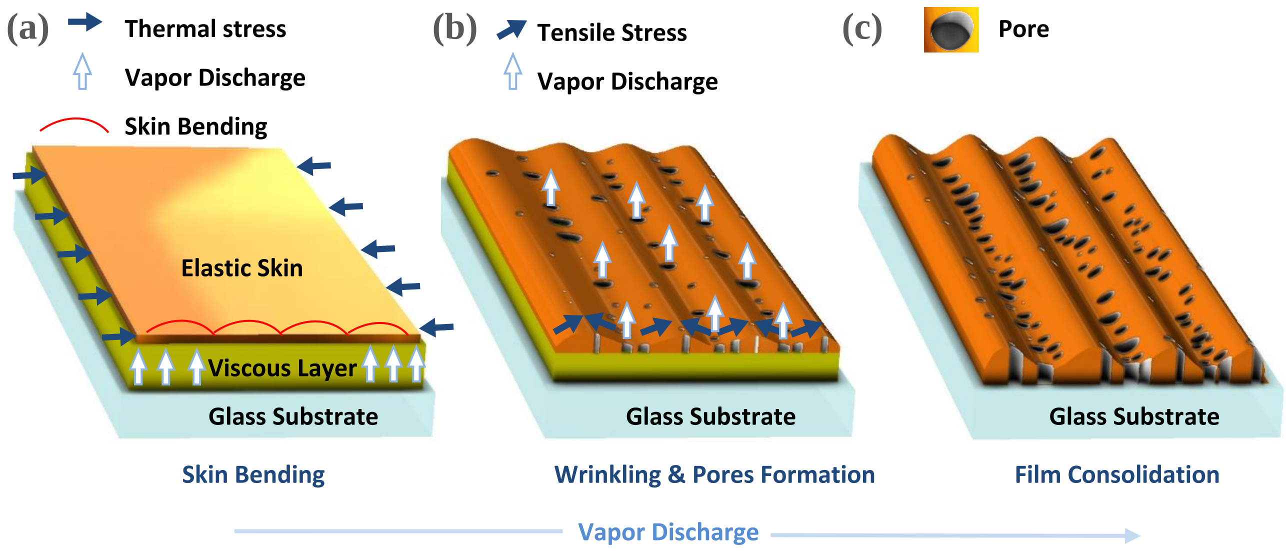

Scheme 3. Schematic diagrams of wrinkling pattern evolution **(a)** Formation of a rigid skin over a viscous layer and vapor build-up in the latter, **(b)** Vapor Discharge, formation of pores, polymerization of the 3D network, and bending of the upper skin n **(c)** Pores stretching and film consolidation.

As the drying continued and the condensation reactions evolved during the preheating step, the solid skin turned thicker and the inner viscous part transformed into a viscoelastic gel as sketched in Scheme 3b. The resulting capillary pressure gradient from the evaporation of the volatile organic components (VOCs), drove these latter to escape the medium leaving behind some open spots for liquids' expulsion, induced by the film shrinkage[31]. Simultaneously, the accumulated internal stress in the films was released during the drying process, resulting in the formation of wrinkles[42]. As a consequence, the created vacant spots by the evaporation of VOCs, became wider as they were stretched by the exerted tensile stress created by film wrinkling and transformed into noticeable pores. As this tensile stress increased when moving from the summit of the ridge toward the bottom of the valleys, the pores grew bigger. This tensile-stress gradient could be explained by the classical surface-energy theory shown in (Eq.1)[71]:

$$G^s = G_0^s + \eta V_M \gamma \qquad \text{(Eq.1)}$$

where, G^s, G_0^s, η, V_M and γ refer respectively to the surface free energy, the free energy of the flat surface, curvature, molar volume, and surface tension. As the curvature for a convex surface is positive while negative for a concave surface, it could be fairly deduced that cavities are characterized by low surface free energy and ridges with higher ones, making them denser. The desired porous and wrinkled structure was then consolidated at the final step of pre-heat treatment, as observed in Scheme 3c.

This analysis came in agreement with the reported equation by Kwon et al.[73] regarding the required total free energy (F_t) to build a wrinkled pattern in sol-gel-derived films (Eq.2):

$$F_t = \left(\frac{2E_m t_m^3 K^2}{32} + \frac{6\tau_p E_m V_E}{\varepsilon^2 K^2}\right)\frac{\varepsilon^2 K^2}{4} \qquad \text{(Eq.2)}$$

E_m, t_m, K, τ_p, V_E & ε refers respectively to Young's modulus, film thickness, wave number of the pattern, relaxation time, volumetric evaporation rate of the solvent per unit area of the films, and amplitude of a wave shape on the film surface. As noticed, the film thickness and solvent discharge (V_E) rate affect directly the total free energy and therefore, play a crucial role in defining the surface morphology. Accordingly, the size evolution of the observed surface porosity along with the protrusive and hollow areas complies with the discussed mechanism. Herein, the located pores at the ridge were characterized by smaller FD (~5 nm < FD < 30 nm) compared with the ones located in the valley (~50 nm < FD < 280 nm).

The subtle tuning of the pre-heat treatment conditions, the evaporation rate, the withdrawal speed, and the sol composition is crucial to controlling the total free energy of the film's surface at the pre-nucleation step, allowing the production of a wrinkled-porous structure. However, poor control of the treatment and the sol-gel conditions prevents the creation of wrinkled structures. For instance, Park et al., Malek et al., and Kim et al. obtained dense ZnO thin films, due to the overlapping of solvent evaporation and crystallization of the 3D network, therefore, hindering any chance for the film to relax[43,44,46]. Similarly, a low preheating temperature or a slow evaporation rate could result as well in dense ZnO films[41,42]. Furthermore, the effect of the heat treatment on the optical properties of the coated material is analyzed in the section 3.3.

3.3 The Effect of Wrinkled Structure on ZnO Optical Properties

Zinc oxide crystallizes under ambient conditions in a Wurtzite structure with a relatively wide bandgap (direct Eg = 3.2–3.4 eV at 300 K), embedding many native defects such as oxygen vacancies (Vo) and interstitial zinc ions (Zni)[44]. The adsorption and desorption of oxygen on the ZnO surface and grain boundaries could significantly affect the mobility of the charge carrier within the oxide material. For these reasons, the enhancement of the optical properties of the as-prepared ZnO films is a crucial step for generating more electron/hole pairs, promoting their conductivity at the grain boundaries, and therefore, producing more reactive oxygen species (ROS) such as $O_2^{\bullet -}/OH^{\bullet}/HO_2^{\bullet}$[74].

In this context, the effect of the heat treatment between 150 and 550 °C on the absorbance of ZnO films was evaluated by a UV-vis spectroscopy between 300 and 800 nm. As the heating temperature increased, a hyperchromic shift was observed accordingly until reaching a maximum at 450 °C (see Figure 3a), probably due to the reduction of the intrinsic bandgap of crystallite ZnO, owing to the electron transitions from the valence band to the conduction one $(O_{2p} \rightarrow Zn_{3d})$[75], as well as to the consolidation and the crystallization of the film (Figure S2).

However, the treatment at 550 °C led to a slight decrease in absorbance. This behavior could be related to the inter-diffusion of elements at the borosilicate/zinc oxide interface[76,77] in addition to the compensation of non-stoichiometric ZnO by induced oxidation from the atmospheric oxygen[78].

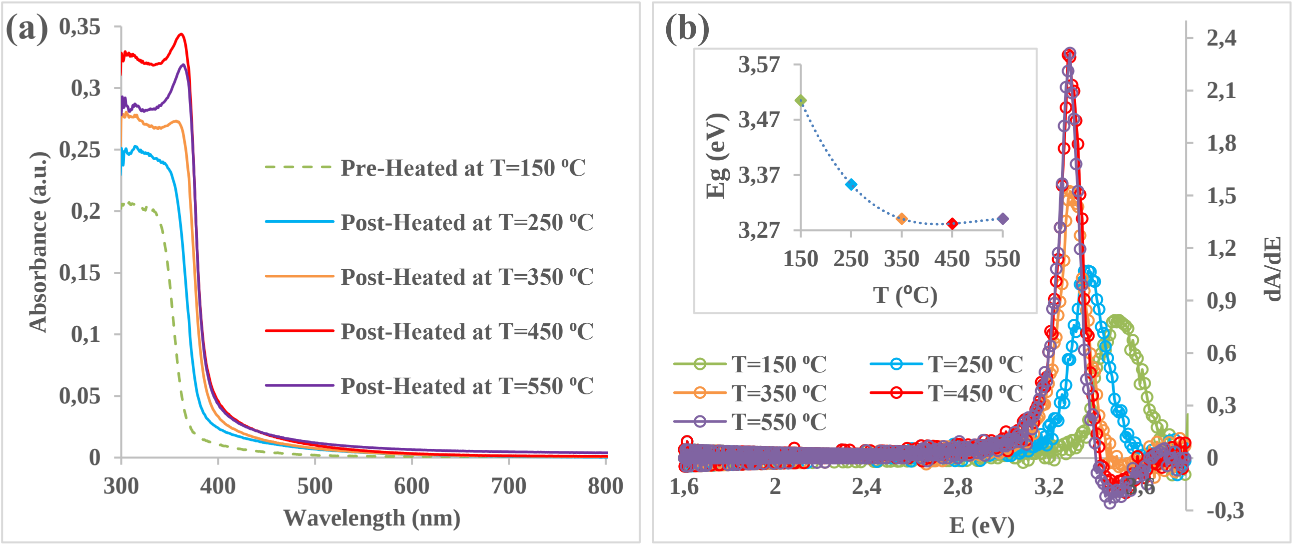

Figure 3. (a) Room-temperature UV-vis absorbance spectrum of a 1 layer ZnO thin film after pre-heat treatment at 150 °C for 5 minutes and after post-heat treatment at T = 250, 350, 450, and 550 °C for 1h, **(b)** Optical bandgap (Eg) obtained from the derivative of the absorbance spectrum for (a) The inset visualizes the variation of Eg in the function of T °C.

The optical band gap (Eg) could be commonly obtained by finding the first maxima at the lower energy side once plotting the first derivative of the absorbance with respect to photon energy (dA/dE), as a function of photon energy (E) (Figure 3b)[79]. A rapid decrease of the Eg from 3.5 to 3.35 eV was noticed when increasing the temperature from 150 (pre-heating step) to 250 °C, while, a slight narrowing of Eg from 3.35 to 3.28 eV was registered between 250 and 450 °C as seen in the inset of Figure 3b. This behavior is probably due to the beginning of ZnO transformation from amorphous to crystalline state at 250 °C because it was shown that in ZnO films prepared out of zinc acetate-2-methoxyethanol-MEA solutions, the crystallization normally occurs between 200 and 300 °C, leading to the relatively high narrowing in the Eg[47]. This was furtherly confirmed by the XRD measurments which shows that the coated ZnO begins its crystallization at 250 °C (Figure S2). At T > 250 °C the minor decrease of Eg is attributed to an enhancement in the crystallinity, accompanied by a reduction of voids at the grain boundaries, in addition to fluctuations in the concentration of impurity energy levels and mixed-valence states in the bandgap of the non-stoichiometric ZnO[75,78]. This comes in agreement with Ma et al.[80] who reported a redshift of the prepared ZnO thin films as the annealing temperature increased, and explained it with the quantum confinement effect due to an increase in the diameter of the grains. For these reasons, an optimum annealing temperature of 450 ºC was adopted.

Moreover, the effect of increasing the number of layers on the optical absorption of the ZnO thin films was measured after an optimum post-heat treatment at 450 ºC. The obtained multilayered films appeared transparent, and showed rainbow-like prismatic colors, as seen in Figure 4a due to the change of film thickness over the glass substrate surface of 11 cm^2.

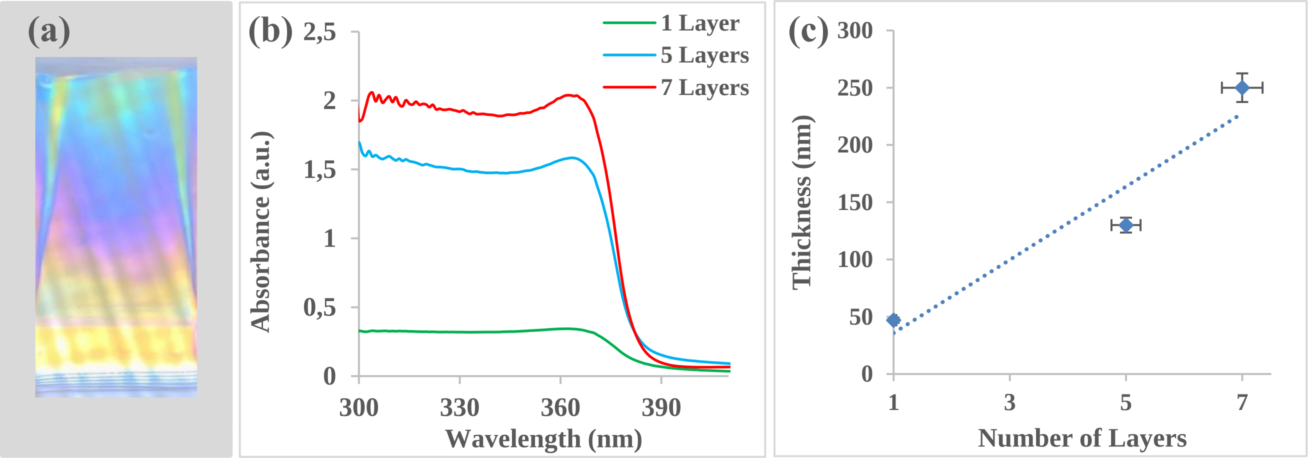

Figure 4. (a) Macroscopic view of a 7 layers film after annealing at 450 ºC for 1h, **(b)** Room temperature UV-vis absorbance spectrum of a 1, 5, and 7 layers ZnO thin film deposited by sol-gel dip-coating on glass substrates after a post-heat treatment at 450 ºC for 1h, and **(c)** Variation of films' thickness as a function of the number of layers (measured by ellipsometry).

The intensity of the absorption spectra augmented as the number of layers increased from 1 to 7 by a factor of 6 with a maximum registered at ~ 365 nm (Figure 4b). This was mainly due to the increase of the films' thickness leading to a maximum generation of electron-hole pairs and consequently to a better photocatalytic efficiency. This increment in the films' thickness was measured by ellipsometry as seen in Figure 4c and found to be 47, 130, and 250 nm for 1, 5, and 7 layers, respectively. The relation between the optical properties of the ZnO films and their photocatalytic performances is discussed in the upcoming section.

3.4 Photocatalytic Efficiency of ZnO films

The photocatalytic activity of ZnO films was measured under UV and LED light by using methylene blue (MB) as a probe molecule. Methylene blue is a heteropolyaromatic dye belonging to the thiazine family[81]. Once dissolved in an aqueous solution, it absorbs the light in both UV and visible regions, with two maxima at ~ 293 nm and 665 nm, referring to the $\pi - \pi^*$ and $n - \pi^*$ transitions respectively[81,82] (Figure S1). Therefore, the absorbance of such irradiations by the MB could lead to its photo-excitation in a singlet state (^{1}MB*) and triplet state (^{3}MB*)[83]. The latter is known to react with the dissolved oxygen to form a superoxide anion radical ($O_2^{\bullet}$), which can mineralize the dye through a chain of free-radical reactions into CO_2 and H_2O[74,84].

To avoid any light absorbance by the dye that could theoretically lead to its photolysis, the photocatalytic activity of the ZnO films was optimized under a UVA (λ = 365 nm) irradiation source wherein, the dye shows a minimum of light absorbance. The photocatalytic efficiency was measured based on the Beer-Lambert law (Eq.3) and plotted with respect to the irradiation time by applying (Eq.4):

$$A_0 = \varepsilon \times L \times C_0 \qquad \text{(Eq.3)}$$

$$MB\ Degradation\,\% = \left(\frac{A}{A_0}\right) \times 100 = \left(\frac{C}{C_0}\right) \times 100 \qquad \text{(Eq.4)}$$

where A_0, A, C_0, C, $\mathcal{E}$ & L refer r espectively to the MB light absorbance at t_0, MB light absorbance at t, MB concentration at t_0, MB concentration at t, molar absorptivity, and length of the light path. The photodegradation of (10 µM) MB with a single layer ZnO thin film was tracked over the experimental time (480 minutes). Under UVA irradiation (λ = 365 nm) and without the use of a ZnO photocatalyst (blank MB solution), the UV-vis spectrum (Figure 5a) showed no significant changes in the absorbance after 480 minutes. However, when the ZnO photocatalyst was added, an important decrease in the absorbance values was observed after the same irradiation time and under the same conditions (Figure 5b). The percentage of MB degradation as a function of time with and without photocatalyst was calculated by applying Eq.4 and plotted in Figure 5c. MB was degraded up to 5 % only without ZnO and up to more than 70 % when the photocatalyst was used confirming that the photolysis mechanism was well prevented and the reduction of MB in the system was only due to the photocatalytic activity of ZnO films.

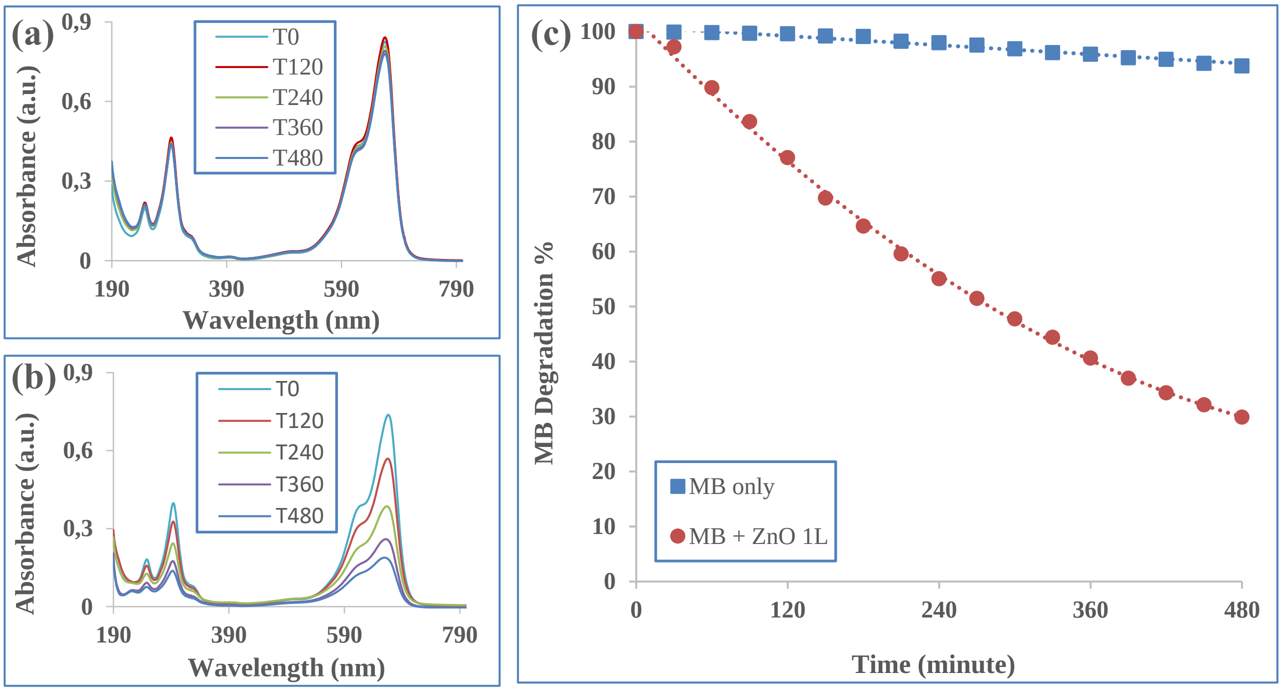

Figure 5. Photocatalytic degradation of 10 µM MB Under UVA (λ=365nm) **(a)** UV-vis spectrum of Blank MB plotted in function of time, **(b)** UV-vis spectrum of MB photodegradation by 1L of ZnO annealed at 250 ºC, plotted in function of time, **(c)** Comparative photodegradation of MB with (red line) and without (blue line) the single layer of ZnO thin film.

3.4.1 Optimization of ZnO photocatalytic Activity

The electron transfer dynamics in the porous and wrinkled ZnO films and therefore, its photocatalytic activity is directly affected by the film's optical properties. For this reason, the photocatalytic kinetics of the coated ZnO were studied as a function of the conducted post-heat treatment and films' thickness.

The photocatalysis kinetic was deduced from the Langmuir–Hinshelwood kinetic model (Eq.5)[85]:

$$r = -\frac{dC}{dt} = \frac{Kr.K.C}{1+K.C} \qquad \text{(Eq.5)}$$

where r, C, K, kr, and t represent the reaction rate, dye concentration at time t, adsorption equilibrium constant, limiting rate constant of reaction at maximum coverage under the given experimental conditions, and contact time respectively.

At small (mM) concentrations, (K.C <<1), the equation could be simplified to the apparent rate order, as presented in Eq.6[85]:

$$r = -\frac{dC}{dt} = K_{app}.C \qquad \text{(Eq.6)}$$

where K_{app}, refers to the apparent degradation rate. Simple integration of this equation (with the same conditions for $C = C_0$ at $t = 0$),) gives the expected relation:

$$\ln\left(\frac{C0}{C}\right) = K_{app}.t \qquad \text{(Eq.7)}$$

Thus, the apparent pseudo-first-order rate constant (K_{app}) is obtained from the slope of the linear curve in the plot of ln (C_0/C) vs. t.

- **Effect of Post-Heat Treatment**

The effect of the film's heat treatment on the photodegradation kinetics of 10 µM MB under a UVA (λ = 365 nm), was shown in Figure 6a. The blank sample of methylene blue (without ZnO photocatalyst) registered a negligible kinetic rate of 0.0001 min^{-1} referred to its very low photolysis at this wavelength. However, when ZnO films were introduced into the system, a remarkable change in the slope values is observed for all samples heat treated between 250 and 550 ºC. An increment in the K_{app} from 0.0028 to 0.0041 min^{-1} corresponding to an increase of 26% in the photodegradation of MB was seen as the heat treatment temperatures of the ZnO photocatalysts increased from 250 to 450 ºC respectively. The additional increase in temperature until 550 ºC had an opposite effect on the degradation rate constant lowering its value to 0.0038 min^{-1}. These results came in good agreement with those observed in Figure 3a where the optical properties of ZnO films were drastically affected by the applied heat treatment. In addition, the important increase in photocatalytic degradation rate between 250 and 450 ºC, was probably related to the enhancement of crystallinity and the reduction of voids at the grain boundaries of ZnO films. In this respect, it was seen in Figure S2 that increasing the heat treatment temperature from 250 to 450 ºC drastically enhanced the films' crystallinity where two new planes (101) and (102) were observed, and the diffraction intensity of the three others (100), (002), and (110) became more prominent.

While it was supposed that an increase in temperature to 550 ºC would enhance the films' efficiency, a remarkable decrease in the photocatalytic rate was observed, probably due to the inter-diffusion of elements at the borosilicate/zinc oxide interface reducing the films' absorbance and its photocatalytic performance.

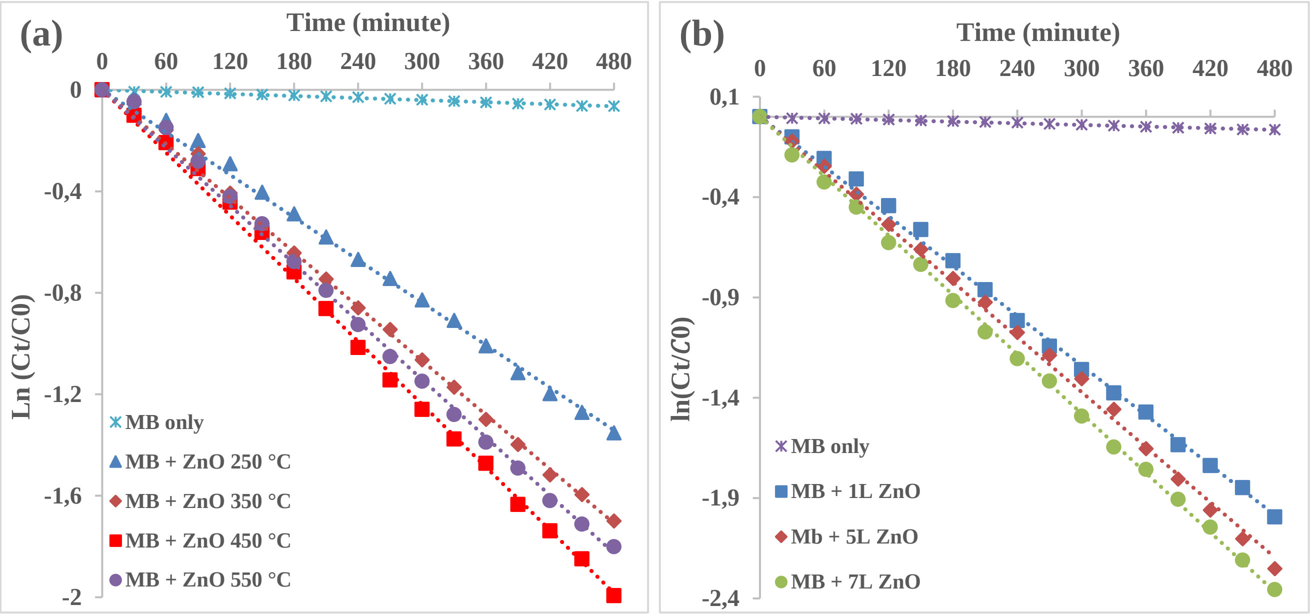

Figure 6. (a) Photodegradation kinetics of 10 µM MB under a UVA light of λ = 365 nm, by single layer ZnO thin films post-heat treated at different temperatures, **(b)** Photodegradation kinetics of 10 µM MB under a UVA light of λ = 365 nm, by multilayers ZnO thin films post-heat treated at 450 ºC.

- **Effect of Films Thickness**

The effect of the number of layers from 1 to 7 on MB degradation, was studied at the optimal heating temperature of 450 ºC and plotted in Figure 6b. The rate constant K_{app} increased from 0.0041 to 0.0046 min^{-1} (by ~ 12 %), as the number of layers went from 1 to 5 and the film got 2.7 times thicker. Thereafter, the photocatalytic activity of the 7 multilayers scored a slight increase of 6 % thus reaching a certain plateau at 0.0049 min^{-1} as the thickness was augmented by 2 times. This increase in rate constants is certainly due to the increase in film thicknesses allowing the absorbance of a higher amount of irradiated light. Thus, the concentration of radical species in the medium will consequently increase, leading to a more rapid degradation rate and higher values of K_{app}. A summary of the evolution of rate constants as a function of the number of layers and the applied heat treatment between 250 and 550 ºC is listed in table 2.

Table 2. *Kapp* of the photodegradation of 10 μM MB under a UVA light of λ = 365 nm using the as-synthesized ZnO layers. 1L = one layer

	MB **Blank**	**MB** **&** **1L ZnO 250 ºC**	**MB** **&** **1L ZnO 350 ºC**	**MB** **&** **1L ZnO 450 ºC**	**MB** **&** **1L ZnO 550 ºC**	**MB** **&** **5L ZnO 450 ºC**	**MB** **&** **7L ZnO 450 ºC**
Kapp **(min^{-1})**	0.0001	0.0028	0.0036	0.0041	0.0038	0.0046	0.0049

- **Effect of Irradiation Source**

As the catalytic performance of oxide materials is closely related to its Bandgap energy and the type of the irradiated light, the photodegradation of MB by using the optimized films (7 layers post-heated at 450 ºC for 1h) was tested under two different irradiation sources i) a day-light LED lamp emitting visible light with no UV or IR emissions, and ii) a UVA of λ = 365 nm. The photocatalytic degradation under each source was plotted in Figure 7.

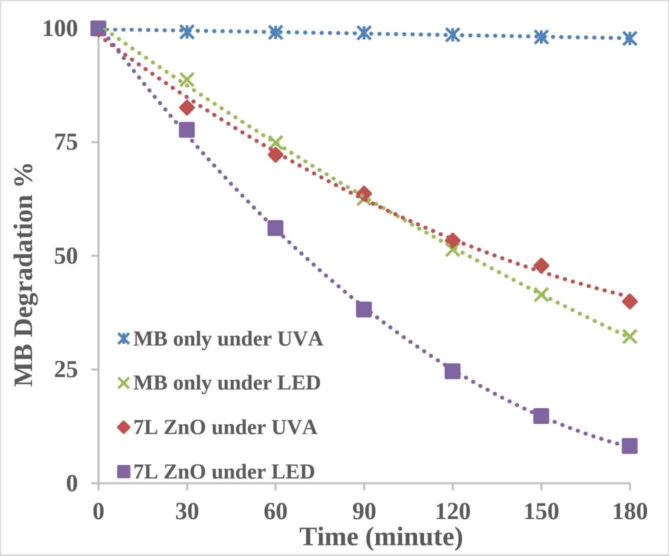

Figure 7. Comparative photodegradation efficiency of optimized ZnO films under a day-light LED and UVA light of λ = 365 nm, tested on 10 µM methylene blue.

Under UVA and without ZnO photocatalyst, MB remained almost stable in the solution due to the prevention of its photolysis at this wavelength. The addition of the photocatalyst under the same conditions led to a degradation of about 60 % after 180 minutes confirming the activity of ZnO under UVA. However, under visible light and despite the absence of the photocatalyst, a comparable degradation of MB was observed (~ 68 %) due to the absorbance of MB between 500 and 700 nm triggering the photolysis mechanism. Furthermore, the usage of ZnO films under visible light promoted this degradation to 92 % of which 24 % was removed by the activity of ZnO photocatalyst. This result confirms the efficacity of ZnO films under both visible and UVA irradiations. This optimized system seems to be more performant than other ZnO films prepared by using high-energy demanding techniques or by adding organic templates and doping elements (see table 3).

Table 3. Comparative MB photodegradation efficiency of the tailored ZnO films with other nanostructured zinc oxide coatings. The percentage of degradation and the apparent degradation constant were normalized to the immersed coated area of each work.

Technique	Precursor	MB (μM.L^{-1})	Light Source	Normalized Degradation (%)	Normalized Kapp (min^{-1})	This study
Chemical Spray Pyrolysis[86]	Zinc Chloride	~ 9.3	Sunlight (Visible + UV)	-	~ 0.0017	C = 10 μM.L^{-1} Kapp = 0.0011 min^{-1} Light Source: Visible LED
Spray Plasma[61]	ZnO Powder	15	UVA	-	~ 0.00011	C = 10 μM.L^{-1} Kapp = 0.00044 min^{-1} C = 30 μM.L^{-1} Kapp = 0.00022 min^{-1} Light Source: UVA
Template-Based by Sol-Gel Spin-coating[87]	Zinc Acetate + Ag-doped	10	UV	~ 5 % in 120 min	-	C = 10 μM.L^{-1} Degradation ~ 5% in 120 min Light Source: UVA
Doctor Blade[88]	Zinc Acetate Dihydrate	30	Visible LED	-	~ 0.00005	C = 10 μM.L^{-1} Kapp = 0.0011 min^{-1} Light Source: Visible LED

For instance, Navdipour et al. used a lower initial concentration of MB (~ 15 μM.L^{-1}) and reported a *kapp* equal to 0.00011 min^{-1}, 2 times lower than the result shown in this study (0.0002 min^{-1})[61]. Moreover, although Faisal et al. employed a template-based approach to synthesize Ag-doped multilayers films of ZnO by sol-gel spin-coating, the percentage of degradation was almost similar to the one obtained in this work[87]. In addition, Wallejo et al, used the Doctor Blade method to produce ZnO thin films with a *kapp* = 0.00005 min^{-1} much lower than the smallest degradation rate reported herein[88]. However, El Fidha et al. recently reported a *kapp* of 0.0017 min^{-1} for a ZnO film deposited by chemical spray pyrolysis, yet under direct sunlight containing both visible and UV irradiations, which highly improves the process kinetics[86].

4. Conclusion

In this study, free template porous and wrinkled ZnO thin films were engineered by the sol-gel dip-coating technique through the optimization of ZnO sol preparation and the coating conditions. In this regard, the dip-coating of 0.1 M ZnO sol on glass substrates preheated at 150 ºC and calcinated at 450 ºC allowed the formation of homogenous thin films with no cracks, and characterized by a surface porosity of 25 %). The photocatalytic activity of the ZnO films was tested on the degradation of methylene blue probe molecule. An efficiency of 60 and 92 % after irradiation of only 180 minutes was observed under UVA (λ=365nm) and day-light LED lamps, respectively. This result shows the efficacy of this facile and low-cost approach of synthesis compared to some more sophisticated and complex methods using organic templates and/or doping metals using organic templates and/or doping metals (published in literature).

AUTHOR INFORMATION

Corresponding Author

Dr. Wael Hamd

E-mail: Wael.Hamd@balamand.edu.lb

Acknowledgment

This work has been supported by the two projects: CLAIM, H2020-BG-2016–2017 [grant number 774586], “Cleaning Litter by developing and Applying Innovative Methods in European seas” and SWaTH, “Sustainable Wastewater Treatment for Hospitals” co-funded by the Erasmus Plus Programme of the European Union. Mr. David Montero, Mr. Mohamad Selmane, and Dr. Cédric

Boissière are gratefully acknowledged for conducting SEM-FEG, XRD, and thermo-ellipsometry measurements at Sorbonne University.

References

(1) World Bank National Accounts Data, and OECD National Accounts Data Files. World Bank Group. https://data.worldbank.org/indicator/NV.IND.TOTL.KD.ZG (accessed 2021-03-16).

(2) Population Reference Bureau, 2020 World Population Data Sheet Shows Older Populations Growing, Total Fertility Rates Declining. https://www.prb.org/2020-world-population-data-sheet/#:~:text=The%20world%20population%20is%20projected,as%20in%20the%20United%20States.; (accessed 2021-03-16).

(3) El Hajj Chehade, A. M.; Daher, E. A.; Assaf, J. C.; Riachi, B.; Hamd, W. Simulation and Optimization of Hydrogen Production by Steam Reforming of Natural Gas for Refining and Petrochemical Demands in Lebanon. *Int. J. Hydrog. Energy* **2020**, *45* (58), 33235–33247. https://doi.org/10.1016/j.ijhydene.2020.09.077.

(4) Ghimire, N.; Wang, S. Biological Treatment of Petrochemical Wastewater. In *Petroleum Chemicals - Recent Insight*; Zoveidavianpoor, M., Ed.; IntechOpen, 2019. https://doi.org/10.5772/intechopen.79655.

(5) Kumari, V.; Tripathi, A. K. Characterization of Pharmaceuticals Industrial Effluent Using GC–MS and FT-IR Analyses and Defining Its Toxicity. *Appl. Water Sci.* **2019**, *9* (8), 185. https://doi.org/10.1007/s13201-019-1064-z.

(6) Kumar, A.; Verma, N. Cu-Fe Bimetal-Carbon Nanofiberous Catalytic Beads for Enhanced Oxidation of Dichlorvos Pesticide and Simultaneous Reduction of Cr(VI) in Wet Air. *Catal. Today* **2020**, *348*, 194–202. https://doi.org/10.1016/j.cattod.2019.08.025.

(7) Arslan-Alaton, I.; Karatas, A.; Pehlivan, Ö.; Koba Ucun, O.; Ölmez-Hancı, T. Effect of UV-A-Assisted Iron-Based and UV-C-Driven Oxidation Processes on Organic Matter and Antibiotic Resistance Removal in Tertiary Treated Urban Wastewater. *Catal. Today* **2021**, *361*, 152–158. https://doi.org/10.1016/j.cattod.2020.02.037.

(8) Gupta, A.; Thakur, I. S. Treatment of Organic Recalcitrant Contaminants in Wastewater. In *Biological Wastewater Treatment and Resource Recovery*; Farooq, R., Ahmad, Z., Eds.; InTech, 2017. https://doi.org/10.5772/66346.

(9) Amin, M. T.; Alazba, A. A.; Manzoor, U. A Review of Removal of Pollutants from Water/Wastewater Using Different Types of Nanomaterials. *Adv. Mater. Sci. Eng.* **2014**, *2014*, 1–24. https://doi.org/10.1155/2014/825910.

(10) Crini, G.; Lichtfouse, E. Advantages and Disadvantages of Techniques Used for Wastewater Treatment. *Environ. Chem. Lett.* **2019**, *17* (1), 145–155. https://doi.org/10.1007/s10311-018-0785-9.

(11) Zhang, M.; Dong, H.; Zhao, L.; Wang, D.; Meng, D. A Review on Fenton Process for Organic Wastewater Treatment Based on Optimization Perspective. *Sci. Total Environ.* **2019**, *670*, 110–121. https://doi.org/10.1016/j.scitotenv.2019.03.180.

(12) Hamd, W. S.; Dutta, J. Heterogeneous Photo-Fenton Reaction and Its Enhancement upon Addition of Chelating Agents. In *Nanomaterials for the Detection and Removal of Wastewater Pollutants*; Elsevier, 2020; pp 303–330. https://doi.org/10.1016/B978-0-12-818489-9.00011-6.

(13) Loeb, S. K.; Alvarez, P. J. J.; Brame, J. A.; Cates, E. L.; Choi, W.; Crittenden, J.; Dionysiou, D. D.; Li, Q.; Li-Puma, G.; Quan, X.; Sedlak, D. L.; David Waite, T.; Westerhoff, P.; Kim, J.-H. The Technology Horizon for Photocatalytic Water Treatment: Sunrise or Sunset? *Environ. Sci. Technol.* **2019**, *53* (6), 2937–2947. https://doi.org/10.1021/acs.est.8b05041.

(14) Zeng, L.; Guo, X.; He, C.; Duan, C. Metal–Organic Frameworks: Versatile Materials for Heterogeneous Photocatalysis. *ACS Catal.* **2016**, *6* (11), 7935–7947. https://doi.org/10.1021/acscatal.6b02228.

(15) Ghosh, S.; Kouamé, N. A.; Ramos, L.; Remita, S.; Dazzi, A.; Deniset-Besseau, A.; Beaunier, P.; Goubard, F.; Aubert, P.-H.; Remita, H. Conducting Polymer Nanostructures for Photocatalysis under Visible Light. *Nat. Mater.* **2015**, *14* (5), 505–511. https://doi.org/10.1038/nmat4220.

(16) Miklos, D. B.; Remy, C.; Jekel, M.; Linden, K. G.; Drewes, J. E.; Hübner, U. Evaluation of Advanced Oxidation Processes for Water and Wastewater Treatment – A Critical Review. *Water Res.* **2018**, *139*, 118–131. https://doi.org/10.1016/j.watres.2018.03.042.

(17) Liu, J.; Li, Y.; Li, Z.; Ke, J.; Xiao, H.; Hou, Y. In Situ Growing of Bi/Bi2O2CO3 on Bi2WO6 Nanosheets for Improved Photocatalytic Performance. *Catal. Today* **2018**, *314*, 2–9. https://doi.org/10.1016/j.cattod.2017.12.001.

(18) Habib, I. Y.; Burhan, J.; Jaladi, F.; Lim, C. M.; Usman, A.; Kumara, N. T. R. N.; Tsang, S. C. E.; Mahadi, A. H. Effect of Cr Doping in CeO2 Nanostructures on Photocatalysis and H2O2 Assisted Methylene Blue Dye Degradation. *Catal. Today* **2021**, *375*, 506–513. https://doi.org/10.1016/j.cattod.2020.04.008.

(19) Ali, Md. E.; Rahman, Md. M.; Sarkar, S. M.; Hamid, S. B. A. Heterogeneous Metal Catalysts for Oxidation Reactions. *J. Nanomater.* **2014**, *2014*, 1–23. https://doi.org/10.1155/2014/192038.

(20) Cui, X.; Li, W.; Ryabchuk, P.; Junge, K.; Beller, M. Bridging Homogeneous and Heterogeneous Catalysis by Heterogeneous Single-Metal-Site Catalysts. *Nat. Catal.* **2018**, *1* (6), 385–397. https://doi.org/10.1038/s41929-018-0090-9.

(21) Lee, K. M.; Lai, C. W.; Ngai, K. S.; Juan, J. C. Recent Developments of Zinc Oxide Based Photocatalyst in Water Treatment Technology: A Review. *Water Res.* **2016**, *88*, 428–448. https://doi.org/10.1016/j.watres.2015.09.045.

(22) Van Khai, T.; Van Thu, L.; Ha, L. T. T.; Thanh, V. M.; Lam, T. D. Structural, Optical and Gas Sensing Properties of Vertically Well-Aligned ZnO Nanowires Grown on Graphene/Si Substrate by Thermal Evaporation Method. *Mater. Charact.* **2018**, *141*, 296–317. https://doi.org/10.1016/j.matchar.2018.04.047.

(23) Chen, J.; Wang, J.; Saravade, V.; Ferguson, I. T.; Hu, W.; Feng, Z. C.; Wan, L. Multi-Technique Investigation of Ni-Doped ZnO Thin Films on Sapphire by Metalorganic Chemical Vapor Deposition. *J. Vac. Sci. Technol. Vac. Surf. Films* **2021**, *39* (2), 023408. https://doi.org/10.1116/6.0000816.

(24) Ryu, Y. Y.; Kim, T.; Han, H. Synthesis of Porous ZnO Nanosheets and Carbon Nanotube Hybrids as Efficient Photocatalysts via Pulsed Laser Ablation. *Catalysts* **2019**, *9* (10), 787. https://doi.org/10.3390/catal9100787.

(25) Rogé, V.; Guignard, C.; Lamblin, G.; Laporte, F.; Fechete, I.; Garin, F.; Dinia, A.; Lenoble, D. Photocatalytic Degradation Behavior of Multiple Xenobiotics Using MOCVD Synthesized ZnO Nanowires. *Catal. Today* **2018**, *306*, 215–222. https://doi.org/10.1016/j.cattod.2017.05.088.

(26) Feng, Y.; Zhou, Y.; Liu, Y.; Zhang, G.; Zhang, X. Photoluminescence Spectra of Nano-Structured ZnO Thin Films. *J. Lumin.* **2006**, *119–120*, 233–236. https://doi.org/10.1016/j.jlumin.2005.12.040.

(27) Chankhanittha, T.; Yenjai, C.; Nanan, S. Utilization of Formononetin and Pinocembrin from Stem Extract of Dalbergia Parviflora as Capping Agents for Preparation of ZnO Photocatalysts for Degradation of RR141 Azo Dye and Ofloxacin Antibiotic. *Catal. Today* **2022**, *384–386*, 279–293. https://doi.org/10.1016/j.cattod.2021.03.002.

(28) Uma, K.; KrishnaKumar, B.; Pan, G.-T.; Yang, T. C.-K.; Lin, J.-H. Enriched Silver Plasmon Resonance Activity on the Sonochemical Synthesis of ZnO Flowers with α-Fe2O3 as an Efficient Catalyst for Photo-Fenton Reaction and Photo-Oxidation of Ethanol. *J. Water Process Eng.* **2020**, *34*, 101089. https://doi.org/10.1016/j.jwpe.2019.101089.

(29) Liu, X.; Xie, L.; Liu, Y.; Zhao, P.; Han, Y.; Cheng, S.; Bai, X.; Li, Y. Rapid Preparation of Highly Stable ZnO-CeO2/CF Cathode by One-Step Electro-Deposition for Efficient Degradation of Ciprofloxacin in Electro-Fenton System. *Catal. Today* **2020**, *355*, 458–465. https://doi.org/10.1016/j.cattod.2019.07.005.

(30) Hamd, W.; Chavarot-Kerlidou, M.; Fize, J.; Muller, G.; Leyris, A.; Matheron, M.; Courtin, E.; Fontecave, M.; Sanchez, C.; Artero, V.; Laberty-Robert, C. Dye-Sensitized Nanostructured Crystalline Mesoporous Tin-Doped Indium Oxide Films with Tunable Thickness for Photoelectrochemical Applications. *J. Mater. Chem. A* **2013**, *1* (28), 8217. https://doi.org/10.1039/c3ta10728k.

(31) Brinker, C. J.; Scherer, G. W. *Sol-Gel Science: The Physics and Chemistry of Sol-Gel Processing*; Academic press: Boston San Diego New York [etc.], 1990.

(32) Grosso, D. How to Exploit the Full Potential of the Dip-Coating Process to Better Control Film Formation. *J. Mater. Chem.* **2011**, *21* (43), 17033. https://doi.org/10.1039/c1jm12837j.

(33) Hamd, W.; Boulle, A.; Thune, E.; Guinebretiere, R. A New Way to Prepare Tin Oxide Precursor Polymeric Gels. *J. Sol-Gel Sci. Technol.* **2010**, *55* (1), 15–18. https://doi.org/10.1007/s10971-010-2206-9.

(34) Kuemmel, M.; Boissière, C.; Nicole, L.; Laberty-Robert, C.; Sanchez, C.; Grosso, D. Highly Ordered Metal Oxide Nanopatterns Prepared by Template-Assisted Chemical Solution Deposition. *J. Sol-Gel Sci. Technol.* **2008**, *48* (1–2), 102–112. https://doi.org/10.1007/s10971-008-1794-0.

(35) Khan, H.; Samanta, S.; Seth, M.; Jana, S. Fabrication and Photoelectrochemical Activity of Hierarchically Porous TiO2–ZnO Heterojunction Film. *J. Mater. Sci.* **2020**, *55* (26), 11907–11918. https://doi.org/10.1007/s10853-020-04858-2.

(36) Hong, M.-H.; Choi, H.; Shim, D. I.; Cho, H. H.; Kim, J.; Park, H.-H. Study of the Effect of Stress/Strain of Mesoporous Al-Doped ZnO Thin Films on Thermoelectric Properties. *Solid State Sci.* **2018**, *82*, 84–91. https://doi.org/10.1016/j.solidstatesciences.2018.05.010.

(37) Edler, K. J. Formation of Ordered Mesoporous Thin Films Through Templating. In *Handbook of Sol-Gel Science and Technology*; Klein, L., Aparicio, M., Jitianu, A., Eds.; Springer International Publishing: Cham, 2017; pp 1–67. https://doi.org/10.1007/978-3-319-19454-7_26-1.

(38) Yang, Z.; Ye, Z.; Xu, Z.; zhao, B. Effect of the Morphology on the Optical Properties of ZnO Nanostructures. *Phys. E Low-Dimens. Syst. Nanostructures* **2009**, *42* (2), 116–119. https://doi.org/10.1016/j.physe.2009.09.010.

(39) Sanchez, C.; Rozes, L.; Ribot, F.; Laberty-Robert, C.; Grosso, D.; Sassoye, C.; Boissiere, C.; Nicole, L. “Chimie Douce”: A Land of Opportunities for the Designed Construction of Functional Inorganic and Hybrid Organic-Inorganic Nanomaterials. *Comptes Rendus Chim.* **2010**, *13* (1–2), 3–39. https://doi.org/10.1016/j.crci.2009.06.001.

(40) Hamd, W.; Cobo, S.; Fize, J.; Baldinozzi, G.; Schwartz, W.; Reymermier, M.; Pereira, A.; Fontecave, M.; Artero, V.; Laberty-Robert, C.; Sanchez, C. Mesoporous α-Fe2O3 Thin Films

Synthesized via the Sol–Gel Process for Light-Driven Water Oxidation. *Phys. Chem. Chem. Phys.* **2012**, *14* (38), 13224. https://doi.org/10.1039/c2cp42535a.

(41) Thongsuriwong, K.; Amornpitoksuk, P.; Suwanboon, S. Structure, Morphology, Photocatalytic and Antibacterial Activities of ZnO Thin Films Prepared by Sol–Gel Dip-Coating Method. *Adv. Powder Technol.* **2013**, *24* (1), 275–280. https://doi.org/10.1016/j.apt.2012.07.002.

(42) Kim, H. T.; Lee, S.-Y.; Park, C. Controls of Surface Morphology on Sol-Gel Derived ZnO Films under Isothermal Treatment Conditions. *Vacuum* **2017**, *143*, 312–315. https://doi.org/10.1016/j.vacuum.2017.06.034.

(43) Park, H.-Y.; Lim, D.; Kim, K.-D.; Jang, S.-Y. Performance Optimization of Low-Temperature-Annealed Solution-Processable ZnO Buffer Layers for Inverted Polymer Solar Cells. *J. Mater. Chem. A* **2013**, *1* (21), 6327. https://doi.org/10.1039/c3ta10637c.

(44) Malek, M. F.; Mamat, M. H.; Khusaimi, Z.; Sahdan, M. Z.; Musa, M. Z.; Zainun, A. R.; Suriani, A. B.; Md Sin, N. D.; Abd Hamid, S. B.; Rusop, M. Sonicated Sol–Gel Preparation of Nanoparticulate ZnO Thin Films with Various Deposition Speeds: The Highly Preferred c-Axis (002) Orientation Enhances the Final Properties. *J. Alloys Compd.* **2014**, *582*, 12–21. https://doi.org/10.1016/j.jallcom.2013.07.202.

(45) Ivanova, T.; Harizanova, A.; Koutzarova, T.; Vertruyen, B.; Stefanov, B. Structural and Morphological Characterization of Sol-Gel ZnO:Ga Films: Effect of Annealing Temperatures. *Thin Solid Films* **2018**, *646*, 132–142. https://doi.org/10.1016/j.tsf.2017.11.042.

(46) Kim, Y.-S.; Tai, W.-P.; Shu, S.-J. Effect of Preheating Temperature on Structural and Optical Properties of ZnO Thin Films by Sol–Gel Process. *Thin Solid Films* **2005**, *491* (1–2), 153–160. https://doi.org/10.1016/j.tsf.2005.06.013.

(47) Ohyama, M.; Kouzuka, H.; Yoko, T. Sol-Gel Preparation of ZnO Films with Extremely Preferred Orientation along (002) Plane from Zinc Acetate Solution. *Thin Solid Films* **1997**, *306* (1), 78–85. https://doi.org/10.1016/S0040-6090(97)00231-9.

(48) Znaidi, L. Sol–Gel-Deposited ZnO Thin Films: A Review. *Mater. Sci. Eng. B* **2010**, *174* (1–3), 18–30. https://doi.org/10.1016/j.mseb.2010.07.001.

(49) Mills, A. An Overview of the Methylene Blue ISO Test for Assessing the Activities of Photocatalytic Films. *Appl. Catal. B Environ.* **2012**, *128*, 144–149. https://doi.org/10.1016/j.apcatb.2012.01.019.

(50) Otsu, N. A Threshold Selection Method from Gray-Level Histograms. *IEEE Trans. Syst. Man Cybern.* **1979**, *9* (1), 62–66. https://doi.org/10.1109/TSMC.1979.4310076.

(51) Kim, E.; Vaynzof, Y.; Sepe, A.; Guldin, S.; Scherer, M.; Cunha, P.; Roth, S. V.; Steiner, U. Gyroid-Structured 3D ZnO Networks Made by Atomic Layer Deposition. *Adv. Funct. Mater.* **2014**, *24* (6), 863–872. https://doi.org/10.1002/adfm.201302238.

(52) Venditti, I.; Barbero, N.; Vittoria Russo, M.; Di Carlo, A.; Decker, F.; Fratoddi, I.; Barolo, C.; Dini, D. Electrodeposited ZnO with Squaraine Sentisizers as Photoactive Anode of DSCs. *Mater. Res. Express* **2014**, *1* (1), 015040. https://doi.org/10.1088/2053-1591/1/1/015040.

(53) Liu, Z.; Jin, Z.; Li, W.; Qiu, J.; Zhao, J.; Liu, X. Synthesis of PS Colloidal Crystal Templates and Ordered ZnO Porous Thin Films by Dip-Drawing Method. *Appl. Surf. Sci.* **2006**, *252* (14), 5002–5009. https://doi.org/10.1016/j.apsusc.2005.07.018.

(54) Yu, L.; Guo, F.; Liu, Z.; Liu, S.; Yang, B.; Yin, M.-L.; Fan, X. Facile Synthesis of Three Dimensional Porous ZnO Films with Mesoporous Walls and Gas Sensing Properties. *Mater. Charact.* **2016**, *112*, 224–228. https://doi.org/10.1016/j.matchar.2015.12.029.

(55) Pauporté, T.; Rathouský, J. Electrodeposited Mesoporous ZnO Thin Films as Efficient Photocatalysts for the Degradation of Dye Pollutants. *J. Phys. Chem. C* **2007**, *111* (21), 7639–7644. https://doi.org/10.1021/jp071465f.

(56) Zhang, J.; Wang, S.; Xu, M.; Wang, Y.; Zhu, B.; Zhang, S.; Huang, W.; Wu, S. Hierarchically Porous ZnO Architectures for Gas Sensor Application. *Cryst. Growth Des.* **2009**, *9* (8), 3532–3537. https://doi.org/10.1021/cg900269a.

(57) Nguyen, T. H. Q.; Ruess, R.; Schlettwein, D. Adjusting Porosity and Pore Radius of Electrodeposited ZnO Photoanodes. *J. Electrochem. Soc.* **2019**, *166* (9), B3040–B3046. https://doi.org/10.1149/2.0101909jes.

(58) Xu, F.; Zhang, P.; Navrotsky, A.; Yuan, Z.-Y.; Ren, T.-Z.; Halasa, M.; Su, B.-L. Hierarchically Assembled Porous ZnO Nanoparticles: Synthesis, Surface Energy, and Photocatalytic Activity. *Chem. Mater.* **2007**, *19* (23), 5680–5686. https://doi.org/10.1021/cm071190g.

(59) Zhang, X.; Dong, Z.; Liu, S.; Shi, Y.; Dong, Y.; Feng, W. Maize Straw-Templated Hierarchical Porous ZnO:Ni with Enhanced Acetone Gas Sensing Properties. *Sens. Actuators B Chem.* **2017**, *243*, 1224–1230. https://doi.org/10.1016/j.snb.2016.12.076.

(60) Kousik, S.; Sipp, D.; Abitaev, K.; Li, Y.; Sottmann, T.; Koynov, K.; Atanasova, P. From Macro to Mesoporous ZnO Inverse Opals: Synthesis, Characterization and Tracer Diffusion Properties. *Nanomaterials* **2021**, *11* (1), 196. https://doi.org/10.3390/nano11010196.

(61) Navidpour, A. H.; Kalantari, Y.; Salehi, M.; Salimijazi, H. R.; Amirnasr, M.; Rismanchian, M.; Azarpour Siahkali, M. Plasma-Sprayed Photocatalytic Zinc Oxide Coatings. *J. Therm. Spray Technol.* **2017**, *26* (4), 717–727. https://doi.org/10.1007/s11666-017-0541-x.

(62) Aksan, O. A.; Oral, Z. B. B. Characterization of TiO2: ZnO Thin Films by Sol-Gel Dip Coating Method; Fethiye, Turkey, 2021; p 040001. https://doi.org/10.1063/5.0058239.

(63) Qawasmi, Y.; Atanasova, P.; Jahnke, T.; Burghard, Z.; Müller, A.; Grassberger, L.; Strey, R.; Bill, J.; Sottmann, T. Synthesis of Nanoporous Organic/Inorganic Hybrid Materials with Adjustable Pore Size. *Colloid Polym. Sci.* **2018**, *296* (11), 1805–1816. https://doi.org/10.1007/s00396-018-4402-z.

(64) Cerda, E.; Mahadevan, L. Geometry and Physics of Wrinkling. *Phys. Rev. Lett.* **2003**, *90* (7), 074302. https://doi.org/10.1103/PhysRevLett.90.074302.

(65) Im, S. H.; Huang, R. Evolution of Wrinkles in Elastic-Viscoelastic Bilayer Thin Films. *J. Appl. Mech.* **2005**, *72* (6), 955–961. https://doi.org/10.1115/1.2043191.

(66) Nikravesh, S.; Ryu, D.; Shen, Y.-L. Direct Numerical Simulation of Buckling Instability of Thin Films on a Compliant Substrate. *Adv. Mech. Eng.* **2019**, *11* (4), 168781401984047. https://doi.org/10.1177/1687814019840470.

(67) Stafford, C. M.; Harrison, C.; Beers, K. L.; Karim, A.; Amis, E. J.; VanLandingham, M. R.; Kim, H.-C.; Volksen, W.; Miller, R. D.; Simonyi, E. E. A Buckling-Based Metrology for Measuring the Elastic Moduli of Polymeric Thin Films. *Nat. Mater.* **2004**, *3* (8), 545–550. https://doi.org/10.1038/nmat1175.

(68) Thune, E.; Boulle, A.; Babonneau, D.; Pailloux, F.; Hamd, W.; Guinebretière, R. Nanostructured Sapphire Vicinal Surfaces as Templates for the Growth of Self-Organized Oxide Nanostructures. *Appl. Surf. Sci.* **2009**, *256* (3), 924–928. https://doi.org/10.1016/j.apsusc.2009.08.089.

(69) Chung, J. Y.; Nolte, A. J.; Stafford, C. M. Surface Wrinkling: A Versatile Platform for Measuring Thin-Film Properties. *Adv. Mater.* **2011**, *23* (3), 349–368. https://doi.org/10.1002/adma.201001759.

(70) Yoo, P. J.; Lee, H. H. Evolution of a Stress-Driven Pattern in Thin Bilayer Films: Spinodal Wrinkling. *Phys. Rev. Lett.* **2003**, *91* (15), 154502. https://doi.org/10.1103/PhysRevLett.91.154502.

(71) Valant, M.; Fanetti, M.; Luin, U. Role of Spinodal-like Wrinkling as a Prenucleation Process in Crystallization of Sol-Gel Derived Thin Films. *Appl. Phys. Lett.* **2016**, *108* (15), 151601. https://doi.org/10.1063/1.4946764.

(72) Livage, J.; Ganguli, D. Sol–Gel Electrochromic Coatings and Devices: A Review. *Sol. Energy Mater. Sol. Cells* **2001**, *68* (3–4), 365–381. https://doi.org/10.1016/S0927-0248(00)00369-X.

(73) Kwon, S. J.; Park, J.-H.; Park, J.-G. Wrinkling of a Sol-Gel-Derived Thin Film. *Phys. Rev. E* **2005**, *71* (1), 011604. https://doi.org/10.1103/PhysRevE.71.011604.

(74) Wolski, L.; Walkowiak, A.; Ziolek, M. Formation of Reactive Oxygen Species upon Interaction of Au/ZnO with H2O2 and Their Activity in Methylene Blue Degradation. *Catal. Today* **2019**, *333*, 54–62. https://doi.org/10.1016/j.cattod.2018.04.004.

(75) Zak, A. K.; Abrishami, M. E.; Majid, W. H. Abd.; Yousefi, R.; Hosseini, S. M. Effects of Annealing Temperature on Some Structural and Optical Properties of ZnO Nanoparticles Prepared by a Modified Sol–Gel Combustion Method. *Ceram. Int.* **2011**, *37* (1), 393–398. https://doi.org/10.1016/j.ceramint.2010.08.017.

(76) Azhniuk, Yu. M.; Prymak, M. V.; Lopushansky, V. V.; Gomonnai, A. V.; Zahn, D. R. T. Optical Characterization of Cd $_{1-x}$ Zn $_{x}$ Se Nanocrystals Grown in Borosilicate Glass: Optical Characterization of Cd $_{1-x}$ Zn $_{x}$ Se Nanocrystals. *Phys. Status Solidi B* **2014**, *251* (3), 669–674. https://doi.org/10.1002/pssb.201350011.

(77) Xu, X.; Wang, P.; Qi, Z.; Ming, H.; Xu, J.; Liu, H.; Shi, C.; Lu, G.; Ge, W. Formation Mechanism of Zn $_{2}$ SiO $_{4}$ Crystal and Amorphous SiO $_{2}$ in ZnO/Si System. *J. Phys. Condens. Matter* **2003**, *15* (40), L607–L613. https://doi.org/10.1088/0953-8984/15/40/L01.

(78) Tang, Y.; Zhou, H.; Zhang, K.; Ding, J.; Fan, T.; Zhang, D. Visible-Light-Active ZnO via Oxygen Vacancy Manipulation for Efficient Formaldehyde Photodegradation. *Chem. Eng. J.* **2015**, *262*, 260–267. https://doi.org/10.1016/j.cej.2014.09.095.

(79) Khorsand Zak, A.; Razali; Abd Majid, W. H. B.; Darroudi, M. Synthesis and Characterization of a Narrow Size Distribution of Zinc Oxide Nanoparticles. *Int. J. Nanomedicine* **2011**, 1399. https://doi.org/10.2147/IJN.S19693.

(80) Ma, S. Y.; Yang, X. H.; Huang, X. L.; Sun, A. M.; Song, H. S.; Zhu, H. B. Effect of Post-Annealing Treatment on the Microstructure and Optical Properties of ZnO/PS Nanocomposite Films. *J. Alloys Compd.* **2013**, *566*, 9–15. https://doi.org/10.1016/j.jallcom.2013.02.179.

(81) Hasnat, M. A.; Safwan, J. A.; Islam, M. S.; Rahman, Z.; Karim, M. R.; Pirzada, T. J.; Samed, A. J.; Rahman, M. M. Electrochemical Decolorization of Methylene Blue at Pt Electrode in KCl Solution for Environmental Remediation. *J. Ind. Eng. Chem.* **2015**, *21*, 787–791. https://doi.org/10.1016/j.jiec.2014.04.013.

(82) Sáenz-Trevizo, A.; Pizá-Ruiz, P.; Chávez-Flores, D.; Ogaz-Parada, J.; Amézaga-Madrid, P.; Vega-Ríos, A.; Miki-Yoshida, M. On the Discoloration of Methylene Blue by Visible Light. *J. Fluoresc.* **2019**, *29* (1), 15–25. https://doi.org/10.1007/s10895-018-2304-6.

(83) Ye, Y.; Bruning, H.; Yntema, D.; Mayer, M.; Rijnaarts, H. Homogeneous Photosensitized Degradation of Pharmaceuticals by Using Red Light LED as Light Source and Methylene Blue as Photosensitizer. *Chem. Eng. J.* **2017**, *316*, 872–881. https://doi.org/10.1016/j.cej.2017.02.053.

(84) Floyd, R. A.; Schneider, J. E.; Dittmer, D. P. Methylene Blue Photoinactivation of RNA Viruses. *Antiviral Res.* **2004**, *61* (3), 141–151. https://doi.org/10.1016/j.antiviral.2003.11.004.

(85) Kumar, K. V.; Porkodi, K.; Rocha, F. Langmuir–Hinshelwood Kinetics – A Theoretical Study. *Catal. Commun.* **2008**, *9* (1), 82–84. https://doi.org/10.1016/j.catcom.2007.05.019.

(86) El Fidha, G.; Bitri, N.; Chaabouni, F.; Acosta, S.; Güell, F.; Bittencourt, C.; Casanova-Chafer, J.; Llobet, E. Physical and Photocatalytic Properties of Sprayed Dy Doped ZnO Thin Films under Sunlight Irradiation for Degrading Methylene Blue. *RSC Adv.* **2021**, *11* (40), 24917–24925. https://doi.org/10.1039/D1RA03967A.

(87) Faisal, M.; Bouzid, H.; Harraz, F. A.; Ismail, A. A.; Al-Sayari, S. A.; Al-Assiri, M. S. Mesoporous Ag/ZnO Multilayer Films Prepared by Repeated Spin-Coating for Enhancing Its Photonic Efficiencies. *Surf. Coat. Technol.* **2015**, *263*, 44–53. https://doi.org/10.1016/j.surfcoat.2014.12.063.

(88) Vallejo, W.; Cantillo, A.; Díaz-Uribe, C. Methylene Blue Photodegradation under Visible Irradiation on Ag-Doped ZnO Thin Films. *Int. J. Photoenergy* **2020**, *2020*, 1–11. https://doi.org/10.1155/2020/1627498.

Supporting Information

New Approach for Designing Wrinkled and Porous ZnO Thin Films for Photocatalytic Applications

Elie A. Daher[‡†], *Bassam Riachi*[‡], *Jean Chamoun*[‡], *Christel Laberty Robert*[†⁑], *Wael Hamd* [₽*]

[‡] Petrochemical Engineering Department, Faculty of Engineering III, CRSI, Lebanese University, Rafic Hariri Campus, Hadat, Lebanon.

[†] Laboratoire Chimie de la Matière Condensée de Paris LCMCP, Sorbonne Université, UPMC Paris 06, 4 Place Jussieu, 75005 Paris, France

[⁑] RS2E, Réseau Français sur le Stockage Electrochimique de l'Energie, CNRS 3459, 80039 Cedex 1 Amiens, France

[₽] Chemical Engineering Department, Faculty of Engineering, University of Balamand, P.O. Box 33, El-Koura, Lebanon.

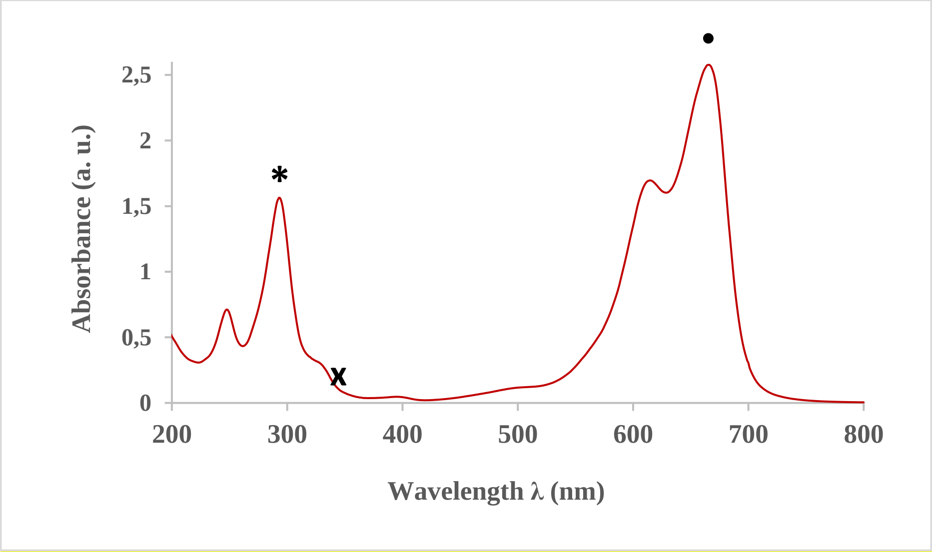

Figure S1. UV-vis spectra of aqueous MB, (*) corresponds to the π – π* transition at λ = 293 nm, (•) corresponds to the n – π* transition at λ = 665 nm and (**x**) corresponds to a minimum of absorbance by the MB molecule (365 nm).

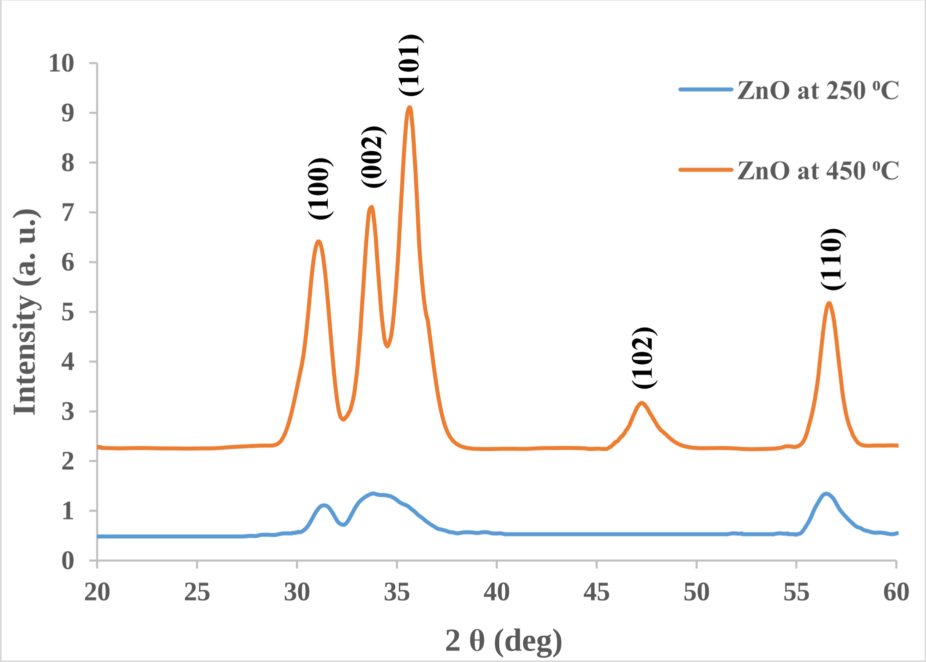

Figure S2. X-ray diffraction pattern of 7 Layers ZnO thin films post-heated at 250 and 450 ºC for 1h.

Chapitre IV

Couplage des Systèmes UVA/ZnO (Photocatalyse) et UVA/Fe^{3+}/H_2O_2 (Photo-Fenton) pour Améliorer les Cinétiques de Dégradation à pH Neutre

Les procédés d'oxydation avancés (AOPs) ont suscité une attention considérable au cours de la dernière décennie[1–4]. Parmi ces AOPs, la photocatalyse hétérogène et les processus de Fenton sont apparus comme des méthodes attrayantes et efficaces pour l'élimination des contaminants émergents dans l'eau et les effluents d'eaux usées[5–8]. Les espèces réactives de l'oxygène (ROS) générées sont bien connues pour leur forte capacité d'oxydation vis-à-vis de la matière organique, conduisant à sa transformation en molécules moins nocives telles que l'H_2O et le CO_2[9]. La photocatalyse est basée sur la génération des radicaux tels que l'hydroxyle ($OH^{\bullet}$) et le superoxyde ($O_2^{\bullet -}$) lors de l'exposition d'un matériau photocatalyseur à une source d'irradiation[10]. Néanmoins, la photo-activité du matériau est limitée par le taux de recombinaison rapide des paires électron – trou ($e^- - h^+$)[5,11–13]. De plus, dans l'oxydation de Fenton, les radicaux $HO_2^{\bullet}$ et $^{\bullet}OH$ sont générés suite aux réactions entre le H_2O_2 et un catalyseur de Fer (Fe^{3+}/ Fe^{2+}). Cependant, ce catalyseur se régénère très lentement et donc ne peut pas être réutilisé dans des cycles supplémentaires, en raison de la formation de boue de fer (sludge) [6]. Malgré les avancées récentes sur les procédés Fenton[6,14], ils sont limités à un domaine de $pH < 3$, à l'utilisation d'agents chélatants et à la formation de boues. Tout ceci limite leur développement à l'échelle industrielle.

Pour pallier les limitations des deux procédés (photocatalyse et photo-Fenton), dans ce chapitre, nous avons conçu un nouveau procédé qui couple le photocatalyseur ZnO avec les réactifs Fe^{3+}/H_2O_2 sous irradiation UVA. Grâce au fonctionnement parallèle des deux procédés, les porteurs de charge photogénérés par le photocatalyseur sont piégés par le fer (III), limitant la recombinaison électron-trou d'une part et accélérant la régénération Fe^{3+}/Fe^{2+} d'autre part.

Le système UVA/ Fe^{3+}/ H_2O_2 /ZnO ainsi utilisé pour la dégradation de 10 ppm de MB à un pH neutre (rapports molaires $[H_2O_2]:[MB] = 52:1$ et $[H_2O_2]:[Fe^{3+}] = 130:1$) présente une constante de vitesse de 0,0049 min^{-1}, dépassant la somme des deux processus individuels. Un pourcentage d'élimination de 94 % est obtenu après 480 minutes d'irradiation.

Références

(1) Serpone, N. Photocatalysis. In *Kirk-Othmer Encyclopedia of Chemical Technology*; John Wiley & Sons, Inc., Ed.; John Wiley & Sons, Inc.: Hoboken, NJ, USA, 2000; p 1608152019051816.a01. https://doi.org/10.1002/0471238961.1608152019051816.a01.

(2) Nakata, K.; Fujishima, A. TiO2 Photocatalysis: Design and Applications. *Journal of Photochemistry and Photobiology C: Photochemistry Reviews* **2012**, *13* (3), 169–189. https://doi.org/10.1016/j.jphotochemrev.2012.06.001.

(3) Zhang, M.; Dong, H.; Zhao, L.; Wang, D.; Meng, D. A Review on Fenton Process for Organic Wastewater Treatment Based on Optimization Perspective. *Science of The Total Environment* **2019**, *670*, 110–121. https://doi.org/10.1016/j.scitotenv.2019.03.180.

(4) Jia, X.; Liu, C.; Xu, X.; Wang, F.; Li, W.; Zhang, L.; Jiao, S.; Zhu, G.; Wang, X. G-C $_3$ N $_4$ -Modified Zr-Fc MOFs as a Novel Photocatalysis-Self-Fenton System toward the Direct Hydroxylation of Benzene to Phenol. *RSC Adv.* **2023**, *13* (28), 19140–19148. https://doi.org/10.1039/D3RA03055E.

(5) Daher, E. A.; Riachi, B.; Chamoun, J.; Laberty-Robert, C.; Hamd, W. New Approach for Designing Wrinkled and Porous ZnO Thin Films for Photocatalytic Applications. *Colloids and Surfaces A: Physicochemical and Engineering Aspects* **2023**, *658*, 130628. https://doi.org/10.1016/j.colsurfa.2022.130628.

(6) Hamd, W. S.; Dutta, J. Heterogeneous Photo-Fenton Reaction and Its Enhancement upon Addition of Chelating Agents. In *Nanomaterials for the Detection and Removal of Wastewater Pollutants*; Elsevier, 2020; pp 303–330. https://doi.org/10.1016/B978-0-12-818489-9.00011-6.

(7) Ghosh, S.; Kouamé, N. A.; Ramos, L.; Remita, S.; Dazzi, A.; Deniset-Besseau, A.; Beaunier, P.; Goubard, F.; Aubert, P.-H.; Remita, H. Conducting Polymer Nanostructures for Photocatalysis under Visible Light. *Nature Mater* **2015**, *14* (5), 505–511. https://doi.org/10.1038/nmat4220.

(8) Zeng, L.; Guo, X.; He, C.; Duan, C. Metal–Organic Frameworks: Versatile Materials for Heterogeneous Photocatalysis. *ACS Catal.* **2016**, *6* (11), 7935–7947. https://doi.org/10.1021/acscatal.6b02228.

(9) Habib, I. Y.; Burhan, J.; Jaladi, F.; Lim, C. M.; Usman, A.; Kumara, N. T. R. N.; Tsang, S. C. E.; Mahadi, A. H. Effect of Cr Doping in CeO2 Nanostructures on Photocatalysis and H2O2 Assisted Methylene Blue Dye Degradation. *Catalysis Today* **2021**, *375*, 506–513. https://doi.org/10.1016/j.cattod.2020.04.008.

(10) Miklos, D. B.; Remy, C.; Jekel, M.; Linden, K. G.; Drewes, J. E.; Hübner, U. Evaluation of Advanced Oxidation Processes for Water and Wastewater Treatment – A Critical Review. *Water Research* **2018**, *139*, 118–131. https://doi.org/10.1016/j.watres.2018.03.042.

(11) Lee, K. M.; Lai, C. W.; Ngai, K. S.; Juan, J. C. Recent Developments of Zinc Oxide Based Photocatalyst in Water Treatment Technology: A Review. *Water Research* **2016**, *88*, 428–448. https://doi.org/10.1016/j.watres.2015.09.045.

(12) Ahmad, I.; Shukrullah, S.; Naz, M. Y.; Bhatti, H. N.; Ahmad, M.; Ahmed, E.; Ullah, S.; Hussien, M. Recent Progress in Rare Earth Oxides and Carbonaceous Materials Modified ZnO Heterogeneous Photocatalysts for Environmental and Energy Applications. *Journal of Environmental Chemical Engineering* **2022**, *10* (3), 107762. https://doi.org/10.1016/j.jece.2022.107762.

(13) Dong, C.; Yang, Y.; Hu, X.; Cho, Y.; Jang, G.; Ao, Y.; Wang, L.; Shen, J.; Park, J. H.; Zhang, K. Self-Cycled Photo-Fenton-like System Based on an Artificial Leaf with a Solar-to-H2O2 Conversion Efficiency of 1.46%. *Nat Commun* **2022**, *13* (1), 4982. https://doi.org/10.1038/s41467-022-32410-0.

(14) Dong, C.; Xing, M.; Zhang, J. Recent Progress of Photocatalytic Fenton-Like Process for Environmental Remediation. *Front. Environ. Chem.* **2020**, *1*, 8. https://doi.org/10.3389/fenvc.2020.00008.

Design of a New ZnO Photocatalytic Fenton-Like Process for Enhancing the Removal of Organic Pollutants at Neutral pH

Elie A. Daher[‡†], *Abbas Al Redda*[‡], *Christel Laberty Robert*[†⁑], *Wael Hamd* [₱]*

[‡] Petrochemical Engineering Department, Faculty of Engineering III, CRSI, Lebanese University, Rafic Hariri Campus, Hadat, Lebanon.

[†] Laboratoire Chimie de la Matière Condensée de Paris LCMCP, Sorbonne Université, UPMC Paris 06, 4 Place Jussieu, 75005 Paris, France

[⁑] RS2E, Réseau Français sur le Stockage Electrochimique de l'Energie, CNRS 3459, 80039 Cedex 1 Amiens, France

[₱] Chemical Engineering Department, Faculty of Engineering, University of Balamand, P.O. Box 33, El-Koura, Lebanon.

KEYWORDS: ZnO thin films, photocatalysis, photo Fenton-like, degradation rate, pseudo-first-order.

ABSTRACT: Increasing the photocatalytic degradation rate of organic pollutants at neutral pH is very challenging. Although doping, nanostructuration, metallization, and binary/ternary oxide systems are widely used to improve the degradation kinetics, rapid electron – hole recombination remains one of the major limitations in photocatalysis. On the other hand, the use of a homogeneous photo-Fenton-like process is suffering from the slow regeneration of Fe^{3+}/Fe^{2+} catalysts and the formation of iron

sludge at pH > 3. In this work, a new catalytic system is designed based on the coupling of nanostructured ZnO thin films with UVA/Fe^{3+}/H_2O_2 for the degradation of methylene blue (MB) molecules at near-neutral pH. This coupled process promotes the formation of additional reactive oxygen species and reduces the formation of sludge by scavenging a part of the photogenerated electrons in the ZnO semiconductor and accelerating the regeneration of the iron catalysts, respectively. The UVA/Fe^{3+}/H_2O_2/ZnO system used for the degradation of 10 ppm MB (molar ratios of [H_2O_2]:[MB] = 52:1, and [H_2O_2]:[Fe^{3+}] = 130:1) exhibits a rate constant of 0.0049 min^{-1} exceeding the sum of both individual processes. A removal percentage of 94 % after 480 minutes of irradiation at pH ~ 7.5 is also observed.

1. Introduction

The low efficiency and high cost of conventional treatment techniques to tackle recalcitrant organic molecules in aqueous mediums have motivated the scientific community to develop alternative and innovative technologies[1]. In this scope advanced oxidation processes (AOPs) have gained significant attention during the last decade[2–5]. Amongst these AOPs, heterogeneous photocatalysis and Fenton processes have emerged as attractive and efficient methods[1,6–8]. For instance, photocatalysis is based on the generation of highly reactive oxygen species (ROS) such as hydroxyl radical ($OH^{\bullet}$) and superoxide radical ($O_2^{\bullet -}$) upon the exposure of a photocatalytic material to an irradiation source[9]. These ROS are well-known for their strong oxidation capacity toward organic matter, leading to their transformation into less hazardous molecules such as H_2O and CO_2[10]. Amongst the photocatalysts, zinc oxide (ZnO) exhibits strong oxidation ability, low production price, and low degree of toxicity to marine/human life[11–14]. Nonetheless, the material photoactivity is hampered by the rapid recombination rate of the electron - hole pairs ($e^- - h^+$) charge carrier[1,11,15,16]. On the other hand, Fenton oxidation is considered an effective technique for the remediation of emerging contaminants in water and wastewater effluents due to the procedure's simplicity, usage of inexpensive reagents, and strong oxidation abilities[6]. Particularly, homogeneous photo-Fenton processes exhibit faster degradation rates compared to conventional Fenton due to the high amount of generated ($OH^{\bullet}$) via the reaction between Fe^{2+} and H_2O_2[17]. However, the iron salt catalyst cannot be reused in additional cycles, due to its precipitation at pH > 3 in the form of iron sludge[6]. Thus, heterogeneous photo-Fenton processes were developed by replacing the Fe^{2+} ions with solid catalysts, then limiting the iron ions from leaching[18–20]. Despite the recent advances in Fenton processes[6,21], they are still suffering from the narrow working pH range, the use of chelating agents, and the formation of sludge, disfavoring then their usage on an industrial scale.

To overcome the limitations of both processes (photocatalysis and photo-Fenton), we designed in this work a new process that couples wrinkled ZnO photocatalyst with Fe^{3+}/H_2O_2 under UVA irradiation. This is designed for the degradation of methylene blue at near-neutral pH. With both processes running concurrently, a win-win situation is achieved, i.e. the photo-generated electrons by the photocatalyst are trapped by the iron (III), inhibiting electron – hole recombination from one side, and accelerating the Fe^{3+}/Fe^{2+} regeneration from the other side. This innovative system enhances the degradation kinetics of the organic pollutants due to the presence of high concentrations of ($OH^{\bullet}$), generated through the presence of "free iron ions" and the ZnO photocatalyst consequently (Rn 1 – 3)[21–23]:

$$Fe^{3+} + H_2O_2 \rightarrow Fe^{2+} + H^+ + HO_2^{\bullet} \qquad \text{(Fenton)} \qquad \text{(Rn. 1)}$$

$$Fe^{2+} + H_2O_2 \rightarrow Fe^{3+} + OH^- + {}^{\bullet}OH \qquad \text{(Fenton)} \qquad \text{(Rn. 2)}$$

$$ZnO + h\nu \rightarrow O_2^{\bullet -} + {}^{\bullet}OH \qquad \text{(Photocatalysis)} \qquad \text{(Rn. 3)}$$

2. Experimental Section

2.1 Reagents and Materials

97% analytical grade zinc acetate dihydrate ($Zn(CH_3COO)_2 \cdot 2H_2O$) was obtained from ACROS organics, propan-2-ol (analytical reagent grade) from Fisher Scientific, monoethanolamine (MEA) (98 % analytical grade) from Fisher Scientific, iron (III) nitrate nonahydrate ($Fe(NO_3)_3 \cdot 9\ H_2O$) 99% for analysis from ACROS Organics, Hydrogen peroxide (H_2O_2) solution 30% (w/w) from Riedel de Haën, methylene blue (MB) laboratory reagent from Paskem. Borosilicate glass slides of 2.5 cm x 7cm and a thickness of 1 mm were obtained from Paksem.

2.2 Characterization

The nanostructure of the films was evaluated by a field emission gun scanning electron microscope (FEG-SEM) model Hitachi SU-70 FESEM. Its crystal nature and the lattice fringe spacing were analyzed by a transmission electron microscope (TEM) model TWIN 120 (TECNAI SPIRIT) equipped with a JEOL 100CF apparatus and coupled with selected area electron diffraction (SAED).

Both the thicknesses and the porosity of the films were measured by using a UV-NIR (193–1690 nm) M-2000DI spectroscopic ellipsometer from J. A. Woolllam. The measurements were conducted on the coated glass slide after soaking its bottom side with silicon oil and deposing it on the rigorous facet of a Silicon wafer. Ellipsometric ψ and Δ angle plots were recorded at 70^o with the CompleteEASE software.

The crystalline phase of the coating was characterized with a D8 Discover X-ray diffractometer (Bruker), using a Cu emitter anode ($K\alpha_1$ and $K\alpha_2$ of wavelength 1.54056 and 1.5444 Å respectively) and a 1D LYNEXEYE XE-T detector. XRD measurements were performed on the coated glass substrates in grazing mode with an incidence angle fixed at 2^o, and 0.05^o steps.

The functional groups at the film's surface were analyzed by Fourier-transformed infrared (FTIR) in attenuated total reflection (ATR) mode with an incidence angle of 45º, and a 4 cm^{-1} resolution, using a Spectrum 400 model from PerkinElmer, equipped with an FR-DTGS detector (fast recovery Deuterated Triglycine Sulfate detector).

2.3 Synthesis of the Wrinkled & Porous ZnO Photocatalyst

Firstly, an alcoholic solution of 0.1 M of Zn^{2+} was obtained by dissolving zinc acetate dihydrate (ZAD) in isopropanol (2-PrOH). Next, monoethanolamine (MEA) was added dropwise with a molar ratio of Zn^{2+}: MEA = 1. The sol was placed in a closed vessel and stirred for 1 hour at T= 70 ºC; below the boiling points of 2-PrOH (82.4 ºC) and MEA (170 ºC).

After aging for 24h at room temperature (RT), ZnO sol was used to prepare multilayer films. Briefly, the glass slides were soaked in the sol and then withdrawn at 9 $mm.s^{-1}$ to an infrared chamber for pre-heat treatment at 150 ºC. The same procedure was repeated 7 consecutive times to reach the desired thickness. Finally, the multilayers were then post-heated for 1h at 450 ºC to promote the crystallization of the ZnO network and remove the rest of the organic molecules. The synthesis procedure of the wrinkled and porous ZnO thin films is detailed in our previous study[1].

2.4 Photo-Fenton and Photocatalysis Processes

- *Experimental Set-Up*

Fenton and photocatalysis experiments were conducted in batch Pyrex vessels of 50 mL, under UVA irradiation of λ = 365 nm. The UVA light source was placed at 5 cm from the reactors and an emitted illuminance of ~ 500 lux by a Testo 450 luxmeter of ±3 % precision from Testo, France. The vessels were filled with 45 ml of MB probe molecule (10 ppm) dissolved in deionized water (DI). The photocatalytic degradation of MB was carried out at room temperature (RT) for a maximum time of 8 hours. The kinetic data was estimated by analyzing the absorbance curves, obtained by UV-vis spectroscopy. For the photo-Fenton-like experiments, H_2O_2, and Fe^{3+} were successively added in various molar ratios from 1:1 to 40000:1 to the MB solution under near-neutral pH (~ 7.5). For the photocatalysis experiments, ZnO thin films (11 cm^2) were immersed in the MB solution for 12 hours in the dark to reach the adsorption equilibrium, before initiating the photocatalytic degradation process. As for the coupling experiments, the MB was added to the as-prepared ZnO films followed by the drop-wise addition of hydrogen peroxide and iron (III) reagent in a molar ratio of 130:1.

- *Kinetic Model*

The kinetics were estimated from the Langmuir–Hinshelwood kinetic model (Eq.1)[24]:

$$r = -\frac{dC}{dt} = \frac{Kr.K.C}{1+K.C} \qquad \text{(Eq.1)}$$

where r, C, K, K_r, and t represent the reaction rate, molecule concentration at time t, adsorption equilibrium constant, limiting rate constant of reaction at maximum coverage, and contact time respectively.

At small (mM) initial concentrations, $(K.C_0 \ll 1)$, Eq. 2 is simplified to the apparent rate order (Eq.2)[24]:

$$r = -\frac{dC}{dt} = K_{app}.C \qquad \text{(Eq.2)}$$

where K_{app}, is the apparent degradation rate. Simple integration of this equation for $C = C_0$ at $t = 0$ = 0 gives:

$$\ln\left(\frac{C_t}{C_0}\right) = -K_{app}.t \qquad \text{(Eq.3)}$$

K_{app} is then obtained from the slope of the linear curve in the plot of $Ln\ (C_t/C_0)$ vs. t, where (C_t/C_0) is equal to (A_t/A_0)according to the Beer-Lambert law Eq.4.

$$A = \varepsilon \times L \times C \qquad \text{(Eq.4)}$$

$A_0, A_t, C_0, C_t, \varepsilon$ & L refer respectively to the molecule light absorbance at t_0, molecule light absorbance at t, molecule concentration at t_0, molecule concentration at t, molar absorptivity, and length of the light path. The percentage of removal is obtained from (Eq. 5) by estimating the concentration of MB during the experimental time.

$$\text{Efficiency} = \frac{C_0 - C_t}{C_0} \text{ x } 100 \qquad \text{(Eq. 5)}$$

3. Results and Discussion

3.1 Characterization of the ZnO Photocatalyst

The films' microstructure was investigated using SEM-FEG and HRTEM (Figure 1a, b). The SEM-FEG micrographs reveal crack-free homogenous wrinkled and porous films. The ridges (protrusive areas) occupy a width between ~ 100 to 220 nm and stretch over a regular cleavage (hollow areas) between ~ 90 to 200 nm (valleys). The film's porosity was assessed by ellipsometry. A value of ~ 25% is achieved with a mean square error (MSE) of ~ 7.

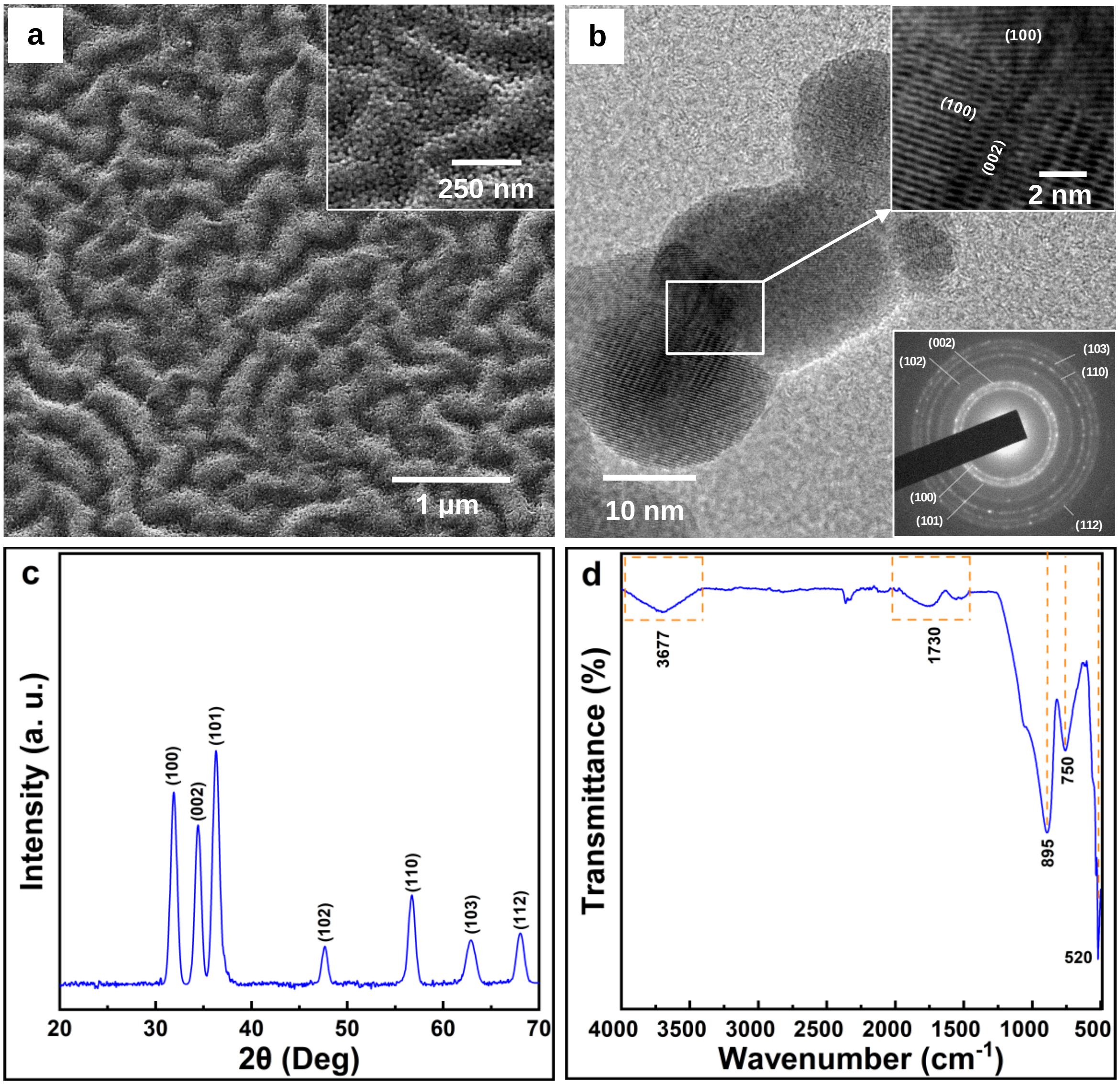

Figure 1. (a) SEM-FEG micrographs of 7 layers' ZnO thin films post-heated treatment at 450 °C, Inset: Cross-sectional view of "a", **(b)** TEM image of the extracted grains from the film. Upper inset: HRTEM of identified grain boundaries. Bottom inset: SAEDpatternr, **(c)** X-ray diffraction pattern of "a", **(d)** ATR-FTIR spectrum of "a".

High-resolution TEM images and SAED pattern (Figure 1b) show well-defined grain boundaries and a polycrystalline structure, respectively. 7 distinctive concentric rings are identified with lattice spacing corresponding to the ZnO wurtzite crystalline structure (indexed in the bottom inset of Figure 1b)[25–27]. Additionally, it can also be noticed the well-defined interface between two adjacent grains, as shown in the upper inset of Figure 1b.

Grazing incidence X-Ray diffraction was performed at an incidence angle of 2^o (Figure 1c). The XRD pattern of the multilayer thin films shows also 7 prominent peaks indexed with the (100), (002), (101), (102), (110), (103), and (112) crystallographic planes, representing a typical polycrystalline ZnO wurtzite structure. This agrees well with the SAED results[25–27]. The peaks' positions are indexed to the JCPDS No. 01-086-3978 with lattice constants: a = b = 3.248 Å and c = 5.202 Å.

The chemical composition of the coating was further supported by ATR-FTIR measurement (Figure 1d). The vibrational behavior of the film's surface is characterized by 5 main functional groups located at 520, 750, 895, 1730, and 3677 cm^{-1}. The pronounced peak at ~ 520 cm^{-1} arises from the stretching vibration of Zn–O bonds[28]. The absorption bands at ~ 750 cm^{-1} and ~ 895 cm^{-1} are assigned to the stretching vibrations of Zn–O bonds[28–31] and the tetrahedral coordination of Zn within the hexagonal ZnO lattice[32], respectively. The broad absorption band at 4000–3500 cm^{-1} is attributed to the ZnO–H stretching, due to the hydroxylation of the film's surface by the atmospheric humidity[33]. The weak absorptions between ~ 1450 cm^{-1} and 2000 cm^{-1} are associated with C–H, C–H_2, C=C, and C=O stretching vibration bands probably due to the film's contamination by traces of organic molecules[34,35].

3.2 Optimization of H_2O_2 and Fe^{3+} Concentrations

In Fenton-like oxidation, reaction kinetics are intimately dependent on the H_2O_2:Fe^{3+} ratio and irradiation light source. Thus, finding adequate proportions and quantities of reagents is crucial for reducing operating costs, and avoiding unwanted reactions[21]. For instance, a surplus of H_2O_2 may scavenge the $^{\bullet}OH$ radicals generated via Rn. 2[17]. In contrast, a low amount of H_2O_2 decreases the generation of $^{\bullet}OH$ and reduces the efficiency of the Fenton process. Furthermore, the application of light energy accelerates the radicals' generation and improves the process efficiency (Figure S1).

The effect of [H_2O_2] concentration on the degradation rate (K_{app}) of MB at 1 ppm [Fe^{3+}] is shown in Figure 2a. For ratios between 1:1 and 700:1, the rate constant follows a single linear trend. However, for higher ratios up to 40000:1, the MB degradation follows two distinct regimes, with slower kinetics between T_0 and 180 minutes, and faster kinetics between 180 and 420 minutes. At the first stage, $^{\bullet}OH$ radicals are scavenged by the excess of H_2O_2 to produce $HO_2^{\bullet}$ radicals with lower oxidation capability, hindering then the process kinetics[36,37]. As the experiment advances, hydrogen peroxide is partially consumed, disfavoring the scavenging reactions and leading to an increase in the $^{\bullet}OH$ free radicals. After 420 minutes, the rate constants become stable because all MB molecules are nearly degraded. The effect of H_2O_2 concentration on the degradation kinetics at 1 ppm [Fe^{3+}] is summarized in Table S1.

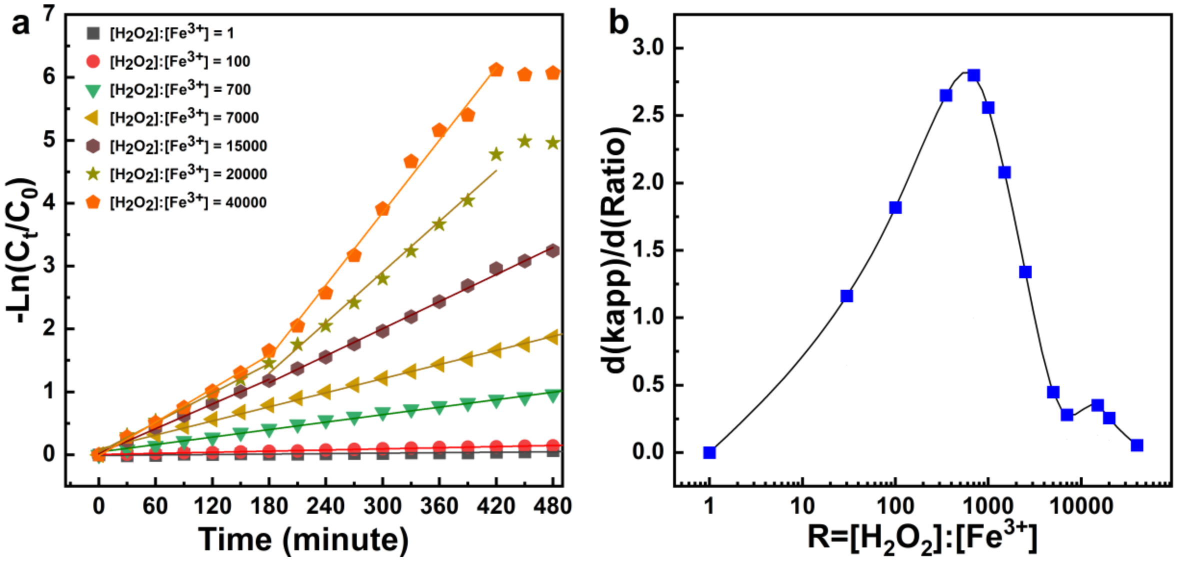

Figure 2. (a) Degradation rates of 10 ppm methylene blue by different $\frac{[H_2O_2]}{[Fe^{3+}]}$ ratios with UVA light of λ = 365 nm, T = 25 °C. [Fe^{3+}] was fixed at 1 ppm, **(b)** Fluctuation of d(K_{app})/dr vs r plots, representing the evolution of the kinetic constants K_{app} (min^{-1}) along the experimental progression of the $\frac{[H_2O_2]}{[Fe^{3+}]}$ ratio (R).

Although the surplus of H_2O_2 improves drastically the kinetics degradation, its use at these concentrations is not recommended due to the increase of cost and risks in the overall process (associated with handling, transportation, and storage)[6].

The selection of the optimal $[H_2O_2]$:$[Fe^{3+}]$ (R) can be made by plotting d(K_{app})/dR vs R (between two consecutive values) as shown in Figure 2b. The first derivative increases by ~ 1.8 times when R goes from 1:1 to 100:1, then reaches a maximum (~ 2.8) at R = 700:1 and finally decreases sharply to 0.04 for R = 40000:1. From this perspective, R = 700:1 yields the highest efficiency considering the given quantity of H_2O_2. Furthermore, this quantity of hydrogen peroxide is found to be equal to the stoichiometric amount ($[H_2O_2]$:[MB] = 52:1) required for the degradation of the 10 ppm MB[38].

In addition, the Fe^{3+} amount should be optimized to increase the degradation kinetics while keeping a low sludge production. To do so, the $[Fe^{3+}]$ range is varied from 1 ppm to 15 ppm at a fixed initial concentration of H_2O_2 ($[H_2O_2]$:[MB] = 52:1) (Figure 3a).

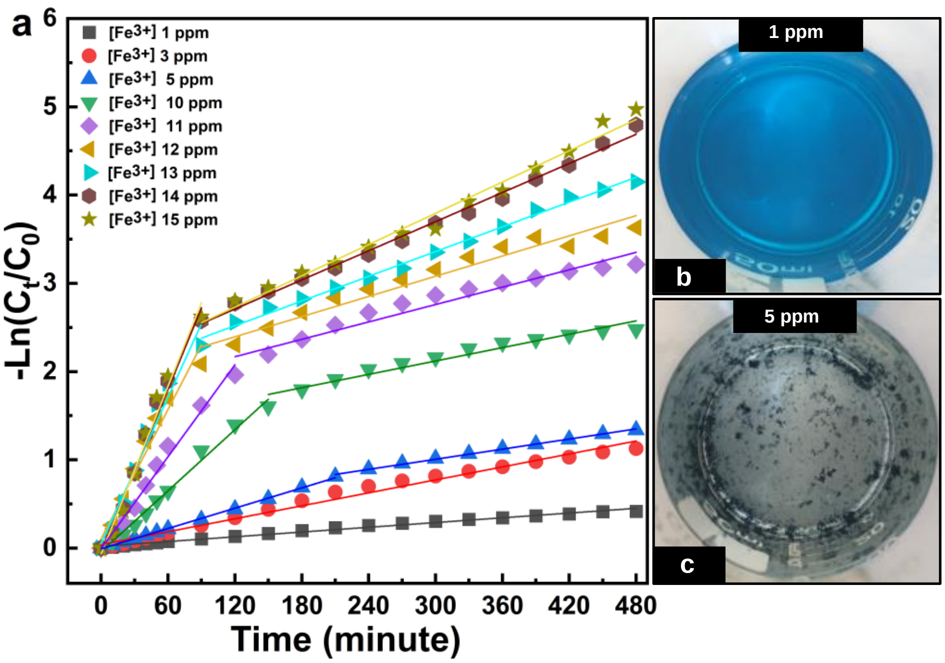

Figure 3. (a) Degradation rates of 10 ppm MB under UVA (λ = 365 nm) at T = 25 ºC, with different loads of Fe^{3+}, $\frac{[H_2O_2]}{[MB]} = 52$. Top view of photo Fenton-like batch reactor with **(b)** 1 ppm, and **(c)** 5 ppm Fe^{3+} after one hour of irradiation.

When the catalyst concentration goes from 1 to 3 ppm, the degradation efficiency attains 22 % in 90 minutes of irradiation, corresponding to an increase in the rate constant by ~ 2.7 times. In this range, a linear degradation regime with no precipitate formation is observed (Figure 3b). Nevertheless, while an increase in the iron(III) concentration to 15 ppm drastically improves the final removal of MB to 94 % in 90 minutes, the degradation kinetics follow two different regimes. The first one is attributed to the formation of additional hydroxyl radicals during the Fe^{3+}/Fe^{2+} regeneration, leading to a rapid increase in rate constants in the early stages of the process. However, the second one corresponds to the accumulation of Fe^{3+} ions in the medium, resulting in a decrease in the degradation rate, and an appearance of an inflection point. For instance, at $[Fe^{3+}]$ = 5 ppm, the inflection appears at 210 minutes, showing the beginning of iron ions precipitation in the form of oxyhydroxide. The formation of this component is classified as a secondary source of pollution (Figure 3c)[6]. This behavior is more pronounced at higher temperatures, where an increase from 25 to 30 ºC shifts the inflection point from

210 to 60 minutes (Figure S2) due to the higher frequency of collisions of species in the medium. In addition, augmenting the [Fe^{3+}] from 5 to 15 ppm moves gradually the inflection point to 90 minutes, confirming the low regeneration of the Fe^{3+} catalyst at high concentrations[6].

The MB removal (%) after 90 minutes of irradiation (Table S2) is quite comparable with other reported homogeneous Fenton systems, working in acidic pH (3 – 4), and using chelating agents such as ethylenediaminetetraacetic acid disodium (EDTA), and S,S-ethylenediamine-N,N-disuccinic acid trisodium salt (EDDS-Na) for reducing sludge formation[22,37,39–41]. However, all these approaches increase the operational cost, Total Organic Carbon (TOC) level in the water matrix, and can promote non-desirable reactions[42,43].

3.3 Coupling of the Photocatalytic and Photo-Fenton-Like Processes

The enhancement of reactions kinetics and the reduction of sludge formation can be realized by increasing the amount of ROS and the lifetime of electron – hole pairs. Accordingly, coupling the ZnO semiconductor with the Fe(III) and Fe(II) catalysts appears as an attractive approach. For instance, the photogenerated electrons in the ZnO conduction band reduce the Fe^{3+} ions instead of being recombined, leading to an increase in the oxidant radicals. To investigate the efficiency of the coupled processes, a [Fe^{3+}] concentration of 5 ppm was chosen at [H_2O_2]:[MB] = 52:1. This ratio corresponds to the beginning of the sludge formation.

Figure 4 presents the kinetics degradation of MB for an irradiation time of 480 minutes, using three systems: i) wrinkled and porous ZnO thin films, ii) photo-Fenton-like, and iii) coupled ZnO with photo-Fenton-like. First, the ZnO thin films demonstrate a relatively low photocatalytic activity compared to the other systems. This is probably due to the low generation of ROS, promoted by the recombination of electron – hole pairs[44,45].

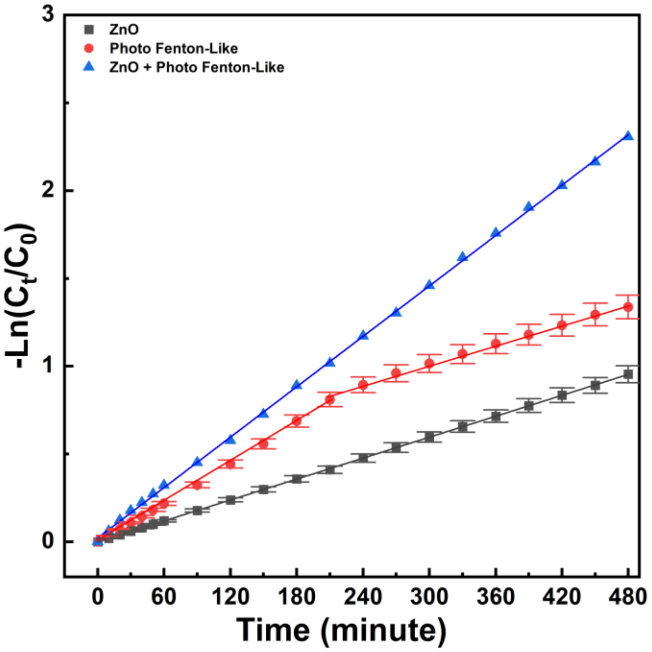

Figure 4. Comparative degradation rate of 10 ppm methylene blue using ZnO photocatalyst, photo-Fenton-like, and the coupling of both under UVA light of λ=365nm, $\frac{[H_2O_2]}{[MB]}$ = 52, and 5 ppm [Fe^{3+}] at T = 25 ºC.

On the other side, the photo-Fenton-like process exhibits a higher degradation kinetic of 0.0038 min^{-1} during the first 210 minutes of irradiation, approximately twice that of the photocatalysis (0.002 min^{-1}). However, as the experiment proceeds, the kinetic of individual photo-Fenton-like starts declining to become close to that of the ZnO photocatalysts. This behavior is explained by the higher generation of radicals in the first part and the beginning of sludge formation in the second one (see section 2.2). On the contrary, the coupled processes exhibit a single degradation rate over the experimental time, with a K_{app} of 0.0049 min^{-1} > K_{app} (photocatalysis) + K_{app} (photo-Fenton-like). This new system is able to enhance the photocatalytic activity of ZnO and the performance of the photo-Fenton-like, simultaneously. When the zinc oxide is irradiated by a 365 nm light source, electron – hole pairs are generated and promote the oxidation/reduction of H_2O and O_2 molecules to produce $O_2^{\bullet -}$ and $^{\bullet}OH$ radicals. This phenomenon can accelerate the regeneration of Fe^{3+}/Fe^{2+} and reduces the electron – hole recombination (Scheme 1). The positioning of the ZnO conduction band (-0.31 V vs Normal Hydrogen Electrode (NHE)) enables the photogenerated electrons to reduce the Fe^{3+} ions to Fe^{2+} ($E_{0_{Fe(III)/Fe(II)}} =$ 0.77 V vs NHE) and consequently limiting the $e^{-} - h^{+}$ recombination[46–48]. The iron(III) reduction is considered the rate-determining step because it is about 6000 times slower than iron(II) oxidation (Rn. 2)[6]. Furthermore, the free $^{\bullet}OH$ radicals produced by the reduction of the dissolved oxygen contribute to the regeneration of Fe^{3+} and the degradation of MB molecules[49–53].

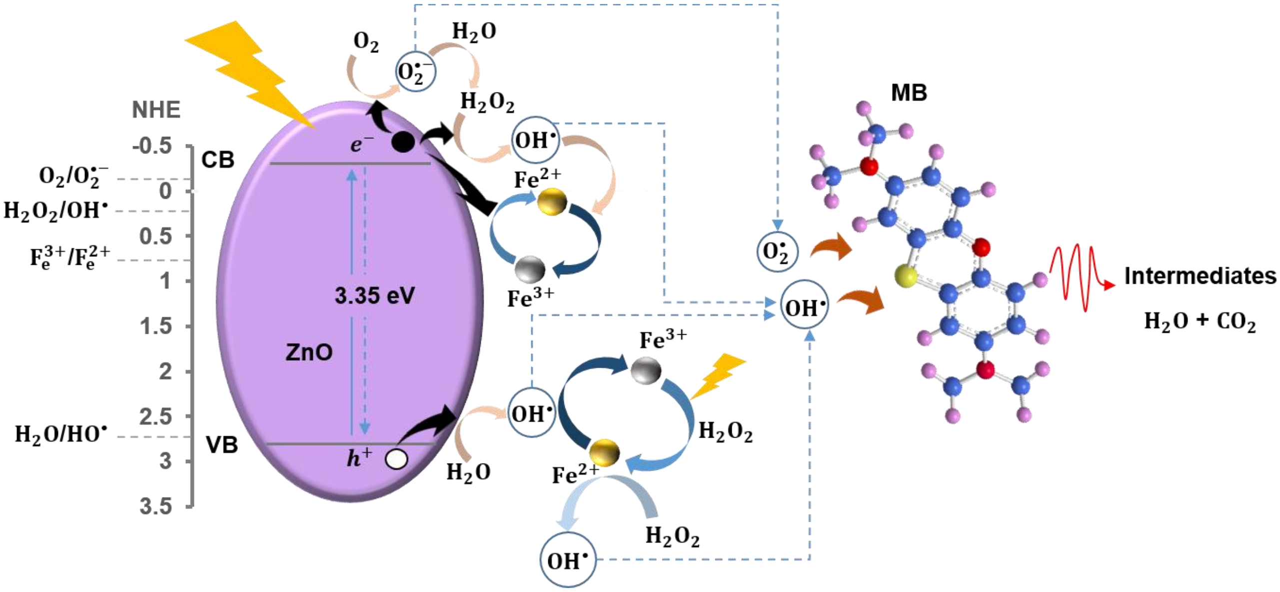

Scheme 1. Coupled system made of the ZnO photocatalyst and the photo-Fenton-like process.

Additionally, the hydroxyl radicals generated by the water oxidation at the ZnO valence band and the oxidation of Fe^{2+} by the hydrogen peroxide, accelerate the Fe^{3+}/Fe^{2+} regeneration and participate in the MB degradation, respectively. Other radicals (e. g $HO_2^{\bullet}$) generated via a classic photocatalytic system are also involved in the oxidation process and contribute to the mechanism in Scheme 1 (not shown for aesthetic purposes).

As a result, coupling the ZnO photocatalysis with the photo-Fenton like increases the rate constant of MB degradation to 0.0049 min^{-1} which bypasses the sum of the obtained kinetics from the individual processes (Figure 4). Interestingly, some Fenton processes have reported high degradation kinetics in acidic pH (3 – 4) conditions and at temperatures between ~30 to 35 ºC, or by using chelating agents. This novel design exhibits better performance than these approaches and other methods including adsorption, heterogeneous Fenton, and non-coupled ZnO photocatalysis (Table 1).

Table 1. Working parameters and the kinetics of the as-synthesized ZnO photocatalyst, photo-Fenton-like, the coupled system, and other different methods such as adsorption, heterogeneous Fenton, and non-coupled ZnO photocatalysis.

Method	Working T (ºC)	Working pH	[MB] (ppm)	[Fe^{3+}] (ppm)	[H_2O_2]: [Fe^{3+}] Molar ratio`	Light source	*Kapp* (min^{-1})	*MB removal* (%)
Fenton-like/Ferrocene[54]	30	4	10	N/A	N/A	N/A	N/A	100 in 90 min
Heterogeneous Fenton/$Fe_{3-x}Ti_xO_4$[55]	RT	6.8	100	N/A	N/A	N/A	N/A	98 in 24 h
Adsorption/MCGO[56]	RT	N/A	30	N/A	N/A	N/A	N/A	96 in 14 h
ZnO nanorods[57]	25	N/A	3	N/A	N/A	Visible	~0.012	N/A
Dense ZnO film[58]	RT	N/A	~ 5	N/A	N/A	UVA	~ 0.0028	N/A
Wrinkled ZnO Photocatalyst (This study)	25	7.5	10	N/A	N/A	UVA (365 nm)	0.002	61 in 480 min
Photo-Fenton Like (This study)	25	7.5	10	5	130	UVA (365 nm)	0.0022 - 0.0038	73 in 480 min
Coupled system (This study)	25	7.5	10	5	130	UVA (365 nm)	0.0049	94 in 480 min

4. Conclusion

In this study, we propose a novel oxidation system to tackle organic pollutants in water at near-neutral pH and room temperature. Wrinkled and porous ZnO thin films are coupled to a homogeneous photo-

Fenton-like process for the degradation of MB organic pollutants. Using a $[H_2O_2]$:[MB] stoichiometric ratio of 52:1; a $[H_2O_2]$:$[Fe^{3+}]$ ratio of 130, a $[Fe^{3+}]$ of 5 ppm, and a $[H_2O_2]$ of 0.059 ppm, yields 94 % MB removal after 480 minutes. The iron catalyst plays the role of electron scavenger, therefore reducing the electron – hole recombination in the ZnO semiconductor. This system shows a higher degradation rate of 0.0049 min^{-1} than the two processes operating separately, due to the increase in free $^{\bullet}OH$ radicals and the rapid regeneration of Fe^{3+}/Fe^{2+}. Interestingly, this prevents the formation of ferrous sludge without using chelating agents. Furthermore, compared to other works, this study presents several advantages including: i) a reduction of the process cost and risks (low $[H_2O_2]$ and $[Fe^{3+}]$), ii) a diminution of the equipements' corrosion (low $[H_2O_2]$ and neutral pH), and iii) a decrease of the secondary pollution (no sludge formation).

AUTHOR INFORMATION

Corresponding Author

Dr. Wael Hamd

E-mail: wael.hamd@balamand.edu.lb

Acknowledgment

This work has been supported by the project: CLAIM, H2020-BG-2016–2017 [grant number 774586], "Cleaning Litter by Developing and Applying Innovative Methods in European seas". Mr. David Montero, Ms. Ferdaous Ben Romdhane, and Mr. Mohamed Selmane are gratefully acknowledged for conducting SEM-FEG, TEM, and XRD measurements at the Sorbonne University.

References

(1) Daher, E. A.; Riachi, B.; Chamoun, J.; Laberty-Robert, C.; Hamd, W. New Approach for Designing Wrinkled and Porous ZnO Thin Films for Photocatalytic Applications. *Colloids Surf. Physicochem. Eng. Asp.* **2023**, *658*, 130628. https://doi.org/10.1016/j.colsurfa.2022.130628.

(2) Serpone, N. Photocatalysis. In *Kirk-Othmer Encyclopedia of Chemical Technology*; John Wiley & Sons, Inc., Ed.; John Wiley & Sons, Inc.: Hoboken, NJ, USA, 2000; p 1608152019051816.a01. https://doi.org/10.1002/0471238961.1608152019051816.a01.

(3) Nakata, K.; Fujishima, A. TiO2 Photocatalysis: Design and Applications. *J. Photochem. Photobiol. C Photochem. Rev.* **2012**, *13* (3), 169–189. https://doi.org/10.1016/j.jphotochemrev.2012.06.001.

(4) Zhang, M.; Dong, H.; Zhao, L.; Wang, D.; Meng, D. A Review on Fenton Process for Organic Wastewater Treatment Based on Optimization Perspective. *Sci. Total Environ.* **2019**, *670*, 110–121. https://doi.org/10.1016/j.scitotenv.2019.03.180.

(5) Jia, X.; Liu, C.; Xu, X.; Wang, F.; Li, W.; Zhang, L.; Jiao, S.; Zhu, G.; Wang, X. G-C $_3$ N $_4$ -Modified Zr-Fc MOFs as a Novel Photocatalysis-Self-Fenton System toward the Direct Hydroxylation of Benzene to Phenol. *RSC Adv.* **2023**, *13* (28), 19140–19148. https://doi.org/10.1039/D3RA03055E.

(6) Hamd, W. S.; Dutta, J. Heterogeneous Photo-Fenton Reaction and Its Enhancement upon Addition of Chelating Agents. In *Nanomaterials for the Detection and Removal of Wastewater Pollutants*; Elsevier, 2020; pp 303–330. https://doi.org/10.1016/B978-0-12-818489-9.00011-6.

(7) Ghosh, S.; Kouamé, N. A.; Ramos, L.; Remita, S.; Dazzi, A.; Deniset-Besseau, A.; Beaunier, P.; Goubard, F.; Aubert, P.-H.; Remita, H. Conducting Polymer Nanostructures for Photocatalysis under Visible Light. *Nat. Mater.* **2015**, *14* (5), 505–511. https://doi.org/10.1038/nmat4220.

(8) Zeng, L.; Guo, X.; He, C.; Duan, C. Metal–Organic Frameworks: Versatile Materials for Heterogeneous Photocatalysis. *ACS Catal.* **2016**, *6* (11), 7935–7947. https://doi.org/10.1021/acscatal.6b02228.

(9) Miklos, D. B.; Remy, C.; Jekel, M.; Linden, K. G.; Drewes, J. E.; Hübner, U. Evaluation of Advanced Oxidation Processes for Water and Wastewater Treatment – A Critical Review. *Water Res.* **2018**, *139*, 118–131. https://doi.org/10.1016/j.watres.2018.03.042.

(10) Habib, I. Y.; Burhan, J.; Jaladi, F.; Lim, C. M.; Usman, A.; Kumara, N. T. R. N.; Tsang, S. C. E.; Mahadi, A. H. Effect of Cr Doping in CeO2 Nanostructures on Photocatalysis and H2O2 Assisted Methylene Blue Dye Degradation. *Catal. Today* **2021**, *375*, 506–513. https://doi.org/10.1016/j.cattod.2020.04.008.

(11) Lee, K. M.; Lai, C. W.; Ngai, K. S.; Juan, J. C. Recent Developments of Zinc Oxide Based Photocatalyst in Water Treatment Technology: A Review. *Water Res.* **2016**, *88*, 428–448. https://doi.org/10.1016/j.watres.2015.09.045.

(12) Uheida, A.; Mejía, H. G.; Abdel-Rehim, M.; Hamd, W.; Dutta, J. Visible Light Photocatalytic Degradation of Polypropylene Microplastics in a Continuous Water Flow System. *J. Hazard. Mater.* **2021**, *406*, 124299. https://doi.org/10.1016/j.jhazmat.2020.124299.

(13) Dobretsov, S.; Sathe, P.; Bora, T.; Barry, M.; Myint, M. T. Z.; Abri, M. A. Toxicity of Different Zinc Oxide Nanomaterials at 3 Trophic Levels: Implications for Development of Low-Toxicity Antifouling Agents. *Environ. Toxicol. Chem.* **2020**, *39* (7), 1343–1354. https://doi.org/10.1002/etc.4720.

(14) Li, Y.; Wei, G.; Shao, L.; Li, Z.; Yu, F.; Liu, J.; Yang, X.; Lu, Q.; Li, A.; Huang, Y.; Zhang, L. Green Synthesis of Red Mud Based ZnO Fe2O3 Composite Used for Photo-Fenton Reaction

under Visible Light. *J. Clean. Prod.* **2019**, *207*, 717–727. https://doi.org/10.1016/j.jclepro.2018.10.051.

(15) Ahmad, I.; Shukrullah, S.; Naz, M. Y.; Bhatti, H. N.; Ahmad, M.; Ahmed, E.; Ullah, S.; Hussien, M. Recent Progress in Rare Earth Oxides and Carbonaceous Materials Modified ZnO Heterogeneous Photocatalysts for Environmental and Energy Applications. *J. Environ. Chem. Eng.* **2022**, *10* (3), 107762. https://doi.org/10.1016/j.jece.2022.107762.

(16) Dong, C.; Yang, Y.; Hu, X.; Cho, Y.; Jang, G.; Ao, Y.; Wang, L.; Shen, J.; Park, J. H.; Zhang, K. Self-Cycled Photo-Fenton-like System Based on an Artificial Leaf with a Solar-to-H2O2 Conversion Efficiency of 1.46%. *Nat. Commun.* **2022**, *13* (1), 4982. https://doi.org/10.1038/s41467-022-32410-0.

(17) Ziembowicz, S.; Kida, M. Limitations and Future Directions of Application of the Fenton-like Process in Micropollutants Degradation in Water and Wastewater Treatment: A Critical Review. *Chemosphere* **2022**, *296*, 134041. https://doi.org/10.1016/j.chemosphere.2022.134041.

(18) Xia, M.; Long, M.; Yang, Y.; Chen, C.; Cai, W.; Zhou, B. A Highly Active Bimetallic Oxides Catalyst Supported on Al-Containing MCM-41 for Fenton Oxidation of Phenol Solution. *Appl. Catal. B Environ.* **2011**, *110*, 118–125. https://doi.org/10.1016/j.apcatb.2011.08.033.

(19) Zhang, M.; Yao, Q.; Guan, W.; Lu, C.; Lin, J.-M. Layered Double Hydroxide-Supported Carbon Dots as an Efficient Heterogeneous Fenton-Like Catalyst for Generation of Hydroxyl Radicals. *J. Phys. Chem. C* **2014**, *118* (19), 10441–10447. https://doi.org/10.1021/jp5012268.

(20) Liu, Y.; Jin, W.; Zhao, Y.; Zhang, G.; Zhang, W. Enhanced Catalytic Degradation of Methylene Blue by α-Fe2O3/Graphene Oxide via Heterogeneous Photo-Fenton Reactions. *Appl. Catal. B Environ.* **2017**, *206*, 642–652. https://doi.org/10.1016/j.apcatb.2017.01.075.

(21) Dong, C.; Xing, M.; Zhang, J. Recent Progress of Photocatalytic Fenton-Like Process for Environmental Remediation. *Front. Environ. Chem.* **2020**, *1*, 8. https://doi.org/10.3389/fenvc.2020.00008.

(22) Sun, C.; Chen, C.; Ma, W.; Zhao, J. Photodegradation of Organic Pollutants Catalyzed by Iron Species under Visible Light Irradiation. *Phys Chem Chem Phys* **2011**, *13* (6), 1957–1969. https://doi.org/10.1039/C0CP01203C.

(23) Bansal, P.; Verma, A.; Mehta, C.; Singla, J.; Toor, A. P. Assessment of Integrated Binary Process by Coupling Photocatalysis and Photo-Fenton for the Removal of Cephalexin from Aqueous Solution. *J. Mater. Sci.* **2018**, *53* (10), 7326–7343. https://doi.org/10.1007/s10853-018-2094-x.

(24) Kumar, K. V.; Porkodi, K.; Rocha, F. Langmuir–Hinshelwood Kinetics – A Theoretical Study. *Catal. Commun.* **2008**, *9* (1), 82–84. https://doi.org/10.1016/j.catcom.2007.05.019.

(25) Liu, Y.; Gao, W. Growth Process, Crystal Size and Alignment of ZnO Nanorods Synthesized under Neutral and Acid Conditions. *J. Alloys Compd.* **2015**, *629*, 84–91. https://doi.org/10.1016/j.jallcom.2014.12.139.

(26) Demianets, L. N.; Kostomarov, D. V. Mechanism of Zinc Oxide Single Crystal Growth under Hydrothermal Conditions. *Ann. Chim. Sci. Matér.* **2001**, *26* (1), 193–198.

(27) Bora, T.; Sathe, P.; Laxman, K.; Dobretsov, S.; Dutta, J. Defect Engineered Visible Light Active ZnO Nanorods for Photocatalytic Treatment of Water. *Catal. Today* **2017**, *284*, 11–18. https://doi.org/10.1016/j.cattod.2016.09.014.

(28) S, M.; N, H.; P.P, V. In Vitro Biocompatibility and Antimicrobial Activities of Zinc Oxide Nanoparticles (ZnO NPs) Prepared by Chemical and Green Synthetic Route— A Comparative Study. *BioNanoScience* **2020**, *10* (1), 112–121. https://doi.org/10.1007/s12668-019-00698-w.

(29) Valerio, T. L.; Maia, G. A. R.; Gonçalves, L. F.; Viomar, A.; Banczek, E. do P.; Rodrigues, P. R. P. Study of the Nb2O5 Insertion in ZnO to Dye-Sensitized Solar Cells. *Mater. Res.* **2019**, *22* (suppl 1), e20180864. https://doi.org/10.1590/1980-5373-mr-2018-0864.

(30) Singh, J.; Kaur, S.; Kaur, G.; Basu, S.; Rawat, M. Biogenic ZnO Nanoparticles: A Study of Blueshift of Optical Band Gap and Photocatalytic Degradation of Reactive Yellow 186 Dye under Direct Sunlight. *Green Process. Synth.* **2019**, *8* (1), 272–280. https://doi.org/10.1515/gps-2018-0084.

(31) Bai, S.; Hu, J.; Li, D.; Luo, R.; Chen, A.; Liu, C. C. Quantum-Sized ZnO Nanoparticles: Synthesis, Characterization and Sensing Properties for NO2. *J. Mater. Chem.* **2011**, *21* (33), 12288. https://doi.org/10.1039/c1jm11302j.

(32) da Silva-Neto, M. L.; de Oliveira, M. C. A.; Dominguez, C. T.; Lins, R. E. M.; Rakov, N.; de Araújo, C. B.; Menezes, L. de S.; de Oliveira, H. P.; Gomes, A. S. L. UV Random Laser Emission from Flexible ZnO-Ag-Enriched Electrospun Cellulose Acetate Fiber Matrix. *Sci. Rep.* **2019**, *9* (1), 11765. https://doi.org/10.1038/s41598-019-48056-w.

(33) Inamuddin; Shakeel, N.; Imran Ahamed, M.; Kanchi, S.; Abbas Kashmery, H. Green Synthesis of ZnO Nanoparticles Decorated on Polyindole Functionalized-MCNTs and Used as Anode Material for Enzymatic Biofuel Cell Applications. *Sci. Rep.* **2020**, *10* (1), 5052. https://doi.org/10.1038/s41598-020-61831-4.

(34) Pramanik, S.; Mondal, S.; Mandal, A. C.; Mukherjee, S.; Das, S.; Ghosh, T.; Nath, R.; Ghosh, M.; Kuiri, P. K. Role of Oxygen Vacancies on the Green Photoluminescence of Microwave-Assisted Grown ZnO Nanorods. *J. Alloys Compd.* **2020**, *849*, 156684. https://doi.org/10.1016/j.jallcom.2020.156684.

(35) Zhang, X.; Shi, H.; Liu, E.; Hu, X.; Zhang, K.; Fan, J. Preparation of Polycrystalline ZnO Nanoparticles Loaded onto Graphene Oxide and Their Antibacterial Properties. *Mater. Today Commun.* **2021**, *28*, 102531. https://doi.org/10.1016/j.mtcomm.2021.102531.

(36) Mohanty, N. R.; Wei, I. W. Oxidation of 2,4-Dinitrotoluene Using Fenton's Reagent: Reaction Mechanisms and Their Practical Applications. *Hazard. Waste Hazard. Mater.* **1993**, *10* (2), 171–183. https://doi.org/10.1089/hwm.1993.10.171.

(37) Dutta, K.; Mukhopadhyay, S.; Bhattacharjee, S.; Chaudhuri, B. Chemical Oxidation of Methylene Blue Using a Fenton-like Reaction. *J. Hazard. Mater.* **2001**, *84* (1), 57–71. https://doi.org/10.1016/S0304-3894(01)00202-3.

(38) Salem, I. A.; El-Maazawi, M. S. Kinetics and Mechanism of Color Removal of Methylene Blue with Hydrogen Peroxide Catalyzed by Some Supported Alumina Surfaces. *Chemosphere* **2000**, *41* (8), 1173–1180. https://doi.org/10.1016/S0045-6535(00)00009-6.

(39) Huang, W.; Brigante, M.; Wu, F.; Hanna, K.; Mailhot, G. Development of a New Homogenous Photo-Fenton Process Using Fe(III)-EDDS Complexes. *J. Photochem. Photobiol. Chem.* **2012**, *239*, 17–23. https://doi.org/10.1016/j.jphotochem.2012.04.018.

(40) Wang, Q.; Tian, S.; Ning, P. Ferrocene-Catalyzed Heterogeneous Fenton-like Degradation of Methylene Blue: Influence of Initial Solution PH. *Ind. Eng. Chem. Res.* **2014**, *53* (15), 6334–6340. https://doi.org/10.1021/ie500115j.

(41) Hu, Y.; Li, Y.; He, J.; Liu, T.; Zhang, K.; Huang, X.; Kong, L.; Liu, J. EDTA-Fe(III) Fenton-like Oxidation for the Degradation of Malachite Green. *J. Environ. Manage.* **2018**, *226*, 256–263. https://doi.org/10.1016/j.jenvman.2018.08.029.

(42) Tran, T. T. T.; Kannoorpatti, K.; Padovan, A.; Thennadil, S. Effect of PH Regulation by Sulfate-Reducing Bacteria on Corrosion Behaviour of Duplex Stainless Steel 2205 in Acidic Artificial Seawater. *R. Soc. Open Sci.* **2021**, *8* (1), 200639. https://doi.org/10.1098/rsos.200639.

(43) Ahile, U. J.; Wuana, R. A.; Itodo, A. U.; Sha'Ato, R.; Dantas, R. F. A Review on the Use of Chelating Agents as an Alternative to Promote Photo-Fenton at Neutral PH: Current Trends, Knowledge Gap and Future Studies. *Sci. Total Environ.* **2020**, *710*, 134872. https://doi.org/10.1016/j.scitotenv.2019.134872.

(44) Vega-Poot, A. G.; Macías-Montero, M.; Idígoras, J.; Borrás, A.; Barranco, A.; Gonzalez-Elipe, A. R.; Lizama-Tzec, F. I.; Oskam, G.; Anta, J. A. Mechanisms of Electron Transport and Recombination in ZnO Nanostructures for Dye-Sensitized Solar Cells. *ChemPhysChem* **2014**, *15* (6), 1088–1097. https://doi.org/10.1002/cphc.201301068.

(45) Abebe, B.; Zereffa, E. A.; Tadesse, A.; Murthy, H. C. A. A Review on Enhancing the Antibacterial Activity of ZnO: Mechanisms and Microscopic Investigation. *Nanoscale Res. Lett.* **2020**, *15* (1), 190. https://doi.org/10.1186/s11671-020-03418-6.

(46) Xi, G.; Ouyang, S.; Ye, J. General Synthesis of Hybrid TiO2 Mesoporous "French Fries" Toward Improved Photocatalytic Conversion of CO2 into Hydrocarbon Fuel: A Case of TiO2/ZnO. *Chem. - Eur. J.* **2011**, *17* (33), 9057–9061. https://doi.org/10.1002/chem.201100580.

(47) Wu, A.; Jing, L.; Wang, J.; Qu, Y.; Xie, Y.; Jiang, B.; Tian, C.; Fu, H. ZnO-Dotted Porous ZnS Cluster Microspheres for High Efficient, Pt-Free Photocatalytic Hydrogen Evolution. *Sci. Rep.* **2015**, *5* (1), 8858. https://doi.org/10.1038/srep08858.

(48) Ding, C.; Chen, L.; Ni, Z.; Chen, Z.; Li, J.; Chen, L.; Su, F.; Huang, Y. Fluorescent Nanoscale Covalent Organic Frameworks with the Theoretically Matched Redox Potential of Fe $^{3+}$ /Fe $^{2+}$ for Monitoring of Adenosine-5′-Triphosphate in Cells. *ACS Appl. Nano Mater.* **2021**, *4* (12), 13132–13139. https://doi.org/10.1021/acsanm.1c02681.

(49) He, W.; Kim, H.-K.; Wamer, W. G.; Melka, D.; Callahan, J. H.; Yin, J.-J. Photogenerated Charge Carriers and Reactive Oxygen Species in ZnO/Au Hybrid Nanostructures with Enhanced Photocatalytic and Antibacterial Activity. *J. Am. Chem. Soc.* **2014**, *136* (2), 750–757. https://doi.org/10.1021/ja410800y.

(50) Zeng, X.; Liu, Y.; Hu, X.; Zhang, X. Photoredox Catalysis over Semiconductors for Light-Driven Hydrogen Peroxide Production. *Green Chem.* **2021**, *23* (4), 1466–1494. https://doi.org/10.1039/D0GC04236F.

(51) Zhang, X.; Zhao, X.; Zhu, P.; Adler, Z.; Wu, Z.-Y.; Liu, Y.; Wang, H. Electrochemical Oxygen Reduction to Hydrogen Peroxide at Practical Rates in Strong Acidic Media. *Nat. Commun.* **2022**, *13* (1), 2880. https://doi.org/10.1038/s41467-022-30337-0.

(52) Li, J.; Jiang, M.; Zhou, H.; Jin, P.; Cheung, K. M. C.; Chu, P. K.; Yeung, K. W. K. Vanadium Dioxide Nanocoating Induces Tumor Cell Death through Mitochondrial Electron Transport Chain Interruption. *Glob. Chall.* **2019**, *3* (3), 1800058. https://doi.org/10.1002/gch2.201800058.

(53) Martin, H. D.; Ruck, C.; Schmidt, M.; Sell, S.; Beutner, S.; Mayer, B.; Walsh, R. Chemistry of Carotenoid Oxidation and Free Radical Reactions. *Pure Appl. Chem.* **1999**, *71* (12), 2253–2262. https://doi.org/10.1351/pac199971122253.

(54) Wang, Q.; Tian, S.; Ning, P. Degradation Mechanism of Methylene Blue in a Heterogeneous Fenton-like Reaction Catalyzed by Ferrocene. *Ind. Eng. Chem. Res.* **2014**, *53* (2), 643–649. https://doi.org/10.1021/ie403402q.

(55) Yang, S.; He, H.; Wu, D.; Chen, D.; Liang, X.; Qin, Z.; Fan, M.; Zhu, J.; Yuan, P. Decolorization of Methylene Blue by Heterogeneous Fenton Reaction Using Fe3−xTixO4 (0≤x≤0.78) at Neutral PH Values. *Appl. Catal. B Environ.* **2009**, *89* (3–4), 527–535. https://doi.org/10.1016/j.apcatb.2009.01.012.

(56) Shi, H.; Li, W.; Zhong, L.; Xu, C. Methylene Blue Adsorption from Aqueous Solution by Magnetic Cellulose/Graphene Oxide Composite: Equilibrium, Kinetics, and Thermodynamics. *Ind. Eng. Chem. Res.* **2014**, *53* (3), 1108–1118. https://doi.org/10.1021/ie4027154.

(57) Baruah, S.; Mahmood, M. A.; Myint, M. T. Z.; Bora, T.; Dutta, J. Enhanced Visible Light Photocatalysis through Fast Crystallization of Zinc Oxide Nanorods. *Beilstein J. Nanotechnol.* **2010**, *1*, 14–20. https://doi.org/10.3762/bjnano.1.3.

(58) Navidpour, A. H.; Kalantari, Y.; Salehi, M.; Salimijazi, H. R.; Amirnasr, M.; Rismanchian, M.; Azarpour Siahkali, M. Plasma-Sprayed Photocatalytic Zinc Oxide Coatings. *J. Therm. Spray Technol.* **2017**, *26* (4), 717–727. https://doi.org/10.1007/s11666-017-0541-x.

Supporting Information

Design of a New ZnO Photocatalytic Fenton-Like Process for Enhancing the Removal of Organic Pollutants at Neutral pH

Elie A. Daher[‡][†]*, Abbas Al Redda*[‡]*, Christel Laberty Robert*[†][⁑]*, Wael Hamd* [₱][*]

[‡] Petrochemical Engineering Department, Faculty of Engineering III, CRSI, Lebanese University, Rafic Hariri Campus, Hadat, Lebanon.

[†] Laboratoire Chimie de la Matière Condensée de Paris LCMCP, Sorbonne Université, UPMC Paris 06, 4 Place Jussieu, 75005 Paris, France

[⁑] RS2E, Réseau Français sur le Stockage Electrochimique de l'Energie, CNRS 3459, 80039 Cedex 1 Amiens, France

[₱] Chemical Engineering Department, Faculty of Engineering, University of Balamand, P.O. Box 33, El-Koura, Lebanon.

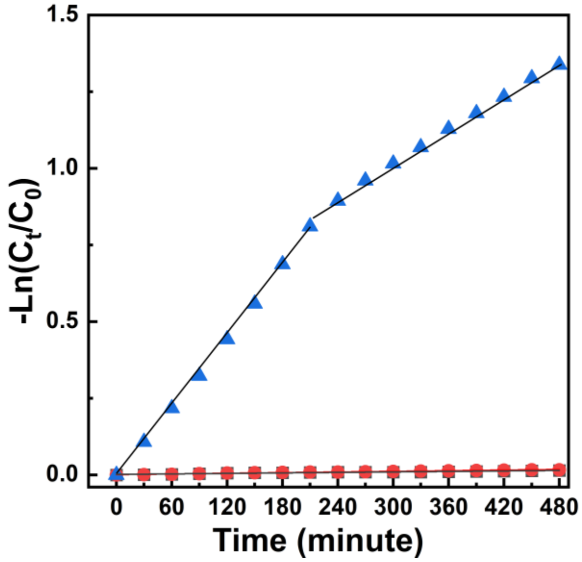

Figure S1. Effect of light on the Fenton process (10 ppm [MB], 5 ppm [Fe^{3+}], [H_2O_2]:[MB] = 52). Blue: Photo-Fenton + MB under UVA, red: MB (blank), and black: Fenton + MB in the dark. T = 25 °C.

Table S1. Effect of H_2O_2 concentration: Photo-Fenton-like degradation of 10 ppm [MB] at pH ~ 7.5, T = 25 ºC, and under 365 nm irradiation.

[H_2O_2] (ppm)	[Fe^{3+}] (ppm)	R(molar) = [H_2O_2]: [Fe^{3+}]	*Kapp* (min^{-1})	MB removal (%) in 480 minutes
0.00008	1	1	0.00012	6
0.0084	1	100	0.0003	13
0.059	1	700	0.002	60
0.59	1	7000	0.0037	84
1.26	1	15000	0.0065 – 0.0071	96
1.68	1	20000	0.0078 – 0.013	99
3.36	1	40000	0.009 – 0.02	100

Table S2. Effect of iron (III) load: Photo-Fenton-like degradation of 10 ppm [MB] at pH ~ 7.5, T = 25 ºC, and under 365 nm irradiation.

[H_2O_2] (ppm)	[Fe^{3+}] (ppm)	R(molar) = [H_2O_2]: [Fe^{3+}]	*Kapp* (min^{-1})	MB removal (%) in 90 minutes	Sludge formation
0.059	1	700	0.002	7.3	no
0.059	3	220	0.00245	22	no
0.059	5	130	0.0032 → 0.0019	27	yes
0.059	10	66	0.012 → 0.0025	67	yes
0.059	11	60	0.015 → 0.003	80	yes
0.059	12	55	0.024 → 0.0038	87	yes
0.059	13	50	0.027 → 0.0046	90	yes
0.059	14	47	0.03 → 0.0055	92	yes
0.059	15	44	0.032 → 0.006	94	yes

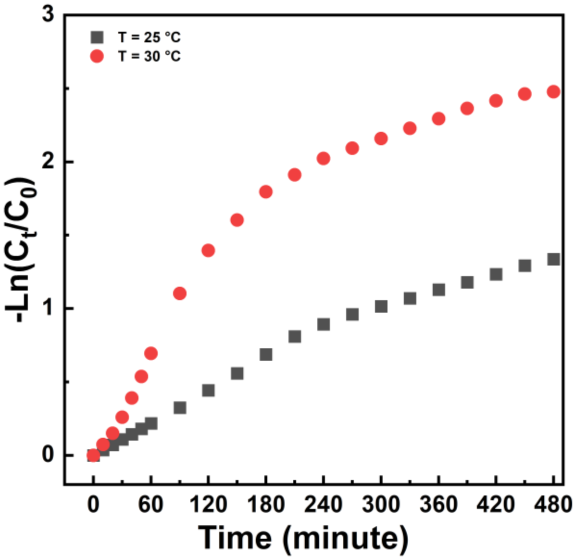

Figure S2. Degradation rate of 10 ppm [MB] using photo-Fenton-like at T = 25 ºC, and 30 ºC. UVA light of λ = 365 nm, $[H_2O_2]$:[MB] = 52, and $[Fe^{3+}]$ = 5 ppm were used.

Chapitre V

Conception de Nouvelles Couches Minces de ZnO Macroporeuses avec des Propriétés d'Auto-Nettoyage Améliorées

Ce chapitre est consacré à la conception de nouvelle structure de ZnO macroporeuse pour des applications d'auto-nettoyage. Contrairement à la photocatalyse aqueuse classique, ce système profit des molécules de H_2O et O_2 absorbées de l'atmosphère environnante pour produire des espèces réactives de l'oxygène (ROS) telles que le radical hydroxyle ($OH^{\bullet}$) et le radical superoxyde ($O_2^{\bullet-}$)[1]. Les revêtements de ZnO macroporeux ont été synthétisés par une approche de chimie douce, combinant l'auto-assemblage de polymères avec un procédé de trempage retrait d'une solution sol-gel. Ainsi, nous présentons une approche basée sur l'auto-assemblage de polymère, suivi d'un traitement « thermique flash » pour synthétiser des macro-pores. L'approche développée est universelle puisqu'elle permet l'utilisation d'une myriade de polymères disponibles commercialement, allant des homo polymères comme le polystyrène aux copolymères di- et triblocs tels que le poly(butadiène)-*b*-poly(oxyde d'éthylène) et le Pluronic F-127, respectivement. De plus, les températures peu élevées de mises en œuvre, permet de l'utiliser sur une variété de supports, présentant des tenues mécaniques différentes : le kapton, les plaquettes de silicium, le verre… Le mécanisme de formation des macropores dans les films inorganique/organique a été étudié en fonction des caractéristiques physico-chimiques de la solution sol-gel, des paramètres de dépôt par trempage (humidité) et du traitement thermique (vitesse de chauffe et palier). En contrôlant le traitement thermique et l'humidité relative, nous avons pu obtenir des films poreux à porosité hiérarchique dont la taille des pores varie de 50 nm à 56 µm. Des mesures optiques montrent que les films sont transparents. Les performances d'auto-nettoyage ont été étudiées par ellipsométrie in situ en utilisant l'acide laurique en tant que modèle de polluant gras. Nos résultats ont montré une dégradation de 100 % en seulement 20 minutes. Selon les analyses SEM-EDX, XRD et électrochimiques, le film macroporeux (via le F-127) présente la meilleure photo-activité en raison de sa surface plus élevée, de sa nanostructure polycristalline et de sa capacité de chimisorption élevée. Cette étude montre une nouvelle approche pour concevoir des films minces macroporeux avec des propriétés d'auto-nettoyage performantes.

Références

(1) Miklos, D. B.; Remy, C.; Jekel, M.; Linden, K. G.; Drewes, J. E.; Hübner, U. Evaluation of Advanced Oxidation Processes for Water and Wastewater Treatment – A Critical Review. *Water Research* **2018**, *139*, 118–131. https://doi.org/10.1016/j.watres.2018.03.042.

Advanced Approach to Self-Cleaning Surfaces: Designing Macroporous ZnO Coatings with Enhanced Photocatalytic Properties

*Elie A. Daher[‡†], Cédric Boissière[†], Christel Laberty Robert[†⁑], Wael Hamd [₱]**

[‡] Petrochemical Engineering Department, Faculty of Engineering III, CRSI, Lebanese University, Rafic Hariri Campus, Hadat, Lebanon.

[†] Laboratoire Chimie de la Matière Condensée de Paris LCMCP, Sorbonne Université, UPMC Paris 06, 4 Place Jussieu, 75005 Paris, France

[⁑] RS2E, Réseau Français sur le Stockage Electrochimique de l'Energie, CNRS 3459, 80039 Cedex 1 Amiens, France

[₱] Chemical Engineering Department, Faculty of Engineering, University of Balamand, P.O. Box 33, El-Koura, Lebanon.

KEYWORDS: Sol-gel dip coating, polymers, macroporous ZnO thin films, self-cleaning, photocatalysis, ellipsometry.

ABSTRACT: Self-cleaning coatings attract a lot of attention because of their potential applications in solar panels and construction materials. The development of novel macroporous ZnO coatings is reported with remarkable self-cleaning properties. The macroporosity is obtained by a flash heating of the hybrid ZnO-polymer film promoting the nucleation of ZnO nanoparticles and the formation of nano- and microbubbles that plays the role of templates. This synthesis method enables the usage of a

myriad of commercially available polymers, ranging from homopolystyrene to di- and triblock copolymers such as poly(butadiene)-poly(ethylene oxide), and Pluronic F-127. The influence of sol-gel components and dip coating parameters on the formation of macropores in the inorganic/organic films was investigated. By controlling the heat treatment, we obtain hierarchical macroporous films with pore diameters of ca. 150 nm – 800 nm. Such macroporous ZnO films show 100 % degradation of solid lauric acid in solely 20 minutes. With the transparent aspect of the ZnO coatings and the versatile choice of coated surfaces such as Kapton, silicon wafers, and glass, our technique offers an elegant and energy-efficient bottom-up strategy toward the design of macroporous thin films with self-cleaning properties.

1. Introduction

Growing interest in the development of smart surfaces has resulted in a plethora of nanocoatings available with unique designs, and functionalities[1–5]. In response to this trend, photoactive self-cleaning materials are increasingly used in modern industries[6–11]. Having initially been applied to self-cleaning glass, they have now spread to a wide range of self-cleaning materials, including tiles, wallpaper, paint, blinds, concrete, and asphalt[6,8,9]. These materials are designed to use photocatalytic processes to break down organic compounds and pollutants on their surfaces when exposed to light. This unique property results from the transformation of light energy into electron-hole pairs in the material's conduction and valence bands, respectively[12]. Highly reactive oxygen species (ROS) with a strong capacity to oxidize organic matter are then formed, ultimately leading to its decomposition into harmless molecules such as H_2O and CO_2[13].

In this context, macroporous photoactive coatings seem very interesting. Because of their large specific surface area, the film's sensitivity to capillary stresses decreases, and better interaction with the organic molecules in the atmosphere becomes possible (at the surface of the coating and more specifically in the pores)[14–17]. Among the various photocatalysts, ZnO is a promising candidate because of its ability to absorb UV light radiation (Eg = 3.37 at room temperature), its low synthesis cost, and its low level of environmental toxicity[18–20].

Macroporous ZnO thin films are manufactured using bottom-up synthesis techniques generally involving colloidal crystal templating (CCT) and breath figures or top-down approaches such as chemical etching, nanoimprint lithography, and laser ablation, that require special equipment, operating conditions, in addition to stringent post-processing protocols[21–32]. For example, while hard CCT often relies on highly corrosive chemicals to remove the template, soft CCT can be equally challenging due to the need for a time-consuming multi-step synthesis of the templates[17]. Additionally, the template removal must be highly controlled to avoid crack formation and collapsing of the porous network[22,33]. On the other hand, techniques such as nanoimprint lithography, and laser ablation can potentially affect the film properties due to the generated heat and mechanical stress[30,34,35].

On the other hand, the usage of polymers, e.g. block copolymers (BCPs), to create micellar templates has received significant attention as this approach allows the synthesis of porous materials such as TiO_2, ZrO_2, Al_2O_3, WO_3, and SnO_2 with pore diameters between 10 and 60 nm[36–38]. Nevertheless, despite the various established techniques, namely solvent evaporation-induced self-assembly (EISA), nanoprecipitation, interfacial self-assembly, and emulsion-induced self-assembly it is still difficult to be applied for the synthesis of highly ordered macroporous ZnO thin films with controlled porosity[39].

Herein, we report the fabrication of macroporous ZnO coatings by flash thermal treatment inducing the rapid decomposition of the polymers in the organic-inorganic films previously deposited by dipping a substrate in a sol. The formation of submicronic to micronic bubbles is possibly at the origin of the porosity observed. Different polymers, including homo, diblock, and triblock copolymers are used as sacrificial templates to induce hierarchical porosity ranging from 400 nm to 56 µm with good reproducibility. Our approach is versatile as various substrates, including Kapton, silicon wafers, and glass, can be used. The formation mechanism of these macroporous films has been studied as a function of several parameters, including the nature of the polymer, the heat treatment, and the heating rate. To our knowledge, no study has yet reported the manufacture of hierarchical macroporous coatings based on this approach. Due to the transparency of all macroporous ZnO films, their photocatalytic self-cleaning performance was investigated using the lauric acid probe molecule and in situ ellipsometry.

2. Results and Discussions

First, we studied the thermal behavior of the mesostructured ZnO films with polybutadiene-*b*-polyethyelene oxide, through Thermal Ellipsometry (TE) analyses (Figure 1a). TE analyses were performed on stabilized hybrid organic-inorganic films at 50 ºC in the wavelength range of 400-900 nm. The ellipsometric data, tan (ψ) and cos(Δ) were fitted at $\lambda = 632$ nm with a Cauchy model and the thickness (h), and the real (n) and imaginary (k) parts of the complex refractive index of the films were evaluated. The variation of the film thickness and the real (n) imaginary part are reported in Figure 1a. The ellipsometry data reveal that the film undergoes rapid shrinkage, from 250 nm to 140 nm, between 50 to 150 ºC, mainly due to the evaporation of the residual solvents such as ethanol and the decomposition of the acetate group, and MEA. This was confirmed by the ATR-FTIR spectra in Figure S1a, where the assigned bands to the acetate anion twisting mode (620 cm^{-1}), acetate anion scissoring (689 cm^{-1}), C–C skeletal vibration mode (846 cm^{-1}), C–CH_3 framework (1056 cm^{-1}), O-H stretching of intramolecular H-bond (3228 cm^{-1}), PB and PEO groups (1112 cm^{-1}, 1342 cm^{-1}, 1397 cm^{-1}, and 1554 cm^{-1}) disappear at 150 ºC[40–43]. The decomposition of the organic compounds is concurrent with the emergence of 540 and 750 cm^{-1} peaks, representing the stretching vibrations of Zn–O bonds (starting at 150 ºC)[44–47]. Additionally, the refractive index exhibits a gradual variation before an abrupt increase to 1.58, between 120 and 150 °C, linked to the film's densification. Then, the refractive index continues to increase up to 250 °C, reaching a value of 1.58. This step may correspond to the crystallization of ZnO and the decomposition of the PEO block to CO and CO$_2$ gases[12,48]. Prior XRD investigations of ZnO films have shown the presence of ZnO peaks on X-rays patterns for 200 °C calcined films (Figure 1b). While the thickness is stabilized at 73 nm after heating at a temperature superior to 250 °C, the refractive index decreases from 1.58 to 1.38 at 500 °C, probably due to the decomposition of PS and the formation of porosity in the films. This is confirmed by post-mortem SEM images (Figure S1b).

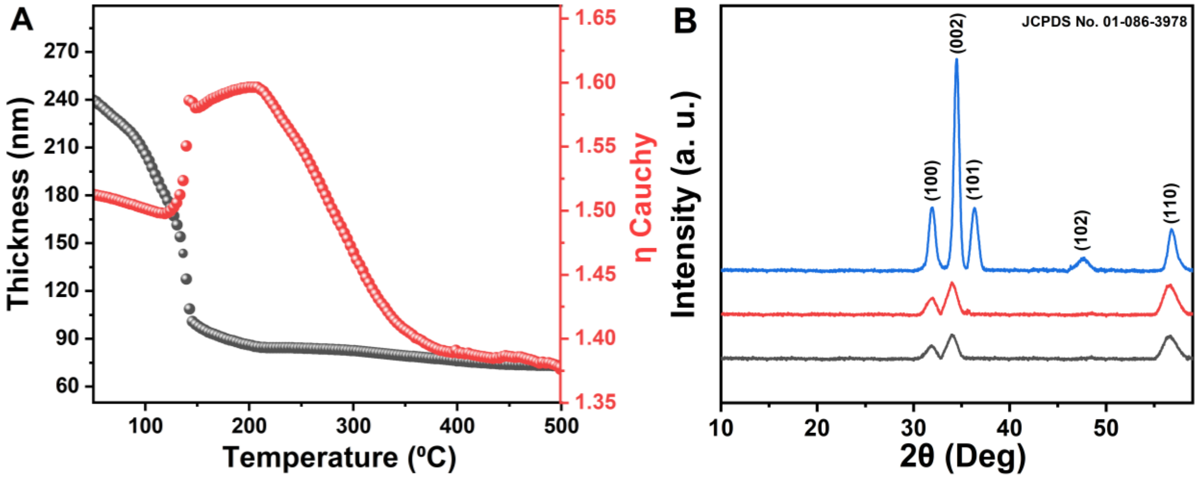

Figure 1. (a) Variation of the thickness h (black) and the refractive index n (rede) as a function of the temperature (heating rate: 10 °C min^{-1}) for synthesized ZnO mesoporous thin films with polybutadiene-*b*-polyethyelene oxide, and stabilized at 50 °C, **(b)** XRD pattern of the flashed mesoporous ZnO film at 200 °C (dark grey), 250 °C (red), and 350 °C (blue).

We then analyzed the evolution of the microstructure of ZnO films during its calcination by FEG-SEM. Figure 2 shows that the flash calcination of the inorganic/organic film under atmospheric conditions yields different morphological structures depending on the temperature. A dense film was obtained at 100 °C (Figure 2a), while ZnO films with intriguing microstructures with features ranging from 100 – 800 nm were obtained at T = 150 °C (Figure 2b). As the temperature increased up to 250 °C, these microstructures evolve into hollow spherical-like shapes, keeping the same size range of ca. 100-800 nm, with the ZnO grains mostly disappearing at the pores' bottom (Figure 2c). Elemental mapping in Figure 2d – o and Table S1 reveals the disappearance of the amine species at an annealing temperature of 100 ºC, as demonstrated by the lack of the azote signal. As the temperature increases from 100 ºC to 250 ºC, the percentage of carbon atoms decreases from 21 % to 14 % due to solvent evaporation, polymer decomposition, and the progressive release of zinc ligands (amine and acetates) triggered by ZnO crystallization (in agreement with thermoellispometry and XRD analyses). Consequently, a stoichiometric ratio of Zn:O close to 1:1 is attained[49].

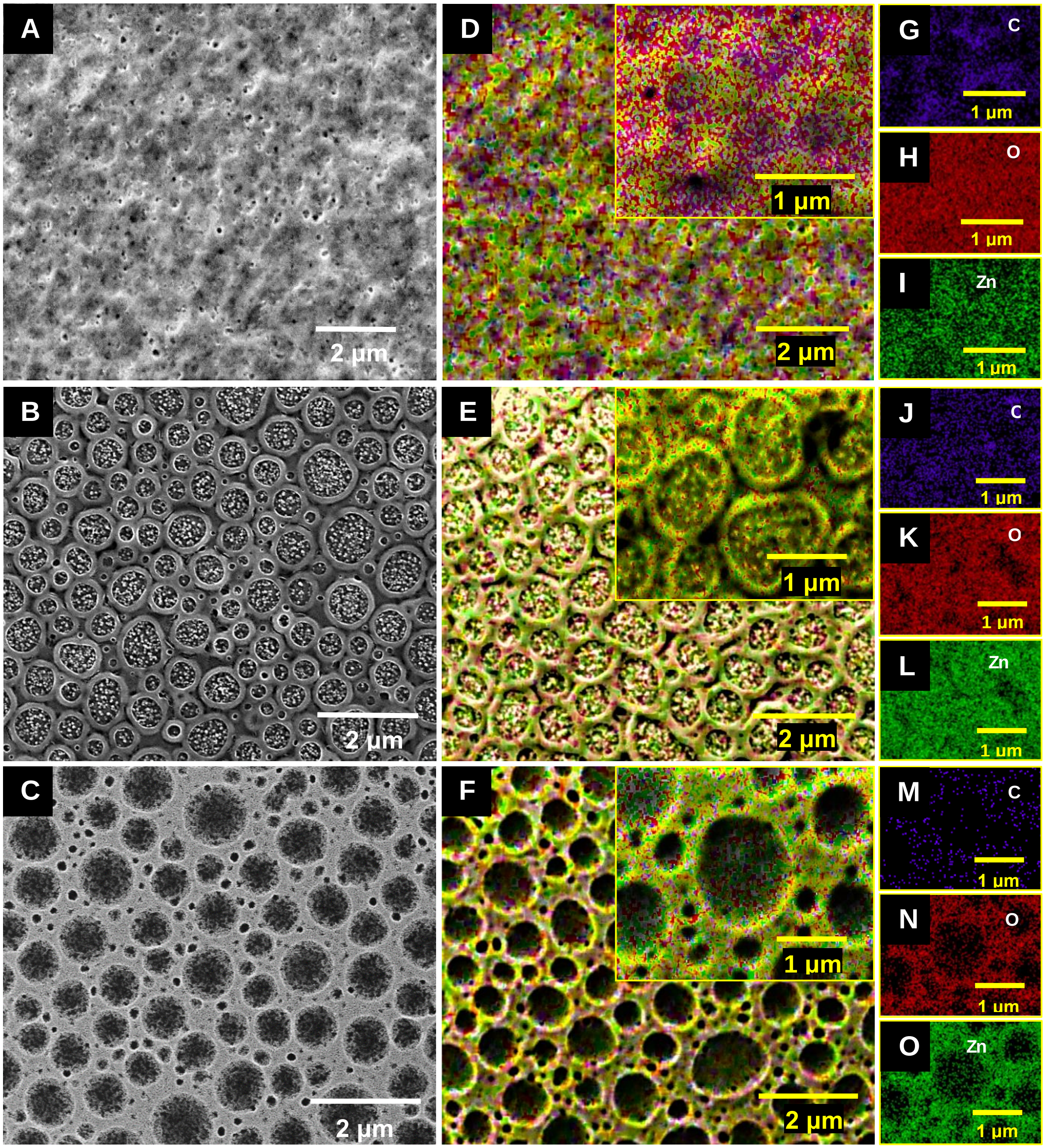

Figure 2. Evolution of the microstructure of ZnO film as a function of the heat treatment. SEM-FEG micrographs of the PB-*b*-PEO/ZnO films flash heated at **(a)** 100 ºC, **(b)** 150 ºC, and **(c)** 250 ºC, **(d-o)** Elemental mapping (SEM-EDX) showing the distribution of C (Blue), O (red), and Zn (green).

Surprisingly, the pore size in these films is hierarchical and varies between 500 nm and 2 microns. These sizes do not correspond to the size of the micelles formed in the sol measured by DLS (see Figure

S2). At this stage, we suspect that the microstructure observed is linked to the flash treatment of our film that induces the formation of “bubbles”, and then creates this macroporous network. To confirm this hypothesis, we have further explored the impact of the heating rate on the microstructure of the ZnO films (Figure 3). A heating rate of 2.25 ºC/s results in the formation of porous films with pores below 50 nm, consistent with the size of the existing micelles in the sol solution. Because ZnO grains have a mean size of 20 – 40 nm, the porosity shape is deformed due to crystal growth and sintering. Furthermore, pre-heating the inorganic/organic film first at a low temperature of 100 ºC and then post-heating it at 500 ºC results in the formation of a cracked surface, (Figure S3). This observation highlights the necessity of the instantaneous heating/quenching process to stimulate the formation of macropores within the ZnO films.

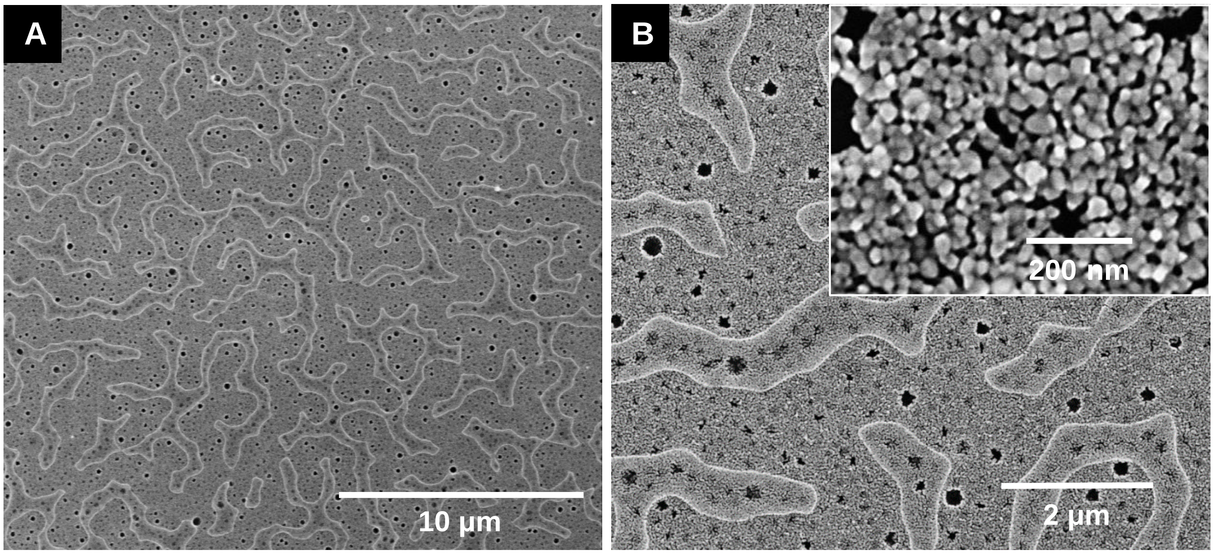

Figure 3. Impact of the heating rate onto the ZnO microstructure. (a) SEM-FEG micrographs of a PB-*b*-PEO/ZnO film heated from RT to 450 ºC, with a ramp of 2.25 ºC/s, **(b)** Zoomed-in view of “A”.

This set of data shows that fast heating enables the formation of macro-pores[50]. This is probably linked to the decomposition of micelles/solvent inside the coating that liberate instantaneously CO and CO_2 and then form pores. As these gases accumulate within a confined space and escape from the coating simultaneously with the consolidation of the ZnO network, they could leave behind a physical impression on the surface. Consequently, vesicle-like imprint structures are observed and become more pronounced as the temperature of the flash treatment increases from 150 to 550 ºC (as previously seen in Figure 2). For instance, our group has previously reported this behavior on MgF_2 thin films made by sol-gel dip coating where a thermally induced porosity has been achieved[50]. Interestingly, when the molecular weight of the PB-*b*-PEO is significantly reduced within the sol (0.25 M Zn^{2+}, Zn^{2+}:MEA = 1:0.5), a similar imprint is obtained on the film's surface (Figure S4). Finally, this macroporous ZnO coating could be achieved on diverse types of surfaces (Figure S5), different types of polymer templates (Figure 4), and under different operating conditions. Changing the substrates to flexible Kapton layers or borosilicate glass does not alternate the porous morphology of the coatings (Figure S5a and b).

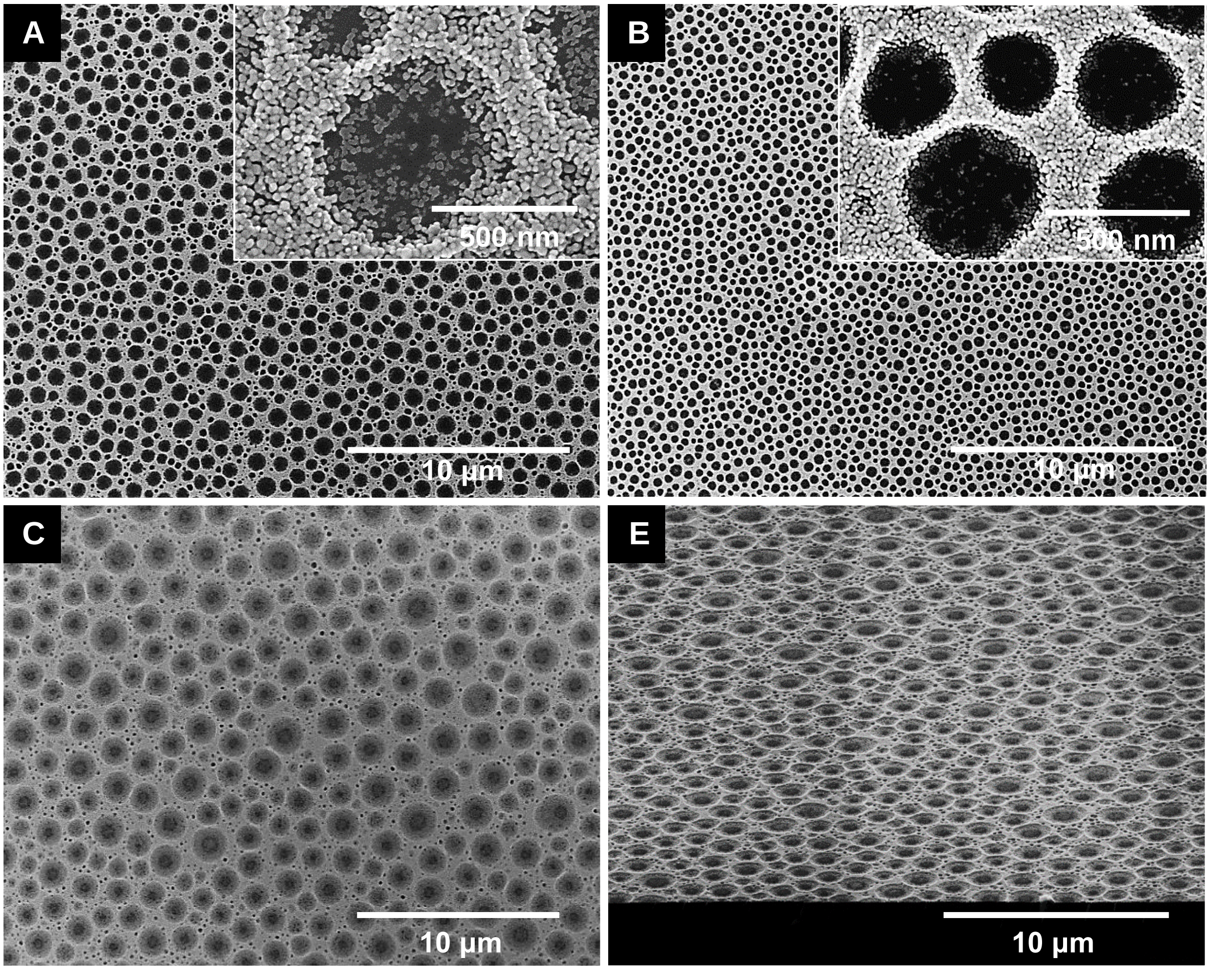

Figure 4. Impact of the nature of the Polymer on the microstructure of ZnO films. SEM-FEG micrographs of Coated films on a silicon wafer, made out of **(a)** PB-*b*-PEO/ZnO sol, **(b)** Polystyrene/ZnO sol, and **(c)**, F-127/ZnO sol. (**d**) Tilted view (at 20 º) of "c". All films are flashed in the air at 450 ºC for 30 minutes.

We have subsequently explored the potential of utilizing cost-effective triblock terpolymers, such as the Pluronics (PEO-PPO-PEO), to produce ZnO films with the goal of modifying the pore's diameter. Macroporous ZnO films were fabricated using a synthesis protocol identical to the previous section, except that the PB-*b*-PEO and PS polymers were replaced with the Pluronic F-127 triBCPs. Interestingly, the films display a consistent distribution of two families of macropores, ca. 1.6 µm, and ca. 120 nm, respectively (Figure 5).

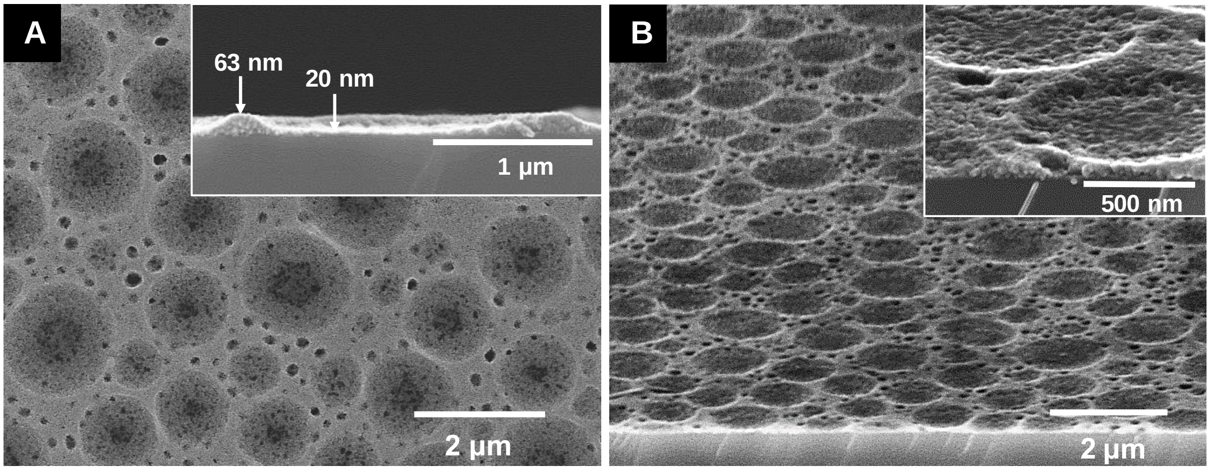

Figure 5. (a) SEM-FEG micrographs of a coated film on silicon wafers made out of F-127/ZnO sol gel (Zn^{2+}:F-127 = 1:0.002). Inset: Cross-section view, **(b)** Tilted view (at 20⁰) of "a". Inset: Zoomed-in views.

More importantly, the insets of Figure 5a and a show that a ~ 22 nm thick bottom and ~ 63 nm walls characterize the wider pores, occupying the largest surface. In contrast to the PB-*b*-PEO/macroporous films that exhibited low ZnO density at the bottoms of the pores, this new topology displays a better surface coverage of ZnO materials. Interestingly, the modification of the Zn^{2+}:F-127 ratio enables effective control of the porosity size (Figure S6). A fourfold increase in the ratio from 1:0.002 to 1:0.008 yields a significant increase in the diameter of the macropores from 1.2 µm to 56 µm, while a decrease of the same magnitude (1:0.002 to 1:0.0005) reduces pore diameters to 400 nm (along with a reduction in overall pore count). Unlike non-pluronic PB-*b*-PEO BCP, which exhibits self-assembly in solution, F-127 is known to undergo evaporation-induced self-assembly (EISA) during heat treatment of the inorganic/organic film, leaving then small mesopores[38]. Interestingly in our study, large surface imprints are obtained. This phenomenon could also be attributed to the release of microbubbles at the film surface during the thermal decomposition of F-127. In addition, an increase in the amount of polymer in the solution leads to more pronounced imprint formation on the film surface, resulting in macroporosity with larger pore sizes. From this perspective, augmenting the quantity of polymers in the confined geometry of the inorganic/organic film and subsequently subjecting it to a flash heat treatment, renders the system more thermodynamically unstable. In response to this instability, the film minimizes its Gibbs free energy by forming gaseous microbubbles in a larger volume. Finally, the macroporous films were characterized by high transmittance of light in the visible range (Figure S7a).

The self-cleaning properties of these coatings have been further studied. The photocatalytic properties of hierarchical macroporous-templated films (thickness of 65 nm) with PB-*b*-PEO (M.W.(PB) = 5500 g.mol^{-1}, M.W.(PEO) = 35000 g.mol^{-1}), and F-127, were investigated. The results were compared to a classic dense layer (Figure S8), made by dip coating with a comparable thickness to investigate the efficiency of these heterostructures. Lauric acid (LA) was selected as a probe molecule due to its physical-chemical properties, which facilitate its homogeneous infiltration and stabilization within porous films[13,51]. The photocatalytic activities of the films were assessed at 35 % humidity, by monitoring the evolution of their refractive index via in situ spectroscopic ellipsometry (Scheme 1)[13].

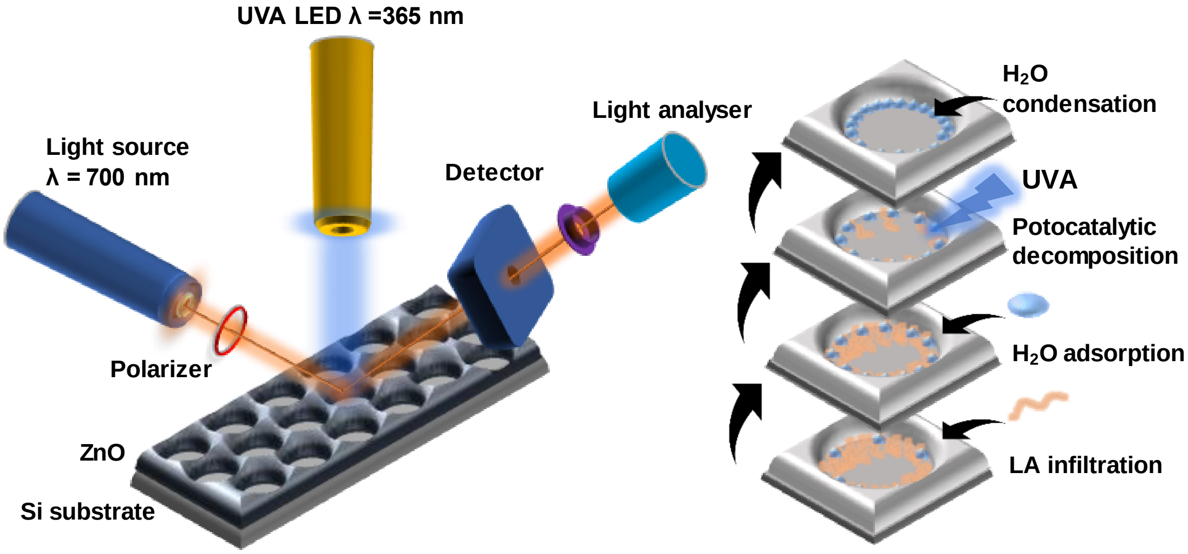

Scheme 1. Left: Scheme of the home-built photocatalytic setup that was used to study the evolution of the refractive index during UVA irradiation. **Right:** Proposed mechanism of the LA photocatalytic decomposition.

Figure 6a illustrates the percentage of volumetric reduction in LA content in each film type. In the dark, a negligible variation is detected (first 5 minutes). Upon the UVA irradiation, it could be seen that in the absence of ZnO coatings, the nude wafer-Si manifests negligible degradation, confirming that lauric acid is not decomposed by photolysis. However, in the presence of a ZnO-based self-cleaning material, significant photocatalytic decomposition of LA is recorded. In particular, films derived from F-127 achieve ~100 % photodegradation in less than 20 minutes, whereas for the dense material, 35 minutes are required. The times are even longer for films derived from PB-*b*-PEO since 60 minutes are necessary for 100 % photodegradation. This confirms the impact of the exposed surface to the contaminating species. Although PB-*b*-PEO templated films display eminent porosity, the pores' bottom is free of ZnO materials. On the contrary, this limitation was mitigated with the morphological aspect of the F-127 based films, as the bottom of the pores is fully covered with ZnO. As a consequence, this latter seems to expose higher surface areas than the other coatings, recording then the best photocatalytic performance.

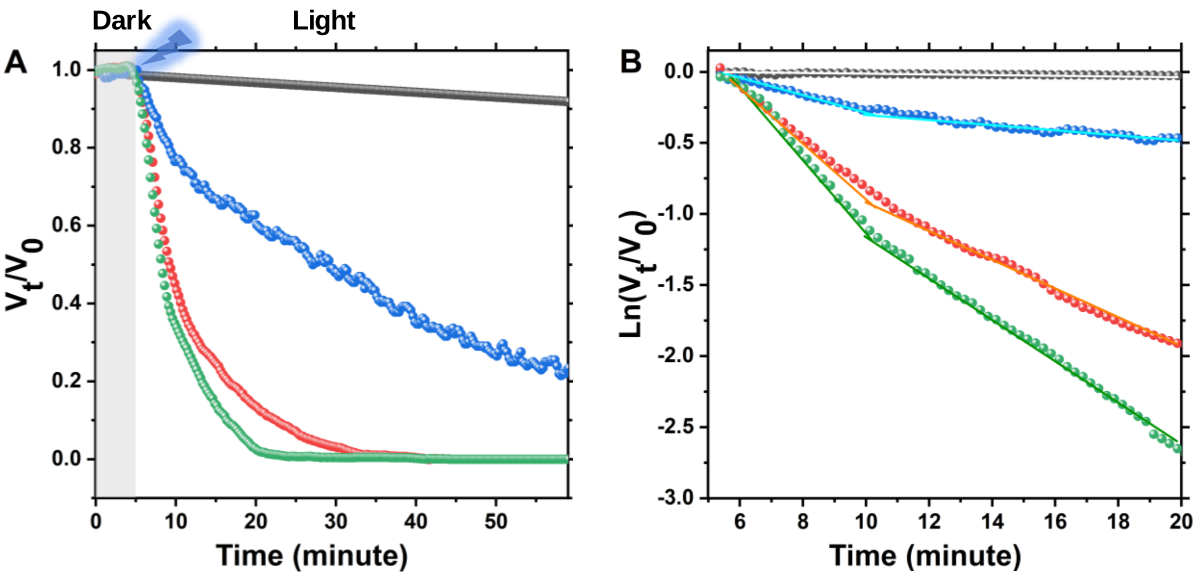

Figure 6. (a) Normalized volume of lauric acid (V_t) to its initial value (V_0), plotted versus time (t). After 5 minutes in the dark (grey area), the light was turned on, **(b)** Corresponding first-order kinetic plots ($\ln(V_t/V_0)$ vs t). The black, blue, red, and green dots represent the blank, PB-*b*-PEO templated film, dense film, and F-127 templated films, respectively.

The apparent constant rates (K_{app}) were estimated from the pseudo-first-order kinetic model (Equation 1) and are plotted for the first 15 minutes.

$$\ln\left(\frac{V_t}{V_0}\right) = K_{app}.t \tag{1}$$

As observed in Figure 6b, the ZnO films exhibit two distinct linear regimes. During the first 5 minutes of photocatalytic degradation, the reaction follows rapid kinetics in the order of F-127 macroporous films K_{app} (0.251 min^{-1}) > Dense K_{app} (0.182 min^{-1}) > PB-*b*-PEO macroporous films K_{app} (0.0529 min^{-1}). For the subsequent experimental time, this order remains the same, yet with a down-shifting to lower constant rates of 0.153 min^{-1}, 0.108 min^{-1}, and 0.021 min^{-1} (for the F-127 films, dense, and PB-*b*-PEO films respectively). Generally, the photocatalytic degradation of organic pollutants in aqueous mediums follows pseudo-first-order kinetics which are estimated from the Langmuir–Hinshelwood model (Equation 2)[12].

$$r = -\frac{dC}{dt} = \frac{Kr.K.C}{1+K.C} \tag{2}$$

where r, C, K, K_r, and t represent the reaction rate, molecule concentration at time t, adsorption equilibrium constant, limiting rate constant of reaction at maximum coverage, and reaction time respectively. In such systems, the adsorption kinetics, and diffusion coefficients of organic species are of great importance. Unlike aqueous photocatalysis, herein there are no pollutant diffusion and adsorption to be taken into account, as the lauric acid molecules are already adsorbed. This condition suggests that the kinetic rate is only governed by the pollutant quantity, and therefore Langmuir–Hinshelwood model is simplified to the apparent rate order in Equation 1. Such a situation implies that $\ln(V_t/V_0)$ vs t plot would yield a linear relationship. Nonetheless, the curves exhibit different slopes, indicating the existence of multiple rate constants. This situation is not solely attributable to the exhaustion of the LA, and other factors can therefore be taken into account. Previous reports demonstrated the role of humidity in photocatalytic kinetics[13,51]. Firstly, the adsorption of H_2O and O_2 on the ZnO surface produces highly reactive oxygen species (ROS) such as the hydroxyl radical ($OH^{\bullet}$) and the superoxide radical ($O_2^{\bullet-}$), which are known to be powerful oxidants of organic matter[13]. However, when the concentration of H_2O adsorbed on the surface of ZnO increases, hydroxyl scavengers are produced and hinder the photocatalytic activity of the material[51]. In our system, LA molecules occupy the catalytic sites at the beginning of photodegradation and then prevent water adsorption (Scheme 2 right). As the LA molecules decompose, water can be adsorbed on the various catalytic site via a condensation mechanism, thus favoring the presence of hydroxyl scavengers. When the water content on the surface of the ZnO film increases, competition between ROS and hydroxyl scavengers becomes more favorable to the latter, and photodegradation rates slow down.

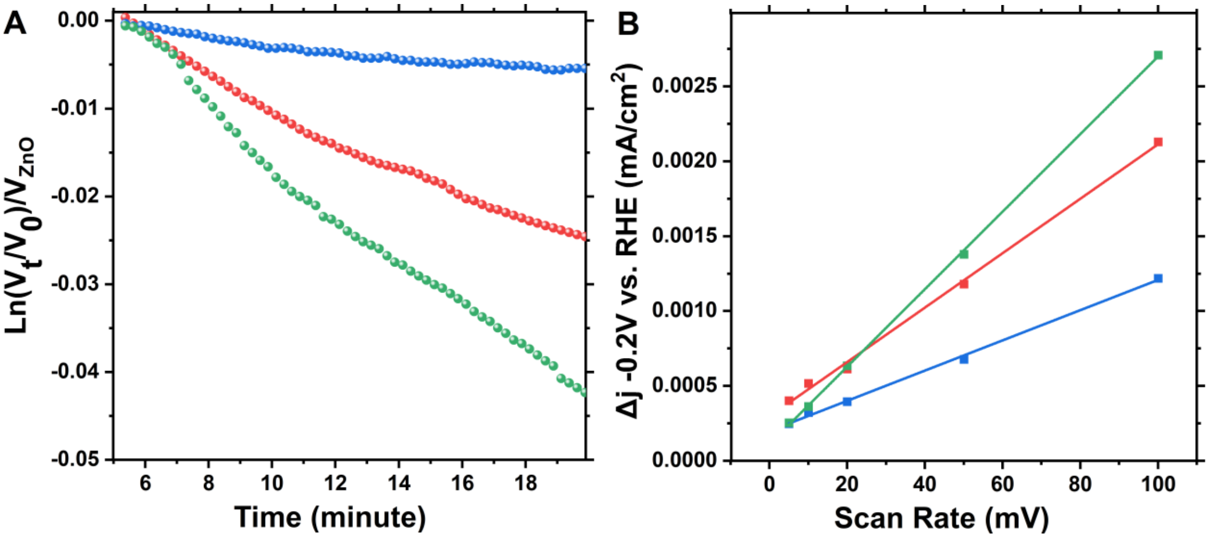

Figure 7. (a) Normalized first-order kinetic plots of ($\ln(V_t/V_0)$ vs t) to the ZnO volume in each film's microstructure. **(b)** Capacitive current plots as a function of the scan rate. The blue, red, and green dots represent the blank, PB-*b*-PEO template, dense, and F-127 templated films, respectively.

To compare the photocatalytic activity of the various ZnO microstructure, the $\ln(V_t/V_0)$ was normalized to the ZnO weight of the individual films (Figure 7a). The photocatalytic activity of Pluronic-derived films exhibits higher photocatalytic activity than that of dense (× 1.7) and PB-*b*-PEO template (× 8) films respectively.

As this photoactivity is mainly based on the transformation of the photonic energy into electron–hole pairs in the conduction and valence bands of ZnO, the material properties as well as its microstructure play a critical role. In particular, the competition between charge-carrier generation and recombination, and thus the overall quantum efficiency of charge transfer are closely dependent on the film's structure, nanostructure, and surface chemistry. X-ray diffraction (XRD) indicates that all the films are polycrystalline with the same structure (Figure S7b). This polycrystallinity is well-known to improve the photocatalytic activity of ZnO films[52–55]. The electrochemically active surface areas (ESCAs) were estimated by measuring the electric double-layer capacitance (C_{dl}) of each film. This capacitance was derived from the CV curves in the nonfaradic region. It is observed in Figure 7b that the ECSA of the

F-127 templated films is 2.5 times bigger than that of the PB-*b*-PEO template ones, and 1.5 times larger than the ESCA of dense ZnO films. This agrees well with the SEM-FEG analyses. Although PB-*b*-PEO derived films generally exhibit a macroporous structure, they are less continuous and homogeneous than the F-127 templated ones. In addition, the microstructure of the latter provides more catalytic sites compared to dense film, explaining then its better photocatalytic activity. As a result, it could be fairly concluded that due to the larger surface area of the F-127 templated films, and their polycrystalline nature, these coatings showed a much superior photocatalytic activity.

3. Conclusion and Outlook

Macroporous ZnO coatings have been synthesized via the flash treatment of hybrid organic-inorganic films deposited by coupling dip-coating and sol solution through the formation of nano- and micro-bubbles during the annealing. The mechanism of formation of these macroporous films was studied by SEM-FEG analysis. It appears to be universal as various types of polymeric chains, PS homopolymer, PB-*b*-PEO diblock, and PEO-PPO-PEO triblock copolymers, result in the formation of macroporous films. Interestingly, the periodic porosity varies between 150 nm to 56 μm, according to the synthesis conditions and more specifically to the polymer/salts ratio. Finally, the robustness of our method enables the deposition of such macroporous films on a versatile range of substrates, such as Kapton, silicon wafers, and glass, extending them their possible applications.

The self-healing properties of these transparent, ZnO macroporous films have been investigated by in-situ ellipsometry using lauric acid, as a model. Interestingly, these films demonstrate high self-cleaning potential towards organic contaminations, due to the semi-conducting character of ZnO enabling a photocatalytic degradation of the organic matter. In contrast to classic aqueous photocatalysis, the absorption of H_2O and O_2 molecules from the surrounding atmosphere in the ZnO macroporosity allows the production of highly reactive oxygen species (ROS) including hydroxyl radical ($OH^•$) and superoxide radical ($O_2^{\bullet -}$). Interestingly, the normalized kinetic data to the weight of zinc oxide shows faster kinetics for the Pluronic-templated film compared to a classic dense one. The former reached 100 % degradation in solely 20 minutes. Based on SEM-EDX, XRD, and electrochemical measurements, the Pluronic-templated film shows the best photoactivity due to its higher surface area, its polycrystalline nanostructure, and its high chemisorption ability.

4. Experimental Section

4.1 Reagents and materials

Zinc acetate dihydrate, ACS reagent grade ($Zn(CH_3COO)_2 \cdot 2H_2O > 98$ %), from Thermo Scientific. Polystyrene, P8610-St, (M.W. = 278000 $g.mol^{-1}$), poly(1, 4-butadiene)-*b*-poly(ethylene oxide), P3902-BdEO, (M.W.(PB) = 5500 $g.mol^{-1}$, M.W.(PEO) = 35000 $g.mol^{-1}$), and poly(1, 4-butadiene)-*b*-poly(ethylene oxide), P8678-BdEO, (M.W.(PB) = 2000 $g.mol^{-1}$, M.W.(PEO) = 2500 $g.mol^{-1}$) from Polymer Source. Pluronic F-127 poly(ethylene oxide)–poly(propylene oxide)–poly(ethylene oxide), $(C_3H_6O.C_2H_4O)_x$, and lauric acid analytical grade ($C_{12}H_{24}O_2 > 99.5$ %), from Sigma Aldrich. Monoethanolamine ACS reagent grade ($C_2H_7NO > 99$ %) from Honeywell Fluka. Ethanol and methanol absolute ACS reagent grade (99.97+%), from VWR Chemicals. All products were used as received without further purification. 6 inch-diameter p-type (100) Si wafer with a resistivity of 1–10 Ω.cm was purchased from Siltronix Silicon Technologies. Deionized water (DI) of ~ 18.2 MΩ.cm was obtained with a Milli-Q system.

4.2 Fabrication of Porous ZnO Thin Films

4.2.1 Sol-Gel Formulation

A sol of 0.5 M of Zn^{2+} was prepared by first dissolving zinc acetate dihydrate (ZAD) in absolute ethanol, then, gradually adding monoethanolamine (MEA) to the mixture with a molar ratio of Zn^{2+}: MEA = 1. By the dropwise introduction of the ligand to the solution, nucleophilic species such as MEA, and acetate counter ions (CH_3COO^-) effectively coordinate with the Zn^{2+} Lewis acid center to form stable complexes, therefore delaying the cation condensation. Additionally, the low-water concentration medium contributes to a relatively slow hydrolysis rate. To accelerate the slow hydrolysis/condensation rate of Zn^{2+} ions, the solution was stirred in a closed vessel for 1 hour at T= 65 ^oC; below the boiling-point temperature of ethanol (82.4 ^oC), and MEA (170 ^oC). Subsequently, the solution was aged at room temperature (RT) for 24 hours. The resulting sol mainly contained soluble complexes of Zn–CH_3COO and Zn–MEA, which are apt to form the ZnO skeleton during the dip coating process[12]. This sol will be referred to as the “precursor sol”. When stored at room temperature (RT), it can be used for over 3 months.

Homopolymer and Diblock Copolymer (DBCP) Templating Systems: 30 mg of polystyrene and poly(1, 4-butadiene)-*b*-poly(ethylene oxide), (PB-*b*-PEO), were separately dissolved in 2.367 g of absolute ethanol (equivalent to 3ml). Transparent solutions were obtained after stirring at 70 ^oC for 1h. Subsequently, the polymer solutions were cooled down at RT, and 3 ml of the zinc “precursor sol” was added dropwise. The concentration of inorganic salts in the final solution is 0.25 M (2.86 g of “precursor solution”). These mixtures were stirred for 30 minutes at 70 ^oC. The resulting polystyrene/zinc and PB-*b*-PEO/zinc systems are respectively referred to, as “Sol A” and “Sol B”.

Triblock Copolymer Templating System: Two different systems were herein employed. The first one consists of dissolving Pluronic F-127 (PEO-PPO-PEO) in ethanol and then stirring the mixture at 70 ^oC for 1h to complete the dissolution of the polymer. After cooling at RT, 3 ml of the zinc “precursor sol” was added dropwise into the cooled surfactant solution to give a final concentration of inorganic salt equal to 0.25 M (Sol C). Herein, Pulronic was added in 4.7, 9.5, 19, 38, 75, and 150 mg to give Zn^{2+}:F-127 ratios of 1:00025, 1:0.0005, 1:0.001, 1:0.002, 1:0.004, 1:0.008 respectively. In the second, a solution was made out of 0.73 g of F-127 dissolved in 45 g of ethanol and 10 g of DI water “D”.

4.2.2 *Dip Coating of the ZnO Thin Films*

Thin films were prepared by using a dip-coater unit (Acedip from SolGelWay Society), equipped with a humidity (RH) chamber, tunable from 0 to 80 % RH. Silicon wafers, Kapton, and borosilicate glass were utilized as different substrates to demonstrate the versatility of coated surfaces. All the substrates were successively cleaned with ethanol and acetone and then dipped in each sol for 10 seconds before being withdrawn at 9 mm.s^{-1}. This immersion time aims to minimize the generated vibrations by the contact between the substrate and the liquid surface. For Sol A, B, and C, the dip coating was performed at room temperature with humidity ranging between 20 to 35 %.

The thermal treatment regime is crucial to induce the hierarchical self-assembly of polymers, concomitantly with the formation of the 3D ZnO network. Thus the coated layers were flash calcined for 30 minutes at different temperatures between 100 and 550 ºC unless denoted differently in the text.

4.3 Characterization

4.3.1 *Scanning Electron Microscopy (SEM) Coupled with Energy Dispersive X-ray Spectroscopy*

The films' morphologies were evaluated by a field emission gun scanning electron microscope (FEG-SEM), model Hitachi SU-70 FESEM (Schottky type gun). Nanoscale was achieved at a voltage of 10 kV with a typical resolving power of 1 nm. The analysis of the elemental composition (EDX) was performed on a ZEISS Gemini SEM 360 equipped with an Oxford Instruments Ultim Max 170 mm^2 detector. SEM images and EDX mapping were obtained by an Inlens SE detector (in the column) at a 5 kV accelerating voltage. Oxford Instrument Aztec software was used for the acquisition of EDX maps.

4.3.2 *X-ray Diffraction (XRD)*

The crystalline phase of each coating was characterized with a D8 Discover X-ray diffractometer (Bruker), using a Cu emitter anode (Kα_1 and Kα_2 of wavelength 1.54056 and 1.5444 Å respectively) and a 1D LYNEXEYE XE-T detector. XRD measurements were performed on the coated substrates in grazing mode with an incidence angle fixed at 2º, and 0.05º steps.

4.3.3 Spectroscopic Ellipsometry

The thicknesses, porosities, and refractive indexes of the films were measured by using a UV-NIR (193 – 1690 nm) M-2000DI spectroscopic ellipsometer from J. A. Woolllam. The measurements were conducted on the Silicon wafer slides. Ellipsometric ψ and Δ angle plots were recorded at 70º with the Complete EASE software. The data were fitted using a suitable model composed of a Si substrate, and a Cauchy layer representing the ZnO material with variable thickness and optical constants, coupled to an EMA layer to model the porosity. The mean-squared error (MSE) was quantified to assure accurate modeling. Typically, the obtained values < 10 are considered a good agreement between modeled and measured data.

4.3.4 In situ Thermal-Ellipsometry

In situ thermal ellipsometry was conducted with an M2000DI ellipsometer (from Woollam), equipped with a thermal environmental chamber, to visualize the evolution of the film's thickness and refractive index. Measurements were performed at 70º in the wavelength range of 350 to 850 nm. After immediate dip coating, the deposited films on the silicon wafer were first heated to 50 ºC before gradually increasing the temperature to 500 ºC with a programmed ramp of 10 ºC/minute. The recorded data were fitted using the Cauchy model.

4.3.5 Dynamic Light Scattering (DLS)

The size distributions of the micelles in the sol gel system were measured by Dynamic Light Scattering apparatus, model Malvern Zetasizer Nano ZS90 (Malvern Instruments Ltd., Worcestershire, UK) equipped with a 4 mW He–Ne laser at a wavelength of 633 nm. Measurements were made at 25 °C at a fixed angle of 90° with a total of three acquisitions of 15 measurements per sample.

4.3.6 Fourier-Transformed Infrared

The functional groups at the film's surface were analyzed by Fourier-transformed infrared (FTIR) in attenuated total reflection (ATR) mode with an incidence angle of 45° and a 4 cm^{-1} resolution using a Spectrum 400 model from PerkinElmer, equipped with an FR-DTGS detector (fast recovery Deuterated Triglycine Sulfate detector).

4.3.7 UV–Vis Absorbance

The optical transmission of the deposited films on glass slides was measured at room temperature by using a dual-beam Carry 5000 UV-Vis spectrophotometer from Agilent technology.

4.3.8 Electrochemical Measurements

Electrochemical measurements were performed with a VSP Analytical potentiostat, from BioLogic, in a three-electrode configuration. 0.1M of KCl was used as an electrolyte[56]. The working electrode consisted of dense films of ZnO as well as the PB-*b*-PEO and F-127 derived films which were all coated on a platinum substrate. Electrical contacts were made by conductive copper scotch (3M Scotch 1245). The reference electrode was Ag/AgCl (in saturated KCl). The measured potentials vs Ag/AgCl were converted to the reversible hydrogen electrode (RHE) scale according to the Nernst Equation:

$$E_{RHE} = E_{Ag/AgCl} + 0.059pH + E^{0}_{Ag/AgCl} \quad (E^{0}_{Ag/AgCl} = 0.198 \text{ V at } 25\ ^{o}\text{C}) \qquad (3)$$

A platinum-enrolled wire was used as a counter electrode. The electrochemical active surface area (ECSA) was measured by recording cyclic voltammetry (CV) scans between -0.3 and -0.1 V vs RHE where capacitive charging/discharging occurred without any faradic reactions taking place. In this range, the resulting differential capacitance equals the double-layer capacitance (C_{DL}). Thus, this capacitance enables calculating the electrochemical active surface area (ECSA) using Equation 4[57]. The specific capacitance (C_S) was assumed approximately constant for the same ZnO material in the coated thin films.

$$ESCA = \frac{C_{DL}}{C_S} \tag{4}$$

The electrochemical double-layer capacitance (C_{dl}) was then estimated by plotting the anodic and cathodic current density differences $\Delta j = (j_{\mathrm{a}} - j_{\mathrm{c}})$ at -0.2 V vs RHE as a function of the scan rates. The slopes of these plots were assumed to be twice the C_{dl} and therefore used to represent the ECSAs. The CVs were performed by increasing scan rates from 5 to 100 mV/s.

4.4 Set-Up of the Photocatalytic Self-Cleaning Systems

The experimental set-up for the self-cleaning photocatalytic test involved investigating the photoactivity of the system by monitoring the refractive index of layers contaminated with lauric acid (LA) under controlled environmental conditions upon UVA irradiation. To introduce the contaminant, the porosity was filled with lauric acid through drop-casting of a 2 wt % LA solution in ethanol. The solvent evaporation was carried out at RT. Following each drop casting, the surface of the film was meticulously wiped to prevent diffusivity and restore optical properties. This cycle was repeated 4 times. Polluted samples were then placed at RH of 37 % and 1 cm under a UVA spot lamp model Dymax Bluewave$^{\mathrm{TM}}$ 200 (365 nm/41.1 mW cm^{-2}). The optical density of the films was recorded using in situ ellipsometry at 20 seconds intervals.

For simplicity, the refractive index of each film was measured at a single wavelength ($\lambda = 700$ nm). To achieve this, the films were impregnated with LA, and resulting in a typical increase of (0.3 ± 10) % in their refractive index. For instance, this led to an increase from $\eta = 1.5$ (for the empty porous film) to

1.7 (for the polluted one). The filling fraction of LA into the ZnO films was evaluated by a three-component Bruggeman effective medium approximation (Equation 5):

$$f_{ZnO}\frac{\tilde{\varepsilon}_{ZnO}-\tilde{\varepsilon}}{\tilde{\varepsilon}_{ZnO}+2\varepsilon}+f_{air}\frac{\tilde{\varepsilon}_{air}-\tilde{\varepsilon}}{\tilde{\varepsilon}_{air}+2\varepsilon}+f_{LA}\frac{\tilde{\varepsilon}_{LA}-\tilde{\varepsilon}}{\tilde{\varepsilon}_{LA}+2\varepsilon}=0 \tag{5}$$

with,

$$f_{ZnO}+f_{air}+f_{LA}=1 \tag{6}$$

For the polluted films, f_{ZnO}, f_{air}, and f_{LA}represent the fraction of ZnO, air, and LA respectively. $\tilde{\varepsilon}_{ZnO}$, $\tilde{\varepsilon}_{air}$, and $\tilde{\varepsilon}_{LA}$ refer to the relative dielectric constants of the three phases. $\tilde{\varepsilon}$ is the effective dielectric constant of the polluted matrix. These dielectric constants can be expressed as the square of their respective refractive indexes since the three phases do not exhibit significant adsorption within the emitted wavelength range by the ellipsometer (700 nm). Assuming the refractive index value of the air is 1, ZnO material and LA filler were modeled with a Cauchy model. The ellipsometric data was then accurately fitted to a single-layer Bruggeman model (on Si substrate) to calculate the f_{LA}volumetric fractions in each LA-polluted film. With obtained MSEs between 0.7 and 6, not only the optical properties of the ZnO coatings are highlighted, yet also the homogenous aspect of the LA-impregnated films. Consequently, the reduction of the pore content in lauric acid during photocatalysis was deduced from the evolution of the f_{LA} volumetric fraction upon UVA irradiation. All the kinetics were compared to coated lauric acid on nude wafer silicon (reference test). This analytical approach provides a straightforward and effective means of evaluating the photocatalytic activities of the films.

5. Acknowledgements

This work has been supported by CLAIM, H2020-BG-2016–2017 [grant number 774586], “Cleaning Litter by Developing and Applying Innovative Methods in European Seas”. Mr. David Montero, and

Mr. Mohamed Selmane are gratefully acknowledged for conducting SEM-FEG, and XRD measurements at Sorbonne University.

References

(1) Li, J.; Zhang, Z.; Xu, J.; Wong, C. Smart Self-Cleaning Materials—Lotus Effect Surfaces. In *Encyclopedia of Smart Materials*; Schwartz, M., Ed.; Wiley, 2005. https://doi.org/10.1002/0471216275.esm089.

(2) Pakdel, E.; Wang, J.; Kashi, S.; Sun, L.; Wang, X. Advances in Photocatalytic Self-Cleaning, Superhydrophobic and Electromagnetic Interference Shielding Textile Treatments. *Advances in Colloid and Interface Science* **2020**, *277*, 102116. https://doi.org/10.1016/j.cis.2020.102116.

(3) *Advances in Smart Coatings and Thin Films for Future Industrial and Biomedical Engineering Applications*; Makhlouf, A. S. H., Abu-Thabit, N. Y., Eds.; Elsevier: Amsterdam, 2020.

(4) Andersson Ersman, P.; Eriksson, J.; Jakonis, D.; Pantzare, S.; Åhlin, J.; Strandberg, J.; Sundin, S.; Toss, H.; Ahrentorp, F.; Daoud, K.; Jonasson, C.; Svensson, H.; Gregard, G.; Näslund, U.; Johansson, C. Integration of Screen Printed Piezoelectric Sensors for Force Impact Sensing in Smart Multifunctional Glass Applications. *Adv Eng Mater* **2022**, *24* (11), 2200399. https://doi.org/10.1002/adem.202200399.

(5) Xiang, X.; Ma, X.; Zhou, L.; Sessler, G. M.; Von Seggern, H.; Dali, O. B.; Kupnik, M.; He, P.; Dai, Y.; Zhang, X. Threadlike Piezoelectric Sensors Based on Ferroelectrets and Their Application in Washable and Breathable Smart Clothing. *Adv Materials Technologies* **2023**, 2202130. https://doi.org/10.1002/admt.202202130.

(6) Chen, J.; Poon, C. Photocatalytic Construction and Building Materials: From Fundamentals to Applications. *Building and Environment* **2009**, *44* (9), 1899–1906. https://doi.org/10.1016/j.buildenv.2009.01.002.

(7) Jin, B.; He, J.; Yao, L.; Zhang, Y.; Li, J. Rational Design and Construction of Well-Organized Macro-Mesoporous SiO_2/TiO_2 Nanostructure toward Robust High-Performance Self-Cleaning Antireflective Thin Films. *ACS Appl. Mater. Interfaces* **2017**, *9* (20), 17466–17475. https://doi.org/10.1021/acsami.7b04140.

(8) Padmanabhan, N. T.; John, H. Titanium Dioxide Based Self-Cleaning Smart Surfaces: A Short Review. *Journal of Environmental Chemical Engineering* **2020**, *8* (5), 104211. https://doi.org/10.1016/j.jece.2020.104211.

(9) Diamanti, M. V.; Luongo, N.; Massari, S.; Lupica Spagnolo, S.; Daniotti, B.; Pedeferri, M. P. Durability of Self-Cleaning Cement-Based Materials. *Construction and Building Materials* **2021**, *280*, 122442. https://doi.org/10.1016/j.conbuildmat.2021.122442.

(10) Moro, C.; Francioso, V.; Lopez-Arias, M.; Velay-Lizancos, M. Modification of Self-Cleaning Activity on Cement Pastes Containing Nano-TiO2 Due to CO2 Curing. *Construction and Building Materials* **2022**, *330*, 127185. https://doi.org/10.1016/j.conbuildmat.2022.127185.

(11) Mills, A.; Johnston, J.; O'Rourke, C. Photocatalyst Activity Indicator Inks, *Paii* s, for Assessing Self-Cleaning Films. *Acc. Mater. Res.* **2022**, *3* (1), 67–77. https://doi.org/10.1021/accountsmr.1c00196.

(12) Daher, E. A.; Riachi, B.; Chamoun, J.; Laberty-Robert, C.; Hamd, W. New Approach for Designing Wrinkled and Porous ZnO Thin Films for Photocatalytic Applications. *Colloids and Surfaces A: Physicochemical and Engineering Aspects* **2023**, *658*, 130628. https://doi.org/10.1016/j.colsurfa.2022.130628.

(13) Carretero-Genevrier, A.; Boissiere, C.; Nicole, L.; Grosso, D. Distance Dependence of the Photocatalytic Efficiency of TiO_2 Revealed by in Situ Ellipsometry. *J. Am. Chem. Soc.* **2012**, *134* (26), 10761–10764. https://doi.org/10.1021/ja303170h.

(14) Davis, M. E. Ordered Porous Materials for Emerging Applications. *Nature* **2002**, *417* (6891), 813–821. https://doi.org/10.1038/nature00785.

(15) Wu, D.; Xu, F.; Sun, B.; Fu, R.; He, H.; Matyjaszewski, K. Design and Preparation of Porous Polymers. *Chem. Rev.* **2012**, *112* (7), 3959–4015. https://doi.org/10.1021/cr200440z.

(16) Sun, H.; Zhu, J.; Baumann, D.; Peng, L.; Xu, Y.; Shakir, I.; Huang, Y.; Duan, X. Hierarchical 3D Electrodes for Electrochemical Energy Storage. *Nat Rev Mater* **2018**, *4* (1), 45–60. https://doi.org/10.1038/s41578-018-0069-9.

(17) Wen, F.; Liu, W. Three-Dimensional Ordered Macroporous Materials for Photocatalysis: Design and Applications. *J. Mater. Chem. A* **2021**, *9* (34), 18129–18147. https://doi.org/10.1039/D1TA04127D.

(18) Davis, K.; Yarbrough, R.; Froeschle, M.; White, J.; Rathnayake, H. Band Gap Engineered Zinc Oxide Nanostructures *via* a Sol–Gel Synthesis of Solvent Driven Shape-Controlled Crystal Growth. *RSC Adv.* **2019**, *9* (26), 14638–14648. https://doi.org/10.1039/C9RA02091H.

(19) Uheida, A.; Mejía, H. G.; Abdel-Rehim, M.; Hamd, W.; Dutta, J. Visible Light Photocatalytic Degradation of Polypropylene Microplastics in a Continuous Water Flow System. *Journal of Hazardous Materials* **2021**, *406*, 124299. https://doi.org/10.1016/j.jhazmat.2020.124299.

(20) Dobretsov, S.; Sathe, P.; Bora, T.; Barry, M.; Myint, M. T. Z.; Abri, M. A. Toxicity of Different Zinc Oxide Nanomaterials at 3 Trophic Levels: Implications for Development of Low-Toxicity Antifouling Agents. *Environ Toxicol Chem* **2020**, *39* (7), 1343–1354. https://doi.org/10.1002/etc.4720.

(21) Peng, L.; Zhai, J.; Wang, D.; Zhang, Y.; Zhao, Q.; Wang, P.; Pang, S.; Fan, Z.; Xie, T. The Enhancement of Oxygen Sensitivity of ZnO Macropore Film by Functionalizing with Azo Pigment. *Photochem Photobiol Sci* **2009**, *8* (6), 875–880. https://doi.org/10.1039/b812937a.

(22) McLachlan, M. A.; Rahman, H.; Illy, B.; McComb, D. W.; Ryan, M. P. Electrochemical Deposition of Ordered Macroporous ZnO on Transparent Conducting Electrodes. *Materials Chemistry and Physics* **2011**, *129* (1–2), 343–348. https://doi.org/10.1016/j.matchemphys.2011.04.021.

(23) Kovačič, S.; Anžlovar, A.; Erjavec, B.; Kapun, G.; Matsko, N. B.; Žigon, M.; Žagar, E.; Pintar, A.; Slugovc, C. Macroporous ZnO Foams by High Internal Phase Emulsion Technique: Synthesis and Catalytic Activity. *ACS Appl. Mater. Interfaces* **2014**, *6* (21), 19075–19081. https://doi.org/10.1021/am5050482.

(24) Han, H.; Wang, T.; Zhang, Y.; Nurpeissova, A.; Bakenov, Z. Three-Dimensionally Ordered Macroporous ZnO Framework as Dual-Functional Sulfur Host for High-Efficiency Lithium–Sulfur Batteries. *Nanomaterials* **2020**, *10* (11), 2267. https://doi.org/10.3390/nano10112267.

(25) Wang, Z.; Tian, Z.; Han, D.; Gu, F. Au-Modified Three-Dimensionally Ordered Macroporous ZnO:In for High-Performance Ethanol Sensors. *J. Mater. Chem. C* **2020**, *8* (8), 2812–2819. https://doi.org/10.1039/C9TC06750G.

(26) Naderi, N.; Ahmad, H.; Yasin, M. Bottom-up Self-Assembly of Macroporous ZnO Nanostructures for Photovoltaic Applications. *Ceramics International* **2023**, *49* (16), 26994–27002. https://doi.org/10.1016/j.ceramint.2023.05.238.

(27) Yu, T.; Chen, Z.; Wang, Y.; Xu, J. Synthesis of ZnO-CuO and ZnO-Co3O4 Materials with Three-Dimensionally Ordered Macroporous Structure and Its H2S Removal Performance at Low-Temperature. *Processes* **2021**, *9* (11), 1925. https://doi.org/10.3390/pr9111925.

(28) Pan, Z.; Sun, F.; Zhu, X.; Chen, Z.; Lin, X.; Zheng, Y.; Zhong, W.; Zhuang, Z.; Gu, F. Electrodeposition-Based *in Situ* Construction of a ZnO-Ordered Macroporous Film Gas Sensor with Enhanced Sensitivity. *J. Mater. Chem. A* **2019**, *7* (3), 1287–1299. https://doi.org/10.1039/C8TA09920K.

(29) Kon, K.; Brauer, C. N.; Hidaka, K.; Löhmannsröben, H.-G.; Karthaus, O. Preparation of Patterned Zinc Oxide Films by Breath Figure Templating. *Langmuir* **2010**, *26* (14), 12173–12176. https://doi.org/10.1021/la904897m.

(30) Yang, K.-Y.; Yoon, K.-M.; Choi, K.-W.; Lee, H. The Direct Nano-Patterning of ZnO Using Nanoimprint Lithography with ZnO-Sol and Thermal Annealing. *Microelectronic Engineering* **2009**, *86* (11), 2228–2231. https://doi.org/10.1016/j.mee.2009.03.078.

(31) Chen, F.; Tang, Y.; Liu, C.; Qian, J.; Wu, Z.; Chen, Z. Synthesis of Porous Structured ZnO/Ag Composite Fibers with Enhanced Photocatalytic Performance under Visible Irradiation. *Ceramics International* **2017**, *43* (16), 14525–14528. https://doi.org/10.1016/j.ceramint.2017.07.158.

(32) Sima, C.; Grigoriu, C.; Besleaga, C.; Mitran, T.; Ion, L.; Antohe, S. Porous Nanostructured ZnO Films Deposited by Picosecond Laser Ablation. *Materials Science and Engineering: B* **2012**, *177* (14), 1188–1193. https://doi.org/10.1016/j.mseb.2012.05.009.

(33) Doan, N.; Vainikka, T.; Rautama, E.-L.; Kontturi, K.; Johans, C. Electrodeposition of Macroporous Zn and ZnO Films from Ionic Liquids. *International Journal of Electrochemical Science* **2012**, *7* (12), 12034–12044. https://doi.org/10.1016/S1452-3981(23)16523-0.

(34) Denkena, B.; Breidenstein, B.; Wagner, L.; Wollmann, M.; Mhaede, M. Influence of Shot Peening and Laser Ablation on Residual Stress State and Phase Composition of Cemented Carbide Cutting Inserts. *International Journal of Refractory Metals and Hard Materials* **2013**, *36*, 85–89. https://doi.org/10.1016/j.ijrmhm.2012.07.005.

(35) Ahmed, N.; Darwish, S.; Alahmari, A. M. Laser Ablation and Laser-Hybrid Ablation Processes: A Review. *Materials and Manufacturing Processes* **2016**, *31* (9), 1121–1142. https://doi.org/10.1080/10426914.2015.1048359.

(36) Grosso, D.; Boissière, C.; Smarsly, B.; Brezesinski, T.; Pinna, N.; Albouy, P. A.; Amenitsch, H.; Antonietti, M.; Sanchez, C. Periodically Ordered Nanoscale Islands and Mesoporous Films Composed of Nanocrystalline Multimetallic Oxides. *Nature Mater* **2004**, *3* (11), 787–792. https://doi.org/10.1038/nmat1206.

(37) Sanchez, C.; Boissière, C.; Grosso, D.; Laberty, C.; Nicole, L. Design, Synthesis, and Properties of Inorganic and Hybrid Thin Films Having Periodically Organized Nanoporosity. *Chem. Mater.* **2008**, *20* (3), 682–737. https://doi.org/10.1021/cm702100t.

(38) Li, C.; Li, Q.; Kaneti, Y. V.; Hou, D.; Yamauchi, Y.; Mai, Y. Self-Assembly of Block Copolymers towards Mesoporous Materials for Energy Storage and Conversion Systems. *Chem. Soc. Rev.* **2020**, *49* (14), 4681–4736. https://doi.org/10.1039/D0CS00021C.

(39) Liu, Z.; Jin, Z.; Li, W.; Qiu, J. Preparation of ZnO Porous Thin Films by Sol–Gel Method Using PEG Template. *Materials Letters* **2005**, *59* (28), 3620–3625. https://doi.org/10.1016/j.matlet.2005.06.064.

(40) Phoohinkong, W.; Foophow, T.; Pecharapa, W. Synthesis and Characterization of Copper Zinc Oxide Nanoparticles Obtained via Metathesis Process. *Adv. Nat. Sci: Nanosci. Nanotechnol.* **2017**, *8* (3), 035003. https://doi.org/10.1088/2043-6254/aa7223.

(41) Pucić, I.; Jurkin, T. FTIR Assessment of Poly(Ethylene Oxide) Irradiated in Solid State, Melt and Aqeuous Solution. *Radiation Physics and Chemistry* **2012**, *81* (9), 1426–1429. https://doi.org/10.1016/j.radphyschem.2011.12.005.

(42) Inamuddin; Shakeel, N.; Imran Ahamed, M.; Kanchi, S.; Abbas Kashmery, H. Green Synthesis of ZnO Nanoparticles Decorated on Polyindole Functionalized-MCNTs and Used as Anode

Material for Enzymatic Biofuel Cell Applications. *Sci Rep* **2020**, *10* (1), 5052. https://doi.org/10.1038/s41598-020-61831-4.

(43) Gürbüz, R.; Sarac, B.; Soprunyuk, V.; Yüce, E.; Eckert, J.; Ozcan, A.; Sarac, A. S. Thermomechanical and Structural Characterization of Polybutadiene/Poly(Ethylene Oxide)/ CNT STRETCHABLE ELECTROSPUN FIBROUS Membranes. *Polym Adv Technol* **2021**, *32* (1), 248–261. https://doi.org/10.1002/pat.5080.

(44) S, M.; N, H.; P.P, V. In Vitro Biocompatibility and Antimicrobial Activities of Zinc Oxide Nanoparticles (ZnO NPs) Prepared by Chemical and Green Synthetic Route— A Comparative Study. *BioNanoSci.* **2020**, *10* (1), 112–121. https://doi.org/10.1007/s12668-019-00698-w.

(45) Valerio, T. L.; Maia, G. A. R.; Gonçalves, L. F.; Viomar, A.; Banczek, E. do P.; Rodrigues, P. R. P. Study of the Nb2O5 Insertion in ZnO to Dye-Sensitized Solar Cells. *Mat. Res.* **2019**, *22* (suppl 1), e20180864. https://doi.org/10.1590/1980-5373-mr-2018-0864.

(46) Singh, J.; Kaur, S.; Kaur, G.; Basu, S.; Rawat, M. Biogenic ZnO Nanoparticles: A Study of Blueshift of Optical Band Gap and Photocatalytic Degradation of Reactive Yellow 186 Dye under Direct Sunlight. *Green Processing and Synthesis* **2019**, *8* (1), 272–280. https://doi.org/10.1515/gps-2018-0084.

(47) Bai, S.; Hu, J.; Li, D.; Luo, R.; Chen, A.; Liu, C. C. Quantum-Sized ZnO Nanoparticles: Synthesis, Characterization and Sensing Properties for NO2. *J. Mater. Chem.* **2011**, *21* (33), 12288. https://doi.org/10.1039/c1jm11302j.

(48) Pielichowski, K.; Flejtuch, K. Non-Oxidative Thermal Degradation of Poly(Ethylene Oxide): Kinetic and Thermoanalytical Study. *Journal of Analytical and Applied Pyrolysis* **2005**, *73* (1), 131–138. https://doi.org/10.1016/j.jaap.2005.01.003.

(49) Renaud, A.; Cario, L.; Rocquefelte, X.; Deniard, P.; Gautron, E.; Faulques, E.; Das, T.; Cheviré, F.; Tessier, F.; Jobic, S. Unravelling the Origin of the Giant Zn Deficiency in Wurtzite Type ZnO Nanoparticles. *Sci Rep* **2015**, *5* (1), 12914. https://doi.org/10.1038/srep12914.

(50) Bass, J. D.; Boissiere, C.; Nicole, L.; Grosso, D.; Sanchez, C. Thermally Induced Porosity in CSD MgF_2 -Based Optical Coatings: An Easy Method to Tune the Refractive Index. *Chem. Mater.* **2008**, *20* (17), 5550–5556. https://doi.org/10.1021/cm8010106.

(51) Li, R.; Faustini, M.; Boissière, C.; Grosso, D. Water Capillary Condensation Effect on the Photocatalytic Activity of Porous TiO_2 in Air. *J. Phys. Chem. C* **2014**, *118* (31), 17710–17716. https://doi.org/10.1021/jp5046468.

(52) Moore, J.; Louder, R.; Thompson, C. Photocatalytic Activity and Stability of Porous Polycrystalline ZnO Thin-Films Grown via a Two-Step Thermal Oxidation Process. *Coatings* **2014**, *4* (3), 651–669. https://doi.org/10.3390/coatings4030651.

(53) Gancheva, M.; Markova-Velichkova, M.; Atanasova, G.; Kovacheva, D.; Uzunov, I.; Cukeva, R. Design and Photocatalytic Activity of Nanosized Zinc Oxides. *Applied Surface Science* **2016**, *368*, 258–266. https://doi.org/10.1016/j.apsusc.2016.01.211.

(54) Fouad, O.; Ismail, A.; Zaki, Z.; Mohamed, R. Zinc Oxide Thin Films Prepared by Thermal Evaporation Deposition and Its Photocatalytic Activity. *Applied Catalysis B: Environmental* **2006**, *62* (1–2), 144–149. https://doi.org/10.1016/j.apcatb.2005.07.006.

(55) Fragua, D. M.; Abargues, R.; Rodriguez-Canto, P. J.; Sanchez-Royo, J. F.; Agouram, S.; Martinez-Pastor, J. P. Au-ZnO Nanocomposite Films for Plasmonic Photocatalysis. *Adv. Mater. Interfaces* **2015**, *2* (11), 1500156. https://doi.org/10.1002/admi.201500156.

(56) Sulciute, A.; Nishimura, K.; Gilshtein, E.; Cesano, F.; Viscardi, G.; Nasibulin, A. G.; Ohno, Y.; Rackauskas, S. ZnO Nanostructures Application in Electrochemistry: Influence of Morphology. *J. Phys. Chem. C* **2021**, *125* (2), 1472–1482. https://doi.org/10.1021/acs.jpcc.0c08459.

(57) Karakaya, C.; Solati, N.; Balkan, T.; Savacı, U.; Keleş, E.; Turan, S.; Kaya, S. Mesoporous Molybdenum Sulfide-Oxide Composite Thin-Film Electrodes Prepared by a Soft Templating Method for the Hydrogen Evolution Reaction. *ACS Appl. Energy Mater.* **2022**, *5* (6), 7006–7015. https://doi.org/10.1021/acsaem.2c00640.

Supporting Information

Advanced Approach to Self-Cleaning Surfaces: Designing Macroporous ZnO Coatings with Enhanced Photocatalytic Properties

Elie A. Daher[‡,†], *Cédric Boissière*[†], *Christel Laberty Robert*[†,⁑], *Wael Hamd* [₽]*

[‡] Petrochemical Engineering Department, Faculty of Engineering III, CRSI, Lebanese University, Rafic Hariri Campus, Hadat, Lebanon.

[†] Laboratoire Chimie de la Matière Condensée de Paris LCMCP, Sorbonne Université, UPMC Paris 06, 4 Place Jussieu, 75005 Paris, France

[⁑] RS2E, Réseau Français sur le Stockage Electrochimique de l'Energie, CNRS 3459, 80039 Cedex 1 Amiens, France

[₽] Chemical Engineering Department, Faculty of Engineering, University of Balamand, P.O. Box 33, El-Koura, Lebanon.

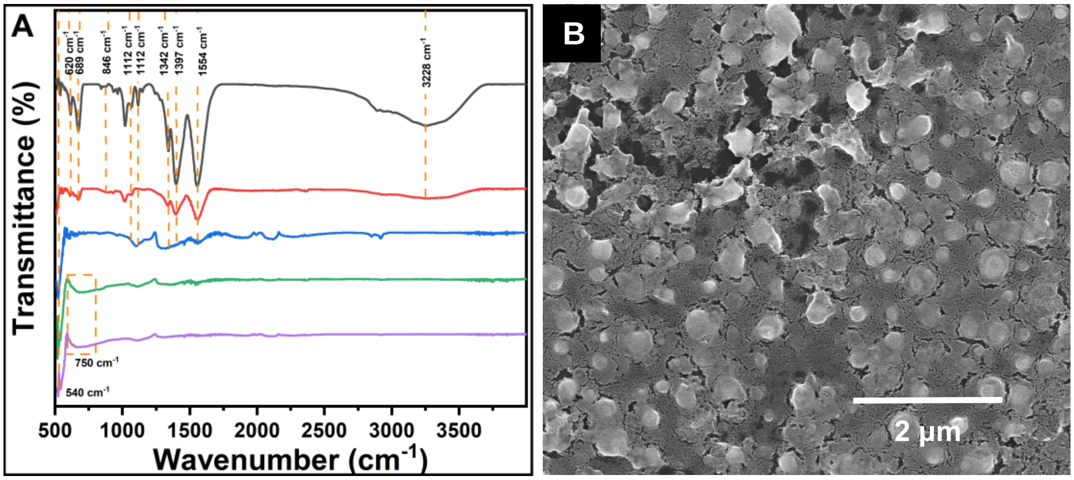

Figure S1. (a) FTIR spectra of dip-coated films with PB-*b*-PEO/Zn^{2+} solution in ethanol (Zn^{2+}:MEA = 1:0.5): at Room temperature (balck), 100 ºC (red), 150 ºC (blue), 250 ºC (green), and 350 ºC (purple), **(b)** SEM-FEG micrographs of the obtained film at the end of the thermo-ellipsometry measurement (T_{final} = 500 ºC).

Table S1. Atomic (%) of carbon (C), azote (N), oxygen (O), and zinc (Zn) as a function of heat treatment temperature.

Atomic Elements	Atomic (%)[a] at T = 100 °C	Atomic (%)[a] at T = 150 °C	Atomic (%)[a] at T = 250 °C
C	20.79 ± 2.42	16.26 ± 1.36	13.82 ± 0.42
N	0.86 ± 0.32	N/A [b]	N/A [b]
O	40.93 ± 0.91	40.38 ± 0.69	41.97 ± 0.36
Zn	37.42 ± 2.2	43.35 ± 0.85	44.21 ± 0.06
Zn:O	**0.91:1**	**1.07:1**	**1.05:1**

[a] (Atomic % of each elements was tabulated as the statistic average for each EDX mapping); [b] (Beyond 100 °C, azote elements became undetectable)**.**

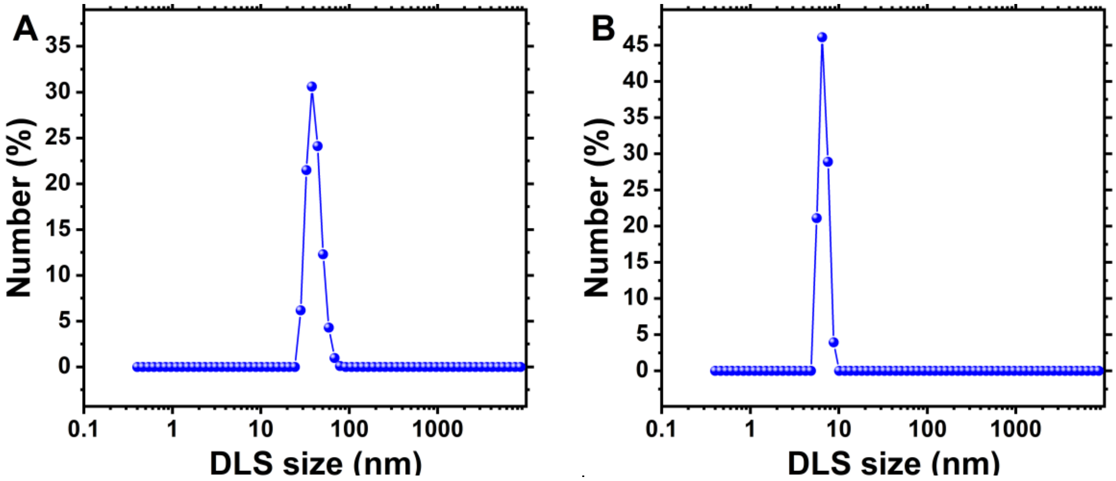

Figure S2. Size distribution determined by dynamic light scattering measurement (DLS) of **(a)** PB-*b*-PEO/Zn^{2+} solution in ethanol (Zn^{2+}:MEA = 1:0.5), **(b)** PS/Zn^{2+} solution in ethanol (Zn^{2+}:MEA = 1:0.5).

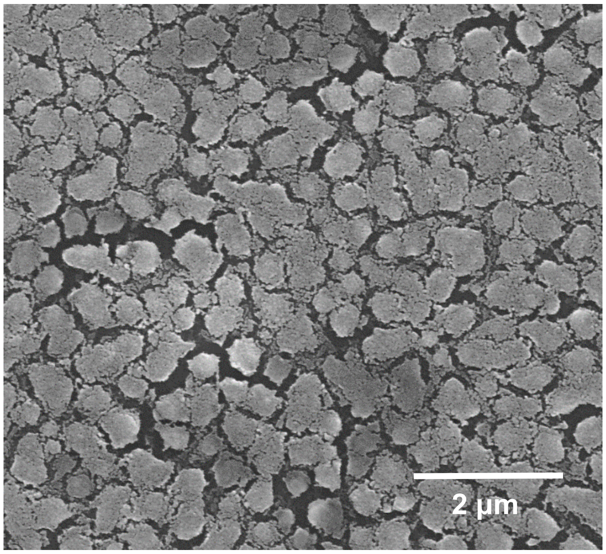

Figure S3. SEM-FEG micrographs of a PB-*b*-PEO/ZnO film flashed at 100 ºC, then post-heated at 500 ºC.

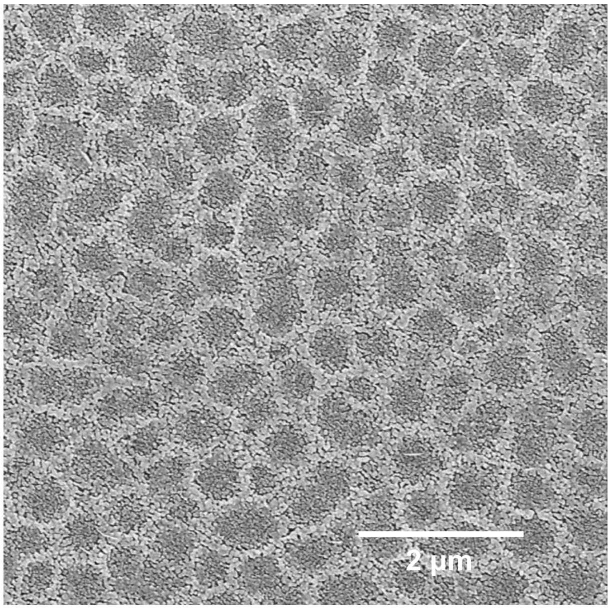

Figure S4. SEM-FEG micrographs of a macroporous ZnO film dipped in 0.25 M Zn^{2+}/ethanol sol-gel (Zn^{2+}:MEA = 1:0.5), with 30 mg of PB-*b*-PEO (M.W.(PB) = 2500 $g.mol^{-1}$, M.W.(PEO) = 2500 $g.mol^{-1}$). The film was flash-heated at 450 ºC.

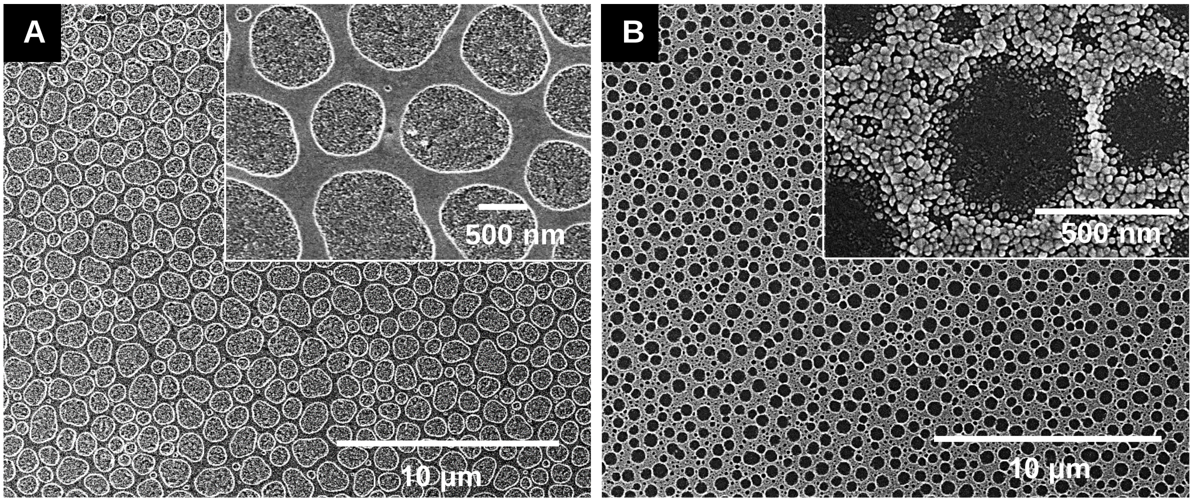

Figure S5. SEM-FEG micrographs of coatings made out of PB-*b*-PEO/ZnO sol-gel over **(a)** Kapton, and **(b)** glass substrates. All films were flashed at 450 ºC.

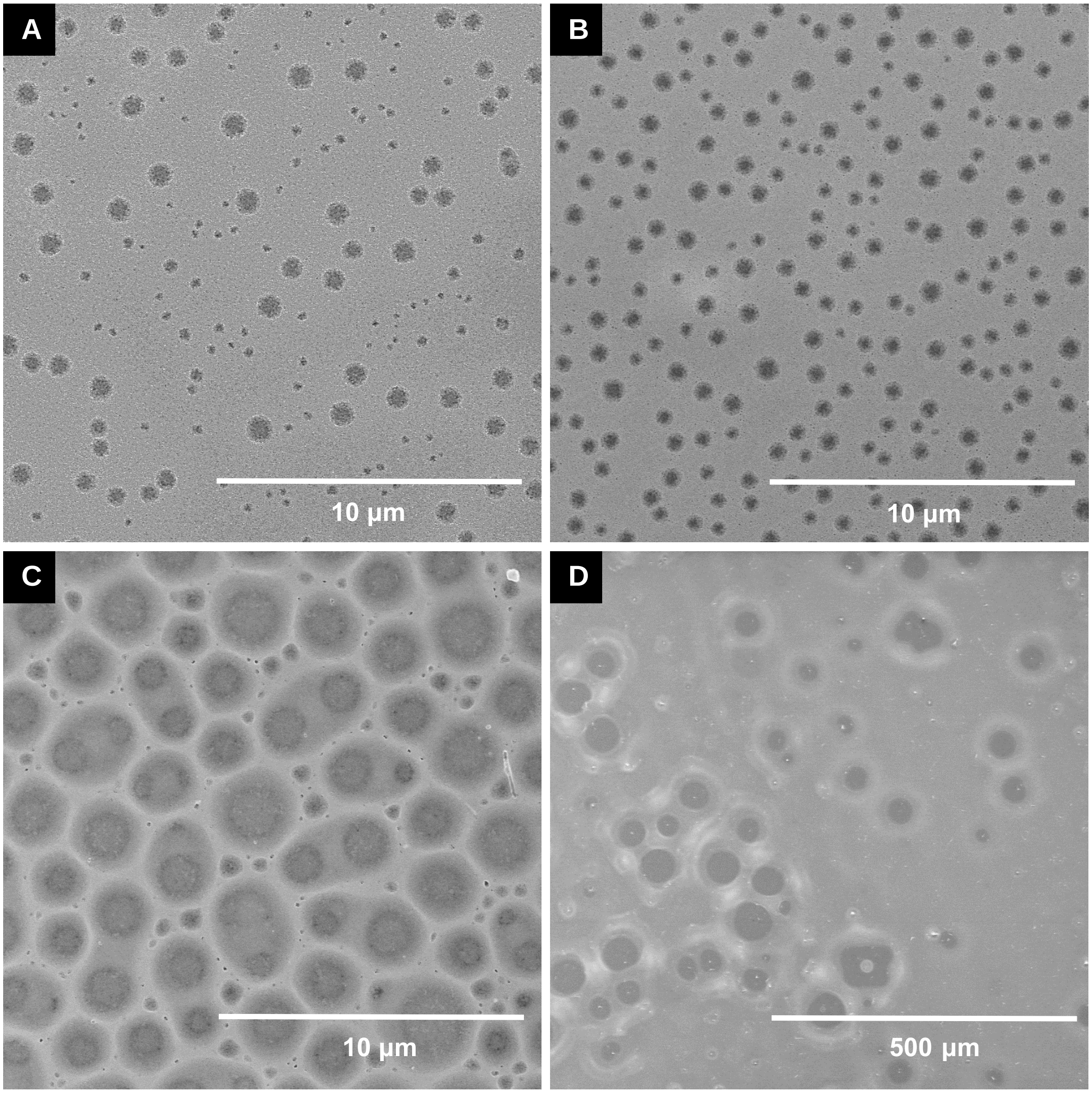

Figure S6. SEM-FEG micrographs of a macroporous ZnO film dipped in F-127/ Zn^{2+}/ethanol sol-gel with Zn^{2+}:MEA ratio of **(a)** 1:0.00025, **(b)** 1:0.0005, **(c)** 1:0.004, and **(d)** 1:0.008. The films were flashed at 450 °C.

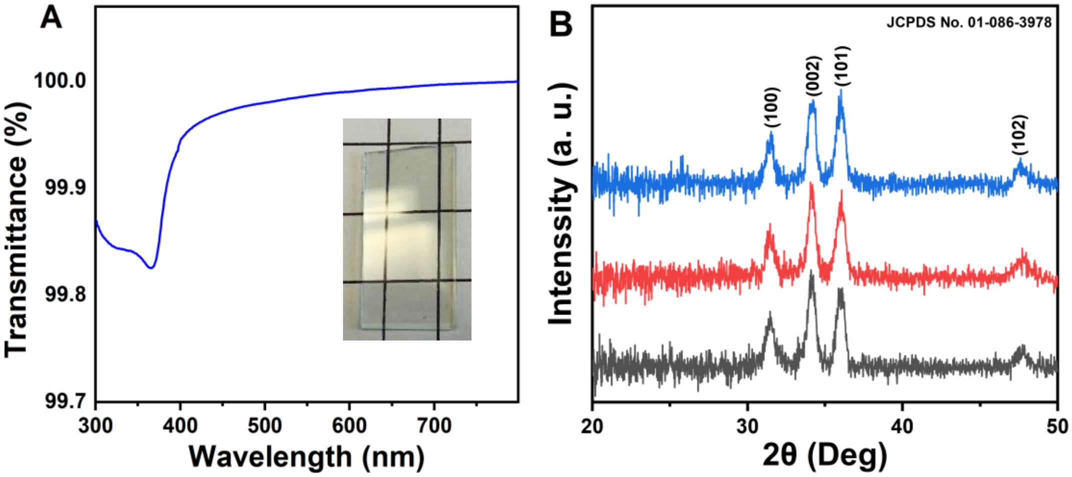

Figure S7. (a) UV-vis transmittance of a macroporous ZnO film dipped in PB-b-PEO/ Zn^{2+}/ethanol sol-gel with Zn^{2+}:MEA ratio = 1:0.5 and flashed at 450 °C. Inset: Photograph. **(b)** XRD pattern of the dense film (black) , PB-*b*-PEO template film (red), and F-127 templated film (blue), flashed at 450 °C.

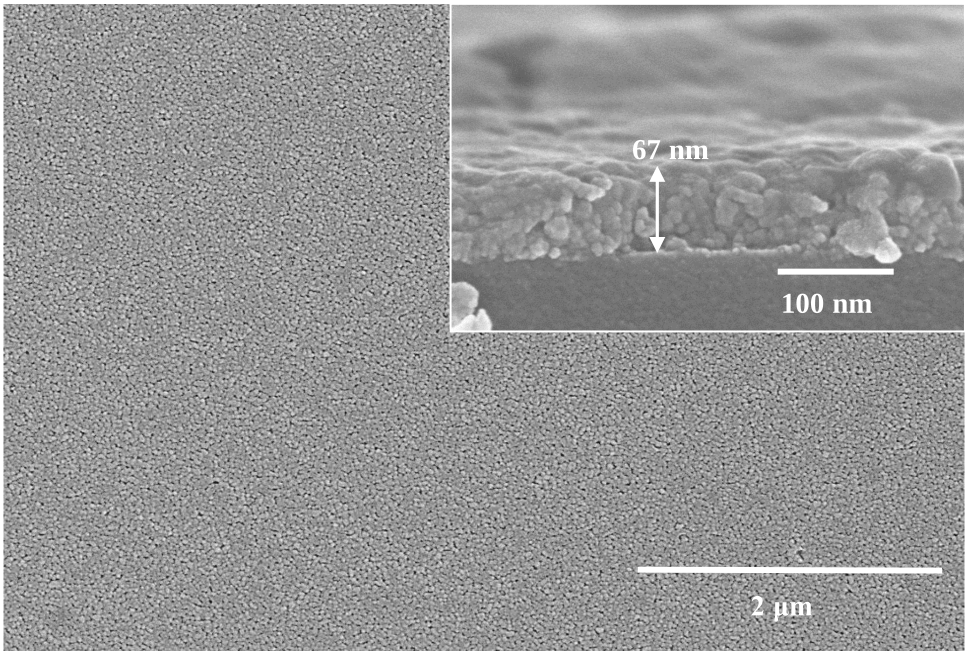

Figure S8. SEM-FEG micrographs of a single layer ZnO dense film flashed at 450 °C. Inset: Cross-section.

Conclusions and Perspectives

In recent years, photocatalysis has emerged as an eco-friendly method for the degradation of various types of organic pollutants in liquid and gas phases. More precisely, photocatalysts like Zinc oxide (ZnO) offer several advantages including low cost, chemical – physical stability, and environmental friendliness. However, this promising new catalytic platform suffers from major drawbacks such as i) fast photogenerated electron–holes recombination; ii) restricted visible-light response-ability and iii) low specific surface area of the photocatalysts. To address these aspects, three different strategies were investigated in this Ph.D. The first one consists of understanding the degradation mechanisms on molecular and particle scales. The second one entails the design of highly porous and nanostructured ZnO by hydrothermal and sol-gel processes for photocatalytic applications. Finally, in the third strategy, the novel ZnO nanostructures are coupled to another advanced oxidation technique like the Fenton process. These strategies are discussed in five separate chapters as follows:

In the first chapter, the impact of the pollutants' chemical structures on their photocatalytic degradation kinetics was investigated in the aqueous phase by using phenol (single aromatic ring), methylene blue (poly-aromatic ring), and humic acid (complex macromolecule), over ZnO nanorods synthesized by hydrothermal growth. The results showed that the kinetics of all the tested molecules obey a pseudo-first-order model regardless of the initial concentrations (5, 10, and 20 ppm). In addition, the apparent rate constants are largely controlled by the bond dissociation energy and the number of oxidation steps in each organic molecule. For instance, at 5 ppm initial concentration, methylene blue presents the weakest dissociation bond energy and the highest degradation rate constant ($k = 0.0714$ min^{-1}) compared to humic acid ($k = 0.0314$ min^{-1}) and phenol ($k = 0.0228$ min^{-1}).

In the second chapter, we explored the photocatalytic degradation of low-density polypropylene (LD-PP) microplastics (MPs) under natural sunlight by using ZnO nanorods, coated onto a glass fiber mesh.

The LD-PP microplastics were chosen due to their low degradability, high toxicity to various living organisms, and capability to attract various pollutants/heavy metals to their surface. The use of glass fibers is ideal to trap the low-density particles while acting as a supporting substrate for the photocatalyst. The oxidation of LD-PPs was assessed by following the evolution of the carbonyl index over time through the ATR-FTIR technique and by analyzing their microstructure by SEM-FEG microscopy. A slow evolution of the carbonyl and hydroxyl absorption bands was detected between 0 and 117 h, due to the formation of a small number of carbonyl groups on the polypropylene surface. As photodegradation progresses, the degradation kinetics increase significantly due to the presence of cracks and the consequent increase in particle surface area. This conclusion was evidenced by microscopy analysis, demonstrating the formation of relatively deep cavities after 196h of solar irradiation.

In the third chapter, novel wrinkled and porous ZnO films were synthesized by sol-gel dip coating. This template-free approach is based on inducing instability-driven organization of the dip-coated film under thermal compression generated by heating it in an infrared chamber (dip coater chamber). As a result, a wrinkled structure with a porosity of ~ 22–25 % and an average pore Ferret diameter of ~24 nm were achieved. The photocatalytic activity of ZnO films was tested on 10 μM methylene blue probe molecule by using UV-vis spectroscopy. Efficiencies of 60 % and 92% only were observed after 180 min under UVA ($\lambda = 365$ nm) and day-light LED lamps, respectively. This result underlines the fact that by a facile and low-cost synthesis approach, it was possible to achieve very interesting results without the need for doping or structuring agents for nanostructuration.

In the fourth chapter, a UVA/Fe^{3+}/H_2O_2/ZnO coupled process was developed to promote the generation of reactive oxygen species (ROS) and enhance therefore the degradation kinetics. To do so, Fe^{3+} and H_2O_2 were added in different ratios to MB in the presence of ZnO at near-neutral pH. Although an acidic medium ($pH < 3$) is necessary to prevent sludge formation in the Fenton process, this facilitates the dissolution of the ZnO films. With both processes running concurrently, the photo-generated electrons by the photocatalyst are trapped by the iron (III), inhibiting electron-hole recombination from one side, and accelerating the Fe^{3+}/Fe^{2+} regeneration from the other side. The coupled system used for the degradation of 10 ppm MB (molar ratios of $[H_2O_2]:[MB] = 52:1$, and $[H_2O_2]:[Fe^{3+}] = 130:1$) exhibited a rate constant of 0.0049 min^{-1} exceeding the sum of both individual processes, with a removal percentage of 94 % after 480 minutes under UVA irradiation (365 nm).

Finally, in the fifth chapter, we reported a new fabrication procedure for macroporous ZnO coatings. The process combines the sol chemistry with various self-assembled polymers. The mechanism of pore formation was investigated as a function of the heat treatment (i.e. temperature/rate), and the sol components. Accordingly, it was possible to tune the porosity between 400 nm to 56 μm. This result provides a straightforward approach to the synthesis of macroporous coatings by using a myriad of different polymers ranging from homo-polystyrene to di- and triblock polybutadiene-b-polyethylene oxide and Pluronics F-127. Moreover, the robustness of the mechanism enables the deposition of such macroporous films on various substrates, such as Kapton, silicon wafers, and glass. The self-cleaning properties of these films were further investigated with a lauric acid probe molecule. These macroporous ZnO thin films demonstrate high self-cleaning potential towards organic contaminations (100% degradation in solely 15 minutes), due to their semi-conducting properties that enable a photocatalytic degradation of the organic matter.

Although the goal of this thesis is to better understand the degradation mechanisms of organic pollutants and improves the photocatalytic activity of ZnO nanostructured materials, several aspects related to the by-products' toxicity, photocatalyst performance, and photoreactor design need further investigations. Thus, we propose below some primary perspectives for future work.

1. *Toxicity analysis:* Because the degradation of organic molecules and particles may produce different types of intermediates with potential hazards, assessing their toxicity is imperative. Therefore, it is crucial first to identify the degradation mechanisms and the obtained compounds by using High-Performance Liquid Chromatography (HPLC) and Gas Chromatography (GC), coupled with mass spectroscopy. Furthermore, the impact on living organisms could be investigated by using an ecotoxicological approach (UNI EN ISO/EPA bioassays) to test water samples after photocatalytic degradation.
2. *Enhancement of the photocatalytic activity:* The photocatalytic performances of ZnO materials were improved by i) designing novel types of nanostructures, ii) coupling with other AOPs, and iii) constructing ZnO/TiO_2 heterostructure (this study is detailed in the Annex chapter). Besides these approaches, we suggest other strategies such as introducing different metal or non-metal dopants (Fe, Cu, Ag, Sn, C, N, F, P, S) and using sacrificial agents (alcohols, acids) to reduce the electron – hole recombination. In addition, as the recombination rate is directly related to the photocatalytic efficiency of optimized systems, it is very important to measure it by using i. e. time-resolved photoluminescence, and electrochemical impedance spectroscopy.

3. *Reactor design and upscaling:* The large-scale photocatalysis application is still challenging due to several factors, such as heat and mass transfer, pressure drop, pollutants selectivity, and safety. Designing a lab-scale prototype is the first step before reaching the industrial application. The Fenton kinetic data obtained in this study was used for designing a cylindrical plug flow photoreactor (serpentine channels). However, this preliminary design still needs major optimizations based on (i) the types of pollutants, (ii) the irradiation light source, and (iii) the reacting mixture's composition and flow rates.

4. *Stability of ZnO photocatalyst:* At extreme pH conditions (pH < 4), ZnO shows poor stability due to the leaching of the Zn^{2+} ions, which reduces its photocatalytic activity. Thus, it will be very important to stabilize the ZnO films by depositing a protective layer of other oxide material i. e. SiO_2 or Al_2O_3.

Annex: Novel 3D $ZnO/TiO_2/FTO$ coating

Our approach behind this tri-component photocatalyst aims to reduce the electron-hole recombination in the ZnO bandgap by pairing it with TiO_2, another n-type semiconductor to develop an n-type/n-type heterojunction[1]. Due to their structural analogies and effective separation of photogenerated electron–hole pairs, heterostructured materials based on coupling these two metal oxides have been attracting much interest[2,3]. In this thesis, we have also studied the electrodeposition of ZnO on a mesoporous TiO_2 film, previously coated on FTO glass substrates by sol-gel dip coating. The choice of FTO-coated glass was also encouraged by its excellent electrical conductivity, which enables the electrodeposition of ZnO onto the TiO_2/FTO electrode. This characteristic allows the characterization of the active electrochemical surface area of the catalyst[4]. The preparation procedure is summarized as follows.

Synthesis and Characterization of the $ZnO/TiO_2/FTO$ Films

Mesoporous TiO_2 was coated on a Fluorine-doped tin oxide (FTO) substrate purchased from SOLEMS (YSUB/ASAHI120/1: 10 × 30 mm/resistivity 80 $\Omega.cm^{-2}$, with an 80–100 nm of FTO on glass). The substrates were carefully wiped with ethanol and acetone before the dip coating process. 11.6 g of $TiCl_4$ (Sigma Aldrich, > 99.9 % trace metals basis) was dropwise poured in 14.3 g of cold absolute ethanol (VWR, AnalaR NORMAPUR® ACS, reagent Ph. Eur analytical reagent (99.9 %) to obtain a molar ratio of 1($TiCl_4$): 5(EtOH). Stored at around 4 °C, the solution can be used over 6 months. Next, 100 mg of block-copolymers Poly(1, 4-butadiene)-*b*-poly(ethylene oxide, PB-*b*-PEO (P4515-BdEO; M.W.(PB) = 11800 $g.mol^{-1}$; M.W.(PEO) = 13500 $g.mol^{-1}$) purchased from Polymer Source, were dissolved in 5.0 g of ethanol and 0.4 g of distilled water (18.2 MΩ.cm). This solution was stirred at 70 °C for 1 h to complete the dissolution of the polymer. After cooling at room temperature, the precursor solution of $TiCl_4$ was poured dropwise into the polymeric solution. The concentration of inorganic salts in the final solution is 2 M. The pre-cleaned FTO was then dip-coated into this solution at a withdrawal speed of 2.5 $\mathrm{mm.s^{-1}}$ in a dry atmosphere (< 5% relative humidity).

For monolayer films, the coated substrates were directly heated for 1 h in a furnace at 500 ºC in air (static atmosphere) to induce the crystallization of the anatase and decompose the block-copolymer, giving rise to the formation of pores.

For multilayer films, the coated substrates were subjected to an intermediate pre-heating treatment at 350 ºC for 1–3 min to start the crystallization, before the total degradation of the polymer. This was repeated to achieve the desired thickness that is controlled by the number of coated layers. A final thermal treatment at 500 ºC for 1 h was then necessary to complete the polymer degradation and allow the inorganic wall to crystallize into an anatase structure. For dense TiO_2 layers, the same procedure was performed, yet without the block copolymers.

ZnO was electrodeposited on the mesoporous TiO_2 by using a 0.1M solution of aqueous zinc nitrate hexahydrate (reagent grade, 98% from Sigma-Aldrich). The electrochemical deposition was performed with a VSP Analytical potentiostat, from BioLogic, in a three-electrode configuration. The working electrode consisted of the TiO_2/FTO substrates. Electrical contacts were made by conductive copper scotch (3M Scotch 1245). The reference electrode was Ag/AgCl (in saturated KCl). The measured potentials vs Ag/AgCl were converted to the reversible hydrogen electrode (RHE) scale according to the Nernst Equation:

$$E_{RHE} = E_{Ag/AgCl} + 0.059pH + E^{0}_{Ag/AgCl} \quad (E^{0}_{Ag/AgCl} = 0.198 \text{ V at } 25\ ^{\circ}\text{C}) \tag{1}$$

A Platinum enrolled wire was used as a counter electrode. The potential applied for the electrodeposition was - 0.8 V vs. Ag/AgCl (at 25 ºC), where the nitrate reduction solely takes place without any other oxido-reduction reactions[5]. For the electrochemical measurements, KOH was used as an electrolyte (10 mM). The electrochemical active surface area (ECSA) was measured by recording cyclic voltammetry (CV) scan between -0.3 and -0.1 V vs RHE where capacitive charging/discharging occurred without any faradic reactions taking place. In this range, the resulting differential capacitance is equal to the double-layer capacitance (C_{DL}). Thus, this capacitance enables calculating the electrochemical active surface area (ECSA) using **Equation 4**.[6] The specific capacitance (C_S) was assumed to be constant for all the ZnO-coated thin films.

$$ESCA = \frac{C_{DL}}{C_S} \tag{2}$$

The electrochemical double-layer capacitance (C_{dl}) was then estimated by plotting the anodic and cathodic current density differences $\Delta j = (j_a - j_c)$ at -0.2 V vs RHE as a function of the scan rates. The slopes of these plots were considered to be twice the C_{dl} and were therefore used to represent the ECSAs. The CVs were performed by increasing scan rates from 5 to 100 mV/s.

Linear sweep voltammetry (LSV) was performed with an AMETEK Solartron Analytical Modulab potentiostat which measured a linear voltage sweep (LVS) and a current in a potentiostatic mode of samples in a three-electrode setup with and without surface irradiation. A Newport UV-vis lamp of 50 – 500 W was used. The LVS were measured from -0.1 V to 1.3 V vs. Ag/AgCl. KCl saturated reference electrode ($E^0_{Ag/AgCl}$ = 0.197 V vs. NHE), with a platinum enrolled wire as a counter electrode and 10 mV $^{s-1}$ scan rate. All current density curves were referenced to the reversible hydrogen electrode (RHE), using the Nernstian relation of E vs. RHE = E vs. Ag/AgCl + 0.197 + 0.059pH. Chronoamperometry measurement under alternative irradiation (UV-visible) was performed using the potentiostatic mode at a fixed potential of 1.23 V vs RHE. 1M potassium phosphate buffer of pH 6.07 was used as an electrolyte. Herein, the TiO_2/FTO and ZnO/TiO_2/FTO working electrodes were tested for the photoelectrolysis of water and particularly for the Oxygen evolution reaction (OER).

The microstructure of the films and film thickness were observed by SU-70 Hitachi field emission gun scanning electron microscopy (FEG-SEM), operating at 10 kV tension and by transmission electron microscope (TEM) model TWIN 120 (TECNAI SPIRIT).

Figure 1 shows a highly periodic and interconnected mesoporous TiO_2 structure. The average pore diameter and the thickness of the 2 layers are ~ 35 nm and 390 nm, respectively.

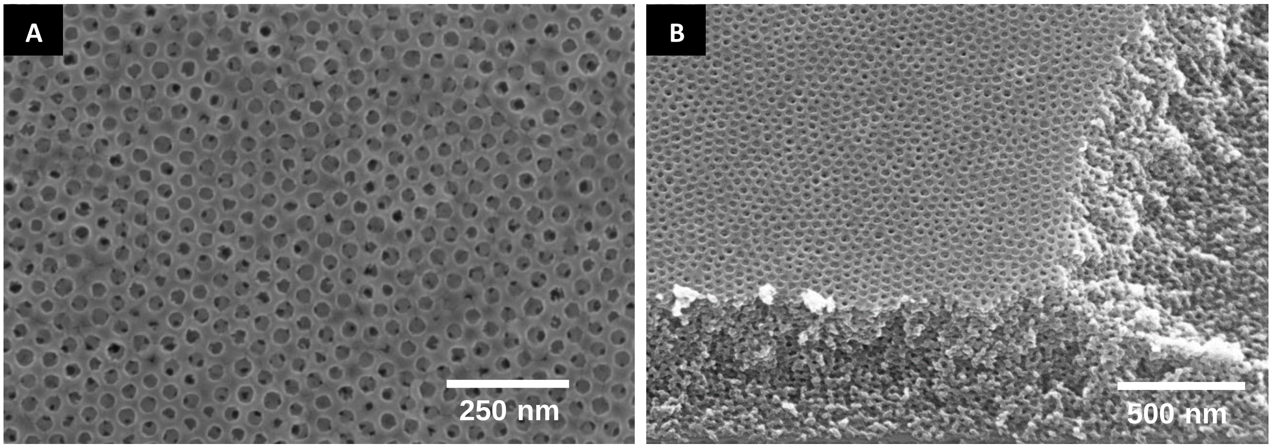

Figure. 1 SEM-FEG micrographs of the mesoporous TiO_2 films (2 layers): **(A)** top view, and **(B)** 20^o tilted view.

The porosity and the film's thickness were assessed by spectroscopic ellipsometry, using a UV-NIR (193–1690 nm) M-2000DI spectroscopic ellipsometer from J. A. Wolfram. Ellipsometric ψ and Δ angle plots were recorded at 70^o and fitted with the Complete EASE software. The mean-squared error (MSE) was quantified to assure accurate modeling. Typically, the obtained values < 10 are considered a good agreement between modeled and measured data. Consequently, a porous film of 40% and 380 nm thickness is detected. This agrees well with the SEM-FEG analysis.

To highlight the efficiency of this mesoporous structure in the photocatalytic application, the mesoporous film was compared to a dense layer of a similar thickness (Figure 2). Methylene blue (MB) was used as a probe molecule under a UVA irradiation of 365 nm. The choice of the latter is promoted by the low photolysis of MB under this wavelength energy. This was confirmed by the negligible degradation in Figure 2c. However, with the employment of TiO_2-based photocatalysts, the degradation rates change drastically. The photocatalytic data of the mesoporous material demonstrates a kinetics that is six times faster compared to the dense films. (*Kapp* equal to 0.0022 min^{-1} and 0.0132 min^{-1} for dense and mesoporous films, respectively). This behavior can be fairly justified by the larger surface area of the mesoporous film. To support this conclusion, the electrochemical surface areas were measured for both materials.

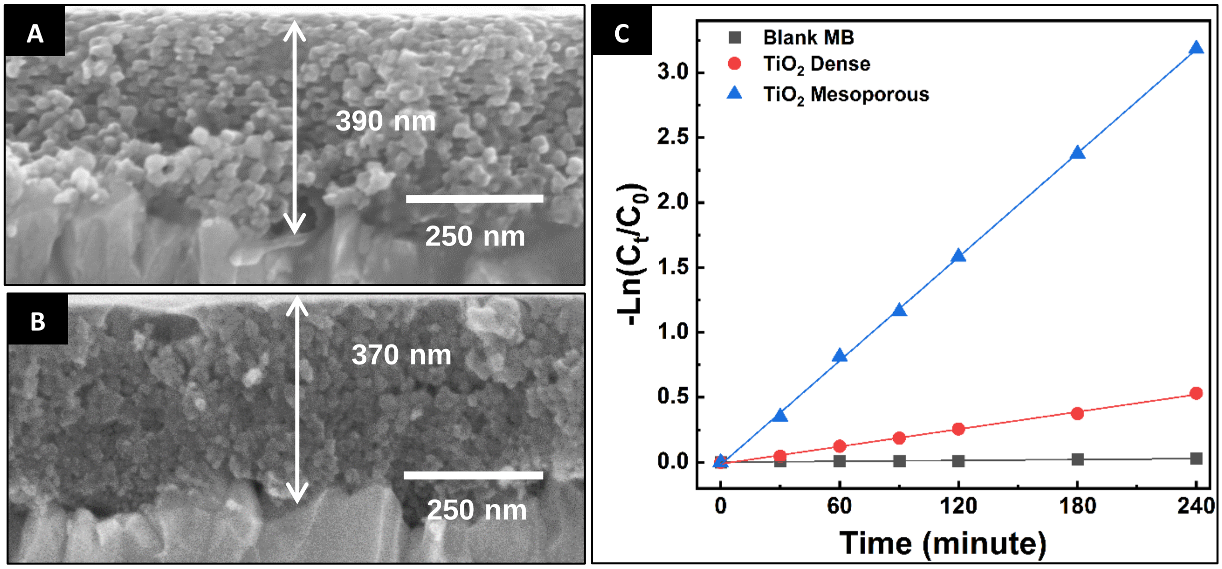

Figure. 2 SEM-FEG micrographs of the mesoporous TiO_2 films (2 layers): **(a)** Mesoporous, and **(b)** Dense. **(c)** Photocatalytic degradation of 10 ppm MB under UVA light of $\lambda = 365$ nm using the films in (A) and (B).

The electrodeposition of ZnO onto mesoporous TiO_2 was then conducted as a function of the deposition time, to obtain a homogeneous thin coating of zinc oxide. The objective was to not clog the pores. As seen in Figure 3, 45 minutes of electrodeposition merely filled all the pores with ZnO particles, while 30 and 15 minutes of deposition resulted in more homogenous coatings

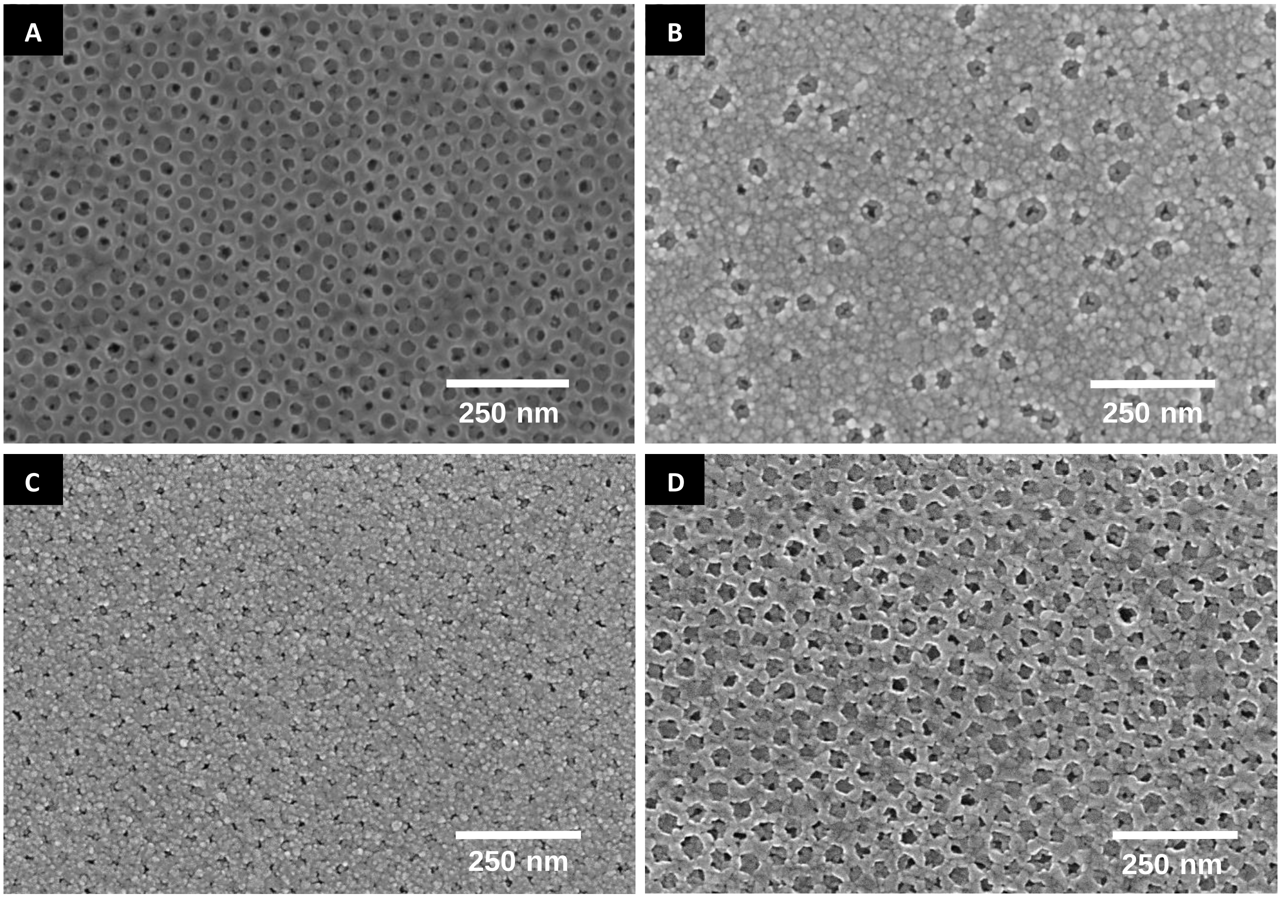

Figure. 3 SEM-FEG micrographs of the **(a)** nude mesoporous TiO_2 films (2 layers) **(b)** Coated (a) by ZnO after 45 minutes of electrodeposition, **(c)** Coated (a) by ZnO after 30 minutes of electrodeposition, and (d) Coated (a) by ZnO after 15 minutes of electrodeposition. All films were calcinated at 450 ºC in the air for 1h.

The photocatalytic activities of these three films were studied and compared (under the same experimental conditions using 10 ppm MB, under UVA irradiation of 365 nm). As seen in Figure 4a, the kinetic results came in the following order: *Kapp* of ZnO/TiO_2 (15 minutes electrodeposition) = 0.0265 min^{-1} > K*app* of ZnO/TiO_2 (30 minutes electrodeposition) = 0.018 min^{-1} > K*app* of ZnO/TiO_2 (45 minutes electrodeposition) = 0.0164 min^{-1} > K*app* of nude TiO_2 = 0.0132 min^{-1}. The highest catalytic activity of the ZnO/TiO_2 films is achieved for 15 minutes of electrodeposition.

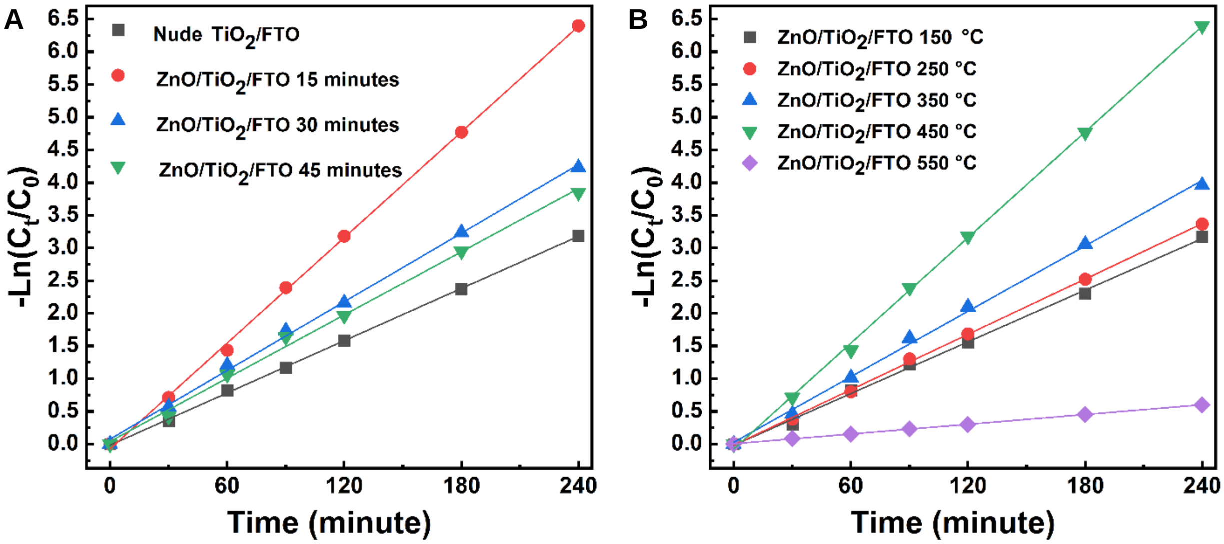

Figure. 4 Photocatalytic degradation of 10 ppm MB under UVA ($\lambda = 365$ nm) using ZnO/TiO_2/FTO films with **(a)** different durations of electrodeposition, **(b)** different heat treatment temperatures.

Additionally, the 15-minute ZnO electrodeposited film was optimized as a function of heat treatment to obtain the maximum photocatalytic efficiency. For this reason, the films were calcined at different temperatures from 150 ºC to 550 ºC. The photocatalytic data in Figure 4b shows that the kinetic rates increase from 0.0131 min^{-1} to 0.0265 min^{-1} as the temperature goes from 150 ºC to 450 ºC, and then drop down to 0.0025 min^{-1} at 550 ºC. The ECSAs are comparable for the various temperatures and cannot explain the observed variation. This important increment in photocatalytic degradation rate between 150 ºC and 450 ºC, is probably correlated with the enhancement of ZnO crystallinity[7]. At the optimal annealing temperature of 450 ºC, the selective area electron diffraction (SAED) pattern reveals mainly the (100), and (101) crystallographic planes of the wurtzite structure of ZnO, in addition to the (101), and (103) planes of the TiO_2 anatase (Figure 5a). The boundary of ZnO/TiO_2 heterojunction is delineated by transmission electron microscopy operating in high-resolution mode (Figure 5b). It can be seen 2 distinct and regular lattice fringes on each part of the TEM images. For instance, the anatase TiO_2 is characterized by an interplanar spacing of $d_{101} = 0.351$ nm whereas the wurtzite ZnO shows a maximum spacing of 0.282 mn (d_{100}). These crystallographic planes are further identified with the fast Fourier transform (FFT) in Figure 5c and d. This suggests that the electrodeposited ZnO follows a preferential orientation in an attempt to match with the TiO_2 crystal structure. As a result, this epitaxial behavior is expected to yield a good ZnO/TiO_2 interface.

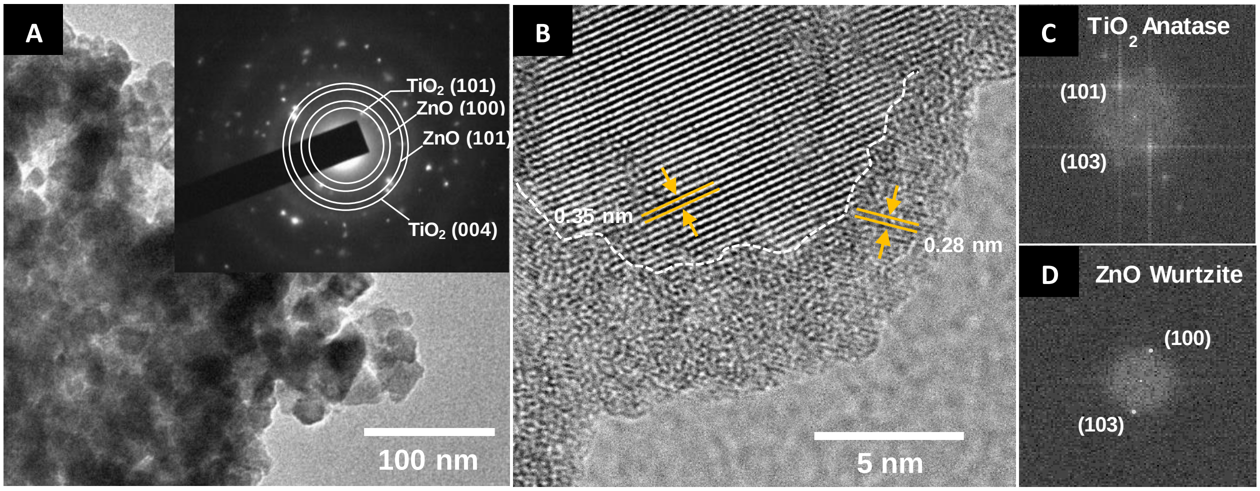

Figure. 5 (a) TEM image of an extracted ZnO/TiO_2 layer corresponding to 15 minutes of electrodeposition and 450 ^{0}C heat treatment. Inset: SAED pattern, and **(b)** HRTEM view of (a). **(c)** and **(d)** FFT pattern.

On the other side, the remarkable decrease in the photocatalytic rate at T= 550 ^{0}C is generally due to some transformation of anatase TiO_2 to the rutile phase, as the latter was commonly reported for heat treatment above 450 ^{0}C[8–10]. Moreover, the photoelectrochemical efficiency of the optimized catalyst was investigated.

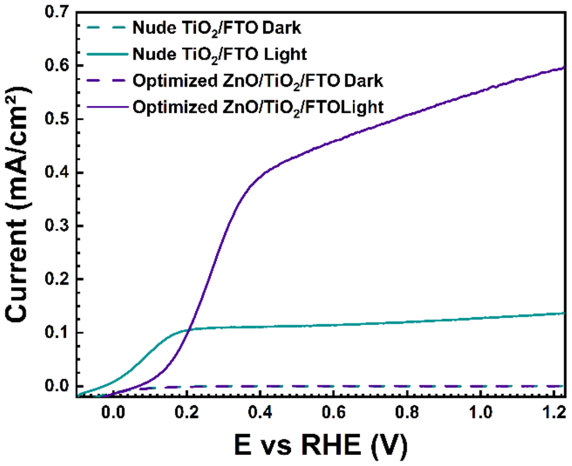

Figure. 6 Linear sweep voltammetry (LSV) pattern for the optimized ZnO/TiO_2/FTO film (electrodeposition for 15 minutes, and post-heat treatment of 450 ºC for 1h) compared to a nude mesoporous TiO_2 coated over FTO. Both films possess the same thickness.

The LSV is reported in Figure 6. The LSV curves exhibit a remarkable onset potential of -0.03 V for all the tested films. Nevertheless, under the light, the photoelectrochemical measurements indicate that coating the mesoporous TiO_2 electrode with ZnO for 15 minutes and optimizing the post-heat treatment resulted in a significant increase in the current density from 0.11 to 0.6V. Furthermore, the stability of this electrode is investigated with chronoamperometry measurements in a relatively low-acidic pH. Indeed this stability can be observed in Figure 7 where both catalysts (TiO_2/FTO and ZnO/TiO_2/FTO) display constant current densities over an experimental time of 2 hours. More interestingly, no current loss is detected due to electron-hole recombination. This observation is mainly due to the efficient charge separation in both films, at the TiO_2/FTO and ZnO/TiO_2/FTO heterojunctions, in accordance with literature[11–15]. These findings are still a topic of ongoing research and aim to open windows on efficient fabrication approaches for highly active catalysts in both photocatalysis and photoelectrocatalysis applications.

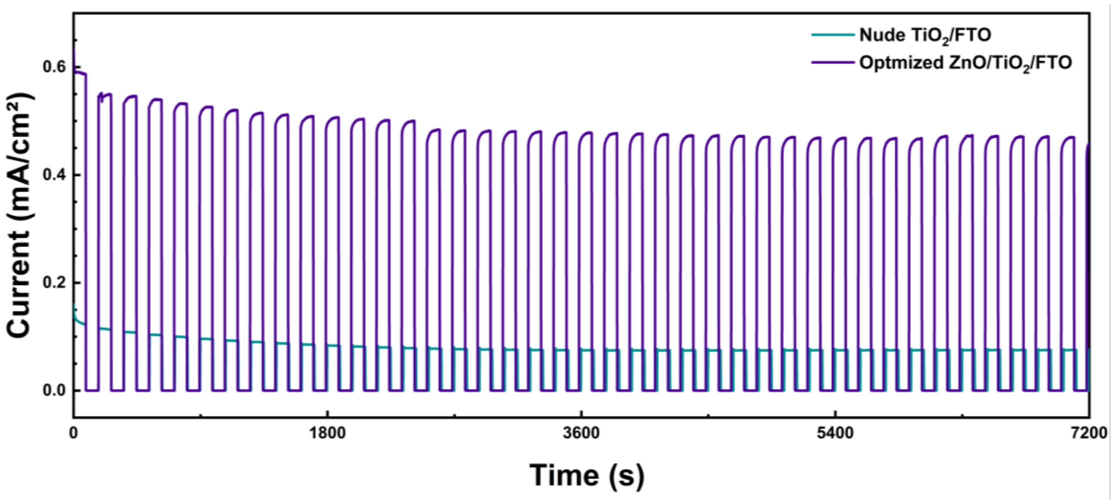

Figure. 7 Chronoamperometry curves for the optimized ZnO/TiO_2/FTO film (electrodeposition for 15 minutes, and post-heat treatment of 450 ºC for 1h) compared to a nude mesoporous TiO_2 coated over FTO (UV-vis lamp of 50 – 500 W). Both films possess the same thickness.

References

(1) Neaţu, F.; Abramiuc, L. E.; Trandafir, M. M.; Negrea, R. F.; Florea, M.; Teodorescu, C. M.; Neaţu, S. Degenerated TiO_2 Semiconductor Modified with Ni and Zn as Efficient Photocatalysts for the Water Splitting Reaction. *ChemCatChem* **2020**, *12* (18), 4642–4651. https://doi.org/10.1002/cctc.202000691.

(2) Guo, S.; Han, S.; Mao, H.; Dong, S.; Wu, C.; Jia, L.; Chi, B.; Pu, J.; Li, J. Structurally Controlled ZnO/TiO2 Heterostructures as Efficient Photocatalysts for Hydrogen Generation from Water without Noble Metals: The Role of Microporous Amorphous/Crystalline Composite Structure. *Journal of Power Sources* **2014**, *245*, 979–985. https://doi.org/10.1016/j.jpowsour.2013.07.044.

(3) Kayaci, F.; Vempati, S.; Ozgit-Akgun, C.; Donmez, I.; Biyikli, N.; Uyar, T. Selective Isolation of the Electron or Hole in Photocatalysis: ZnO–TiO2 and TiO2–ZnO Core–Shell Structured Heterojunction Nanofibers via Electrospinning and Atomic Layer Deposition. *Nanoscale* **2014**, *6* (11), 5735. https://doi.org/10.1039/c3nr06665g.

(4) Prasad Kafle, B. Effect of Precursor Fluorine Concentration Optical and Electrical Properties of Fluorine Doped Tin Oxide Thin Films. *Materials Today: Proceedings* **2021**, *47*, 6389–6397. https://doi.org/10.1016/j.matpr.2021.08.173.

(5) Eyraud, M.; Cadena, G. J.; Chassigneux, C.; Vacandio, F.; Comini, E.; Sberveglieri, G.; Djenizian, T. Electrochemical Fabrication of Oriented ZnO Nanorods on TiO<SUB Align="right">2 Nanotubes. *IJNT* **2012**, *9* (3/4/5/6/7), 295. https://doi.org/10.1504/IJNT.2012.045333.

(6) Karakaya, C.; Solati, N.; Balkan, T.; Savacı, U.; Keleş, E.; Turan, S.; Kaya, S. Mesoporous Molybdenum Sulfide-Oxide Composite Thin-Film Electrodes Prepared by a Soft Templating Method for the Hydrogen Evolution Reaction. *ACS Appl. Energy Mater.* **2022**, *5* (6), 7006–7015. https://doi.org/10.1021/acsaem.2c00640.

(7) Daher, E. A.; Riachi, B.; Chamoun, J.; Laberty-Robert, C.; Hamd, W. New Approach for Designing Wrinkled and Porous ZnO Thin Films for Photocatalytic Applications. *Colloids and Surfaces A: Physicochemical and Engineering Aspects* **2023**, *658*, 130628. https://doi.org/10.1016/j.colsurfa.2022.130628.

(8) Liu, S.; Yu, J.; Jaroniec, M. Anatase TiO_2 with Dominant High-Energy {001} Facets: Synthesis, Properties, and Applications. *Chem. Mater.* **2011**, *23* (18), 4085–4093. https://doi.org/10.1021/cm200597m.

(9) Li, J.; Liu, L.; Sham, T.-K. 2D XANES–XEOL Spectroscopy Studies of Morphology-Dependent Phase Transformation and Corresponding Luminescence from Hierarchical TiO_2 Nanostructures. *Chem. Mater.* **2015**, *27* (8), 3021–3029. https://doi.org/10.1021/acs.chemmater.5b00363.

(10) Zhang, Q.; Li, C. High Temperature Stable Anatase Phase Titanium Dioxide Films Synthesized by Mist Chemical Vapor Deposition. *Nanomaterials* **2020**, *10* (5), 911. https://doi.org/10.3390/nano10050911.

(11) Ashok, A.; Vijayaraghavan, S. N.; Nair, S. V.; Shanmugam, M. Molybdenum Trioxide Thin Film Recombination Barrier Layers for Dye Sensitized Solar Cells. *RSC Adv.* **2017**, *7* (77), 48853–48860. https://doi.org/10.1039/C7RA08988K.

(12) Jiang, L.; Yu, H.; Shi, L.; Zhao, Y.; Wang, Z.; Zhang, M.; Yuan, S. Optical Band Structure and Photogenerated Carriers Transfer Dynamics in FTO/TiO 2 Heterojunction Photocatalysts. *Applied Catalysis B: Environmental* **2016**, *199*, 224–229. https://doi.org/10.1016/j.apcatb.2016.05.070.

(13) Shen, K.; Wu, K.; Wang, D. Band Alignment of Ultra-Thin Hetero-Structure ZnO/TiO2 Junction. *Materials Research Bulletin* **2014**, *51*, 141–144. https://doi.org/10.1016/j.materresbull.2013.12.013.

(14) Kighuta, K.; Gopalan, A.-I.; Lee, D.-G.; Kim, S.-W.; Park, S.-S.; Lee, D.-E.; Lee, K.-P.; Kim, W.-J. Novel Visible Light Active Ternary TiO2-ZnO-WO3 Composites: Facile Preparation Strategy and Performance Evaluation Using the Response Surface Design. *Journal of Environmental Chemical Engineering* **2022**, *10* (5), 108224. https://doi.org/10.1016/j.jece.2022.108224.

(15) John K, A.; Naduvath, J.; Mallick, S.; Pledger, J. W.; Remillard, S. K.; DeYoung, P. A.; Thankamoniamma, M.; Shripathi, T.; Philip, R. R. Electrochemical Synthesis of Novel Zn-Doped TiO2 Nanotube/ZnO Nanoflake Heterostructure with Enhanced DSSC Efficiency. *Nano-Micro Lett.* **2016**, *8* (4), 381–387. https://doi.org/10.1007/s40820-016-0099-z.